Tension Testing of Ultra-High Performance Concrete

PUBLICATION NO. FHWA-HRT-17-053

FEBRUARY 2019

U.S. Department of Transportation
Federal Highway Administration

Research, Development, and Technology
Turner-Fairbank Highway Research Center
6300 Georgetown Pike
McLean, VA 22101-2296

FOREWORD

Ultra-high performance concrete (UHPC) is an advanced construction material that affords new opportunities for future highway infrastructure. The Federal Highway Administration (FHWA) has been engaged in research on the optimal uses of UHPC in highway bridge infrastructure since 2001 and has witnessed deployment of various forms of UHPC technology in bridges around the United States. For UHPC to become a widely engaged and commonly deployed structural material, design specifications, construction specifications, and material qualification test methods must be developed. This report presents results of a study aimed at developing test methods to quantify the tensile response of UHPC, thus facilitating both the drafting of design specifications that engage this response and the practical use of UHPC materials in structures that rely on this response.

The research discussed herein was conducted jointly through a collaboration between the respective structural concrete research programs within the Federal-level highway research agencies in the United States (FHWA's Turner-Fairbank Highway Research Center) and France (French Institute of Science and Technology for Transport, Development and Networks). Owners, consultants, contractors, and technical experts interested in the use of UHPC in transportation-related structures will benefit from the information contained herein.

Cheryl Allen Richter, Ph.D., P.E.
Director, Office of Infrastructure
Research and Development

TECHNICAL REPORT DOCUMENTATION PAGE

1. Report No. FHWA-HRT-17-053	2. Government Accession No.	3. Recipient's Catalog No.
4. Title and Subtitle Tension Testing of Ultra-High Performance Concrete		5. Report Date February 2019
		6. Performing Organization Code:
7. Author(s) Benjamin A. Graybeal (ORCID: 0000-0002-3694-1369) and Florent Baby		8. Performing Organization Report No.
9. Performing Organization Name and Address Office of Infrastructure Research and Development Federal Highway Administration 6300 Georgetown Pike McLean, VA 22101-2296		10. Work Unit No.
		11. Contract or Grant No.
12. Sponsoring Agency Name and Address Office of Infrastructure Research and Development Federal Highway Administration 6300 Georgetown Pike McLean, VA 22101-2296		13. Type of Report and Period Covered Final Report; January 2010–December 2012
		14. Sponsoring Agency Code HRDI-40

15. Supplementary Notes
This research project was led by the Federal Highway Administration (FHWA). The French Roads and Bridges Research Agency partnered with FHWA on the planning and execution of the project.

16. Abstract
Ultra-high performance concrete (UHPC) is a class of cementitious composite materials designed to exhibit exceptional mechanical and durability properties, including sustained postcracking tensile strength. Laboratory tests of structural elements have clearly indicated that UHPC components can exhibit tensile mechanical properties far in excess of those expected from conventional or fiber-reinforced concretes. This study developed a material scale direct tension test applicable to UHPC that relates the full range of uniaxial tensile behaviors through strain localization and can be completed on cast or extracted specimens. In order to demonstrate applicability, the test method was carried out in parallel with other UHPC tension test methods. This research model allowed for both development of a practical test method along with direct determination of the tensile mechanical properties of two commercially available UHPC-class materials.

17. Key Words	18. Distribution Statement
Ultra-high performance concrete, UHPC, Fiber-reinforced concrete, Direct tension test, Prism flexure test, Uniaxial tensile mechanical response	No restrictions. This document is available to the public through the National Technical Information Service, Springfield, VA 22161. http://www.ntis.gov

19. Security Classif. (of this report)	20. Security Classif. (of this page)	21. No. of Pages	22. Price
Unclassified	Unclassified	206	N/A

Form DOT F 1700.7 (8-72) Reproduction of completed page authorized.

SI* (MODERN METRIC) CONVERSION FACTORS

APPROXIMATE CONVERSIONS TO SI UNITS

Symbol	When You Know	Multiply By	To Find	Symbol
		LENGTH		
in	inches	25.4	millimeters	mm
ft	feet	0.305	meters	m
yd	yards	0.914	meters	m
mi	miles	1.61	kilometers	km
		AREA		
in^2	square inches	645.2	square millimeters	mm^2
ft^2	square feet	0.093	square meters	m^2
yd^2	square yard	0.836	square meters	m^2
ac	acres	0.405	hectares	ha
mi^2	square miles	2.59	square kilometers	km^2
		VOLUME		
fl oz	fluid ounces	29.57	milliliters	mL
gal	gallons	3.785	liters	L
ft^3	cubic feet	0.028	cubic meters	m^3
yd^3	cubic yards	0.765	cubic meters	m^3
		NOTE: volumes greater than 1000 L shall be shown in m^3		
		MASS		
oz	ounces	28.35	grams	g
lb	pounds	0.454	kilograms	kg
T	short tons (2000 lb)	0.907	megagrams (or "metric ton")	Mg (or "t")
		TEMPERATURE (exact degrees)		
^oF	Fahrenheit	5 (F-32)/9 or (F-32)/1.8	Celsius	^oC
		ILLUMINATION		
fc	foot-candles	10.76	lux	lx
fl	foot-Lamberts	3.426	$candela/m^2$	cd/m^2
		FORCE and PRESSURE or STRESS		
lbf	poundforce	4.45	newtons	N
lbf/in^2	poundforce per square inch	6.89	kilopascals	kPa

APPROXIMATE CONVERSIONS FROM SI UNITS

Symbol	When You Know	Multiply By	To Find	Symbol
		LENGTH		
mm	millimeters	0.039	inches	in
m	meters	3.28	feet	ft
m	meters	1.09	yards	yd
km	kilometers	0.621	miles	mi
		AREA		
mm^2	square millimeters	0.0016	square inches	in^2
m^2	square meters	10.764	square feet	ft^2
m^2	square meters	1.195	square yards	yd^2
ha	hectares	2.47	acres	ac
km^2	square kilometers	0.386	square miles	mi^2
		VOLUME		
mL	milliliters	0.034	fluid ounces	fl oz
L	liters	0.264	gallons	gal
m^3	cubic meters	35.314	cubic feet	ft^3
m^3	cubic meters	1.307	cubic yards	yd^3
		MASS		
g	grams	0.035	ounces	oz
kg	kilograms	2.202	pounds	lb
Mg (or "t")	megagrams (or "metric ton")	1.103	short tons (2000 lb)	T
		TEMPERATURE (exact degrees)		
^oC	Celsius	1.8C+32	Fahrenheit	^oF
		ILLUMINATION		
lx	lux	0.0929	foot-candles	fc
cd/m^2	$candela/m^2$	0.2919	foot-Lamberts	fl
		FORCE and PRESSURE or STRESS		
N	newtons	0.225	poundforce	lbf
kPa	kilopascals	0.145	poundforce per square inch	lbf/in^2

*SI is the symbol for the International System of Units. Appropriate rounding should be made to comply with Section 4 of ASTM E380.
(Revised March 2003)

TABLE OF CONTENTS

LIST OF FIGURES

LIST OF TABLES

LIST OF ABBREVIATIONS AND SYMBOLS

Abbreviations

AFGC	Association Française de Génie Civil
AFGC-SETRA	Association Farnçaise de Génie Civil–Service d'étude des transports, des routes et de leure aménagement
DTT	direct tension test
ECC	engineered cementitious composite
FHWA	Federal Highway Administration
FRC	fiber-reinforced concrete
FT	flexure test
JCI	Japanese Concrete Institute
LVDT	linear variable displacement transducer
MOR	modulus of rupture
PE-ECC	polyethylene fiber-reinforced engineered cementitious composite
SCT	splitting cylinder test
SHCC	strain-hardening cementitious composite
SI	International System of Units
UHPC	ultra-high performance concrete

Symbols

a	shear span length
a_1, a_2, and b_2	parameters defining the stress versus crack opening relationship
$A - B$	relative deviation between methods A and B
b	width of test specimen
c	slope of the stress–strain curve
$C - B$	relative deviation between methods C and B
d	deflection capacity
dz	differential with respect to distance from the tensile face
E	modulus of elasticity
E_c	modulus of cementitious matrix
E_{cc}	precracking stiffness
EMD_{j+1}	experimental midspan deflection at increment $j + 1$
E_f	modulus of elasticity of fibers

E_{pc}	stiffness at peak load
E_{t1}	slope of the elastic tensile curve
E_{t2}	slope of the inelastic tensile curve
f_{bc}	compressive stress limit
f'_c	compressive strength
f_{tb}	effective tensile strength
f_{tc}	first cracking strength
f_{tcm}	cementitious matrix strength (without fibers)
$f_{tcm\text{-}chara}$	characteristic cementitious matrix strength (without fibers)
f_{tj}	tensile strength of the cementitious matrix
f_{tu}	ultimate tensile strength
f_{tuj}	ultimate tensile strength
g	stress intercept of the stress–strain curve
$G_{Average\text{-}f,A,n}$	average fracture energy dissipated during strain hardening per unit area to generate a number of cracks (n_{cr})
G_f	fracture energy
$g_{f,A}$	fracture energy dissipated during strain hardening per unit volume
$G_{f,A}$	fracture energy dissipated during strain hardening per unit area for area A
$G_{f,B}$	fracture energy dissipated during strain hardening per unit area for area B
$G_{f,A,n}$	fracture energy dissipated during strain hardening per unit area to generate a number of cracks (n_{cr})
$G^*_{f,A,n}$	characteristic fracture energy dissipated during strain hardening per unit area to generate cracks
$G_{f,B}$	fracture energy dissipated during softening per unit area
h	depth (height) of specimen
h_0	distance between the two linear variable displacement transducers
i	data point
I	moment of inertia
j	increment
K	stress ratio (dimensionless)
$k(n)$	Student coefficient depending on the number of tested specimens
L	span length
L_f	fiber length

$L_{f\text{-}max}$	maximum fiber length
L_g	gauge length
M	moment
M_c	compressive component of the applied moment
M_{cj}	compressive component of the applied moment at increment j
min	minimum of the values
M_j	moment at increment j
$M_{cj\,+\,1}$	compressive component of the applied moment at increment j + 1
$M_{j\,+\,1}$	moment at increment j + 1
$M_{j\text{-}experimental}$	experimental moment at increment j
M_{max}	maximum moment
$M^{max}{}_{Average\text{-}curve}$	maximum moment of the average curve
$M^{max}{}_{Chara\text{-}curve}$	maximum moment of the characteristic curve
M'_{max}	maximum moment resulting from the assumption of intermediate stress value σ_3
M_r	resistant moment of the section
M_t	tensile component of the applied moment
M_{tj}	tensile component of the applied moment at increment j
$M_{tj\,+\,1}$	tensile component of the applied moment at increment j + 1
$MD_{j\,+\,1}$	model-based midspan deflection at increment j + 1
n	number of data points
N	normal force
N_c	compressive component of the normal force
N_{cj}	compressive component of the normal force at increment j
$N_{cj\,+\,1}$	compressive component of the formal force at increment j + 1
n_{cr}	number of cracks
n_{spe}	number of specimens
N_t	tensile component of the normal force
N_{tj}	tensile component of the normal force at increment j
$N_{tj\,+\,1}$	tensile component of the normal force at increment j + 1
OPD	off-plane distance
P	point load
P_i	experimental load at the corresponding deflection

$\widehat{P}_i$	load obtained by the model for a certain deflection
PD	predicted deviation for tensile strain capacity considering the standard deviation of the deflection capacity
s	hinge extension
S	standard deviation
s_{cr}	crack spacing
SD	standard deviation of the deflection capacity
V_f	percentage of fibers
w	crack opening
W	dissipated work
w_{pc}	permanent crack opening
w_u	maximum crack opening
w_1	crack opening at point 1
w_2	crack opening at point 2
z	distance from the tensile face of the test specimen
z_1	cementitious matrix strength depth parameter
α	unitless parameter to determine height of a specimen with respect to the total height of the specimen
α_1	distance from the tensile face to the linear elastic tensile limit divided by the height of the specimen
α_2	distance from the tensile face to the point of maximum tensile stress divided by the height of the specimen
α_3	distance from the tensile face to the linear elastic compressive limit divided by the height of the specimen
α_4	distance from the tensile face to the point of maximum compressive stress divided by the height of the specimen
α_n	distance from the tensile face to the neutral axis divided by the height of the specimen
α_{n1}	distance from the tensile face to the neutral axis divided by the height of the specimen at the initial increment
α_{nj}	distance from the tensile face to the neutral axis divided by the height of the specimen at increment j
α_{nj+1}	distance from the tensile face to the neutral axis divided by the height of the specimen for increment $j + 1$
α_w	cracked depth divided by the height of the specimen
δ	deflection

δ_m	midspan deflection
δ_{mj}	midspan deflection at increment j
δ_{min}	minimum midspan deflection limit from the tests
δ_p	deflection at the load point
δ_u	ultimate deflection
ε	strain
$\varepsilon_{1,}\ \varepsilon_{2,}\ \varepsilon_{3,}\ \varepsilon_4$	strain associated with intermediate stress values σ_1, σ_2, σ_3, and σ_4
ε'_1	strain at the start of intermediate stress value σ_3
ε_{1u}	strain at maximum load as measured by the upper linear variable displacement transducer
ε_{2u}	strain at maximum load as measured by the lower linear variable displacement transducer
$\varepsilon^a{}_1$	elastic strain limit associated with method A
$\varepsilon^a{}_{min}$	minimum strain limit associated with method A
$\varepsilon^a{}_{min\text{-}ppt}$	minimum strain limit associated with method A determined by a point-by-point analysis method
$\varepsilon_{Average\text{-}Hardening\text{-}Strain}$	average hardening strain
$\varepsilon^b{}_1$	elastic strain limit associated with method B
$\varepsilon^b{}_{min}$	minimum strain limit associated with method B
ε_{bc}	strain corresponding to f_{bc}
ε_c	compressive strain
$\varepsilon^c{}_1$	elastic strain limit associated with method C
ε_{cc}	first cracking strain
$\varepsilon_c(z)$	compressive strain as a function of distance from the tensile face
$\varepsilon^c{}_{min}$	minimum strain limit associated with method C
$\varepsilon_{corrected}$	corrected midspan strain at the bottom flange
$\varepsilon^d{}_1$	elastic strain limit associated with method D
$\varepsilon^d{}_{min}$	minimum strain limit associated with method D
$\varepsilon^d{}_{min\text{-}simp}$	minimum strain limit associated with method D determined by a simplified analysis method
$\varepsilon^e{}_1$	elastic strain limit associated with method E
ε_e	tensile strain capacity of the cementitious matrix
$\varepsilon^e{}_{min}$	minimum strain limit associated with method E
ε_{end}	strain limit

ε_{end1}	strain limit associated with the average hardening strain
ε_{end2}	strain limit associated with an irreversible decrease of the stress–strain relationship
$\varepsilon_{end\text{-}dtt}$	strain limit as determined by the direct tension test
$\varepsilon_{end\text{-}ppt}$	strain limit as determined by a point-by-point analysis method
$\varepsilon_{end\text{-}simp}$	strain limit as determined by a simplified analysis method
$\varepsilon_{measured}$	measured midspan strain at the bottom flange
ε_{min}	minimum strain limit from the series of tests
$\varepsilon_{min\text{-}crack}$	average strain corresponding to the minimum of both staggered linear variable displacement transducers measured at crack localization
$\varepsilon_{Min\text{-}Hardening\text{-}Strain}$	average minimum hardening strain
$\varepsilon_{Min\text{-}specimen\text{-}i}$	minimum measured strain value
ε_{pc}	strain associated with maximum postcracking stress
ε_{real}	actual midspan strain at the bottom flange
$\varepsilon_{specimen\text{-}i}$	hardening strain
ε_{t}	tensile strain
ε_{t1}	tensile strain at increment 1
ε_{tf}	strain at the extreme tensile fiber
ε_{tfj}	strain at the extreme tensile fiber at increment j
ε_{tfj+1}	strain at the extreme tensile fiber at increment j+1
ε_{tj}	tensile strain at increment *j*
$\varepsilon_{tj\,+\,1}$	tensile strain at increment *j + 1*
$\varepsilon_{tj\,+\,1\text{-}measured}$	measured tensile strain at increment *j + 1*
ε_{tu}	tensile strain capacity
ε'_{tu}	predicted tensile strain capacity
$\varepsilon_{tu,b}$	ultimate tensile strain
ε_{u}	strain capacity
σ	stress
σ_1, σ_2, σ_3, and σ_4	intermediate stress values
$\sigma^a{}_1$	cracking stress associated with method A
$\sigma^a{}_2$	maximum stress associated with method A
σ_b	stresses in the uncracked depth
$\sigma^b{}_1$	cracking stress associated with method B

$\sigma^b{}_2$	maximum stress associated with method B
σ_c	compressive stress
$\sigma^c{}_1$	cracking stress associated with method C
$\sigma^c{}_2$	maximum stress associated with method C
$\sigma_c(z)$	compressive stress as a function of distance from the tensile face
σ_{cc}	first cracking stress
$\sigma^d{}_1$	cracking stress associated with method D
$\sigma^d{}_2$	maximum stress associated with method D
$\sigma^e{}_1$	cracking stress associated with method E
$\sigma^e{}_2$	maximum stress associated with method E
σ_E	equivalent stress
$\Delta\sigma_E$	change in equivalent stress
σ_{equi}	equivalent bending stress
σ_f	stress in the cracked depth
$\sigma_{Linear\text{-}Part}$	straight sections of the equivalent stress–midspan deflection curve beyond the change in equivalent stress
σ_{pc}	maximum postcracking stress
$\sigma_{plastic}$	plateau stress in a tensile stress–strain response
$\sigma_{Raw\text{-}Curve}$	any section of the equivalent stress–midspan deflection curve
σ_t	tensile stress
σ_{t1}	tensile stress at increment 1
σ_{tj}	tensile stress at increment *j*
σ_{tj+1}	tensile stress at increment *j + 1*
ϕ	beam curvature
ϕ_0	beam curvature at tensile elastic limit
$\phi^{\acute{e}}$	beam curvature at the elastic limit
$\phi^{\acute{e}}{}_j$	beam curvature at the elastic limit at increment *j*
$\phi^{\acute{e}}{}_{j+1}$	beam curvature at the elastic limit at increment *j* + 1
ϕ_j	beam curvature at increment *j*
ϕ_{j+1}	beam curvature at increment *j + 1*
$\phi_{j+1Assumed}$	assumed beam curvature at increment *j + 1*
$\phi_{j\text{-}experimental}$	experimental beam curvature at increment *j*

ϕ_{min}	minimum beam curvature limit from the series of tests
ϕ_u	beam curvature at maximum load
ψ	coefficient of orientation

CHAPTER 1. INTRODUCTION

INTRODUCTION

Ultra-high performance concrete (UHPC) is a class of cementitious composite materials designed to exhibit exceptional mechanical and durability properties, including sustained postcracking tensile strength.[1–9] Laboratory tests of structural elements have clearly indicated that UHPC components can exhibit tensile mechanical properties far in excess of those expected from conventional and fiber-reinforced concretes (FRCs).[10–16] However, there are currently no practical test methods available that directly assess these tensile mechanical properties. The research discussed herein focused on developing an appropriate tension test method for assessing UHPC tensile response.

OBJECTIVE

The objective of this research program was to develop a direct tension test (DTT) applicable to UHPC that relates the full range of uniaxial tensile behaviors through strain localization and can be completed on cast or extracted specimens.

SUMMARY OF APPROACH

The research discussed herein focused on developing a tension test for UHPC that directly relates the uniaxial tensile properties of the concrete from global elastic behavior through localization of strain within an individual crack. In order to facilitate standardization, the test was developed with a focus on the use of commercially available testing equipment, the use of prismatic specimens, and the completion of individual tests in less than 1 hour. In order to demonstrate applicability, the test method was carried out, as is discussed in further detail throughout this report, in parallel with other UHPC tension test methods. This research model allowed for both the development of a practical test method along with direct determination of the tensile mechanical properties of two commercially available UHPC-class materials. Select results from this research program have been published in journal papers focusing on the DTT method and the flexure test (FT) method.[17–19]

REPORT ORGANIZATION

This report is organized into the following eight chapters:

- Chapter 1 introduces the study.
- Chapter 2 provides relevant background information.
- Chapter 3 presents the test program, details the specimens, and provides compression mechanical properties.
- Chapter 4 presents the results from the DTTs.
- Chapter 5 presents the results from the FTs.

- Chapter 6 presents the results from the splitting cylinder tests (SCTs).
- Chapter 7 provides a compilation of the results as well as the analysis.
- Chapter 8 presents the conclusions and recommendations for future research.

CHAPTER 2. BACKGROUND

INTRODUCTION

This chapter introduces UHPC and provides background information on test methods traditionally used to assess the tensile mechanical properties of concrete, FRC, and UHPC.

ULTRA-HIGH PERFORMANCE CONCRETE (UHPC)

The term "UHPC" refers to a class of advanced cementitious composite materials. Many of the technological advances in the field of cement and concrete science have been brought together in the development of this class of concretes. In general terms, these concretes can be classified as high-strength, fiber-reinforced cementitious composites with discontinuous pore structures and enhanced durability properties. These concretes tend to have exceptionally low water-to-cementitious materials ratios and an optimized gradation of granular materials.

UHPC frequently includes discontinuous, dispersed fiber reinforcement. This fiber reinforcement is included with the other constituents during initial mixing and, after concrete placement and curing, provides for enhanced tensile mechanical behaviors. Structural applications of UHPC frequently include short lengths of steel fiber reinforcement, which is included at moderately high percentages, such as 2 percent by volume.

Within this research project, the postcracking tensile mechanical behaviors commonly associated with UHPC were of critical importance. Previous laboratory tests of structural elements have clearly indicated that UHPC components can exhibit tensile mechanical properties far in excess of those expected from conventional concretes and traditional FRCs. However, the lack of standard test procedures for assessing the tensile mechanical properties has become a hurdle, leading to hesitancy among designers considering the engagement of these properties in UHPC components within the civil infrastructure.

TENSION TEST METHODS FOR FIBER-REINFORCED CONCRETES (FRCs)

The need to assess the tensile mechanical properties of concrete depends on the tensile demand placed on the concrete. Additionally, the test methods available for accurately assessing these tensile mechanical properties are limited. The advent of concretes with higher tensile strength and FRCs that display sustained postcracking tensile strength has necessitated the development of appropriate test methods. However, specific quantification of these properties has proven difficult, hindering the broad deployment of this class of concretes.

Indirect Test Methods

Due to its comparatively small tensile stress and strain capacities, conventional concrete does not lend itself to the application of DTT methods. As such, indirect test methods have been developed to assess elastic tensile response through first cracking. Common indirect-tension test methods include the ASTM C78 FT and the ASTM C496 SCT.[20,21] Over the years, these test methods have been modified and expanded to facilitate testing of FRC and strain-hardening

cementitious composites (SHCCs). Test methods, such as the one identified in ASTM C1609, fall into this category.[22]

However, determining the uniaxial tensile stress–strain response of a concrete based on these tests has proven difficult. Common concerns with unnotched flexure-type indirect test methods include the strain gradient allowing for restraint of the most heavily loaded tensile face as well as the assumptions and computations necessary to backcalculate the uniaxial behavior. Additional concerns are raised when flexure-type indirect tests are modified to include a notch that predisposes the failure location. However, this kind of test can be useful for softening materials and has been used successfully for assessing the performance of extracted prisms to qualify the orientation of fibers in a structure.[4]

There has also been some interest in splitting-type indirect tests for assessing FRC tensile behavior; however, these tests raise concerns with the biaxial state of stress and the impact that this stress state has on the bonding performance of the fiber reinforcement bridging a crack.[23]

Direct Test Methods

DTTs have been conducted since at least 1928, when Gonnerman and Shuman tested 152-mm (6-inch)-diameter conventional concrete cylinders by gripping the specimen ends with cylindrical steel straps friction clamped to the concrete circumference.[24] In the following years, DTT method development for concrete has progressed along two parallel paths. One path can be generally described as test methods that use adhesives to affix the end surfaces of a tensile specimen to testing machine fixturing, after which a uniaxial tensile load is applied. Examples include both standardized and nonstandardized test methods.[25–32] A significant benefit of this type of test is that the specimen can be loaded in uniaxial tension without the imposition of significant bending stresses. However, such a test requires the specimen be glued between the crossheads of the test machine, thus significantly increasing the duration of individual tests. Moreover, local stress effects in a specimen near the adhered surfaces frequently result in premature, nonuniform specimen failure.

The second path can be broadly classified as test methods that grip parallel sides at each end of the concrete specimen. Prior work along this path has tended toward the use of custom fabricated dog bone–shaped specimens.[33–41] However, some work on prismatic specimens has been completed, as well.[42–45] Although tests requiring custom fabrication can relate valuable results, this type of test has inherent limitations as it is not generally applicable to the types of extracted specimens that would accurately represent the tensile properties in a structural element. Some of these test methods allow for relative rotation of the ends of a specimen, thus reducing initial bending while invalidating the postcracking response. (See references 33, 34, 42, and 44.) Others notch the specimen at the midspan, thus predetermining the failure location while simultaneously imparting a large stress concentration.[42,43]

CHAPTER 3. TEST PROGRAM

INTRODUCTION

The objective of this research program was to develop a quantitative test method for assessing the tensile mechanical properties of UHPC-class materials. The test program was developed to allow for the creation of the novel test method and then assess the performance of the test method as compared to alternate test procedures (i.e., FT and SCT, which are discussed in further detail in this report). This chapter provides an overview of the test program, discusses the general characteristics of the UHPC-class materials engaged in the project, explains the fabrication procedure, and presents the compression mechanical properties of the UHPCs.

TEST PROGRAM

The test program was designed to allow for the development and assessment of a new type of DTT for measuring the tensile mechanical properties of UHPC. As such, the test program included the new DTT specimens as well as specimens to be tested through more traditional tension test methods. Specifically, two different DTT configurations, three different FT configurations, and one SCT configuration were included.

In order to facilitate generalization of the test method, the test program included multiple UHPC-class materials that were expected to present a variety of uniaxial tensile mechanical responses. Details on the sets of specimens cast for the test program are provided in table 1. The first two characters in the specimen batch name refer to the UHPC type and to the curing regime applied, respectively. The third character in the specimen batch name is a letter that sequentially increases with each additional batch.

Two different commercialized UHPC types were engaged. UHPC-F is a product of a multinational construction materials supplier. This UHPC represents the normal set version of the North American formulation of this product. It was cast with two different volumetric percentages of steel-fiber reinforcement. It was also cured under two curing regimens, steam curing and ambient lab curing. UHPC-B is a product of a multinational European construction firm. Specimens cast from this concrete were fabricated in Europe and then shipped to the United States for testing.

Table 1. Sets of test specimens.

Specimen Batch Name	UHPC Type	Steel Fiber Reinforcement Volumetric Percentage	Curing Regime	DTT Specimens		FT Specimens			Split Cylinder
				Short	Long	Short	Long	Large	
F1A	UHPC-F	2	Steam	X	X	X	X	—	X
F2A	UHPC-F	2	Lab	X	X	X	X	—	X
F1B	UHPC-F	2	Steam	X	—	X	X	—	X
F1C	UHPC-F	2.5	Steam	X	X	X	X	—	X
B2A	UHPC-B	2.5	Lab	X	—	X	X	X	X

XThis testing configuration was included in the testing program.
—This testing configuration was not included in the testing program.

Laboratory curing indicates that the specimens were maintained in a common laboratory environment from casting through testing. The environment was maintained at a temperature of 23 °C (73 °F) and 50 percent relative humidity. Steam curing indicated that the specimens in that set were subjected to a 48-hour duration steam environment beginning 3 or 4 days after casting. The steam environment was 90 °C (194 °F) and 95 percent relative humidity.

SPECIMEN FABRICATION

Each set of test specimens was cast from an individual batch of UHPC. The UHPC-F specimens were fabricated at the Federal Highway Administration's (FHWA's) Turner-Fairbank Highway Research Center. The UHPC was mixed in approximately 0.028-m^3 (1-ft^3) batches in a pan mixer. The UHPC-B specimens were fabricated in a precast factory in France. The UHPC was mixed in approximately 0.5-m^3 (17.8-ft^3) batches in a pan mixer.

After mixing, for both UHPCs, the concrete mix was placed into the specimen molds. The prismatic specimens were cast horizontally in open-top rigid steel molds. The UHPC was poured into the form at one end and allowed to flow toward the other end. Prismatic specimens with dimensions of 50.8 by 50.8 by 431.8 mm (2 by 2 by 17 inches) and 50.8 by 50.8 by 279.4 mm (2 by 2 by 11 inches) were cast for use in both the bending tests and the DTTs. For UHPC-B, the specimens were cast according to the Association Française de Génie Civil (AFGC) provisions on UHPC, which recommend a preferred standard size for molded specimens of 400 by 100 by 100 mm (15.7 by 3.9 by 3.9 inches) in relation to a fiber length of 20 mm (0.79 inch).[(4)] Six 400- by 100- by 100-mm (15.7- by 3.9- by 3.9-inch) specimens were also cast for testing in bending.

Cylindrical specimens were cast for use in the assessment of compressive mechanical properties and splitting tension tests. The cylindrical specimens were cast in vertically oriented plastic molds as follows:

- **UHPC-F**: 76.2-mm (3-inch)-diameter specimens were cast for compression testing and 101.6-mm (4-inch)-diameter specimens were cast for splitting tension tests.

- **UHPC-B**: 112.8-mm (4.4-inch)-diameter specimens were cast for compression testing and for splitting tension tests.

After casting, the exposed surface of each specimen was screeded and then loosely covered with sheet plastic to retard dehydration.

ULTRA-HIGH PERFORMANCE CONCRETE (UHPC) CYLINDER COMPRESSION MECHANICAL PROPERTIES

During the fabrication of each batch of UHPC specimens, a set of cylinders was cast to allow for the assessment of compression mechanical properties. Three cylinders were cast for the UHPC-B batch, while five or six cylinders were cast for each of the UHPC-F batches. The UHPC-B batch cylinders were 110 mm (4.33 inches) in diameter, while the UHPC-F batch cylinders were 76 mm (3 inches) in diameter. The cylinders were cast, cured, and stored with the remainder of the test specimens in each batch.

The cylinders were prepared for testing by grinding both ends to create parallel surfaces through the use of a fixed-end grinder. After preparation, the cylinders exhibited length-to-diameter ratios of approximately 1.9. Three tests were carried out on the cylinders: density, compressive strength, and modulus of elasticity. During the modulus of elasticity tests, the strain readings were electronically captured continuously from the initiation of loading through the application of the peak compressive load. Density measurements were obtained through conventional means by measuring the weight of each cylinder and dividing it by the volume.

The compressive strength and modulus of elasticity tests were completed according to ASTM C39 and ASTM C469.[46,47] Some of the cylinders were only tested for compressive strength, while others were tested for modulus of elasticity and then immediately thereafter for compressive strength. The ASTM C469 alternate procedure was engaged wherein the loading and data collection were continued through compressive failure without the removal of the strain measurement device.[47] Also, the load rate was increased to 1 MPa/second (150 psi/second). Tests completed according to ASTM C39 were also modified to include an increased load rate of 1 MPa/second (150 psi/second).[46] Strains were measured via a trio of linear variable displacement transducers (LVDTs) attached to a pair of parallel rings that were mounted on the cylinder. The gauge length for the UHPC-B batch specimens was 101.6 mm (4.0 inches), while the gauge length for the UHPC-F batch specimens was 50.8 mm (2.0 inches). The modulus of elasticity was calculated based on a best fit approximation of the stress–strain response between 10 and 30 percent of the failure load for each cylinder.

The test results for the cylinders are presented in table 2. The tests were completed approximately 4 months after casting, which was similar to the timeframe of test completion for the other tests discussed in this report.

Table 2. Cylinder density, compressive strength, and modulus of elasticity test results.

Batch Name	Specimen Number	Density, kg/m^3 (lb/ft^3)	Compressive Strength, MPa (ksi)	Modulus of Elasticity, GPa (ksi)
B2A	1	2,693 (168.1)	212.0 (30.74)	64.2 (9,310)
B2A	2	2,690 (168.0)	211.6 (30.69)	62.9 (9,120)
B2A	3	2,688 (167.8)	215.0 (31.18)	64.7 (9,390)
F1A	1	—	211.7 (30.71)	61.0 (8,840)
F1A	2	2,576 (160.8)	229.2 (33.24)	62.9 (9,120)
F1A	3	2,564 (160.1)	214.5 (31.11)	59.0 (8,560)
F1A	4	2,564 (160.0)	223.2 (32.37)	—
F1A	5	2,575 (160.7)	223.3 (32.39)	—
F1B	1	2,568 (160.3)	236.9 (34.36)	60.0 (8,700)
F1B	2	2,578 (160.9)	230.0 (33.35)	62.9 (9,120)
F1B	3	2,571 (160.5)	237.5 (34.45)	62.7 (9100)
F1B	4	2,571 (160.5)	235.0 (34.08)	—
F1B	5	2,556 (159.6)	224.9 (32.62)	—
F1B	6	2,567 (160.2)	220.2 (31.94)	—
F1C	1	2,574 (160.7)	209.4 (30.37)	60.3 (8,740)
F1C	2	2,560 (159.8)	202.9 (29.42)	59.4 (8,620)
F1C	3	2,563 (160.0)	209.2 (30.34)	61.1 (8,860)
F1C	4	2,581 (161.1)	217.8 (31.58)	—
F1C	5	2569 (160.4)	219.7 (31.86)	—
F2A	1	2,536 (158.3)	189.5 (27.49)	64.3 (9,320)
F2A	2	2,551 (159.3)	193.9 (28.12)	59.8 (8,670)
F2A	3	2546 (158.9)	194.5 (28.22)	64.5 (9350)
F2A	4	2547 (159.0)	192.9 (27.98)	—
F2A	5	2545 (158.9)	191.2 (27.73)	—

—The value was not captured for that particular test specimen.

The density results were consistent within each batch of specimens. The average density of the UHPC-B specimen B2A was 2,690 kg/m^3 (168 lb/ft^3). The average densities of steam-treated UHPC-F specimens F1A, F1B, and F1C were 2,570, 2,568, and 2,569 kg/m^3 (160.4, 160.3, and 160.4 lb/ft^3), respectively. The average density of the untreated UHPC-F specimens was 2,545 kg/m^3 (158.9 lb/ft^3).

The average compressive strength for batch B2A was 213 MPa (30.9 ksi) with a standard deviation of 1.8 MPa (0.27 ksi). The average compressive strength for batch F1A was 220 MPa (32.0 ksi) with a standard deviation of 7.1 MPa (1.0 ksi). The average compressive strength for batch F1B was 231 MPa (33.5 ksi) with a standard deviation of 7.0 MPa (1.0 ksi). The average compressive strength for batch F1C was 212 MPa (30.7 ksi) with a standard deviation of 6.9 MPa (1.0 ksi). The average compressive strength for batch F2A was 192 MPa (27.9 ksi) with a standard deviation of 2.0 MPa (0.3 ksi).

The average modulus of elasticity for batch B2A was 63.9 GPa (9,270 ksi) with a standard deviation of 1.0 GPa (140 ksi). The average modulus of elasticity for batch F1A was 61.0 GPa (8,840 ksi) with a standard deviation of 1.9 GPa (280 ksi). The average modulus of elasticity for

batch F1B was 61.9 GPa (8,970 ksi) with a standard deviation of 1.6 GPa (240 ksi). The average modulus of elasticity for batch F1C was 60.3 GPa (8740 ksi) with a standard deviation of 0.8 GPa (120 ksi). The average modulus of elasticity for batch F2A was 62.8 GPa (9,110 ksi) with a standard deviation of 2.6 GPa (380 ksi).

CHAPTER 4. DIRECT TENSION TEST (DTT) METHOD

INTRODUCTION

This chapter focuses on the DTT method developed within this study. The test method is discussed first, beginning with the preliminary studies that guided the effort and concluding with the implemented test method. The results obtained from the implementation of the test method are then presented.

TEST METHOD

The DTT method discussed herein was developed through a test program intended to develop an appropriate method of assessment for the tensile mechanical properties of strain-hardening FRCs. Prior to the start of this test program, a set of precursor tests was completed as part of a separate research effort. These tests are presented first. Next, the development of the DTT is presented within a discussion of pilot tests that were completed. Finally, the implemented test method is discussed.

Precursor Testing

A study was recently completed to assess the structural response of a UHPC beam simultaneously subjected to structural and environmental loading.[48] The results of this study include a discussion of a mechanical test that assessed the direct tensile behavior of a UHPC prism extracted from the tensile face of a UHPC beam. The need for this test originated from a desire to assess the longitudinal tensile performance of the UHPC near the extreme tensile fiber of the beam. Traditional methods of tensile mechanical property assessment were dismissed by the study authors as impractical or incapable of capturing the desired behaviors. Extraction of a thin specimen from the cover concrete below the discrete steel reinforcement was feasible, but no standard test for DTT of the specimen was available.

For strain-hardening FRCs, the authors of the study hypothesized that it may be possible to capture the tensile behavior of concrete through the implementation of a tension test method similar to that commonly used for metals. ASTM E8, presents a set of standardized tests for metals.[49] One particular test, the tension test for plate-type specimens, allows for the uniaxial tension testing of a prismatic metal specimen in a commonly available computer-controlled, closed-loop hydraulic uniaxial testing machine. In practice, hydraulic-actuated wedge grips are used to grasp the enlarged grip length of the dog bone–shaped metallic specimen. The free length between the grips inclusive of the transition areas is 300 mm (12 inches), while the gauge length of the prismatic cross section over which the strain is measured is 200 mm (8 inches). The metallic specimen is loaded in tension at a constant cross-head displacement rate.

The concepts supporting this mechanical test for metals were extended to strain-hardening concretes. A specimen was extracted from a larger component, as shown in figure 1. The dimensions of the resulting prism were 25.4 by 50.8 by 300 mm (1.0 by 2.0 by 11.9 inches). The prismatic UHPC specimen was then loaded into the 500-kN (112-kip) capacity, computer-controlled, closed-loop hydraulic uniaxial testing machine, as shown in figure 2.

Source: FHWA.

Figure 1. Photo. Extraction of a prismatic specimen from a beam tensile face.

Source: FHWA.

A. Vertical cut view (parent beam's top to bottom).

Source: FHWA.

B. Side view at a 45-degree angle.

Figure 2. Photos. DTT of a UHPC prism.

The specimen was loaded to failure three times, each time with an increasingly shorter free length between the grip faces. The cross-head movement of the testing machine was recorded, but the strain along the free length of the specimen was not. In each test, the strain localization failure occurred near a grip face. The largest remaining piece of the specimen was then loaded again through strain localization failure. Figure 3 shows the specimen after the completion of the three tests.

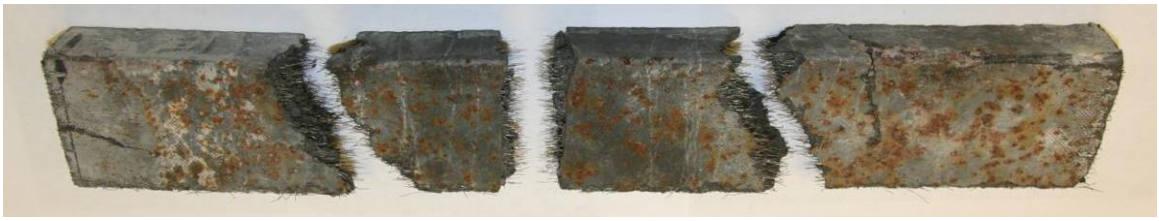

Source: FHWA.

Figure 3. Photo. Failed UHPC tensile prism after the completion of three tension tests.

These precursor tests provided an introduction to the testing concept and demonstrated that a uniaxial tension test of this type is feasible for strain-hardening concretes. Overall, these tests demonstrated that the test setup used for uniaxial mechanical testing of metallic plate-type specimens can be applied to the uniaxial tension testing of concrete specimens. However, it was also recognized that the failures of the specimen tended to occur in the free length near the wedge grip face, indicating that nonuniform stresses were being introduced into the specimen and would need to be addressed as the test method was further developed. Figure 4 shows the strain localization and fiber pullout occurring near a grip face.

Source: FHWA.

Figure 4. Photo. Strain localization and fiber pullout in first DTT.

Pilot Testing

The goal of this test program was to develop a test procedure that related to uniaxial tensile properties of strain-hardening FRCs and was applicable to both cast and extracted specimens. The precursor testing demonstrated that the DTT concept developed herein was viable. However, the development of the test procedure required many more iterations prior to standardized implementation on sets of test specimens. These iterations were completed though DTT of UHPC specimens within the pilot testing phase of the program.

At the start of the overall DTT procedure development, a set of basic requirements was specified. This set included the following:

- The test should be able to be completed using a commercially available testing apparatus.
- The test should be applicable to both cast and extracted concrete specimens.
- The preparation of test specimens and the implementation of the test procedure should be able to be completed by one technician.
- The concrete portion of the test specimen should not require the use of machining or shaping beyond that which can be completed through the use of a diamond blade concrete saw, a cylinder coring machine, or a handheld grinder.
- The measurement of specimen strain should be able to be completed through a reusable device.
- Individual tests should be able to be completed within a short time frame, allowing for sets of six or more tests to be completed within 4 hours or less.
- The test method should be sufficiently robust to allow for a high likelihood that any individual test will be completed successfully.
- The test should allow for the capture of both pre- and postcracking behaviors of the concrete without facilitating the premature localization of strain.
- The test method should minimize the application of nonuniaxial forces on the instrumented cross section of the specimen.
- The test specimen's least dimension should not be less than 50 mm (2 inches).

Given these requirements, a significant portion of the test procedure was effectively predefined. Uniaxial testing machines are readily available from commercial manufacturers of mechanical testing equipment. In this program, the testing apparatus included a 1,000-kN (225-kip) capacity uniaxial testing frame with a computer-controlled, closed-loop hydraulic actuator.

The requirement that individual tests must be able to be completed within a short timeframe precluded the use of testing machine platens or grips as surfaces to which to chemically bond (i.e., glue) the test specimen. As such, the test procedure required that the specimen be

mechanically attached to the test frame. Test machines can be equipped with hydraulic-actuated wedge grips that apply pressure in order to grip flat faces near the ends of test specimens. These off-the-shelf components are available for the testing of metallic specimens up to 63 mm (2.5 inches) thick and 100 mm (4 inches) wide. This simple gripping mechanism was engaged in this test program. Given the geometric limitations, the test method was developed for use with prismatic concrete specimens that were 50.8 mm (2 inches) thick and deep.

The capture of specimen strain through the use of a reusable device necessitated the development of a simple strain-measurement device that could attach to and detach from the specimen at appropriate points in the test. Using the compressometer described in ASTM C469 as inspiration, the researchers of this report developed a parallel-ring extensometer for use as a strain capture device.[47] Other concepts for strain measurement devices are certainly viable; however, the prevalence of the compressometer concept lends familiarity to this extensometer concept.

Given the requirement that the test specimens must be able to be either cast or extracted, rectangular prismatic specimens were deemed to be most viable. FRC specimens can be extracted from larger components through cutting or coring, making both cylindrical and prismatic specimens viable. However, the placement methods used in the casting of FRCs can impact the tensile mechanical properties. Prismatic specimens can be cast so as to provide consistent, although not necessarily random, fiber orientation. Cylindrical cast specimens often contain inconsistently oriented fiber reinforcement.

The requirement that specimens be able to be cast or extracted also precluded the use of dog bone–shaped specimens. Although the casting of a dog bone–shaped specimen with a prismatic cross section through the instrumented length has been demonstrated by many researchers, the creation of this specimen geometry in an extracted specimen is prohibitively difficult. As such, the uniform prismatic cross-sectional geometry previously described was used.

Other test setup parameters were sequentially modified to assess their impact on observed specimen behaviors. Modified parameters included the length of the test specimen, the length of specimen over which strain was monitored, the use of chemically adhered grip plates between the specimen and the machine wedge grips, the geometry of the grip plates, and the chemical adherence application geometry for the grip plates. The impact of each of these parameters on test results was assessed by testing UHPC specimens in a variety of configurations.

This testing encompassed 28 UHPC specimens with 50.8- by 50.8-mm (2- by 2-inch) cross sections. These cast prisms were produced over a period of nearly 8 years within 5 different research programs and 10 different UHPC batches. In short, leftover, untested test specimens from prior UHPC material characterization studies were used. (See references 6, 10, 13, 45, and 50.) As such, a direct quantitative specimen-to-specimen comparison of results was not possible. However, these tests did provide qualitative indications as to the appropriateness of particular test setup parameters.

The summary of the pilot test results are presented in table 3 (International System of Units (SI)) and table 4 (U.S. customary units). They were completed in four sets, namely tests 1–4, 5–7, 8–18, and 19–28. With each set of tests, the test parameters under consideration were reduced, and the test procedure was refined.

Table 3. Pilot series test specimen configurations and results (SI units).

Test No.	Prism Length (mm)	Gauge Length (mm)	Grip Length (mm)		Grip Plate Type	Grip Plate Dimensions (mm)				Localization Relative to Gauge Length	Remarks
			Top	Bottom		Thickness	Top Length	Bottom Length	Distance Between Plates		
1	304.8	50.8	82.6	63.5	None	—	—	—	—	Outside	Limited cracking; failure near grip
2	304.8	76.2	76.2	63.5	None	—	—	—	—	Inside	Limited cracking
3	431.8	203.2	69.9	69.9	None	—	—	—	—	Outside	Limited cracking; failure near grip
4	304.8	—	120.7	95.3	None	—	—	—	—	Outside	Limited cracking; failure near grip
5	431.8	203.2	57.2	50.8	Straight	6.35	118.1	98.0	215.9	Outside	Limited cracking; failure near plate
6	304.8	50.8	44.5	44.5	Straight	6.35	143.5	98.0	63.5	Inside	Multicracking
7	431.8	152.4	57.2	50.8	Straight	6.35	168.9	98.0	165.1	Inside	Limited cracking; failure near plate
8	431.8	101.6	50.8	50.8	Straight	6.35	158.8	158.8	114.3	Inside	Limited cracking; failure near plate
9	431.8	101.6	50.8	50.8	Straight	3.18	158.8	158.8	114.3	Inside	Some multicracking
10	431.8	101.6	50.8	50.8	Transverse taper	6.35	158.8	158.8	114.3	Inside	Limited cracking; failure near plate
11	431.8	101.6	88.9	88.9	Transverse taper	3.18	158.8	158.8	114.3	Inside	Limited cracking; failure near plate
12	431.8	101.6	88.9	88.9	Straight	4.76	158.8	158.8	114.3	Inside	Some multicracking
13	431.8	101.6	88.9	88.9	Straight	3.18	158.8	158.8	114.3	Inside	Some multicracking
14	431.8	101.6	88.9	88.9	Linear decrease*	4.76	158.8	158.8	114.3	Outside	Distributed multicracking
15	431.8	101.6	88.9	88.9	Radial decrease*	4.76	158.8	158.8	114.3	Inside	Distributed multicracking
16	431.8	101.6	88.9	88.9	Transverse taper	4.76	158.8	158.8	114.3	Outside	Limited cracking; failed under plate
17	431.8	101.6	88.9	88.9	Linear decrease*	6.35	158.8	158.8	114.3	Inside	Distributed multicracking
18	431.8	101.6	88.9	88.9	Radial decrease	6.35	158.8	158.8	114.3	Outside	Multicracking; failed under plate
19	431.8	101.6	88.9	88.9	Linear decrease	4.76	158.8	158.8	114.3	Inside	Limited cracking
20	304.8	76.2	44.5	44.5	Linear decrease	4.76	108.0	108.0	88.9	Outside	Distributed multicracking
21	304.8	76.2	44.5	44.5	Linear decrease	4.76	108.0	108.0	88.9	Inside	Distributed multicracking
22	304.8	76.2	44.5	44.5	Linear decrease	4.76	108.0	108.0	88.9	Inside	Distributed multicracking
23	431.8	101.6	88.9	88.9	Linear decrease*	4.76	158.8	158.8	114.3	Inside	Limited cracking
24	431.8	101.6	88.9	88.9	Linear decrease	4.76	158.8	158.8	114.3	Inside	Limited cracking
25	431.8	101.6	88.9	88.9	Linear decrease	4.76	158.8	158.8	114.3	Inside	Limited cracking
26	431.8	101.6	88.9	88.9	Linear decrease*	4.76	158.8	158.8	114.3	Inside	Limited cracking
27	431.8	101.6	88.9	88.9	Linear decrease	4.76	158.8	158.8	114.3	Inside	Some multicracking
28	431.8	101.6	88.9	88.9	Linear decrease	4.76	158.8	158.8	114.3	Inside	Some multicracking

1 mm = 0.039 inch; No. = number.

*Each bonded grip plate was intentionally debonded from the specimen for a 25.4-mm (1-inch)-long span in the transition region.

—Not relevant to this particular test.

Table 4. Pilot series test specimen configurations and results (U.S. customary units).

Test No.	Length of Prism (Inches)	Gauge Length (Inches)	Grip Length (inches)		Grip Plate Type	Grip Plate Dimensions (Inches)				Localization Relative to Gauge Length	Remarks
			Top	Bottom		Thickness	Top Length	Bottom Length	Distance Between Plates		
1	12	2	3.25	2.5	None	—	—	—	—	Outside	Limited cracking; failure near grip
2	12	3	3	2.5	None	—	—	—	—	Inside	Limited cracking
3	17	8	2.75	2.75	None	—	—	—	—	Outside	Limited cracking; failure near grip
4	12	-	4.75	3.75	None	—	—	—	—	Outside	Limited cracking; failure near grip
5	17	8	2.25	2	Straight	0.25	4.65	3.86	8.5	Outside	Limited cracking; failure near plate
6	12	2	1.75	1.75	Straight	0.25	5.65	3.86	2.5	Inside	Multicracking
7	17	6	2.25	2	Straight	0.25	6.65	3.86	6.5	Inside	Limited cracking; failure near plate
8	17	4	2	2	Straight	0.25	6.25	6.25	4.5	Inside	Limited cracking; failure near plate
9	17	4	2	2	Straight	0.125	6.25	6.25	4.5	Inside	Some multicracking
10	17	4	2	2	Transverse taper	0.25	6.25	6.25	4.5	Inside	Limited cracking; failure near plate
11	17	4	3.5	3.5	Transverse taper	0.125	6.25	6.25	4.5	Inside	Limited cracking; failure near plate
12	17	4	3.5	3.5	Straight	0.1875	6.25	6.25	4.5	Inside	Some multicracking
13	17	4	3.5	3.5	Straight	0.125	6.25	6.25	4.5	Inside	Some multicracking
14	17	4	3.5	3.5	Linear decrease*	0.1875	6.25	6.25	4.5	Outside	Distributed multicracking
15	17	4	3.5	3.5	Radial decrease*	0.1875	6.25	6.25	4.5	Inside	Distributed multicracking
16	17	4	3.5	3.5	Transverse taper	0.1875	6.25	6.25	4.5	Outside	Limited cracking; failed under plate
17	17	4	3.5	3.5	Linear decrease*	0.25	6.25	6.25	4.5	Inside	Distributed multicracking
18	17	4	3.5	3.5	Radial decrease	0.25	6.25	6.25	4.5	Outside	Multicracking; failed under plate
19	17	4	3.5	3.5	Linear decrease	0.1875	6.25	6.25	4.5	Inside	Limited cracking
20	12	3	1.75	1.75	Linear decrease	0.1875	4.25	4.25	3.5	Outside	Distributed multicracking
21	12	3	1.75	1.75	Linear decrease	0.1875	4.25	4.25	3.5	Inside	Distributed multicracking
22	12	3	1.75	1.75	Linear decrease	0.1875	4.25	4.25	3.5	Inside	Distributed multicracking
23	17	4	3.5	3.5	Linear decrease*	0.1875	6.25	6.25	4.5	Inside	Limited cracking
24	17	4	3.5	3.5	Linear decrease	0.1875	6.25	6.25	4.5	Inside	Limited cracking
25	17	4	3.5	3.5	Linear decrease	0.1875	6.25	6.25	4.5	Inside	Limited cracking
26	17	4	3.5	3.5	Linear decrease*	0.1875	6.25	6.25	4.5	Inside	Limited cracking
27	17	4	3.5	3.5	Linear decrease	0.1875	6.25	6.25	4.5	Inside	Some multicracking
28	17	4	3.5	3.5	Linear decrease	0.1875	6.25	6.25	4.5	Inside	Some multicracking

1 inch = 25.4 mm; No. = number.

*Each bonded grip plate was intentionally debonded from the specimen for a 25.4-mm (1-inch)-long span in the transition region.

—Not relevant to this particular test.

The first set of pilot tests, tests 1–4, focused on the necessity of chemically bonded grip plates between the specimen faces and the hydraulic wedge grips. For overall test simplicity, it would be desirable to allow for direct gripping of the specimen by the wedge grips; however, this gripping procedure may also introduce undesirable local stresses into the specimen leading to premature specimen failure adjacent to the end of the grip. These four tests assessed this potential by allowing the wedge grips to bear directly on the concrete. In three of the four cases, the specimens failed immediately adjacent to the wedge grip. Additionally, all of the specimens showed limited multicracking, indicating that local, nonuniform stresses may have been leading to premature strain localization. From these results, it was determined that each test specimen would require the application of bonded grip plates.

The second set of pilot tests, tests 5–7, focused on the general configuration of grip plates. To facilitate greater compatibility and smoother load transfer between the plates and the specimen, it was determined that grade 6061 aluminum plates would be used. Throughout the test program, these plates were bonded to the surface of each specimen through the use of a high-strength, high-modulus structural epoxy. In these three tests, 6.35-mm (0.25-inch) constant thickness plates, referred to as “straight” plates, were used. The length of plates along the specimen and the length of the specimen varied. These test results demonstrated that the grip plates were effective at eliminating stress concentrations caused by the wedge grips. In one test, true multicracking was observed within the measured gauge length. However, these tests also indicated that the strain localization failure was still likely to occur at the termination of the grip plate instead of randomly within the free length between the grip plates.

The third set of pilot tests, tests 8–18, were designed to investigate the thickness, shape, and bond length of the grip plates. It was hypothesized that thinner grip plates, grip plates with thickness transitions, and grip plates with intermittent bonding might allow for a more uniform transfer of stress to the specimen and reduce the likelihood of cracking and strain localization failure at the terminations of the plates. Three plate thicknesses were investigated: 6.35, 4.76, and 3.18 mm (0.25, 0.188, and 0.125 inch). Within these thicknesses, four different transition geometries were considered: straight, linear decrease, transverse taper, and radial decrease. Also, in a few cases, the chemical bond between the specimen and the plate was interrupted for a 25-mm (1-inch)-long span midway along the ungripped length of the plates. The plate geometries are shown in figure 5. Note that the geometries shown pertain specifically to the 4.76-mm (0.1875-inch)-thick plates. For other thicknesses, all shown dimensions remain the same aside from the thickness.

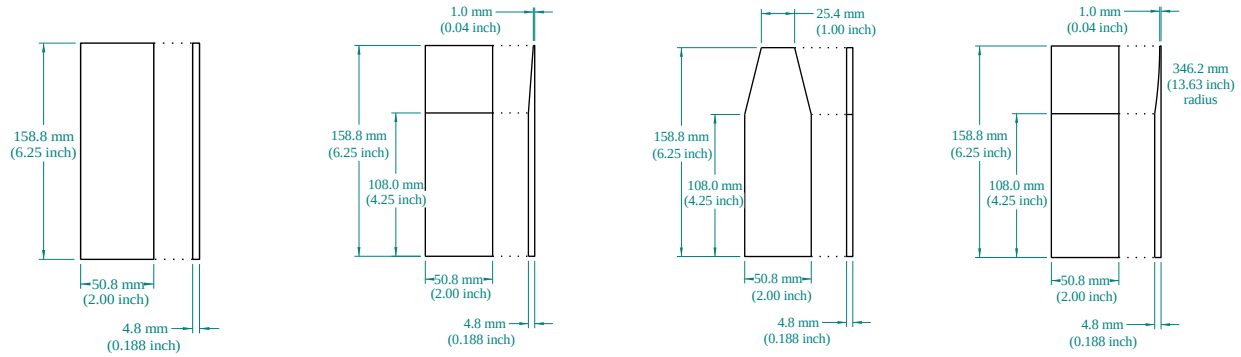

Source: FHWA. Source: FHWA. Source: FHWA. Source: FHWA.

A. Straight. B. Linear decrease. C. Transverse taper. D. Radial decrease.

Figure 5. Illustrations. Long specimen grip plate geometries.

A gradual decrease in the thickness of the grip plate increased the likelihood of acceptable specimen performance near the termination of the grip plate. As such, the straight and transverse taper plates were eliminated from consideration. Additionally, the fact the radial decrease plates required more sophisticated fabrication and did not provide a clear benefit above the linear decrease plates led to their elimination from consideration. In terms of plate thickness, the qualitative assessment of results indicated that the 4.76-mm (0.188-inch)-thick plate was the most appropriate. Overall, this set of tests demonstrated that acceptable performance could be achieved through the use of specific geometries of bonded aluminum plates extending beyond the wedge grips.

The fourth and final set of pilot tests, tests 19–28, were designed to finalize the design of the plates and the bonding procedure. The grip plates all were 4.76 mm (0.188 inch) thick with a linear decrease in thickness as they extended away from the wedge grips. These two plate geometries are shown in figure 6. Two different specimen lengths were tested, and as in the third pilot test series, some of the specimens had plates that were fully bonded, while others had intermittently bonded plates. Although only 2 of the 10 specimens displayed fully acceptable behavior, most of the less-than-acceptable behavior was attributed to the poor quality of the original as-cast UHPC specimens. Additionally, the specimens wherein the plate bond was interrupted did not provide a clear benefit over fully bonded plates, so this concept was eliminated from consideration.

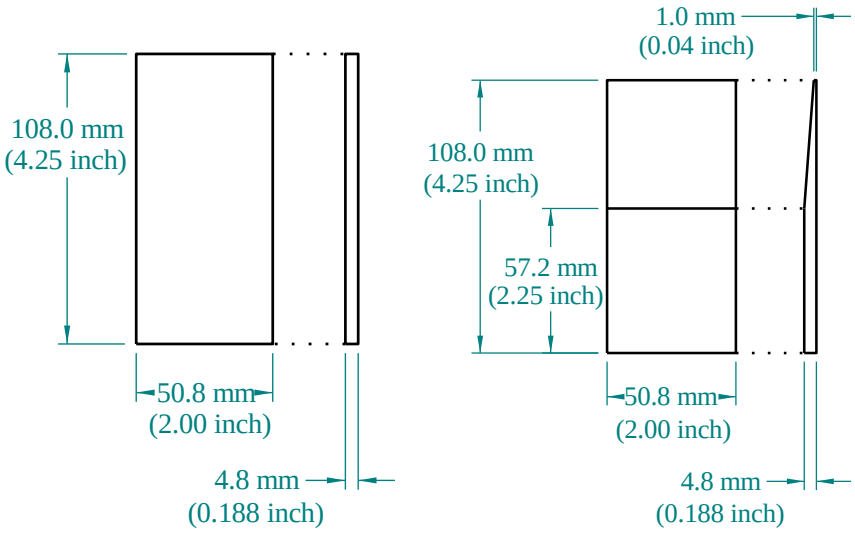

Source: FHWA. Source: FHWA.

A. Straight. B. Linear decrease.

Figure 6. Illustrations. Short specimen grip plate geometries.

Implemented Test Method

The test method implemented throughout the remainder of this research project was founded directly on the results of the pilot testing phase. The pilot tests allowed for an assessment of various test setup configurations and facilitated the determination of the most appropriate one. In order to allow for the use of this test method with either shorter or longer specimens, the outcome of the pilot tests included a pair of similar test configurations. Figure 7 shows the test configuration for the 431.8-mm (17-inch)-long specimen, while figure 8 shows the test configuration for the 304.8-mm (12-inch)-long specimen. The setups for these two configurations were generally similar, with the shorter configuration having decreased grip length, transition length, and gauge length. The grip plate dimensions are shown in figure 9.

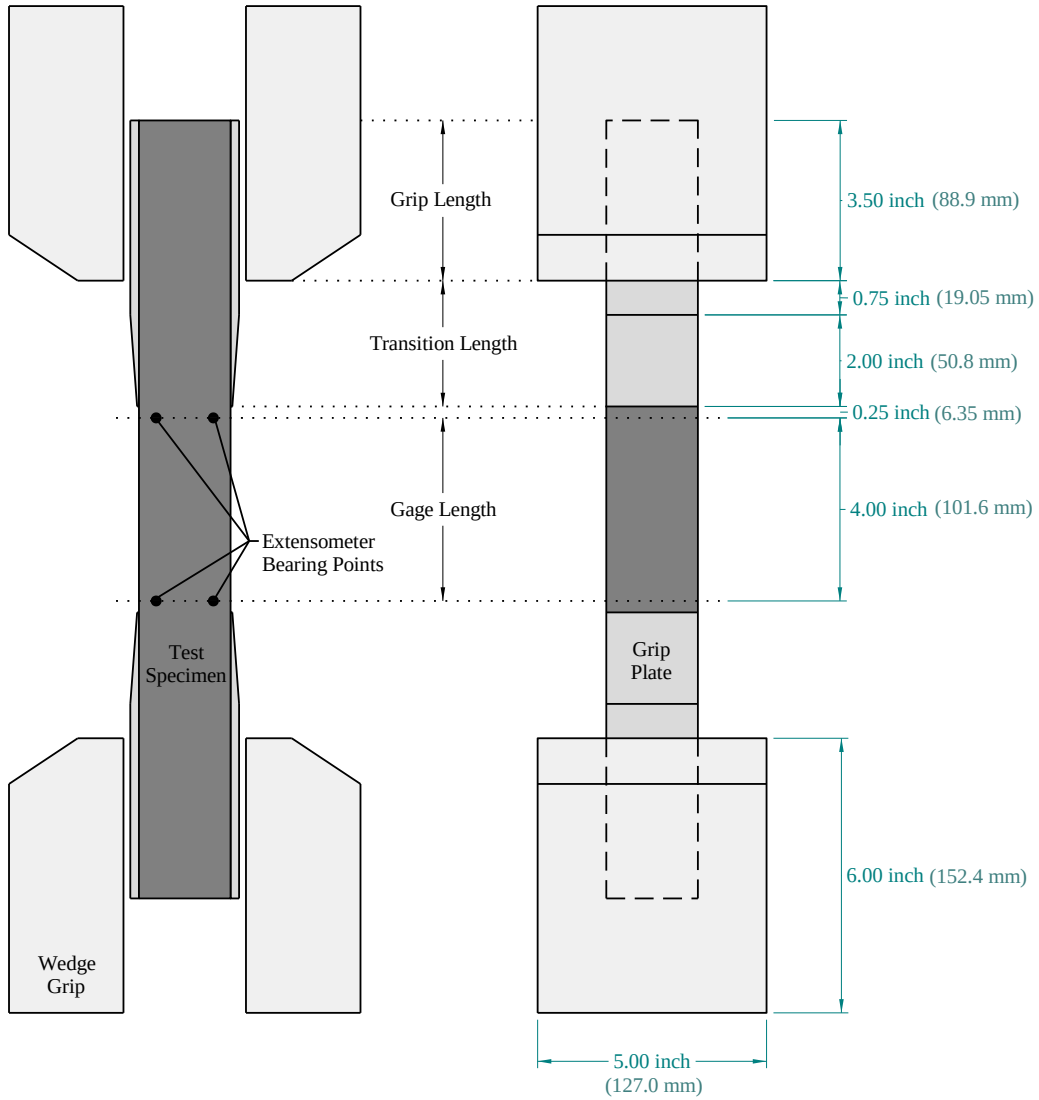

Source: FHWA.

Figure 7. Illustration. DTT setup for the longer 431.8-mm (17-inch)-long specimen showing side view (left) and front view (right).

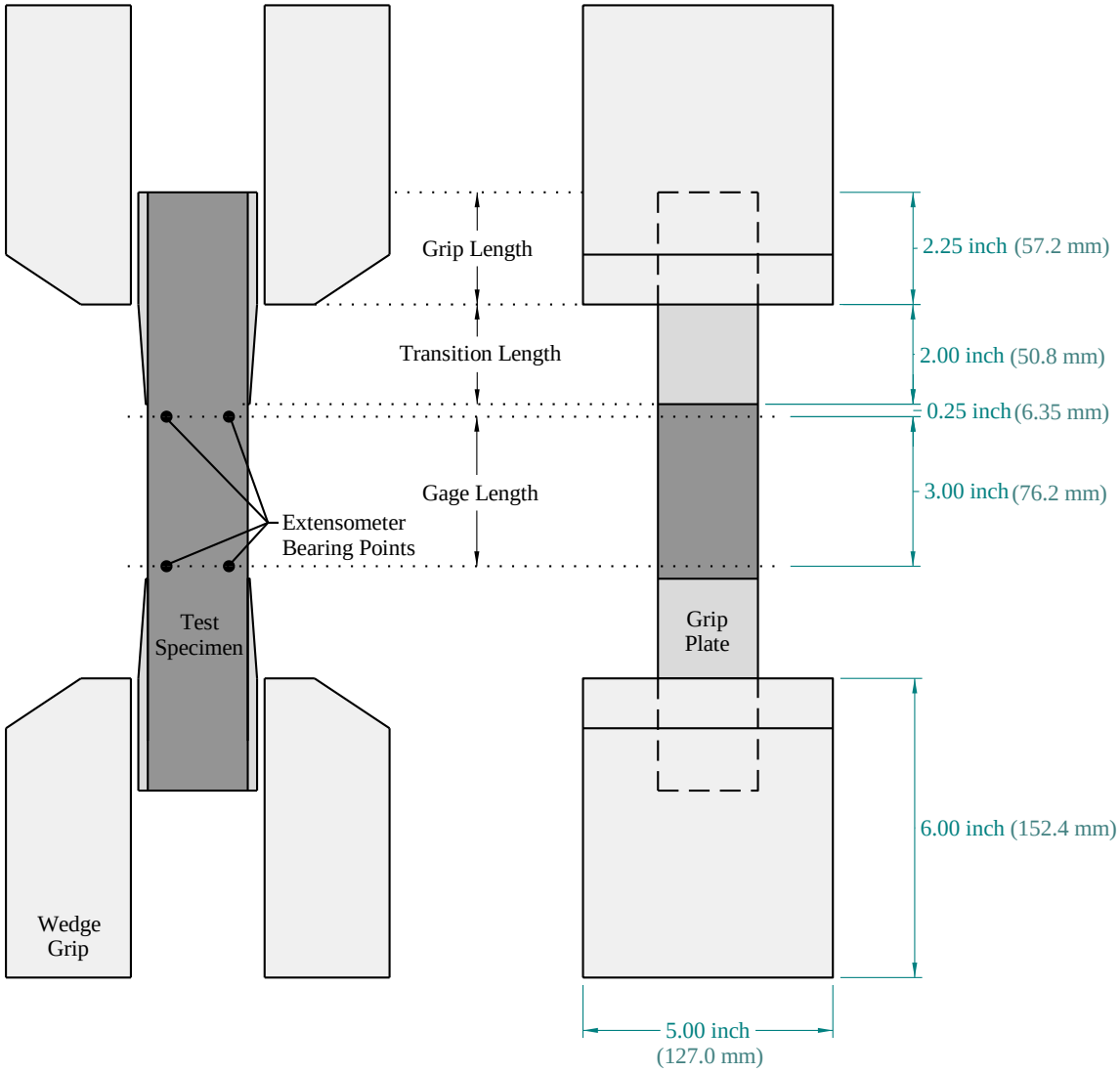

Source: FHWA.

Figure 8. Illustration. DTT setup for the shorter 304.8-mm (12-inch)-long specimen showing side view (left) and front view (right).

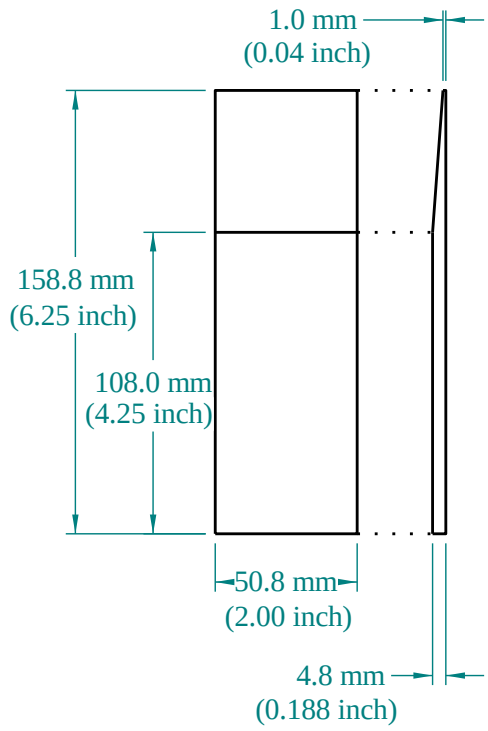

Source: FHWA.

A. Grip plate for 431.8-mm (17-inch) specimens.

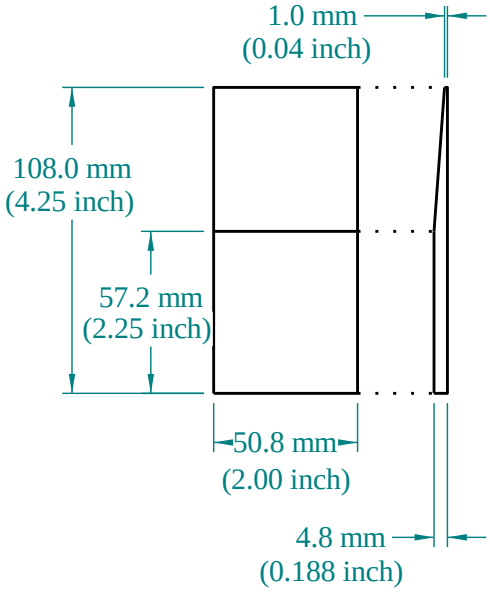

Source: FHWA

B. Grip plate for 304.8-mm (12-inch) specimens.

Figure 9. Illustrations. Grip plates used for the longer- and shorter-length specimens.

For all tests, a 1,000-kN (225-kip) capacity uniaxial testing frame with a computer-controlled, closed-loop hydraulic actuator was used. Diamond-faced, hydraulic-actuated wedge grips applied lateral pressure onto opposing surfaces on each end of the specimen to grip the specimen. The strain on the specimen was measured over the gauge length centered on the mid-length cross section. It was measured via a parallel ring extensometer, which contained four LVDTs. An illustration of the upper extensometer ring is provided in figure 10 (SI units) and figure 11 (U.S. customary units). This ring held the LVDTs. Aside from plugs being inserted into the LVDT holder locations, the lower extensometer ring was identical to the upper ring. Within this test program, the extensometer was set for a 101.6-mm (4-inch) gauge length on the long specimens and a 76.2-mm (3-inch) gauge length on the short specimens.

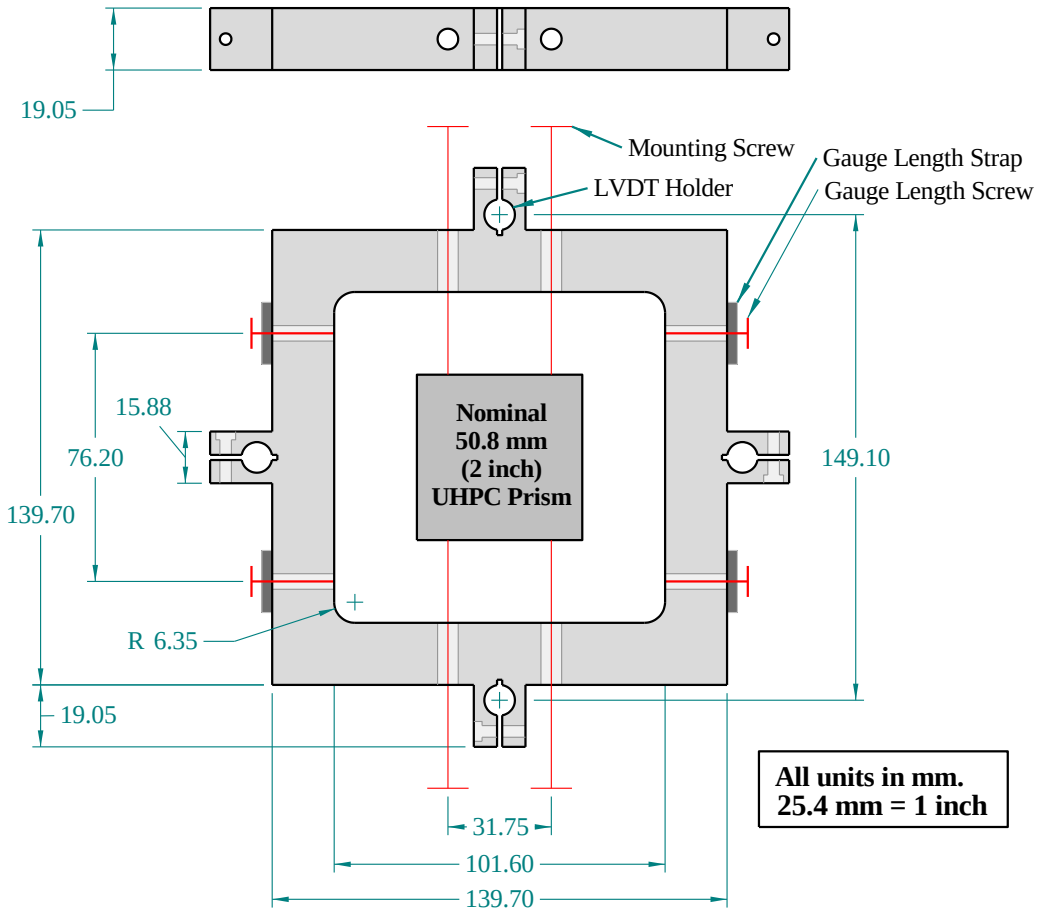

Source: FHWA.
1 mm = 0.039 inch.

Figure 10. Illustration. DTT axial strain measurement apparatus (SI units).

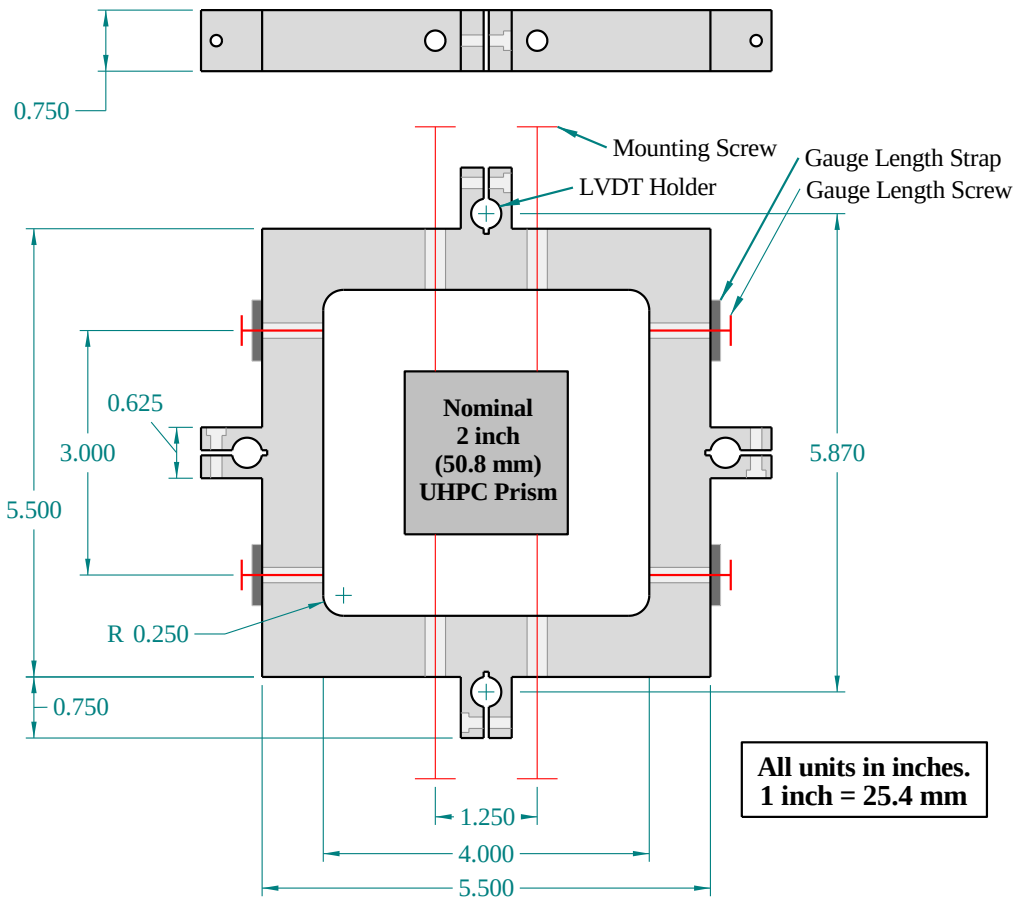

Source: FHWA.
1 inch = 25.4 mm.

Figure 11. Illustration. DTT axial strain measurement apparatus (U.S. customary units).

Figure 12 provides an overview of the test setup, including annotations indicating significant features. Figure 13 shows one of the longer 431.8-mm (17-inch)-long specimens during a test, while figure 14 shows one of the shorter 304.8-mm (12-inch)-long specimens during a test.

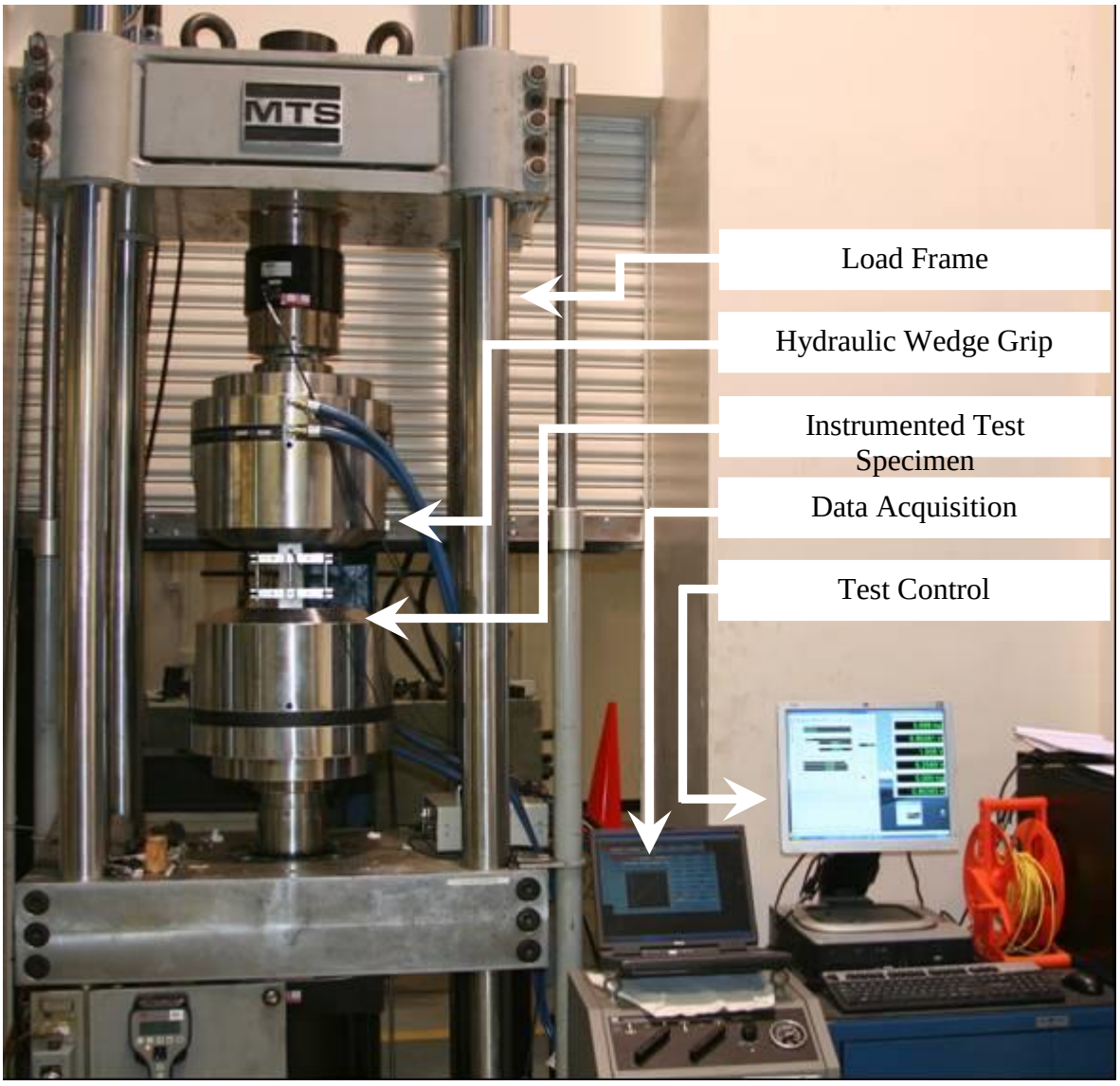

Source: FHWA.

Figure 12. Photo. Overall test setup with test machine and control computers.

Source: FHWA.

Figure 13. Photo. Testing of a longer 431.8-mm (17-inch)-long specimen.

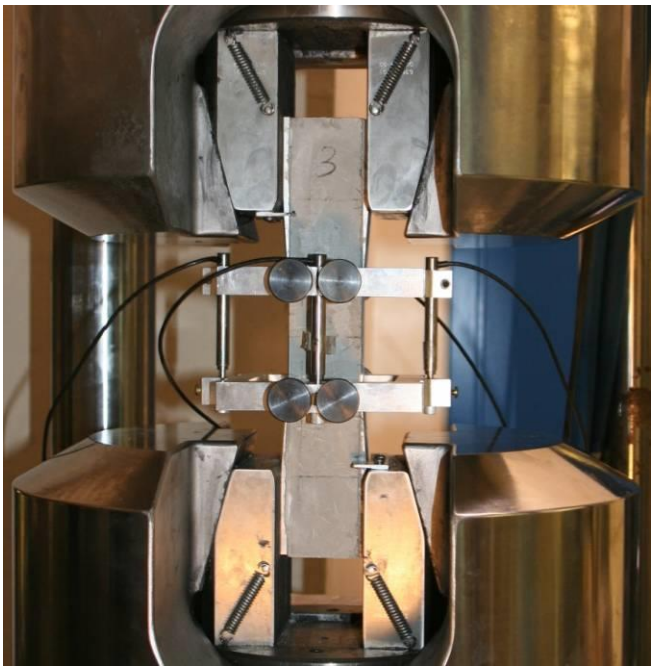

Source: FHWA.

Figure 14. Photo. Testing of a shorter 304.8-mm (12-inch)-long specimen.

The preparation procedure for each specimen included the following steps:

1. Fabricate the grip plates, including lightly roughening the bonding faces.

2. Dress the corners of prismatic specimen to ensure that no stray fibers or concrete extend beyond the surfaces onto which the grip plates will be bonded.

3. Clean and degrease the bonding surfaces of the test specimen and the grip plates.

4. Bond the grip plates to the specimen through the use of high-strength, high-stiffness structural epoxy. Apply the thin, uniform layer of epoxy to both mating surfaces, align the plates in the desired location, and then clamp.

5. Allow the epoxy to cure for at least 18 hours.

6. Mark the extensometer attachment points onto the surface of specimen.

The testing procedure for each specimen included the following steps:

1. Activate the testing machine and the control software. Ensure that the machine is in displacement control.

2. Install the parallel ring extensometer onto the specimen.

3. Place the specimen between the wedge grips with the appropriate grip length embedded into the upper wedge grip.

4. Align the specimen with the axis of the testing machine.

5. Close the upper wedge grip. Apply approximately 180 kN (40.4 kip) of lateral force onto the specimen, which equates to approximately 40 MPa (5.8 ksi) in the long specimen and 62 MPa (9.0 ksi) in the short specimen.

6. Adjust the lower wedge grip so that the appropriate grip length is embedded.

7. Begin data collection, including axial load, machine cross-head displacement, and four LVDT readings.

8. Activate the load control within the machine control software.

9. Close the lower wedge grip. The grip pressure in these grips should be the same as in the upper grip.

10. Activate the displacement control within the machine control software.

11. Load the specimen in the displacement control at a rate of –0.00254 mm/second (–0.00010 inch/second) until a compressive load of 17.8 kN (4,000 lb) is reached.

12. Halt loading and set the displacement rate at 0.00254 mm/second (0.00010 inch/second). Apply a tensile load until either (1) the average extensometer strain reads at least 25,000 microstrain or (2) strain localization has occurred.

13. Continue loading at a displacement rate of 0.0254 mm/second (0.0010 inch/second) until either (1) the average displacement along the gauge length is at least 5.1 mm (0.2 inch) or (2) strain localization has occurred.

14. Halt loading and release the lower wedge grip followed by the upper wedge grip. Remove the specimen from the testing machine, and remove the extensometer from the specimen.

15. Assess cracking in the test specimen.

TEST RESULTS

A total of 43 DTTs were successfully completed in this test program. All specimens were prepared, and all tests were completed according to the test procedure previously described. All of the tests were completed during a 2-week period. The time to complete an individual test, from the start of a test to the start of the subsequent test, ranged from 20 to 45 minutes depending on the type of failure exhibited by the specimen.

Electronic data and visual observations were collected during each test. The induced distress caused by the testing was also documented after the conclusion of testing. The captured electronic data included the elapsed time of the test, the applied load, the actuator axial displacement, and the displacements recorded by each of the four LVDTs. These LVDTs were located adjacent to the north, east, south, and west faces of the specimen and thus were labeled by those directional indicators. The data capture rate was 5 Hz.

The data collected for each specimen were analyzed and compiled in a standard format for easy review. The compiled results included a listing of parameters and their associated values, three plots, an illustration indicating specimen dimensions and localization location, and a photo showing the west face of the specimen after the conclusion of the test. The full results for each specimen were compiled and can be made available upon requests.

The terms used to describe the results are defined as follows:

- **Area**: This value is the product of the average dimension along the north–south and east–west directions within the gauge length.

- **Gauge length**: This value is the distance between attachment points of the extensometer.

- **Elastic phase**: This portion of the specimen behavior is defined by fully linear–elastic behavior. This phase precedes the first cracking of the specimen.

- **Multicracking phase**: This portion of the specimen behavior is defined by repeated cracking of the cementitious matrix, with fiber reinforcement bridging cracks and without the significant widening of any individual crack. This phase concludes at crack saturation.

- **Crack-straining phase**: This portion of the specimen behavior is defined by an increase in load-carrying capacity, which occurs after the multicracking phase. This phase concludes at crack localization.

- **Localized phase**: This portion of the specimen behavior is defined by the accumulation of significant strain within individual cracks as the load-carrying capacity of the specimen decreases. This phase begins at crack localization.

- **Elastic modulus**: This value is calculated as the slope of the stress–strain response on the tensile portion of the loading program between the average cross-sectional stresses of −7 to 0 MPa (−1.0 to 0.0 ksi).

- **Facial axial strain**: This is strain at the center of a face of the specimen. During the gripping phase, it is calculated based on the LVDT adjacent to each face under the assumptions of elastic flexural behavior on plane sections over the given gauge length. The neutral axis is assumed to be midway between opposing faces of the specimen. After the gripping stage, it is calculated as the sum of the facial axial strain at the conclusion of the gripping stage and the average overall specimen strain occurring after the gripping phase.

- **Facial axial stress**: This is the stress on the middle of a face of the specimen. Prior to first cracking, it is calculated as the product of the facial axial strain and the modulus of elasticity. After first cracking, it is calculated as stress at first cracking plus the post-first-cracking load increment divided by the average cross-sectional area.

- **Gripping facial strain**: This value is the strain on a face of the specimen during the gripping phase at the start of the test.

- **Average axial stress at first cracking**: This is the average stress in the specimen at the time of the first discontinuity (i.e., crack) during the tensile loading of the specimen. The stress is calculated as the load divided by the cross-sectional area.

- **Average axial strain at first cracking**: This is the average strain in the specimen at the time of the first discontinuity (i.e., crack) during the tensile loading of the specimen. The strain is calculated as the average of the values reported by the four LVDTs divided by the gauge length.

- **Maximum facial axial stress at first cracking**: This is the largest stress observed on a face of the specimen at the time of the first discontinuity (i.e., crack) during the tensile loading of the specimen. This value is calculated based on the assumptions of pure bending during specimen gripping and pure axial loading during axial force application.

- **Maximum facial axial strain at first cracking**: This is the largest strain observed on a face of the specimen at the time of the first discontinuity (i.e., crack) during the tensile loading of the specimen. This value is calculated based on the assumptions of pure bending during specimen gripping and pure axial loading during axial force application.

- **Postcracking strain**: This is the strain observed after first cracking of the specimen. If the term is used in reference to a directional indicator, then it refers to the facial axial strain observed beginning at first cracking. If the term is used in reference to the average, then it refers to the overall specimen average postcracking strain as calculated from the average of the four LVDTs.

- **Average stress during multicracking**: This is the average stress on the specimen cross section during the multicracking phase of the specimen behavior. The stress is calculated as the load divided by the cross-sectional area.

- **Crack indications**: These are electronically observed indications of cracking of the cementitious matrix as assessed through discontinuities in the recorded average stress versus average strain result. All crack indications occur within the multicracking phase and are inclusive of first cracking. Crack indications are based on discontinuities in the recorded average axial stress data. For a data point i with a stress σ, the following conditions must be met in order for the data point to be considered a crack indication:

    - $\sigma_i > (\sigma_{i-5}, \sigma_{i-4}, \sigma_{i-3}, \text{and } \sigma_{i-2})$.
    - $\sigma_i \geq (\sigma_{i-1})$.
    - $\sigma_i > (\sigma_{i+1}, \sigma_{i+2}, \sigma_{i+3}, \sigma_{i+4})$.
    - $\sigma_i > 0.99 \times \text{Average } (\sigma_{i+5}, \sigma_{i+6}, \sigma_{i+7}, \sigma_{i+8}, \sigma_{i+9}, \text{and } \sigma_{i+10})$.

    Given that data were collected at 5 Hz, this set of parameters ensures that cracks were local maxima that may not be indicated more than once per 2 seconds.

- **Average stress at multicracking cracks**: This is the average of the stress values observed during the crack indications.

- **Maximum average stress**: This is the maximum load observed throughout the duration of the test divided by the average cross-sectional area.

- **Average axial strain at crack straining**: This is the average axial strain at the start of the strain-hardening phase.

- **Average axial strain at localization**: This is the average axial strain at the start of the localization phase.

- **Average axial stress at localization**: This is the load divided by the average cross-sectional area at the start of the localization phase.

A sample version of the first of the three plots that were created for each test specimen can be found in figure 15. It presents the average axial stress versus average axial strain results. This plot provides a clear indication of the general tensile behavior of the specimen from elastic loading through strain localization. This two-part graph includes a left side, which displays the tensile response between average axial strains of 0.0000 and 0.0005. It focuses on first cracking of the specimen. The right side displays the tensile response between average axial strains of 0.000 and 0.010. It presents the full tensile behavior through and beyond localization of strain in a discrete crack. In both graphs, the average axial strain is calculated by averaging the results of the four LVDTs at each data collection interval.

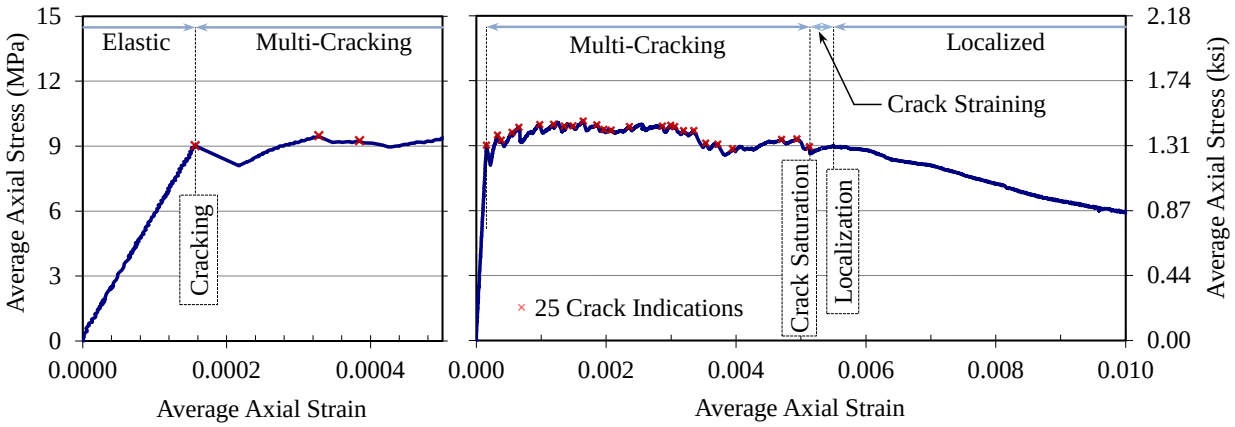

Source: FHWA.

A. Initial response.

Source: FHWA.

B. Full response.

Figure 15. Graphs. Average axial tensile response of an individual test specimen.

The phase of the test response is indicated along the top of the graphs in figure 15. The phases include elastic, multicracking, crack straining, and localized. The intersections between these phases are also noted sequentially as cracking, crack saturation, and localization. Each electronically indicated crack is also identified on this plot by a red "X" on the stress–strain response. The total number of indications is also listed in the graph.

A sample version of the second of the three plots shows that was produced for each specimen can be found in figure 16. It presents the axial stress on each of the four faces of the specimen during an elapsed time of 200 seconds near the start of the test. This plot provides a graphical indication of two important results. First, it provides an indication of the bending stresses introduced into the specimen through the gripping process. Second, it provides an indication of the facial stress at first cracking. This facial stress can be interpreted as the first cracking strength of the specimen. It includes annotations that indicate the start of specimen gripping, compressive loading, and tensile loading. The graph shows that this particular specimen incurred a tensile facial gripping stress of approximately 2.0 MPa (0.29 ksi) on the south face and that the stress on this face of the specimen was commensurately higher than average at first cracking.

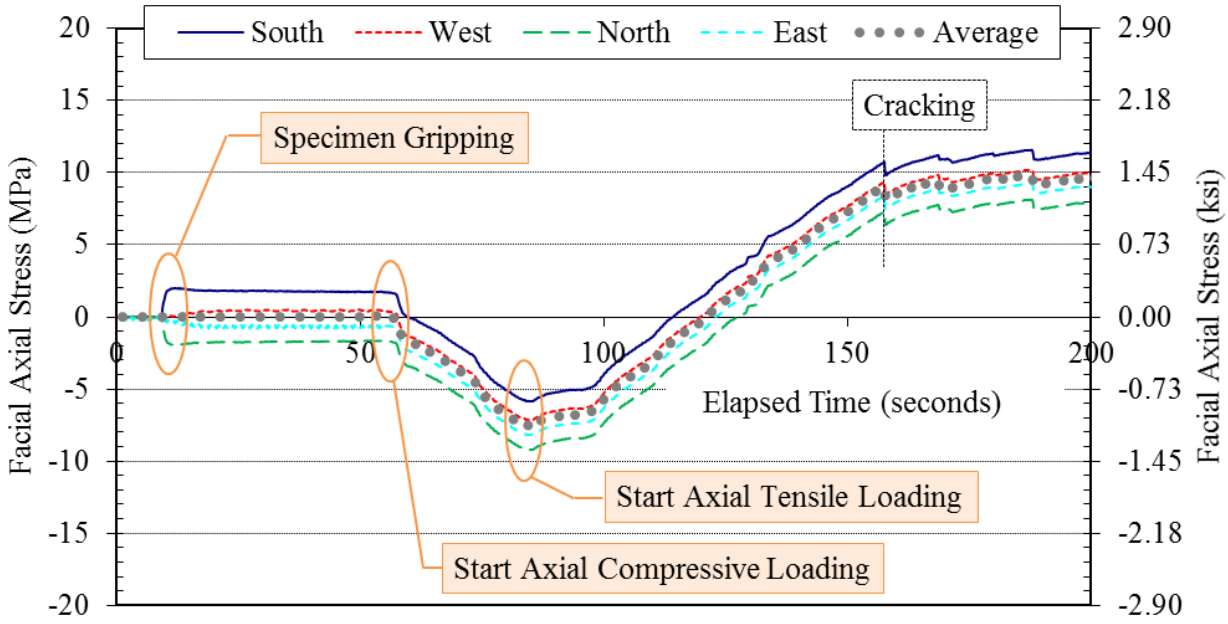

Source: FHWA.

Figure 16. Graph. Disparity between facial stresses prior to first cracking.

The axial stress for each face was calculated based on a combination of the LVDT adjacent to that face and the average applied load. During the initial portion of the test, bending displacements induced into the specimen by the gripping procedure were recorded by each LVDT. Assuming elastic bending on plane sections over a given gauge length, these displacements were transformed into facial strains on the specimen. Assuming linear elastic behavior, these strains were then multiplied by the modulus of elasticity to determine the facial stress. After the specimen was completely gripped and just before the axial loading was initiated, the specimen was assumed to carry load uniformly over the cross section. Thereafter, the applied loads were divided by the total cross-sectional area to determine the added stress on the specimen. Thus, the displayed facial axial stress values were the additive compilation of the initial bending stresses and the overall applied axial stresses. Note that the average stress is also shown in the graph in figure 16; this stress is indicative of the stress in the center of the specimen cross section as calculated from the average of the LVDT displacement readings.

A sample version of the third plot produced for each test specimen in shown in figure 17. It shows the ratio of the facial postcracking strain to the average postcracking strain plotted against the average axial strain. All strain values are based on the displacements measured by the LVDTs. The data were plotted from the first cracking of the specimen through cessation of the test. The average strain and average postcracking strain were both calculated based on the average displacement recorded by the LVDTs divided by the gauge length. The facial postcracking strain was calculated by dividing the postcracking displacement recorded by the LVDT adjacent to each face by the gauge length. It provides a general indication of the performance of the test specimen during the post-elastic phases. Successfully completed tests tended to show ratios that remained constant or trended toward 1.0 in the multicracking and crack-straining phases. Behaviors such as crack localization outside the gauge length or nonsymmetric crack localization within the gauge length are clearly evident through this presentation of data.

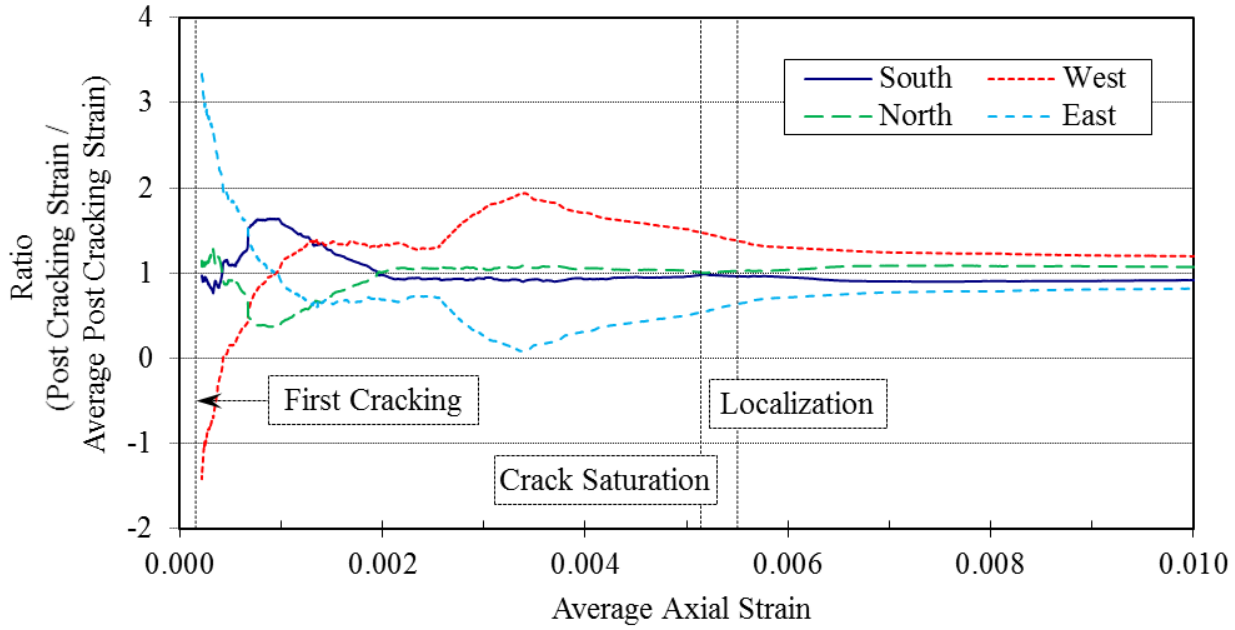

Source: FHWA.

Figure 17. Graph. Disparity between facial strains after first cracking.

The results related to nine specific parameters are summarized in table 5 through table 13 for the 43 test specimens. The results are summarized by set, including individual test results, average per set, and standard deviation per set.

Table 5 presents the modulus of elasticity results. The presented results pertain to a best-fit linear regression applied to the stress–strain response. The analysis was completed on data that were collected during the tensile loading branch of the test procedure over the average cross-sectional stress range from –7 to 0 MPa (–1 to 0 ksi). Other load ranges were considered, specifically –7 to 3.5 MPa (–1.0 to 0.5 ksi) and –3.5 MPa to 3.5 MPa (–0.5 to 0.5 ksi), but they were determined to be inadequate because they increased the likelihood of requiring dismissal of individual specimens whose response displayed first cracking prior to achieving an average tensile stress of 3.5 MPa (0.5 ksi).

Table 5. DTT specimen modulus of elasticity results.

Specimen Name	Modulus of Elasticity, GPa (ksi)		
	Value	Average	Standard Deviation
B2A40	60.3 (8,750)	61.7 (8,940)	2.51 (363)
B2A41	63.0 (9,140)	61.7 (8,940)	2.51 (363)
B2A42	64.4 (9,340)	61.7 (8,940)	2.51 (363)
B2A43	58.9 (8,540)	61.7 (8,940)	2.51 (363)
B2A44	—	61.7 (8,940)	2.51 (363)
B2A45	—	61.7 (8,940)	2.51 (363)
F1A15	55.2 (8,010)	55.8 (8,090)	0.83 (121)
F1A20	54.8 (7,950)	55.8 (8,090)	0.83 (121)
F1A21	55.8 (8,100)	55.8 (8,090)	0.83 (121)
F1A22	55.8 (8,100)	55.8 (8,090)	0.83 (121)
F1A23	57.0 (8,270)	55.8 (8,090)	0.83 (121)
F1A40	—	54.5 (7,910)	0.73 (106)
F1A41	—	54.5 (7,910)	0.73 (106)
F1A42	—	54.5 (7,910)	0.73 (106)
F1A43	54.0 (7,830)	54.5 (7,910)	0.73 (106)
F1A45	55.0 (7,980)	54.5 (7,910)	0.73 (106)
F1B40	57.8 (8,380)	56.9 (8,260)	1.09 (158)
F1B41	57.6 (8,360)	56.9 (8,260)	1.09 (158)
F1B42	58.0 (8,410)	56.9 (8,260)	1.09 (158)
F1B43	56.9 (8,250)	56.9 (8,260)	1.09 (158)
F1B44	55.4 (8,040)	56.9 (8,260)	1.09 (158)
F1B45	55.8 (8,090)	56.9 (8,260)	1.09 (158)
F1C15	53.6 (7,780)	54.2 (7,870)	1.03 (150)
F1C21	53.2 (7,710)	54.2 (7,870)	1.03 (150)
F1C22	55.4 (8,040)	54.2 (7,870)	1.03 (150)
F1C23	54.7 (7,940)	54.2 (7,870)	1.03 (150)
F1C40	56.5 (8,200)	56.1 (8,140)	2.01 (292)
F1C41	55.2 (8,000)	56.1 (8,140)	2.01 (292)
F1C42	55.0 (7,980)	56.1 (8,140)	2.01 (292)
F1C43	54.0 (7,830)	56.1 (8,140)	2.01 (292)
F1C44	56.1 (8,140)	56.1 (8,140)	2.01 (292)
F1C45	59.8 (8,670)	56.1 (8,140)	2.01 (292)
F2A11	55.0 (7,970)	56.5 (8,200)	2.09 (303)
F2A12	59.1 (8,570)	56.5 (8,200)	2.09 (303)
F2A13	57.1 (8,280)	56.5 (8,200)	2.09 (303)
F2A14	57.6 (8,360)	56.5 (8,200)	2.09 (303)
F2A15	53.9 (7,820)	56.5 (8,200)	2.09 (303)
F2A40	56.9 (8,250)	55.4 (8,040)	1.32 (191)
F2A41	57.1 (8,280)	55.4 (8,040)	1.32 (191)
F2A42	55.0 (7,970)	55.4 (8,040)	1.32 (191)
F2A43	53.8 (7,810)	55.4 (8,040)	1.32 (191)
F2A44	55.2 (8,010)	55.4 (8,040)	1.32 (191)
F2A45	54.4 (7,890)	55.4 (8,040)	1.32 (191)

—Specimen likely cracked during initial gripping.

Table 6 presents the results pertaining to the gripping of each specimen. It shows both the maximum (i.e., maximum tensile) and minimum (i.e., maximum compressive) gripping strains as calculated for the centers of the faces of each specimen. The results demonstrate that the magnitudes of the tensile and compressive gripping strains on the specimens were similar. The lone exception to this was specimen B2A44, which cracked due to bending induced during gripping, thus resulting in a shift of the neutral axis toward the compressive face.

These results also demonstrate that the test method can be implemented without inducing exceptionally large tensile strains into the specimen. Of the 42 specimens where strain was properly captured, only 12 of them incurred maximum gripping strains greater than 0.000100 and 16 were less than 0.000050. Overall, the average maximum tensile gripping strain was 0.000077.

Table 6. DTT specimen gripping strain results.

Specimen Name	Maximum Gripping Strain			Minimum Gripping Strain		
	Value	Average	Standard Deviation	Value	Average	Standard Deviation
B2A40	0.000022	0.000129	0.000149	–0.000019	–0.000117	0.000122
B2A41	0.000099	0.000129	0.000149	–0.000091	–0.000117	0.000122
B2A42	0.000010	0.000129	0.000149	–0.000017	–0.000117	0.000122
B2A43	0.000085	0.000129	0.000149	–0.000089	–0.000117	0.000122
B2A44	0.000415	0.000129	0.000149	–0.000347	–0.000117	0.000122
B2A45	0.000145	0.000129	0.000149	–0.000137	–0.000117	0.000122
F1A15	0.000055	0.000069	0.000025	–0.000061	–0.000072	0.000024
F1A20	0.000112	0.000069	0.000025	–0.000112	–0.000072	0.000024
F1A21	0.000058	0.000069	0.000025	–0.000058	–0.000072	0.000024
F1A22	0.000071	0.000069	0.000025	–0.000075	–0.000072	0.000024
F1A23	0.000051	0.000069	0.000025	–0.000054	–0.000072	0.000024
F1A40	0.000204	0.000126	0.000071	–0.000204	–0.000126	0.000069
F1A41	—	0.000126	0.000071	—	–0.000126	0.000069
F1A42	0.000166	0.000126	0.000071	–0.000164	–0.000126	0.000069
F1A43	0.000076	0.000126	0.000071	–0.000079	–0.000126	0.000069
F1A45	0.000057	0.000126	0.000071	–0.000058	–0.000126	0.000069
F1B40	0.000038	0.000053	0.000044	–0.000040	–0.000053	0.000043
F1B41	0.000021	0.000053	0.000044	–0.000020	–0.000053	0.000043
F1B42	0.000029	0.000053	0.000044	–0.000029	–0.000053	0.000043
F1B43	0.000094	0.000053	0.000044	–0.000088	–0.000053	0.000043
F1B44	0.000122	0.000053	0.000044	–0.000123	–0.000053	0.000043
F1B45	0.000016	0.000053	0.000044	–0.000017	–0.000053	0.000043
F1C15	0.000008	0.000034	0.000025	–0.000009	–0.000033	0.000025
F1C21	0.000063	0.000034	0.000025	-0.000063	–0.000033	0.000025
F1C22	0.000045	0.000034	0.000025	–0.000043	–0.000033	0.000025
F1C23	0.000018	0.000034	0.000025	–0.000018	–0.000033	0.000025
F1C40	0.000019	0.000055	0.000048	–0.000018	–0.000053	0.000050
F1C41	0.000120	0.000055	0.000048	–0.000126	–0.000053	0.000050
F1C42	0.000029	0.000055	0.000048	–0.000028	–0.000053	0.000050
F1C43	0.000113	0.000055	0.000048	–0.000109	–0.000053	0.000050
F1C44	0.000019	0.000055	0.000048	–0.000022	–0.000053	0.000050
F1C45	0.000029	0.000055	0.000048	–0.000018	–0.000053	0.000050
F2A11	0.000051	0.000067	0.000033	–0.000051	–0.000066	0.000032
F2A12	0.000110	0.000067	0.000033	–0.000108	–0.000066	0.000032
F2A13	0.000093	0.000067	0.000033	–0.000092	–0.000066	0.000032
F2A14	0.000035	0.000067	0.000033	–0.000034	–0.000066	0.000032
F2A15	0.000045	0.000067	0.000033	–0.000044	–0.000066	0.000032
F2A40	0.000106	0.000082	0.000047	–0.000110	–0.000085	0.000046
F2A41	0.000050	0.000082	0.000047	–0.000051	–0.000085	0.000046
F2A42	0.000061	0.000082	0.000047	–0.000061	–0.000085	0.000046
F2A43	0.000105	0.000082	0.000047	–0.000103	–0.000085	0.000046
F2A44	0.000150	0.000082	0.000047	–0.000154	–0.000085	0.000046
F2A45	0.000020	0.000082	0.000047	–0.000028	–0.000085	0.000046

—Specimen strain was not captured properly.

Table 7 presents the average axial specimen stress and the average axial strain at the occurrence of first specimen cracking. The average axial specimen stress was calculated based on the total applied load divided by the average cross-sectional area. It did not include any adjustment for any bending that may have been induced in the specimen during initial gripping. Similarly, the average axial strain was calculated from the average of the four LVDTs and also did not include any adjustments for any bending.

Table 7. DTT specimen global first cracking results.

Specimen Name	Average Axial Stress at First Cracking, MPa (ksi)			Average Axial Strain at First Cracking		
	Value	Average	Standard Deviation	Value	Average	Standard Deviation
B2A40	7.97 (1.16)	6.18 (0.90)	1.70 (0.25)	0.000144	0.000110	0.000033
B2A41	5.32 (0.77)	6.18 (0.90)	1.70 (0.25)	0.000122	0.000110	0.000033
B2A42	7.18 (1.04)	6.18 (0.90)	1.70 (0.25)	0.000111	0.000110	0.000033
B2A43	4.24 (0.61)	6.18 (0.90)	1.70 (0.25)	0.000065	0.000110	0.000033
B2A44	—	6.18 (0.90)	1.70 (0.25)	—	0.000110	0.000033
B2A45	—	6.18 (0.90)	1.70 (0.25)	—	0.000110	0.000033
F1A15	10.23 (1.48)	9.09 (1.32)	1.99 (0.29)	0.000178	0.000160	0.000038
F1A20	6.50 (0.94)	9.09 (1.32)	1.99 (0.29)	0.000114	0.000160	0.000038
F1A21	10.96 (1.59)	9.09 (1.32)	1.99 (0.29)	0.000195	0.000160	0.000038
F1A22	10.33 (1.50)	9.09 (1.32)	1.99 (0.29)	0.000191	0.000160	0.000038
F1A23	7.42 (1.08)	9.09 (1.32)	1.99 (0.29)	0.000124	0.000160	0.000038
F1A40	—	8.52 (1.24)	1.09 (0.16)	—	0.000154	0.000020
F1A41	—	8.52 (1.24)	1.09 (0.16)	—	0.000154	0.000020
F1A42	—	8.52 (1.24)	1.09 (0.16)	—	0.000154	0.000020
F1A43	7.75 (1.12)	8.52 (1.24)	1.09 (0.16)	0.000140	0.000154	0.000020
F1A45	9.29 (1.35)	8.52 (1.24)	1.09 (0.16)	0.000169	0.000154	0.000020
F1B40	11.02 (1.60)	9.03 (1.31)	1.99 (0.29)	0.000191	0.000164	0.000030
F1B41	10.87 (1.58)	9.03 (1.31)	1.99 (0.29)	0.000196	0.000164	0.000030
F1B42	8.99 (1.30)	9.03 (1.31)	1.99 (0.29)	0.000152	0.000164	0.000030
F1B43	6.49 (0.94)	9.03 (1.31)	1.99 (0.29)	0.000137	0.000164	0.000030
F1B44	6.79 (0.98)	9.03 (1.31)	1.99 (0.29)	0.000126	0.000164	0.000030
F1B45	9.99 (1.45)	9.03 (1.31)	1.99 (0.29)	0.000183	0.000164	0.000030
F1C15	9.41 (1.36)	9.07 (1.32)	0.91 (0.13)	0.000196	0.000175	0.000019
F1C21	9.74 (1.41)	9.07 (1.32)	0.91 (0.13)	0.000182	0.000175	0.000019
F1C22	7.73 (1.12)	9.07 (1.32)	0.91 (0.13)	0.000152	0.000175	0.000019
F1C23	9.39 (1.36)	9.07 (1.32)	0.91 (0.13)	0.000171	0.000175	0.000019
F1C40	8.52 (1.24)	8.41 (1.22)	2.51 (0.36)	0.000169	0.000152	0.000045
F1C41	6.38 (0.93)	8.41 (1.22)	2.51 (0.36)	0.000107	0.000152	0.000045
F1C42	10.64 (1.54)	8.41 (1.22)	2.51 (0.36)	0.000192	0.000152	0.000045
F1C43	4.49 (0.65)	8.41 (1.22)	2.51 (0.36)	0.000085	0.000152	0.000045
F1C44	10.75 (1.56)	8.41 (1.22)	2.51 (0.36)	0.000192	0.000152	0.000045
F1C45	9.67 (1.40)	8.41 (1.22)	2.51 (0.36)	0.000165	0.000152	0.000045
F2A11	7.01 (1.02)	6.67 (0.97)	1.50 (0.22)	0.000130	0.000119	0.000026
F2A12	5.09 (0.74)	6.67 (0.97)	1.50 (0.22)	0.000088	0.000119	0.000026
F2A13	6.27 (0.91)	6.67 (0.97)	1.50 (0.22)	0.000107	0.000119	0.000026
F2A14	9.05 (1.31)	6.67 (0.97)	1.50 (0.22)	0.000156	0.000119	0.000026
F2A15	5.92 (0.86)	6.67 (0.97)	1.50 (0.22)	0.000111	0.000119	0.000026
F2A40	5.18 (0.75)	5.91 (0.86)	1.65 (0.24)	0.000083	0.000105	0.000030
F2A41	6.16 (0.89)	5.91 (0.86)	1.65 (0.24)	0.000111	0.000105	0.000030
F2A42	7.71 (1.12)	5.91 (0.86)	1.65 (0.24)	0.000136	0.000105	0.000030
F2A43	5.11 (0.74)	5.91 (0.86)	1.65 (0.24)	0.000110	0.000105	0.000030
F2A44	3.53 (0.51)	5.91 (0.86)	1.65 (0.24)	0.000058	0.000105	0.000030
F2A45	7.77 (1.13)	5.91 (0.86)	1.65 (0.24)	0.000134	0.000105	0.000030

—Specimen likely cracked during initial gripping.

Table 8 presents the first cracking stress and strain results as analyzed to attribute the strains and stresses to the cross section with the inclusion of bending considerations due to gripping. Facial axial strains and facial axial stresses, as previously defined, were calculated based on the assumption of linear elastic plane section behavior. In simple terms, the facial axial stress at first cracking was greater than the average stress at first cracking by an increment equivalent to the bending stress induced during gripping.

Table 8. DTT specimen facial first cracking results.

Specimen Name	Maximum Facial Stress at First Cracking, MPa (ksi)			Maximum Facial Strain at First Cracking		
	Value	Average	Standard Deviation	Value	Average	Standard Deviation
B2A40	9.20 (1.33)	9.29 (1.35)	1.51 (0.22)	0.000179	0.000179	0.000034
B2A41	11.26 (1.63)	9.29 (1.35)	1.51 (0.22)	0.000227	0.000179	0.000034
B2A42	7.58 (1.10)	9.29 (1.35)	1.51 (0.22)	0.000158	0.000179	0.000034
B2A43	9.11 (1.32)	9.29 (1.35)	1.51 (0.22)	0.000151	0.000179	0.000034
B2A44	—	9.29 (1.35)	1.51 (0.22)	—	0.000179	0.000034
B2A45	—	9.29 (1.35)	1.51 (0.22)	—	0.000179	0.000034
F1A15	13.24 (1.92)	12.83 (1.86)	1.61 (0.23)	0.000258	0.000239	0.000040
F1A20	12.57 (1.82)	12.83 (1.86)	1.61 (0.23)	0.000221	0.000239	0.000040
F1A21	13.80 (2.00)	12.83 (1.86)	1.61 (0.23)	0.000279	0.000239	0.000040
F1A22	14.34 (2.08)	12.83 (1.86)	1.61 (0.23)	0.000261	0.000239	0.000040
F1A23	10.20 (1.48)	12.83 (1.86)	1.61 (0.23)	0.000178	0.000239	0.000040
F1A40	—	12.05 (1.75)	0.39 (0.06)	—	0.000217	0.000013
F1A41	—	12.05 (1.75)	0.39 (0.06)	—	0.000217	0.000013
F1A42	—	12.05 (1.75)	0.39 (0.06)	—	0.000217	0.000013
F1A43	11.78 (1.71)	12.05 (1.75)	0.39 (0.06)	0.000207	0.000217	0.000013
F1A45	12.33 (1.79)	12.05 (1.75)	0.39 (0.06)	0.000226	0.000217	0.000013
F1B40	11.88 (1.72)	11.59 (1.68)	1.10 (0.16)	0.000219	0.000215	0.000032
F1B41	11.18 (1.62)	11.59 (1.68)	1.10 (0.16)	0.000207	0.000215	0.000032
F1B42	10.58 (1.53)	11.59 (1.68)	1.10 (0.16)	0.000228	0.000215	0.000032
F1B43	11.68 (1.69)	11.59 (1.68)	1.10 (0.16)	0.000175	0.000215	0.000032
F1B44	13.56 (1.97)	11.59 (1.68)	1.10 (0.16)	0.000268	0.000215	0.000032
F1B45	10.67 (1.55)	11.59 (1.68)	1.10 (0.16)	0.000196	0.000215	0.000032
F1C15	9.81 (1.42)	10.34 (1.50)	0.73 (0.11)	0.000223	0.000219	0.000029
F1C21	11.41 (1.65)	10.34 (1.50)	0.73 (0.11)	0.000243	0.000219	0.000029
F1C22	10.16 (1.47)	10.34 (1.50)	0.73 (0.11)	0.000234	0.000219	0.000029
F1C23	9.99 (1.45)	10.34 (1.50)	0.73 (0.11)	0.000178	0.000219	0.000029
F1C40	9.46 (1.37)	11.09 (1.61)	1.16 (0.17)	0.000222	0.000247	0.000054
F1C41	12.82 (1.86)	11.09 (1.61)	1.16 (0.17)	0.000252	0.000247	0.000054
F1C42	11.55 (1.67)	11.09 (1.61)	1.16 (0.17)	0.000227	0.000247	0.000054
F1C43	10.45 (1.52)	11.09 (1.61)	1.16 (0.17)	0.000196	0.000247	0.000054
F1C44	11.59 (1.68)	11.09 (1.61)	1.16 (0.17)	0.000232	0.000247	0.000054
F1C45	10.69 (1.55)	11.09 (1.61)	1.16 (0.17)	0.000351	0.000247	0.000054
F2A11	8.65 (1.25)	10.08 (1.46)	1.50 (0.22)	0.000180	0.000172	0.000023
F2A12	11.23 (1.63)	10.08 (1.46)	1.50 (0.22)	0.000141	0.000172	0.000023
F2A13	11.49 (1.67)	10.08 (1.46)	1.50 (0.22)	0.000193	0.000172	0.000023
F2A14	10.77 (1.56)	10.08 (1.46)	1.50 (0.22)	0.000191	0.000172	0.000023
F2A15	8.29 (1.20)	10.08 (1.46)	1.50 (0.22)	0.000155	0.000172	0.000023
F2A40	11.04 (1.60)	10.25 (1.49)	1.35 (0.20)	0.000170	0.000183	0.000029
F2A41	8.36 (1.21)	10.25 (1.49)	1.35 (0.20)	0.000144	0.000183	0.000029
F2A42	10.91 (1.58)	10.25 (1.49)	1.35 (0.20)	0.000200	0.000183	0.000029
F2A43	10.65 (1.55)	10.25 (1.49)	1.35 (0.20)	0.000194	0.000183	0.000029
F2A44	11.75 (1.70)	10.25 (1.49)	1.35 (0.20)	0.000225	0.000183	0.000029
F2A45	8.81 (1.28)	10.25 (1.49)	1.35 (0.20)	0.000163	0.000183	0.000029

—Specimen likely cracked during initial gripping.

Comparison of the results from table 7 and table 8 demonstrates that the facial first cracking stress was greater than the average first cracking stress by approximately 3 MPa (0.4 ksi). Obviously, it would be desirable to reduce the induced bending due to gripping and thus observe greater similarity between the average first cracking stress and the facial first cracking stress. Additionally, these results demonstrate that the consistency of first cracking stress results between specimens in a set increased by analyzing first cracking in terms of facial stresses.

Table 9 presents the maximum average tensile stress resisted by each specimen throughout the duration of a test. As defined previously, the maximum average stress was calculated as the maximum load divided by the average cross-sectional area. This stress is the maximum resistance provided by the specimen. It may occur either at or after first cracking depending on whether the specimen displayed strain-hardening behavior. For the specimens that exhibited strain-softening behavior, the maximum average stress was equal to the first cracking stress and was less than the facial first cracking stress.

Table 9. DTT specimen maximum average stress results.

Specimen Name	Maximum Average Stress, MPa (ksi)		
	Value	Average	Standard Deviation
B2A40	10.52 (1.53)	10.53 (1.53)	0.48 (0.07)
B2A41	10.67 (1.55)	10.53 (1.53)	0.48 (0.07)
B2A42	10.02 (1.45)	10.53 (1.53)	0.48 (0.07)
B2A43	9.93 (1.44)	10.53 (1.53)	0.48 (0.07)
B2A44	11.20 (1.62)	10.53 (1.53)	0.48 (0.07)
B2A45	10.82 (1.57)	10.53 (1.53)	0.48 (0.07)
F1A15	11.13 (1.61)	11.20 (1.62)	0.44 (0.06)
F1A20	10.93 (1.58)	11.20 (1.62)	0.44 (0.06)
F1A21	11.84 (1.72)	11.20 (1.62)	0.44 (0.06)
F1A22	10.71 (1.55)	11.20 (1.62)	0.44 (0.06)
F1A23	11.39 (1.65)	11.20 (1.62)	0.44 (0.06)
F1A40	9.93 (1.44)	10.29 (1.49)	0.89 (0.13)
F1A41	9.89 (1.43)	10.29 (1.49)	0.89 (0.13)
F1A42	11.65 (1.69)	10.29 (1.49)	0.89 (0.13)
F1A43	10.64 (1.54)	10.29 (1.49)	0.89 (0.13)
F1A45	9.35 (1.36)	10.29 (1.49)	0.89 (0.13)
F1B40	11.02 (1.60)	9.83 (1.42)	1.33 (0.19)
F1B41	10.87 (1.58)	9.83 (1.42)	1.33 (0.19)
F1B42	8.99 (1.30)	9.83 (1.42)	1.33 (0.19)
F1B43	7.56 (1.10)	9.83 (1.42)	1.33 (0.19)
F1B44	10.52 (1.53)	9.83 (1.42)	1.33 (0.19)
F1B45	9.99 (1.45)	9.83 (1.42)	1.33 (0.19)
F1C15	12.06 (1.75)	11.56 (1.68)	0.54 (0.08)
F1C21	10.85 (1.57)	11.56 (1.68)	0.54 (0.08)
F1C22	11.90 (1.73)	11.56 (1.68)	0.54 (0.08)
F1C23	11.44 (1.66)	11.56 (1.68)	0.54 (0.08)
F1C40	12.07 (1.75)	11.36 (1.65)	0.51 (0.07)
F1C41	10.93 (1.59)	11.36 (1.65)	0.51 (0.07)
F1C42	11.81 (1.71)	11.36 (1.65)	0.51 (0.07)
F1C43	11.13 (1.61)	11.36 (1.65)	0.51 (0.07)
F1C44	10.76 (1.56)	11.36 (1.65)	0.51 (0.07)
F1C45	11.45 (1.66)	11.36 (1.65)	0.51 (0.07)
F2A11	8.35 (1.21)	9.18 (1.33)	0.72 (0.10)
F2A12	9.35 (1.36)	9.18 (1.33)	0.72 (0.10)
F2A13	9.42 (1.37)	9.18 (1.33)	0.72 (0.10)
F2A14	10.17 (1.48)	9.18 (1.33)	0.72 (0.10)
F2A15	8.61 (1.25)	9.18 (1.33)	0.72 (0.10)
F2A40	8.83 (1.28)	8.56 (1.24)	0.58 (0.08)
F2A41	8.70 (1.26)	8.56 (1.24)	0.58 (0.08)
F2A42	8.46 (1.23)	8.56 (1.24)	0.58 (0.08)
F2A43	7.82 (1.13)	8.56 (1.24)	0.58 (0.08)
F2A44	9.45 (1.37)	8.56 (1.24)	0.58 (0.08)
F2A45	8.11 (1.18)	8.56 (1.24)	0.58 (0.08)

Table 10 presents the average multicracking stress observed during the multicracking phase. The averaging process included all data collected during the multicracking phase of each specimen. The results provide an indication of the average strength of the specimen during the phase of loading wherein the specimen was undergoing multicracking within the monitored gauge length.

Table 10. DTT Specimen average multicracking stress results.

Specimen Name	Average Multicracking Stress, MPa (ksi)		
	Value	Average	Standard Deviation
B2A40	9.33 (1.35)	9.36 (1.36)	0.64 (0.09)
B2A41	9.52 (1.38)	9.36 (1.36)	0.64 (0.09)
B2A42	8.83 (1.28)	9.36 (1.36)	0.64 (0.09)
B2A43	8.81 (1.28)	9.36 (1.36)	0.64 (0.09)
B2A44	10.52 (1.53)	9.36 (1.36)	0.64 (0.09)
B2A45	9.11 (1.32)	9.36 (1.36)	0.64 (0.09)
F1A15	10.09 (1.46)	9.97 (1.45)	0.43 (0.06)
F1A20	10.10 (1.47)	9.97 (1.45)	0.43 (0.06)
F1A21	10.49 (1.52)	9.97 (1.45)	0.43 (0.06)
F1A22	9.32 (1.35)	9.97 (1.45)	0.43 (0.06)
F1A23	9.86 (1.43)	9.97 (1.45)	0.43 (0.06)
F1A40	8.55 (1.24)	9.18 (1.33)	0.52 (0.08)
F1A41	9.22 (1.34)	9.18 (1.33)	0.52 (0.08)
F1A42	9.47 (1.37)	9.18 (1.33)	0.52 (0.08)
F1A43	9.85 (1.43)	9.18 (1.33)	0.52 (0.08)
F1A45	8.79 (1.27)	9.18 (1.33)	0.52 (0.08)
F1B40	8.43 (1.22)	7.75 (1.12)	1.17 (0.17)
F1B41	8.55 (1.24)	7.75 (1.12)	1.17 (0.17)
F1B42	7.22 (1.05)	7.75 (1.12)	1.17 (0.17)
F1B43	6.64 (0.96)	7.75 (1.12)	1.17 (0.17)
F1B44	9.28 (1.35)	7.75 (1.12)	1.17 (0.17)
F1B45	6.37 (0.92)	7.75 (1.12)	1.17 (0.17)
F1C15	11.26 (1.63)	10.59 (1.54)	0.73 (0.11)
F1C21	9.62 (1.39)	10.59 (1.54)	0.73 (0.11)
F1C22	11.01 (1.60)	10.59 (1.54)	0.73 (0.11)
F1C23	10.49 (1.52)	10.59 (1.54)	0.73 (0.11)
F1C40	11.13 (1.61)	10.49 (1.52)	0.60 (0.09)
F1C41	10.10 (1.47)	10.49 (1.52)	0.60 (0.09)
F1C42	11.18 (1.62)	10.49 (1.52)	0.60 (0.09)
F1C43	10.14 (1.47)	10.49 (1.52)	0.60 (0.09)
F1C44	9.73 (1.41)	10.49 (1.52)	0.60 (0.09)
F1C45	10.64 (1.54)	10.49 (1.52)	0.60 (0.09)
F2A11	8.01 (1.16)	8.47 (1.23)	0.64 (0.09)
F2A12	8.02 (1.16)	8.47 (1.23)	0.64 (0.09)
F2A13	8.63 (1.25)	8.47 (1.23)	0.64 (0.09)
F2A14	9.53 (1.38)	8.47 (1.23)	0.64 (0.09)
F2A15	8.19 (1.19)	8.47 (1.23)	0.64 (0.09)
F2A40	8.09 (1.17)	7.76 (1.13)	0.53 (0.08)
F2A41	8.15 (1.18)	7.76 (1.13)	0.53 (0.08)
F2A42	7.18 (1.04)	7.76 (1.13)	0.53 (0.08)
F2A43	7.40 (1.07)	7.76 (1.13)	0.53 (0.08)
F2A44	8.44 (1.22)	7.76 (1.13)	0.53 (0.08)
F2A45	7.31 (1.06)	7.76 (1.13)	0.53 (0.08)

Table 11 presents the results related to the cracking indications that occurred during the multicracking phase of each specimen. Both the number of multicracking crack indications and the average specimen stress values that were observed at each of these crack indications are shown. In simple terms, this table presents the average overall stress in the specimen at the occurrence of crack indications in the specimen cementitious matrix. Assuming that the cementitious matrix expresses a relatively homogenous performance in terms of cracking, it is reasonable to assume that the average stress at multicracking crack indications is a strong indicator of the cracking strength of the cementitious matrix.

Table 11. DTT specimen multicracking results.

Specimen Name	Number of Multicracking Crack Indications			Average Stress at Multicracking Cracks, MPa (ksi)		
	Value	Average	Standard Deviation	Value	Average	Standard Deviation
B2A40	7	5.5	2.0	9.27 (1.34)	9.59 (1.39)	0.61 (0.09)
B2A41	3	5.5	2.0	9.65 (1.40)	9.59 (1.39)	0.61 (0.09)
B2A42	6	5.5	2.0	8.98 (1.30)	9.59 (1.39)	0.61 (0.09)
B2A43	7	5.5	2.0	9.08 (1.32)	9.59 (1.39)	0.61 (0.09)
B2A44	3	5.5	2.0	10.61 (1.54)	9.59 (1.39)	0.61 (0.09)
B2A45	7	5.5	2.0	9.93 (1.44)	9.59 (1.39)	0.61 (0.09)
F1A15	23	16.6	5.5	10.31 (1.49)	10.24 (1.49)	0.31 (0.04)
F1A20	14	16.6	5.5	10.17 (1.47)	10.24 (1.49)	0.31 (0.04)
F1A21	22	16.6	5.5	10.63 (1.54)	10.24 (1.49)	0.31 (0.04)
F1A22	11	16.6	5.5	9.77 (1.42)	10.24 (1.49)	0.31 (0.04)
F1A23	13	16.6	5.5	10.33 (1.50)	10.24 (1.49)	0.31 (0.04)
F1A40	11	13.0	1.6	9.27 (1.34)	9.60 (1.39)	0.56 (0.08)
F1A41	13	13.0	1.6	9.40 (1.36)	9.60 (1.39)	0.56 (0.08)
F1A42	15	13.0	1.6	10.21 (1.48)	9.60 (1.39)	0.56 (0.08)
F1A43	14	13.0	1.6	10.16 (1.47)	9.60 (1.39)	0.56 (0.08)
F1A45	12	13.0	1.6	8.95 (1.30)	9.60 (1.39)	0.56 (0.08)
F1B40	14	10.5	3.6	8.79 (1.27)	8.00 (1.16)	1.23 (0.18)
F1B41	14	10.5	3.6	8.63 (1.25)	8.00 (1.16)	1.23 (0.18)
F1B42	6	10.5	3.6	7.49 (1.09)	8.00 (1.16)	1.23 (0.18)
F1B43	8	10.5	3.6	6.95 (1.01)	8.00 (1.16)	1.23 (0.18)
F1B44	13	10.5	3.6	9.68 (1.40)	8.00 (1.16)	1.23 (0.18)
F1B45	8	10.5	3.6	6.45 (0.94)	8.00 (1.16)	1.23 (0.18)
F1C15	14	18.8	3.6	11.19 (1.62)	10.71 (1.55)	0.58 (0.08)
F1C21	22	18.8	3.6	9.90 (1.44)	10.71 (1.55)	0.58 (0.08)
F1C22	21	18.8	3.6	11.06 (1.60)	10.71 (1.55)	0.58 (0.08)
F1C23	18	18.8	3.6	10.67 (1.55)	10.71 (1.55)	0.58 (0.08)
F1C40	16	16.0	4.0	11.32 (1.64)	10.73 (1.56)	0.54 (0.08)
F1C41	17	16.0	4.0	10.50 (1.52)	10.73 (1.56)	0.54 (0.08)
F1C42	16	16.0	4.0	11.39 (1.65)	10.73 (1.56)	0.54 (0.08)
F1C43	23	16.0	4.0	10.49 (1.52)	10.73 (1.56)	0.54 (0.08)
F1C44	12	16.0	4.0	9.97 (1.45)	10.73 (1.56)	0.54 (0.08)
F1C45	12	16.0	4.0	10.68 (1.55)	10.73 (1.56)	0.54 (0.08)
F2A11	6	12.2	7.6	8.20 (1.19)	8.73 (1.27)	0.60 (0.09)
F2A12	9	12.2	7.6	8.62 (1.25)	8.73 (1.27)	0.60 (0.09)
F2A13	8	12.2	7.6	8.98 (1.30)	8.73 (1.27)	0.60 (0.09)
F2A14	25	12.2	7.6	9.62 (1.40)	8.73 (1.27)	0.60 (0.09)
F2A15	13	12.2	7.6	8.21 (1.19)	8.73 (1.27)	0.60 (0.09)
F2A40	15	12.0	3.3	8.32 (1.21)	7.99 (1.16)	0.62 (0.09)
F2A41	13	12.0	3.3	8.21 (1.19)	7.99 (1.16)	0.62 (0.09)
F2A42	7	12.0	3.3	7.36 (1.07)	7.99 (1.16)	0.62 (0.09)
F2A43	13	12.0	3.3	7.57 (1.10)	7.99 (1.16)	0.62 (0.09)
F2A44	15	12.0	3.3	8.98 (1.30)	7.99 (1.16)	0.62 (0.09)
F2A45	9	12.0	3.3	7.52 (1.09)	7.99 (1.16)	0.62 (0.09)

Table 12 presents the results related to the initiation of the crack-straining phase. It shows the average strain and average stress for each specimen at the start of the crack-straining phase. Note that approximately one-third of the specimens exhibited localization outside of the instrumented gauge length; thus, the crack straining and localization phases of the performance could not be monitored. The start of the crack-straining phase indicated the cessation of the multicracking phase and thus, the cessation of the creation of additional cracks. As such, the start of the crack-straining phase indicated the start of individual crack widening within the concrete.

Table 12. DTT specimen crack saturation results.

Specimen Name	Strain at Crack Saturation			Stress at Crack Saturation, MPa (ksi)		
	Value	Average	Standard Deviation	Value	Average	Standard Deviation
B2A40	0.003279	0.004228	0.000784	9.27 (1.35)	9.75 (1.41)	0.56 (0.08)
B2A41	0.004114	0.004228	0.000784	10.07 (1.46)	9.75 (1.41)	0.56 (0.08)
B2A42	0.004004	0.004228	0.000784	9.24 (1.34)	9.75 (1.41)	0.56 (0.08)
B2A43	0.005639	0.004228	0.000784	9.35 (1.36)	9.75 (1.41)	0.56 (0.08)
B2A44	0.004399	0.004228	0.000784	10.66 (1.55)	9.75 (1.41)	0.56 (0.08)
B2A45	0.003931	0.004228	0.000784	9.89 (1.43)	9.75 (1.41)	0.56 (0.08)
F1A15	0.004762	0.004172	0.000995	9.31 (1.35)	9.28 (1.35)	0.57 (0.08)
F1A20	—	0.004172	0.000995	9.93 (1.44)	9.28 (1.35)	0.57 (0.08)
F1A21	0.004732	0.004172	0.000995	9.70 (1.41)	9.28 (1.35)	0.57 (0.08)
F1A22	0.003023	0.004172	0.000995	8.51 (1.23)	9.28 (1.35)	0.57 (0.08)
F1A23	—	0.004172	0.000995	8.95 (1.30)	9.28 (1.35)	0.57 (0.08)
F1A40	—	0.005386	0.002026	8.14 (1.18)	8.57 (1.24)	0.55 (0.08)
F1A41	0.007595	0.005386	0.002026	8.32 (1.21)	8.57 (1.24)	0.55 (0.08)
F1A42	—	0.005386	0.002026	8.21 (1.19)	8.57 (1.24)	0.55 (0.08)
F1A43	0.004947	0.005386	0.002026	9.48 (1.37)	8.57 (1.24)	0.55 (0.08)
F1A45	0.003615	0.005386	0.002026	8.73 (1.27)	8.57 (1.24)	0.55 (0.08)
F1B40	0.005677	0.004712	0.001365	7.91 (1.15)	7.18 (1.04)	0.91 (0.13)
F1B41	0.003747	0.004712	0.001365	7.90 (1.15)	7.18 (1.04)	0.91 (0.13)
F1B42	—	0.004712	0.001365	6.82 (0.99)	7.18 (1.04)	0.91 (0.13)
F1B43	—	0.004712	0.001365	6.64 (0.96)	7.18 (1.04)	0.91 (0.13)
F1B44	—	0.004712	0.001365	8.02 (1.16)	7.18 (1.04)	0.91 (0.13)
F1B45	—	0.004712	0.001365	5.77 (0.84)	7.18 (1.04)	0.91 (0.13)
F1C15	0.005202	0.005240	0.000038	11.49 (1.67)	10.48 (1.52)	1.24 (0.18)
F1C21	—	0.005240	0.000038	8.77 (1.27)	10.48 (1.52)	1.24 (0.18)
F1C22	0.005278	0.005240	0.000038	11.31 (1.64)	10.48 (1.52)	1.24 (0.18)
F1C23	0.005239	0.005240	0.000038	10.36 (1.50)	10.48 (1.52)	1.24 (0.18)
F1C40	0.004263	0.004838	0.001057	11.05 (1.60)	10.38 (1.51)	0.88 (0.13)
F1C41	0.003864	0.004838	0.001057	10.35 (1.50)	10.38 (1.51)	0.88 (0.13)
F1C42	—	0.004838	0.001057	11.22 (1.63)	10.38 (1.51)	0.88 (0.13)
F1C43	0.006274	0.004838	0.001057	10.51 (1.52)	10.38 (1.51)	0.88 (0.13)
F1C44	—	0.004838	0.001057	8.74 (1.27)	10.38 (1.51)	0.88 (0.13)
F1C45	0.004950	0.004838	0.001057	10.43 (1.51)	10.38 (1.51)	0.88 (0.13)
F2A11	0.001542	0.003046	0.001563	8.13 (1.18)	8.43 (1.22)	0.23 (0.03)
F2A12	0.002246	0.003046	0.001563	8.24 (1.20)	8.43 (1.22)	0.23 (0.03)
F2A13	0.003256	0.003046	0.001563	8.63 (1.25)	8.43 (1.22)	0.23 (0.03)
F2A14	0.005140	0.003046	0.001563	8.64 (1.25)	8.43 (1.22)	0.23 (0.03)
F2A15	—	0.003046	0.001563	8.50 (1.23)	8.43 (1.22)	0.23 (0.03)
F2A40	—	0.003897	0.001322	7.24 (1.05)	7.40 (1.07)	0.69 (0.10)
F2A41	—	0.003897	0.001322	8.36 (1.21)	7.40 (1.07)	0.69 (0.10)
F2A42	—	0.003897	0.001322	6.60 (0.96)	7.40 (1.07)	0.69 (0.10)
F2A43	0.004440	0.003897	0.001322	7.36 (1.07)	7.40 (1.07)	0.69 (0.10)
F2A44	0.004860	0.003897	0.001322	8.05 (1.17)	7.40 (1.07)	0.69 (0.10)
F2A45	0.002390	0.003897	0.001322	6.81 (0.99)	7.40 (1.07)	0.69 (0.10)

—Specimen localized outside of the gauge length.

Table 13 presents the results related to the initiation of the localized phase. It shows the average strain and the average stress for each specimen at the start of the localized phase. Note that approximately one-third of the specimens exhibited localization outside of the instrumented gauge length; thus, the localization phase of the performance could not be monitored. The initiation of localization behavior indicates the initiation of the declining branch of the response, wherein additional load cannot be supported and additional deformations will be focused within a small number of localized cracks.

Table 13. DTT specimen localization results.

Specimen Name	Strain at Localization			Stress at Localization, MPa (ksi)		
	Value	Average	Standard Deviation	Value	Average	Standard Deviation
B2A40	0.007257	0.006476	0.001248	10.51 (1.52)	10.49 (1.52)	0.45 (0.07)
B2A41	0.005671	0.006476	0.001248	10.67 (1.55)	10.49 (1.52)	0.45 (0.07)
B2A42	0.007771	0.006476	0.001248	10.00 (1.45)	10.49 (1.52)	0.45 (0.07)
B2A43	0.007681	0.006476	0.001248	9.92 (1.44)	10.49 (1.52)	0.45 (0.07)
B2A44	0.004831	0.006476	0.001248	11.07 (1.61)	10.49 (1.52)	0.45 (0.07)
B2A45	0.005647	0.006476	0.001248	10.78 (1.56)	10.49 (1.52)	0.45 (0.07)
F1A15	0.005272	0.004717	0.001122	9.47 (1.37)	9.63 (1.40)	0.62 (0.09)
F1A20	—	0.004717	0.001122	10.30 (1.49)	9.63 (1.40)	0.62 (0.09)
F1A21	0.005453	0.004717	0.001122	10.21 (1.48)	9.63 (1.40)	0.62 (0.09)
F1A22	0.003425	0.004717	0.001122	8.85 (1.28)	9.63 (1.40)	0.62 (0.09)
F1A23	—	0.004717	0.001122	9.30 (1.35)	9.63 (1.40)	0.62 (0.09)
F1A40	—	0.005921	0.001822	8.77 (1.27)	8.86 (1.29)	0.38 (0.06)
F1A41	0.007689	0.005921	0.001822	8.39 (1.22)	8.86 (1.29)	0.38 (0.06)
F1A42	—	0.005921	0.001822	8.73 (1.27)	8.86 (1.29)	0.38 (0.06)
F1A43	0.006024	0.005921	0.001822	9.43 (1.37)	8.86 (1.29)	0.38 (0.06)
F1A45	0.004051	0.005921	0.001822	9.00 (1.30)	8.86 (1.29)	0.38 (0.06)
F1B40	0.006462	0.005239	0.001729	8.28 (1.20)	7.40 (1.07)	0.95 (0.14)
F1B41	0.004017	0.005239	0.001729	8.11 (1.18)	7.40 (1.07)	0.95 (0.14)
F1B42	—	0.005239	0.001729	6.99 (1.01)	7.40 (1.07)	0.95 (0.14)
F1B43	—	0.005239	0.001729	7.00 (1.02)	7.40 (1.07)	0.95 (0.14)
F1B44	—	0.005239	0.001729	8.14 (1.18)	7.40 (1.07)	0.95 (0.14)
F1B45	—	0.005239	0.001729	5.87 (0.85)	7.40 (1.07)	0.95 (0.14)
F1C15	0.005903	0.005842	0.000105	12.02 (1.74)	10.80 (1.57)	1.37 (0.20)
F1C21	—	0.005842	0.000105	8.96 (1.30)	10.80 (1.57)	1.37 (0.20)
F1C22	0.005721	0.005842	0.000105	11.66 (1.69)	10.80 (1.57)	1.37 (0.20)
F1C23	0.005901	0.005842	0.000105	10.57 (1.53)	10.80 (1.57)	1.37 (0.20)
F1C40	0.005973	0.005685	0.000810	12.06 (1.75)	10.95 (1.59)	0.95 (0.14)
F1C41	0.004809	0.005685	0.000810	10.80 (1.57)	10.95 (1.59)	0.95 (0.14)
F1C42	—	0.005685	0.000810	11.81 (1.71)	10.95 (1.59)	0.95 (0.14)
F1C43	0.006666	0.005685	0.000810	10.78 (1.56)	10.95 (1.59)	0.95 (0.14)
F1C44	—	0.005685	0.000810	9.38 (1.36)	10.95 (1.59)	0.95 (0.14)
F1C45	0.005291	0.005685	0.000810	10.89 (1.58)	10.95 (1.59)	0.95 (0.14)
F2A11	0.001801	0.003407	0.001695	8.35 (1.21)	8.71 (1.26)	0.33 (0.05)
F2A12	0.002395	0.003407	0.001695	8.55 (1.24)	8.71 (1.26)	0.33 (0.05)
F2A13	0.003828	0.003407	0.001695	9.12 (1.32)	8.71 (1.26)	0.33 (0.05)
F2A14	0.005606	0.003407	0.001695	9.00 (1.31)	8.71 (1.26)	0.33 (0.05)
F2A15	—	0.003407	0.001695	8.53 (1.24)	8.71 (1.26)	0.33 (0.05)
F2A40	—	0.004760	0.000999	7.76 (1.12)	7.52 (1.09)	0.65 (0.09)
F2A41	—	0.004760	0.000999	8.05 (1.17)	7.52 (1.09)	0.65 (0.09)
F2A42	—	0.004760	0.000999	6.82 (0.99)	7.52 (1.09)	0.65 (0.09)
F2A43	0.003668	0.004760	0.000999	7.51 (1.09)	7.52 (1.09)	0.65 (0.09)
F2A44	0.005628	0.004760	0.000999	8.31 (1.21)	7.52 (1.09)	0.65 (0.09)
F2A45	0.004983	0.004760	0.000999	6.71 (0.97)	7.52 (1.09)	0.65 (0.09)

—Specimen localized outside of gauge length.

The combined stress–strain responses from each of the eight sets of specimens are shown in figure 18 through figure 25. These figures present the average stress versus average strain results, effectively demonstrating the global response of each specimen. The specimens were ordered within each graph so that those that displayed greater proportions of multicracking and localization within the monitored gauge length are shown first. For example, in figure 18, specimens F1A21, F1A15, and F1A22 display greater cracking and localization performance than F1A20 and F1A23. Thus, these first three specimens present a full set of results, while the latter two only present a partial set of results. Note that a partial set of results from some specimen sets is largely the result of the test method and its implementation and is not necessarily indicative of substandard concrete tensile performance.

It is also possible to compare sets of specimens in individual batches. For example, batch F1A results related to the two different test specimen lengths are presented in figure 18 and figure 19, batch F2A results related to the two different test specimen lengths are presented in figure 20 and figure 21, and batch F1C results related to the two different test specimen lengths are presented in figure 22 and figure 23.

A qualitative assessment of the results of the tests completed on the eight sets of specimens demonstrates that the test method is capable of producing consistent uniaxial tensile stress–strain results. However, it is also clear that successful completion of a test with a full set of results, including localization within the gauge length, is not ensured, with these results indicating that as few as two of five tests in a set may be successful. In addition, these results demonstrate concretes that exhibit postcracking strengths greater than first cracking strengths, such that batches F1C and B2A are more likely to be successfully completed with a full set of results.

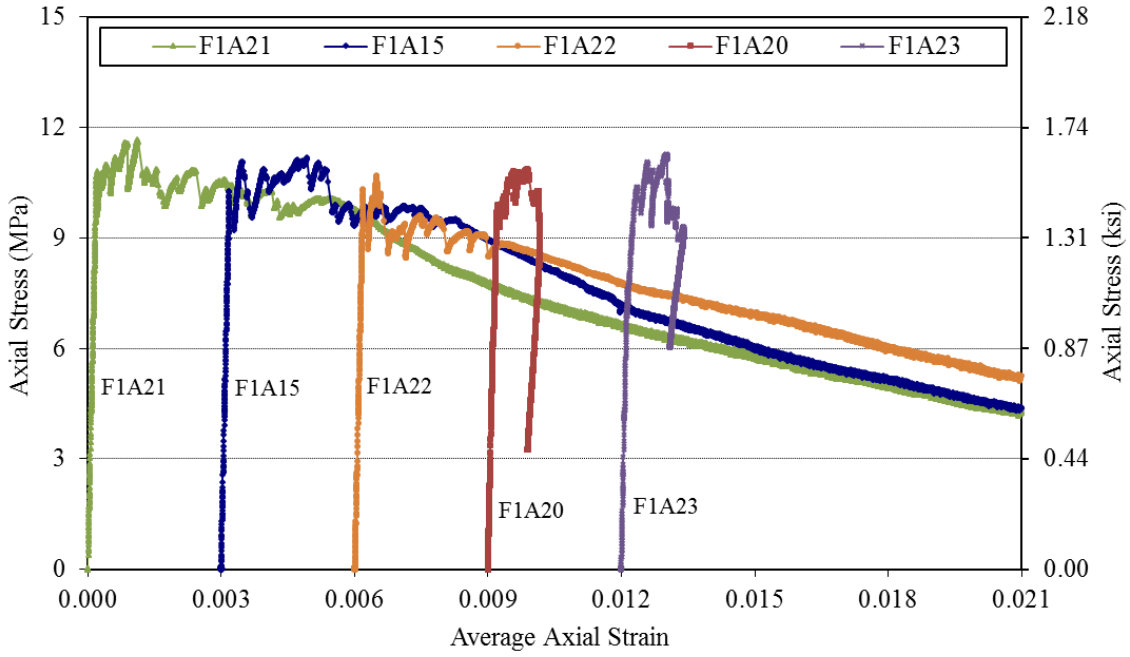

Source: FHWA.

Figure 18. Graph. DTT stress–strain results for batch F1A with 431.8-mm (17-inch)-long specimen.

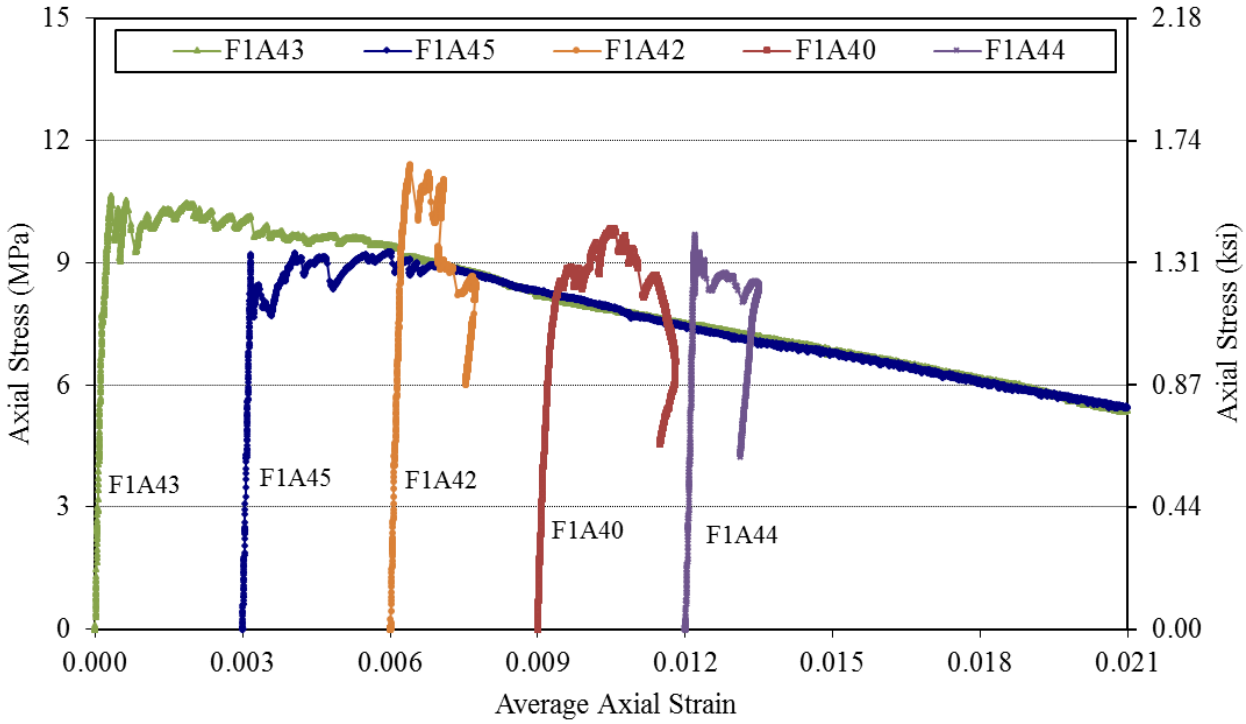

Source: FHWA.

Figure 19. Graph. DTT stress–strain results for batch F1A with 304.8-mm (12-inch)-long specimen.

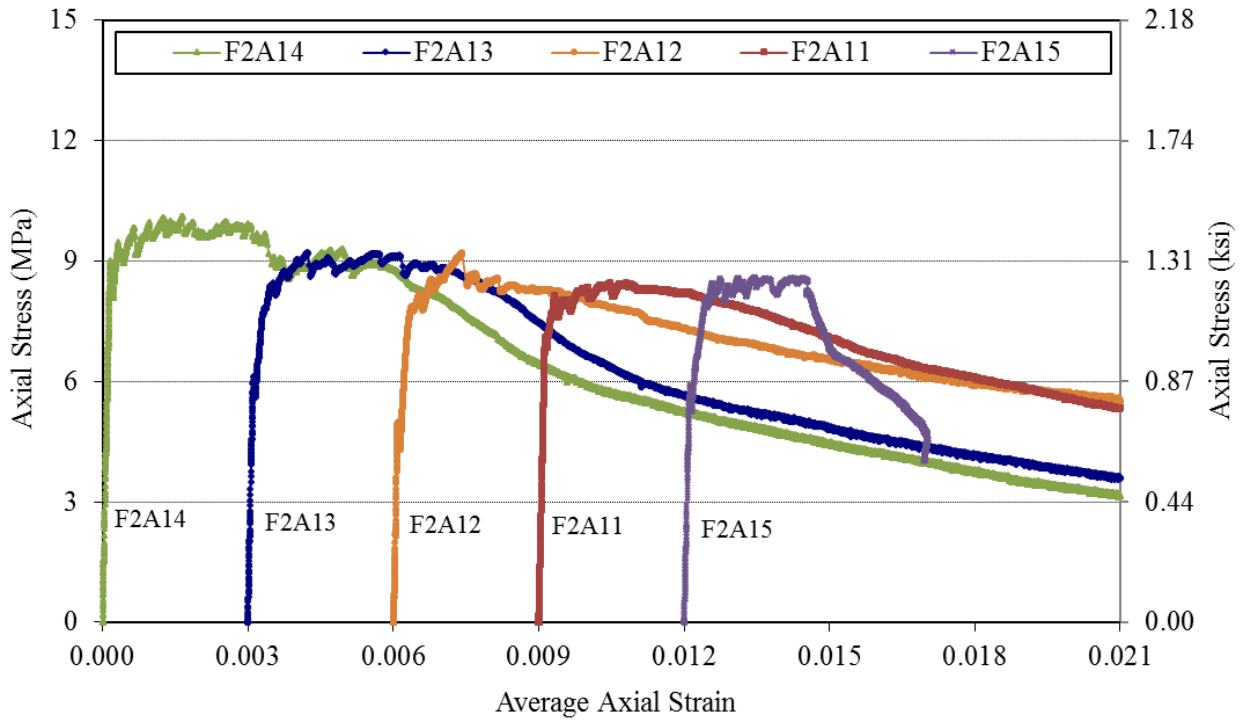

Source: FHWA.

Figure 20. Graph. DTT stress–strain results for batch F2A with 431.8-mm (17-inch)-long specimen.

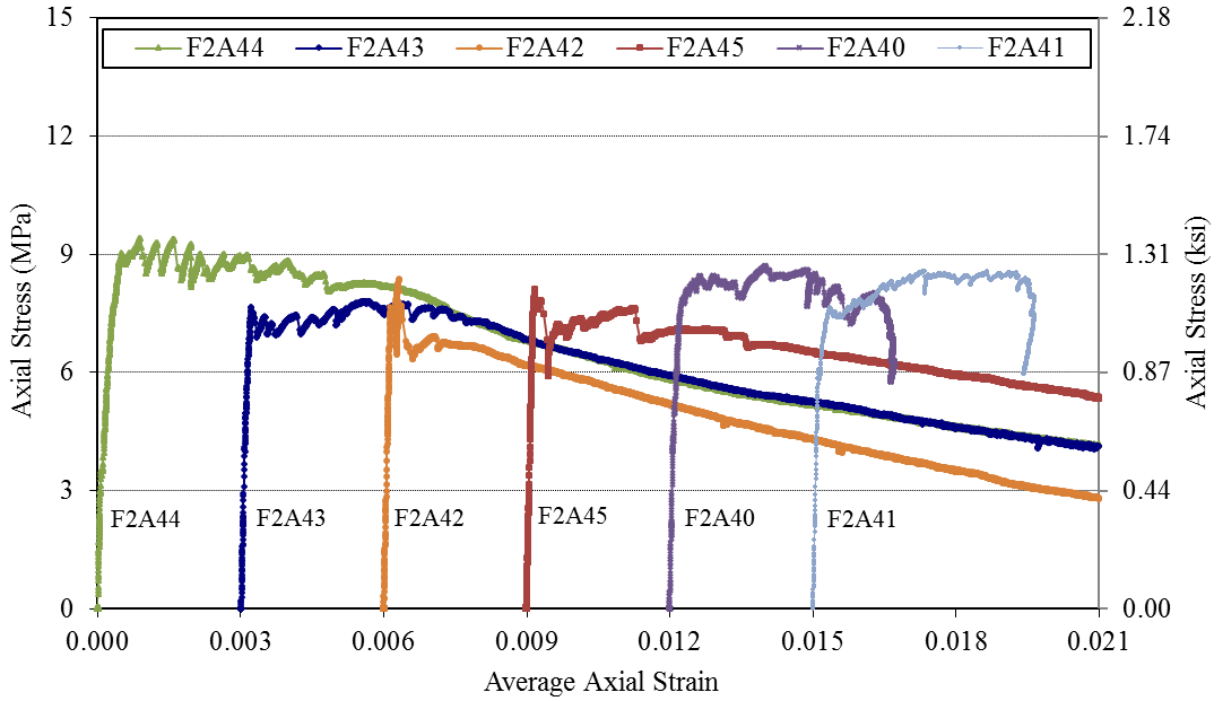

Source: FHWA.

Figure 21. Graph. DTT stress–strain results for batch F2A with 304.8-mm (12-inch)-long specimen.

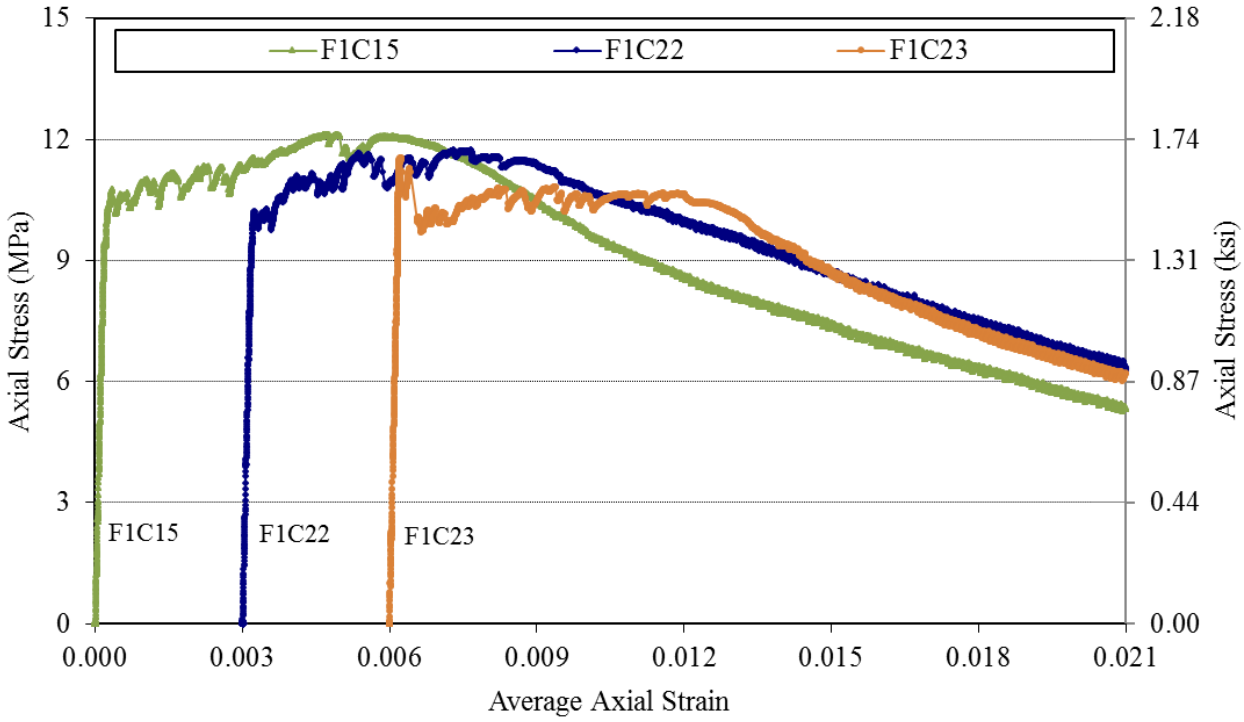

Source: FHWA.

Figure 22. Graph. DTT stress–strain results for batch F1C with 431.8-mm (17-inch)-long specimen.

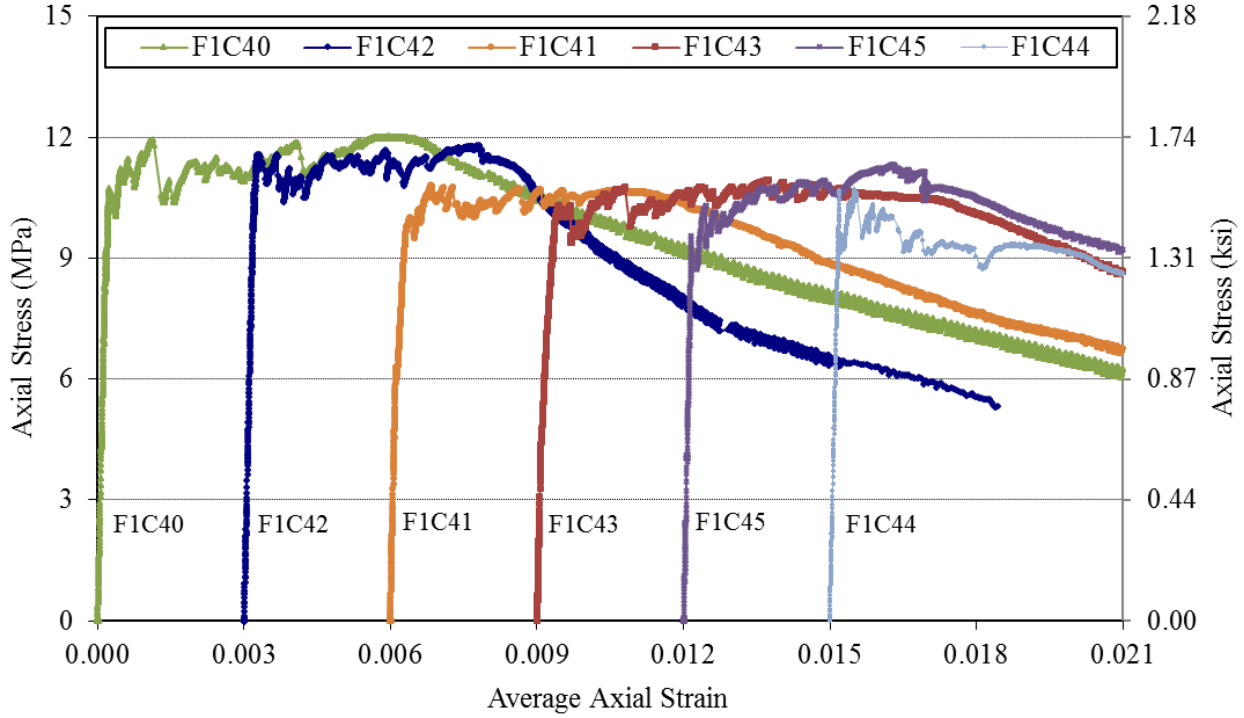

Source: FHWA.

Figure 23. Graph. DTT stress–strain results for batch F1C with 304.8-mm (12-inch)-long specimen.

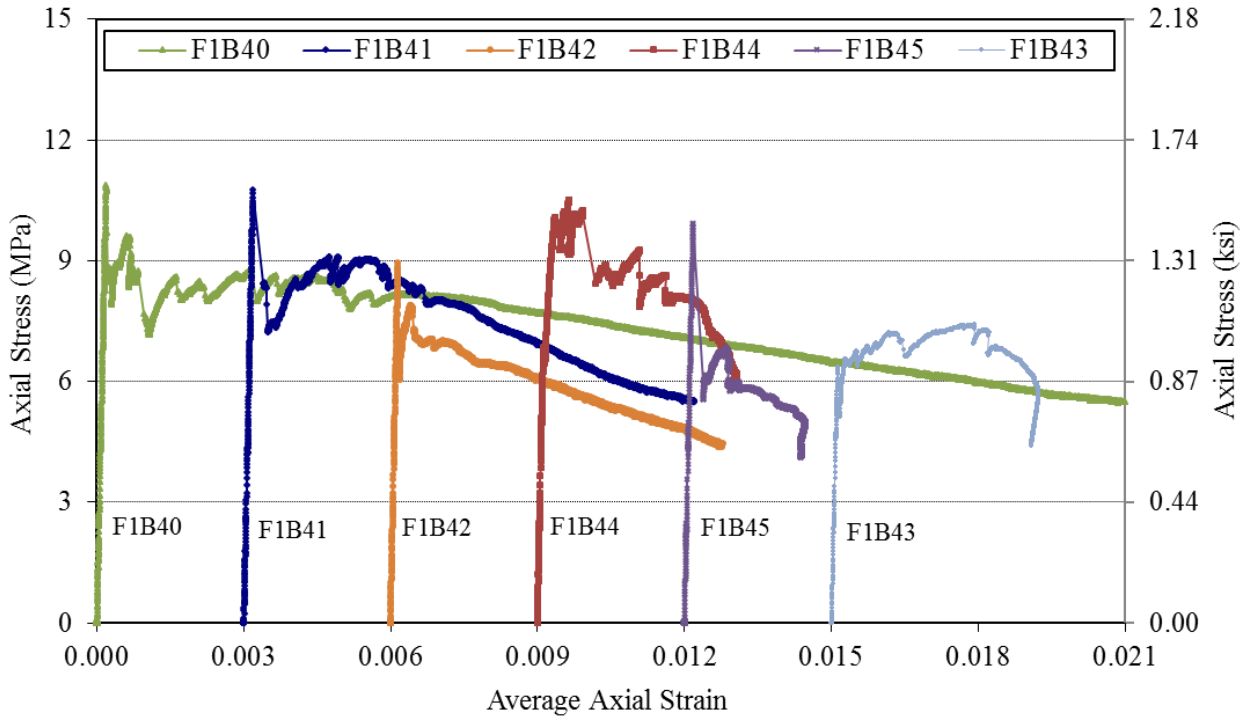

Source: FHWA.

Figure 24. Graph. DTT stress–strain results for batch F1B with 304.8-mm (12-inch)-long specimen.

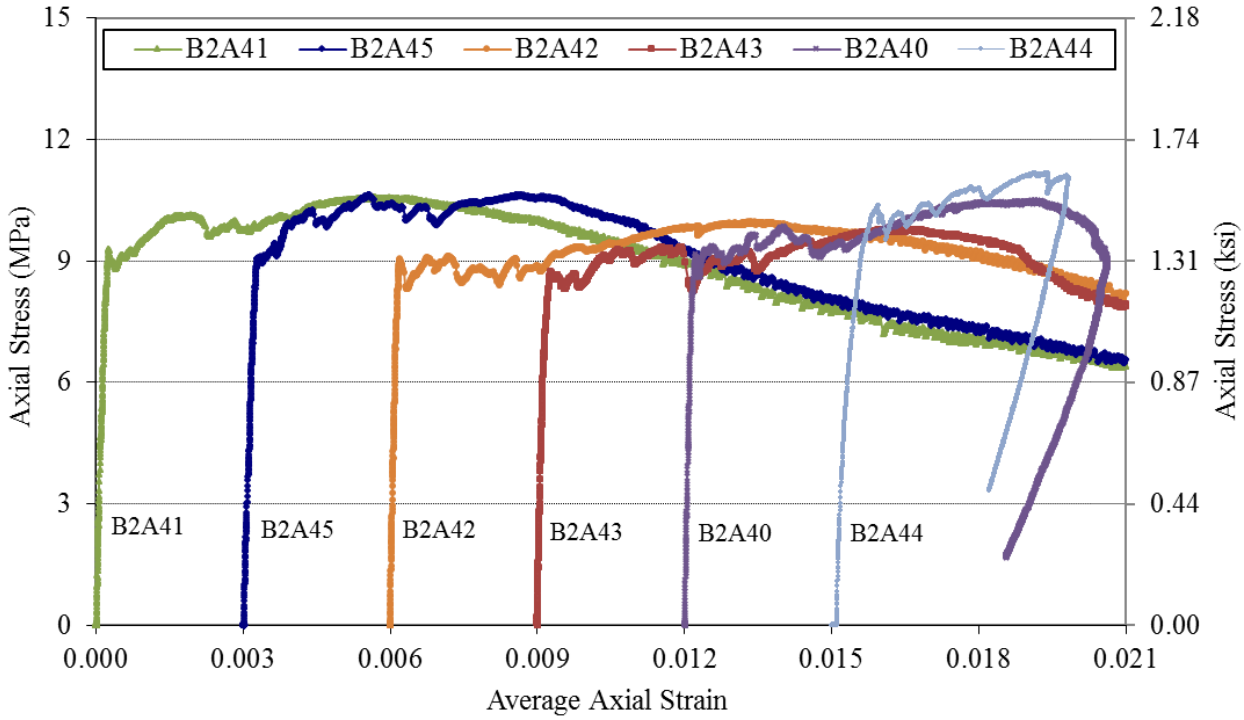

Source: FHWA.

Figure 25. Graph. DTT stress–strain results for batch B2A with 304.8-mm (12-inch)-long specimen.

CHAPTER 5. PRISM FLEXURE TEST (FT)

INTRODUCTION

This chapter focuses on the bending test method developed within this study. The test method is detailed first, beginning with the presentation of existing methods and concluding with the proposed test method. The results obtained from the implementation of the test method are then presented.

EXISTING TEST METHODS

Many researchers have attempted to develop test methods to assess the tensile performance of FRC. Test methods have included both direct and indirect assessments, and some have been standardized.[26,51] Most of them are based on the definition of a stress-crack-opening law, which is consistent with design methods of reinforced concrete and conventional FRC structures. Due to the multiple-fine-cracking behavior of UHPC elements, however, a stress–strain approach is more appropriate.

When using an FT for identifying a stress–strain constitutive law, an inverse analysis is necessary to determine the uniaxial tensile behavior. Analytical inverse analyses for an FT on UHPC or high-performance, fiber-reinforced cementitious composites have been developed by many researchers with some success.[4,52–55] The following section details these inverse analyses.

BACKGROUND

This section presents background on inverse analysis methods, proposed flexural test methods, as well as specimens and loading considerations.

Inverse Analysis Based on Strain Measurement

This section presents a suite of different inverse analysis methods.

Japanese Concrete Institute (JCI) Method[56,57]

The Japanese Concrete Institute (JCI) method focuses on the bending moment curvature curve of fiber-reinforced cementitious composites, as discussed in JCI Standard JCI-S-003-2007.[58] It is based on the measurement of the applied load and the bending-moment–curvature during an FT. The test specimen was a prism that had a square cross section that was 100 mm (3.94 inches) deep, 100 mm (3.94 inches) wide, and 400 mm (15.75 inches) long. The curvature-measuring equipment consisted of LVDTs and jigs used for fixing LVDTs. LVDTs were set to measure the displacement of the pure bending span at positions of 15 and 85 mm (0.59 and 3.35 inches) from the lower surface of the test specimen, as shown in figure 26.

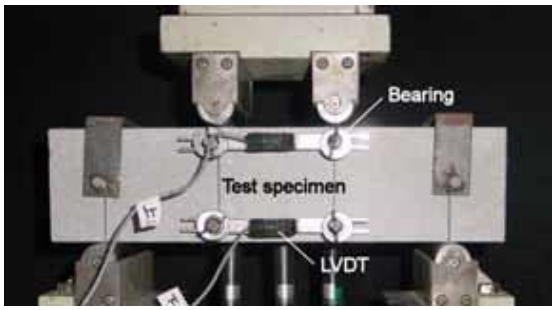

Figure 26. Photo. LVDT setup for the strain measurement.

The method used to obtain the stress–strain relationship of the tested material was a simplified inverse analysis. The comparison between the tensile strength and ultimate tensile strain evaluated by this method, and the actual tensile stress–strain behavior is shown in figure 27.

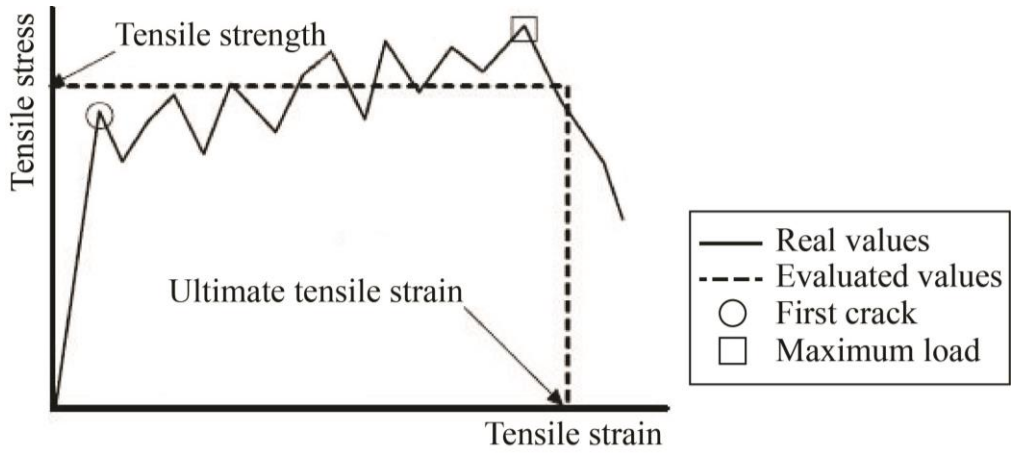

A. Strain-hardening type.

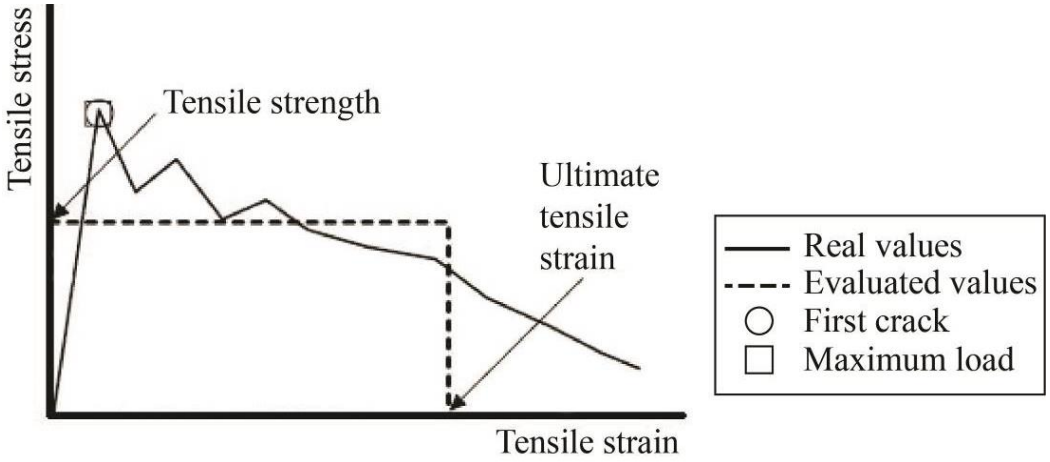

B. Strain-softening type.

Figure 27. Graphs. Tensile stress–strain curves (real and evaluated).[56]

This simplified inverse analysis was based on the following assumptions for stress distribution under the maximum bending moment:

- The stress distribution on the compression side is triangular.
- The stress distribution on the tension side is uniform.

It is assumed that the elastic modulus is equal to the static modulus obtained by compression testing.

JCI Standard JCI-S-003-2007considers, in the case of strain-hardening-type concrete, that the tensile strength and ultimate tensile strain evaluated by this method generally correspond to the tensile stress and strain at the maximum point obtained by uniaxial tension test.[58] For strain-softening-type, ductile-fiber-reinforced cementitious composites, the tensile strength and ultimate tensile strain evaluated by this method correspond to certain values that show its tensile behavior as representative values.

The method first accounts for the equilibrium of moments and normal forces under the maximum bending moment in a section analysis, as shown in figure 28 and equation 1 through equation 5.

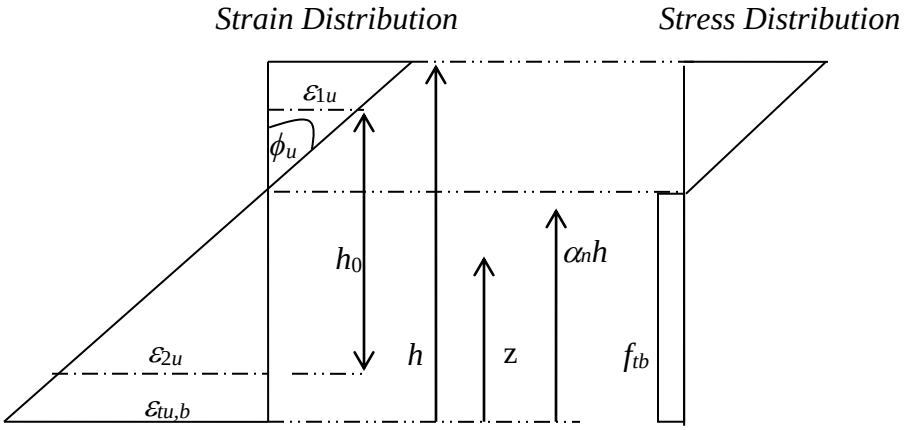

Figure 28. Graph. Strain and assumed stress distribution in the section under maximum bending moment in JCI method.

Where:

ε_{1u} = strain at maximum load as measured by the upper LVDT.
ϕ_u = beam curvature at the maximum load.
ε_{2u} = strain at maximum load as measured by the lower LVDT.
$\varepsilon_{tu,b}$ = ultimate tensile strain.
h_0 = distance between the two LVDTs.
h = depth of the specimen.
z = distance from the tensile face of the test specimen.
α_n = distance from the tensile face to the neutral axis divided by the height of the test specimen.
f_{tb} = effective tensile strength.

$$M_{max} = b \times \phi_u \times E \times (1-\alpha_n)^3 \times \frac{1}{3} \times h^3 + \frac{1}{2} \times b \times \alpha_n^2 \times h^2 \times f_{tb} \quad (1)$$

Where:

M_{max} = maximum moment.
b = width of the test specimen.
E = modulus of elasticity.

$$f_{tb} \cdot \alpha_n h - \phi_u \cdot E \cdot (1-\alpha_n)^2 \cdot h^2 = 0 \quad (2)$$

Substituting f_{tb} from equation 1 into equation 2 solves for equation 3 as follows:

$$\alpha_n^3 - 3 \times \alpha_n + 2 - \frac{6 \cdot M_{max}}{E \times \phi_u \times b \times h^3} = 0 \quad (3)$$

Thus, f_{tb} and $\varepsilon_{tu,b}$ are determined with equation 4 and equation 5.

$$f_{tb} = \frac{E \times \phi_u \times h^2 \times (1-\alpha_n)^2}{\alpha_n h} \quad (4)$$

$$\varepsilon_{tu,b} = \phi_u \times \alpha_n h \quad (5)$$

The assumption of uniform stress distribution along the tensile height induces a strength overestimation as explained in figure 29.

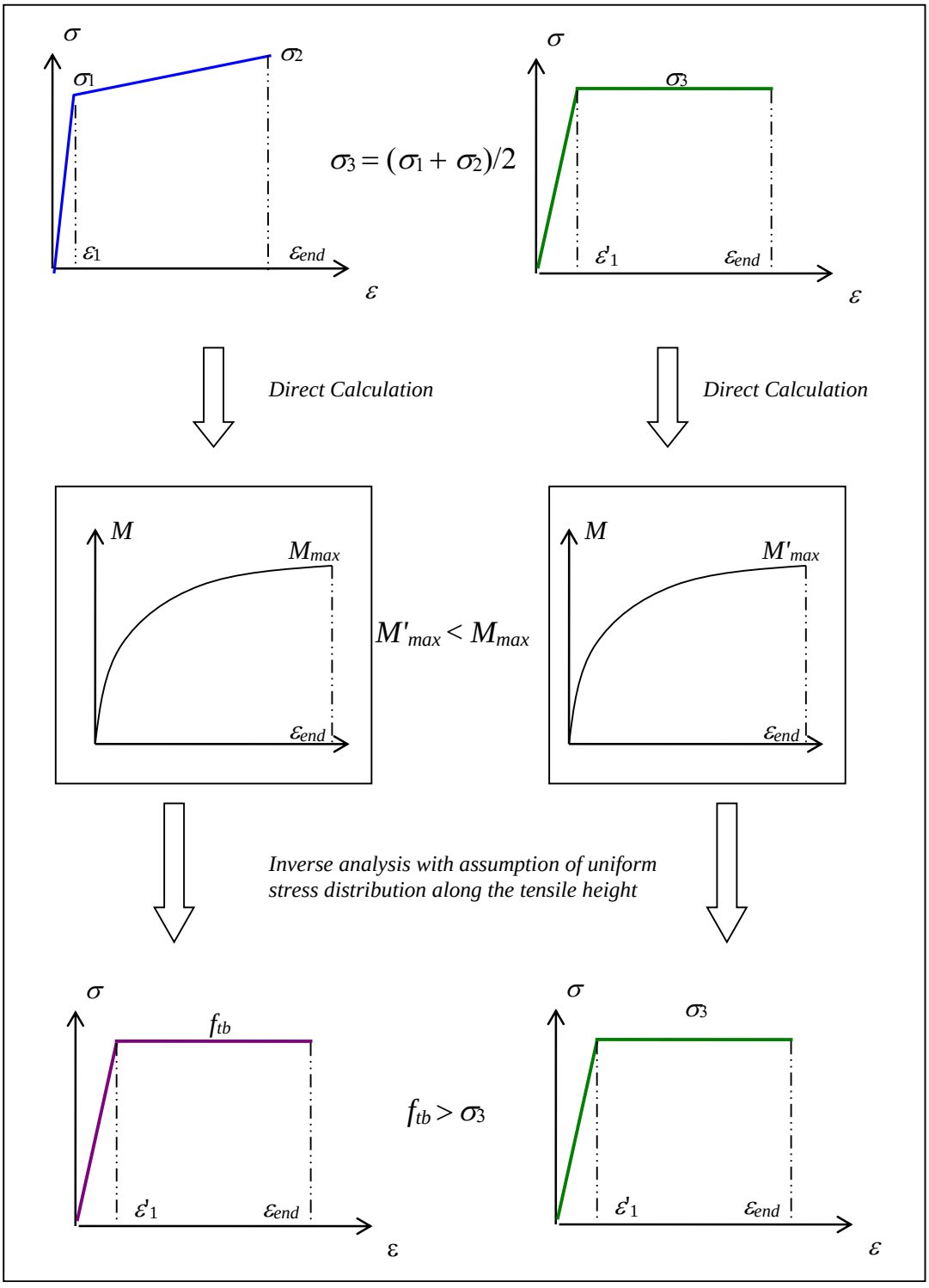

Figure 29. Flowchart. Strength overestimation induced by the assumption of uniform stress distribution along the tensile height.

Where:

σ = stress.
σ_1, σ_2, σ_3 = intermediate stress values.
ε_1 = strain at σ_1.
ε_{end} = strain limit.
ε'_1 = strain at start of σ_3.
M = moment.
M'_{max} = maximum moment resulting from assumption of σ_3.
ε = strain.

Inverse Analysis Based on Deflection Measurement

Qian and Li Method[59,54,60]

The Qian and Li method, which is based on the measurement of the applied load and the load point deflection (stroke) during an FT, can be used as a simplified inverse analysis to determine the tensile strain and the strength capacities. The following subsections highlight this determination.

Tensile Strain Capacity[59]

By conducting parametric studies based on a flexural behavior model of SHCCs, a master curve was constructed in terms of tensile strain capacity with respect to deflection capacity. Based on the deflection capacity of an FT and master curve from the parametric studies, the tensile strain capacities of the SHCCs were derived.

The flexural behavior model used in this method is based on the work of Maalej and Li.[61] The actual SHCC considered in the model was polyethylene fiber-reinforced engineered cementitious composite (PE-ECC) material. To simplify the analysis, the stress–strain behavior of the engineered cementitious composite (ECC) was assumed as bilinear curves in both tension and compressive (as shown in figure 30). Based on a linear strain profile, equilibrium of forces, and moment in a section, the relation between flexural stress and tensile strain at the extreme tension fiber can be determined as a function of basic material properties.

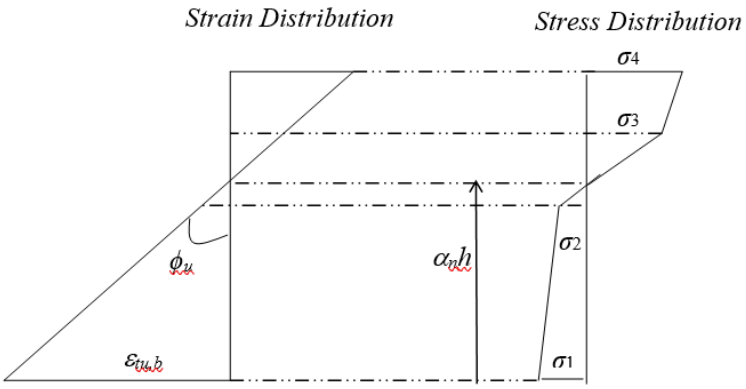

Figure 30. Graph. Strain and assumed stress distribution in the section under maximum bending moment in Qian and Li method.

Based on geometrical considerations, the beam curvature was computed as the ratio of tensile strain at the extreme tension fiber (simplified as critical tensile strain) to the distance from bottom side to the neutral axis, which is shown in equation 6.

$$\phi = \frac{\varepsilon_{tu,b}}{\alpha_n h} \quad (6)$$

An equation to relate the deflection of the prism to the curvature at the load point was then used. This equation is based on elastic structural mechanics and is considered reasonably valid for nonlinear behavior. The modeled system is shown in figure 31.

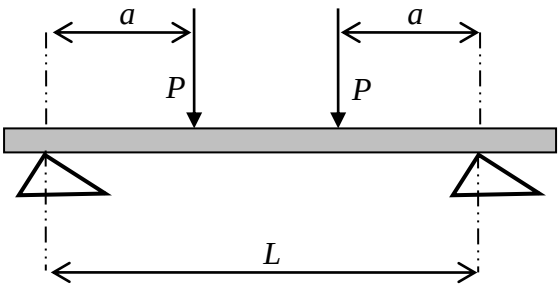

Figure 31. Illustration. FT setup for relating load to deflection and curvature.

Where:

a = shear span length.
P = point load.
L = span length.

In the case of FTs on specimens subjected to linear elastic behavior, the deflection at the load point (δ_p) is defined in equation 7.

$$\delta_p = \frac{15 \times P \times a \times L^2}{162 \times E \times I} \quad (7)$$

Where *I* is the moment of inertia.

δ_p can be expressed using the curvature, $\phi = \frac{P \cdot a}{E \cdot I}$, where ϕ is the beam curature, in equation 8.

$$\delta_p = \frac{15 \times \phi \times L^2}{162} \approx 0.1 \times \phi \times L^2 \quad (8)$$

Deflection due to shear deformation was neglected, and the curvature was considered constant along the middle-third span between the two load points. Concerning the experimental tests, it is important to notice if the specimen was not fully contacted with the test apparatus as the initial

loading stage may show unrealistically low stiffness. This can be corrected by discounting this part of deflection from the load point deflection.

The relation between flexural stress and tensile strain capacity, ε_{tu}, was already established; therefore, the flexural stress and load point deflection could be predicted. A parametric study (prism dimensions of 51 by 76 by 356 mm (2.01 by 2.99 by 14.02 inches) with a span length of 305 mm (12.01 inches)) was conducted to investigate the influence of material uniaxial tensile and compressive properties (parametric values) on the flexural response of SHCCs based on the previously mentioned flexural model. The overall results showed a linear relation between ε_{tu} and deflection capacity. All linear curves were in a narrow band regardless of the values of other material properties, which suggests that the beam deflection capacity was most sensitive to tensile strain capacity for a fixed geometry.

For ease of quality control on site, a master curve was constructed as a line with uniform thickness to cover all parametric case studies (as shown in figure 32). For conservatism, the top edge of the master curve was made to coincide with the upper boundary of all curves.

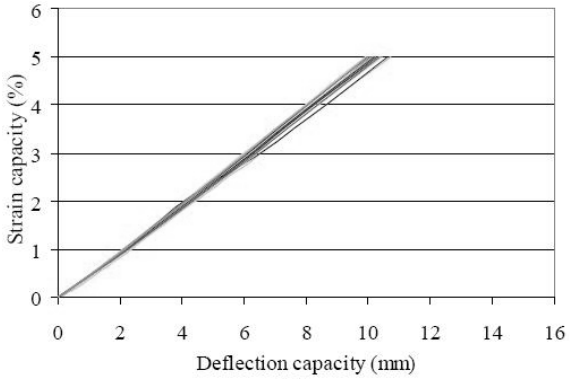

1 mm = 0.039 inch.

A. Tensile strain capacity versus deflection capacity relation obtained from parametric study.

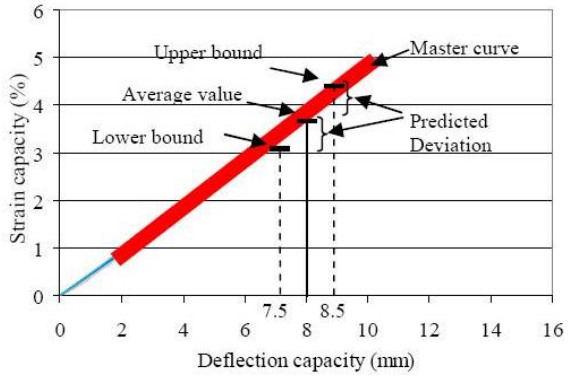

1 mm = 0.039 inch.

B. Master curve transforming deflection capacity into tensile strain capacity.

Figure 32. Graphs. Parametric study and master curve for determining tensile strain capcity.[(59)]

Based on the master curve obtained from the parametric study, the deflection capacity from a simple prism bending test could be easily converted to material tensile strain capacity. Equation 9 and equation 10 were developed to simplify the conversion procedure.

$$\varepsilon'_{tu} = 0.5 \times \delta_u - 0.22 \quad (9)$$

Where:

ε'_{tu} = predicted tensile strain capacity (percent).
δ_u = ultimate deflection obtained from FT (mm).

$$PD = 0.5 \times SD + 0.18 \quad (10)$$

Where:

PD = predicted deviation for tensile strain capacity (percent) considering the standard deviation of the deflection capacity.
SD = standard deviation of the deflection capacity (mm) (assumed to be 0.5 mm (0.02 inch) in that case).

It should be noted that equation 9 and equation 10 can only be applied to specimens with the same geometry and loading conditions. Should the geometry and/or any of these loading conditions change, another set of master curves and corresponding conversion equations should be developed for that purpose.

Tensile Strength[54]

Parametric studies were conducted from a simplified flexural behavior model of SHCCs, as shown in figure 33.

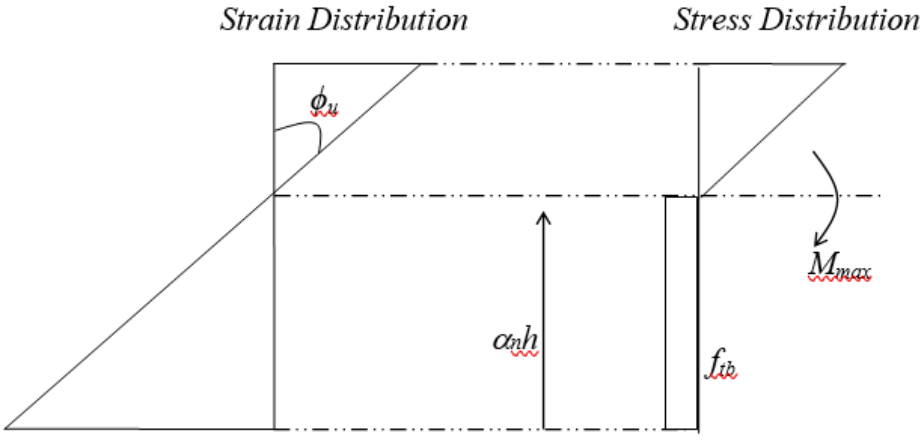

Figure 33. Graph. Assumption of strain and stress distribution under maximum bending moment for a par5ametric study.[54]

Compared to the model associated with figure 30, this model assumes the following:

- The first cracking strength was assumed to be equal to the ultimate tensile strength and was labeled as the effective tensile strength f_{tb}, where $\sigma_1 = \sigma_2 = f_{tb}$.

- The strain distribution in the compressed zone was considered to be linear.

A master curve was constructed in figure 34 in terms of normalized modulus of rupture (MOR) (or possibly maximum equivalent bending stress) divided by effective tensile strength (labeled f_{tb} in the figure) with respect to tensile strain capacity. The tensile strain capacity was obtained via the strain capacity–deflection capacity master curve described in figure 33.

All curves derived from the parametric study were in a relatively narrow band regardless of actual material properties. For ease of quality control, a master curve was constructed by considering two lines (up and lower boundaries) to cover all parametric case studies, as shown in figure 34.

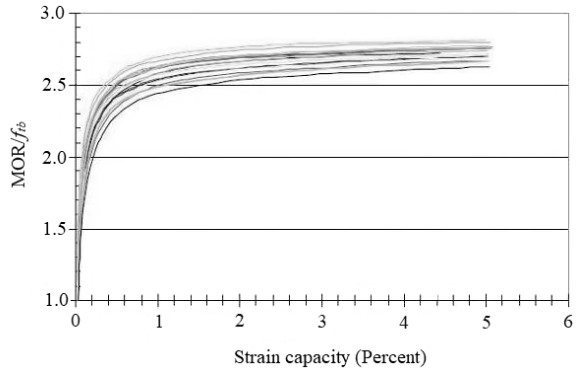

A. For all cases.

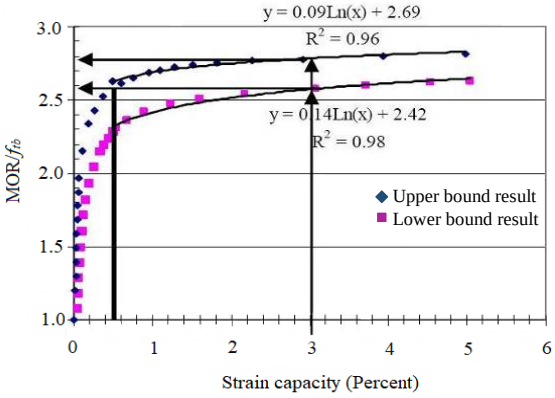

B. For two extreme cases with upper and lower boundaries (with strain capacity <0.5 percent).

Figure 34. Graphs. Relation of MOR/f_{tb} with tensile strain capacity derived from the parametric study.(54)

To understand the shapes of these curves, the expression for the ratio MOR/f_{tb} is necessary. From the equilibrium of moments and normal forces under the maximum bending moment in a section analysis, equation 1 and equation 2 were derived. They can be simplified to obtain the expression for f_{tb} (equation 4) and MOR (equation 11).

$$MOR = \frac{6M_{max}}{b \cdot h^2} = 2 \cdot E \cdot h \cdot \phi_u \cdot (1-\alpha_n)^3 + 3 \cdot f_{tb} \cdot \alpha_n^2 \quad (11)$$

The ratio MOR/f_{tb} can be expressed as a function of α_n using equation 12.

$$\frac{MOR}{f_{tb}} = 4\alpha_n - \alpha_n^2 \quad (12)$$

The ratio MOR/f_{tb} only depends on α_n. Thus, it is possible to plot the value of α_n with respect to the tensile strain at the bottom flange.

The following values and concepts have been used in order to fix the different parameters:

- ***b***: 50.8 mm (2 inches).
- ***h***: 50.8 mm (2 inches).
- ***E***: 50 GPa (8,700 ksi).
- **Tensile stress–strain relationship**: Elastic-perfectly plastic where plateau stress in a tensile stress–strain relationship ($\sigma_{plastic}$) = 6 MPa (0.87 ksi).
- **Tensile strain capacity**: 0.030.

Figure 35 presents the α_n tensile strain at the bottom flange curve for the studied case. The specimen dimensions were 50.1 by 50.1 mm (1.97 by 1.97 inch) with a tensile stress–strain relationship with elastic-perfectly plastic at 6 MPa (0.87 ksi).

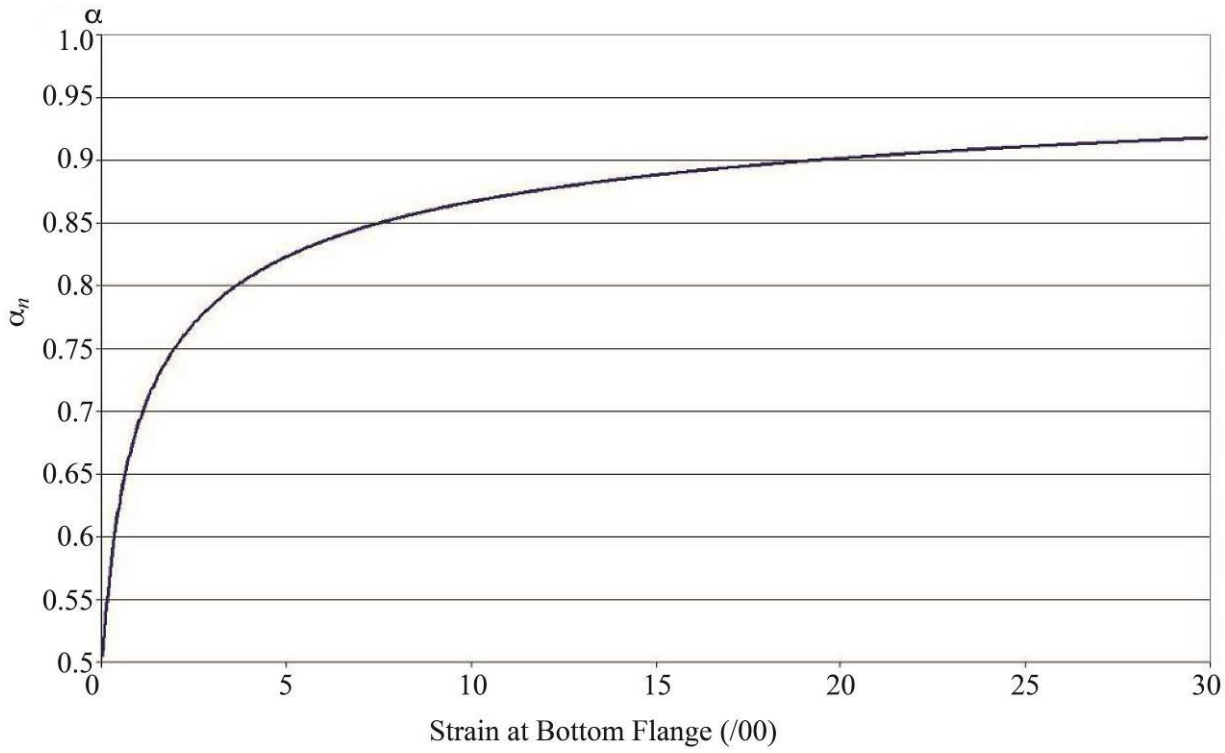

Figure 35. Graph. α_n tensile strain at the bottom flange.

Where α is a unitless parameter to determine height of a specimen with respect to the total height of the specimen.

In the first phase (tensile strain at the bottom flange less than 0.005), α_n increased with a relatively high intensity to tend to a plateau in the second step. Thus, the dependence of α_n (as well as the ratio MOR/f_{tb}) on the tensile strain capacity decreased when the latter increased.

Equation 12 can be used to qualify the ductility of a material. Thus, for an elastic-perfectly plastic material like steel, this ratio is equal to 3. For an elastic-perfectly brittle material like glass, the ratio is equal to 1. Concerning SHCC materials, figure 34 shows that the ratio is bracketed between 1 and 3 depending on the tensile strain capacity. Nevertheless, this expression of MOR/f_{tb} should not be used for cases when α_n is close to 0.5 corresponding with a small strain capacity (which is the case for some UHPC-class materials) due to the great simplification of tensile stress distribution. The global process presented in the Qian and Li method to obtain a simplified tensile stress–strain relationship is described in figure 36.[54]

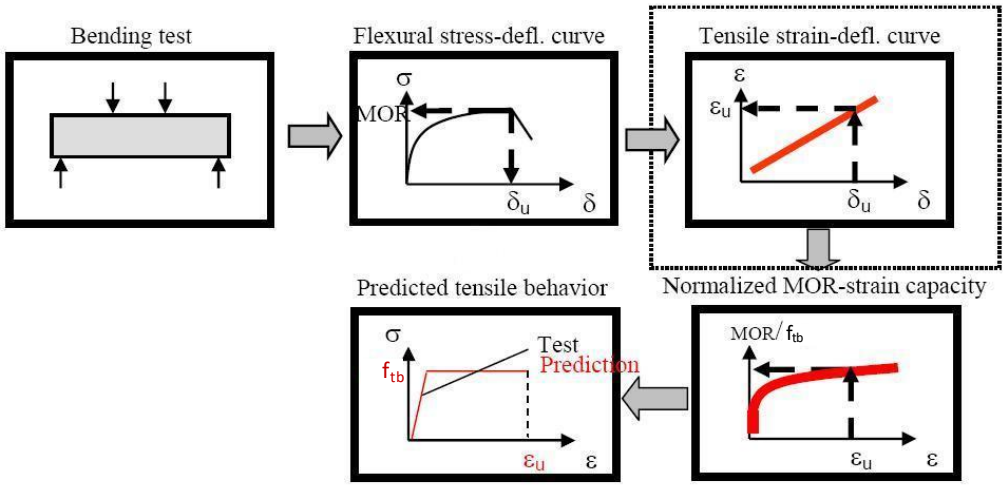

δ = deflection.
ε_u = strain capacity.

Figure 36. Flowchart. Process of Qian and Li method.[54]

Hinge Model[52]

The Hinge Model, which was developed by Ostergaard et al. and is based on the measurement of the applied load and the midspan deflection during an FT, can be used to obtain the stress–strain relationship of the tested material. The flexural behavior model used in this method (figure 37) is inspired by the work of Maalej and Li.[61] The actual SHCC considered in the model was PE-ECC, as discussed previously. The model takes into account the influence of the localization and the softening stress versus crack opening behavior (in using a bilinear approximation) of the studied material on the pre-peak response during an FT. Indeed, up to 50 percent of the pre-peak response may be associated with localization.[52] This is due to the ductile behavior of the ECC, which influences the stress versus crack opening (i.e., σ-w) relationship.[62]

The modeling is based on the nonlinear hinge concept described in Olesen's "Fictitious Crack Propagation in Fiber-Reinforced Concrete Beams."[63] Olesen states the following:[63]

The propagating crack is modelled within the element boundaries as a layer of independent spring elements. These spring elements are formed by incremental horizontal strips, and are attached at each end to a rigid boundary. Each boundary may rotate and translate such that it may be joined with an uncracked beam modelled according to the classical beam theory. (p. 272)

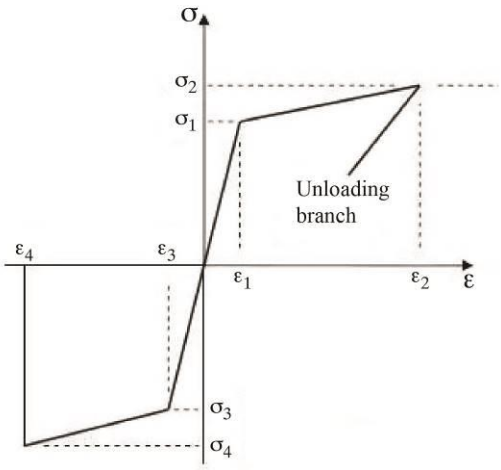

A. Assumed compressive and tensile stress–strain relationship before crack localization.

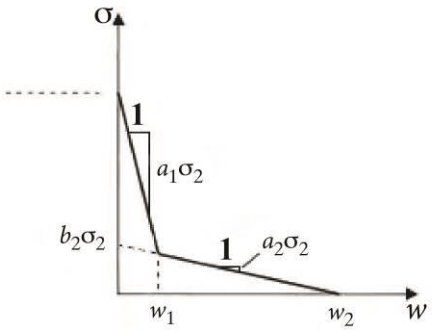

B. Tensile σ-w relationship after crack localization.

Figure 37. Graphs. Assumed compressive and tensile stress–strain relationship before and after crack localization.(52)

Where:

a_1, a_2, and b_2 = parameters defining the stress versus crack opening relationship.
w_1 = crack opening at point 1.
w_2 = crack opening at point 2.

Figure 38 presents the hinge and the stress distribution in the hinge. Based on this distribution, the entire hinge behavior can be described.

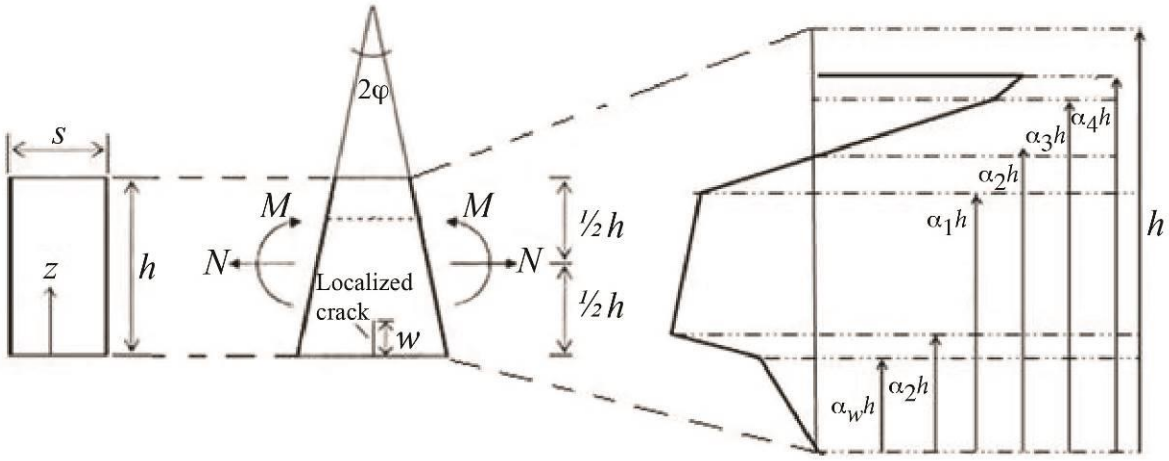

Figure 38. Illustration. Geometry, loading, and deformation of the hinge element and stress distribution in the hinge element when crushing and localization of the crack have occurred.(52)

Where:

s = hinge extension.
z = distance from the tensile face of the test specimen.
h = height of the specimen.
N = normal force.
M = moment.
ϕ= beam curvature.
α_w = cracked depth divided by the height of the specimen.
α_1 = distance from the tensile face to the linear elastic tensile limit divided by the height of the specimen.
α_2 = distance from the tensile face to the point of maximum tensile stress divided by the height of the specimen.
α_3 = distance from the tensile face to the linear elastic compressive limit divided by the height of the specimen.
α_4 = distance from the tensile face to the point of maximum compressive stress divided by the height of the specimen.

The Hinge model has been implemented in the FT. The localized deformation was determined from the actual localization mechanism (i.e., identified from experimental observations for each tested specimens). The case of multilocalization can be taken into account by superposing the mechanisms. At that point, the unknown parameter is *s*. This value has been calibrated from finite element models. The best results are obtained with *s* equal to 0.9*h*.

An inverse analysis was realized by using the squared sum of differences between the experimental result and the model result as object function, as shown in equation 13.

$$\min_{(f_{tc}, f_{tu}, E_{t1}, E_{t2})} = \sum_{i=1}^{n} \left(\frac{\hat{P}_i - P_i}{P_i} \right)^2 \quad (13)$$

Where:

min = minimum of the values.
f_{tc} = first cracking strength.
f_{tu} = ultimate tensile strength.
E_{t1}= slope of the elastic tensile curve.
E_{t2} = slope of the inelastic tensile curve.
n = total number of data points.
i = data point.
$\hat{P}_i$ = load obtained by the model for a certain deflection.
P_i = experimental load at the corresponding deflection.

The compressive behavior is considered as already determined. A parametric study was completed with different specimen sizes. The knowledge of the σ-w relationship and s were unimportant for a certain range of height. For thin beams (h = 10 mm (0.39 inch)) or thick beams ($h \geq$ 100 mm (3.94 inches)), realistic values of s and the σ-w parameter were necessary to avoid an error on strain-hardening properties, which can be close to 30 percent. In these latter cases, the uniqueness of solution was also checked in a given range of precision.

Rigaud et al. Method[(55)]

The Rigaud et al. method, which is based on the measurement of the applied load and the midspan deflection during an FT, can be used to obtain the stress–strain relationship of the tested material.[(55)] Concerning the instrumentation, the test setup requires that the deflection-measuring system measures "net deflection at the midspan exclusive of any effects due to seating or twisting of the specimen on its supports"(p. 512).[(64)] To meet these requirements, a yoke similar to that described in ASTM C1018 is necessary to measure the midspan deflection.[(64)]

The experimental bending-moment midspan deflection curve is converted into the bending-moment-curvature curve thanks to the relationship between the midspan deflection of the prism and the curvature along the middle-third span. This relationship is based on elastic structural mechanics and considered as reasonably valid for nonlinear behavior. The modeled system has been presented previously (see figure 31).

In the case of FTs on specimens exhibiting linear elastic behavior, the deflection at the midspan can be solved for using equation 14.

$$\delta_m = \frac{P \cdot L^3}{24 \times E \times I} \times \left(\frac{3a}{L} - \frac{4a^3}{L^3} \right) \quad (14)$$

Where δ_m is the midspan deflection. This equation can be expressed using the curvature, where $\phi = \frac{P \cdot a}{E \cdot I}$, in equation 15 as follows:

$$\delta_m = \frac{23}{216} \times \phi \times L^2 \quad (15)$$

Deflection due to shear deformation was neglected, and the curvature was considered constant along the middle-third span between the two load points. This evaluation method is based on the equilibrium of moments and forces in a section analysis for each value of curvature and corresponding bending moment. The strain distribution and the stress distribution in the compressed zone are considered as linear. The modeled system is shown in figure 39.

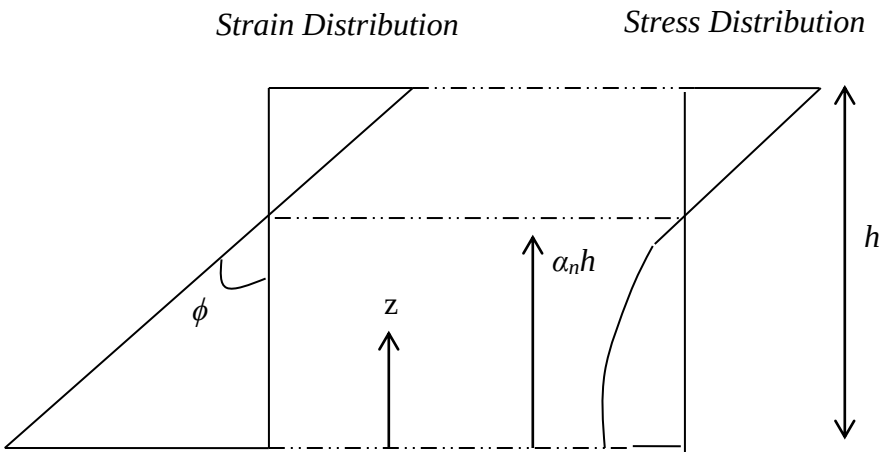

Figure 39. Graph. Strain and stress distributions.

For the zone in compression, equation 16 and equation 17 are used.

$$N_c = \int_{\alpha_n h}^{h} b \times \sigma_c(z) \times dz = b \times \int_{\alpha_n h}^{h} E \times \varepsilon_c(z) \times dz = b \times E \times \phi \times \int_{\alpha_n h}^{h} (z - \alpha_n h) \times dz = b \times E \times \phi \times (\alpha_n - 1)^2 \times \frac{h^2}{2} \quad (16)$$

Where:

N_c = compressive component of the normal force.
h = height of the specimen.
b = width of the specimen.
$\sigma_c(z)$ = compressive stress as a function of distance from the tensile face.
z = distance from tensile face of the test specimen.
dz = differential with respect to distance from the tensile face
E = modulus of elasticity.
$\varepsilon_c(z)$ = compressive strain as a function of distance from the tensile face.
ϕ = beam curvature.
α_n = distance from tensile face to neutral axis divided by the height of specimen.

$$M_c = \int_{\alpha_n h}^{h} b \times \sigma_c(z) \times z \times dz = b \times E \times \phi \times \left(2 + \alpha_n{}^3 - 3\alpha_n\right) \times \frac{h^3}{6} \quad (17)$$

Where M_c is the compressive component of the applied moment. For the zone in tension, equation 18 through equation 20 are used.

$$N_t = \int_0^{\alpha_n h} b \times \sigma_t(\varepsilon_t) \times dz \tag{18}$$

Where:

N_t = tensile component of the normal force.
σ_t = tensile stress.
ε_t = tensile strain.

$$M_t = \int_0^{\alpha_n h} b \times \sigma_t(\varepsilon_t) \times z \times dz \tag{19}$$

Where M_t is the tensile component of the applied moment.

$$\varepsilon_t = \varepsilon_t(z) = \phi \times (\alpha_n h - z) \tag{20}$$

Based on equation 20, z can be solved for using equation 21.

$$z = \alpha_n h - \frac{\varepsilon_t}{\phi} \tag{21}$$

Where the following is true:

- For $z = 0$, ε_t = the strain at the extreme tension fiber (ε_{tf}).
- For $z = \alpha h$, where α is the unitless parameter to determine the height of a specimen with respect to the total height of the specimen $\varepsilon_t = 0$ (neutral axis).
- N_t and M_t can thus be presented as a function of strain in equation 22 and equation 23.

$$N_t = b \times \int_0^{\varepsilon_{tf}} \frac{\sigma_t(\varepsilon_t)}{\phi} \times d\varepsilon \tag{22}$$

$$M_t = b \times \int_0^{\varepsilon_{tf}} \sigma_t(\varepsilon_t) \times \left(\frac{\alpha_n h}{\phi} - \frac{\varepsilon_t}{\phi^{\acute{e}}} \right) \times d\varepsilon = \alpha_n h \times N_t - b \times \int_0^{\varepsilon_{tf}} \frac{\sigma_t(\varepsilon_t) \times \varepsilon_t}{\phi^2} \times d\varepsilon \tag{23}$$

Where $\phi^{\acute{e}}$ is the beam curvature at the elastic limit.

Then the tensile stress–strain relationship of the tested material is discretized to incremental tensile strain at increment j (ε_{tj}) and tensile stress at increment j (σ_{tj}). Equation 22 and equation 23 can be written in considering two successive loading steps in the section: the loading at increment j and the loading at the increment $j + 1$. Between these two loading steps, the tensile

strain at increment j (ε_{tj}) increased to the tensile strain at increment $j + 1$ (ε_{tj+1}), and the corresponding tensile stress at increment j (σ_{tj+1}) increased to the tensile stress at increment $j + 1$ (σ_{tj+1}). For these two steps of loading, there are two different curvatures and two neutral axis positions. Therefore, equation 24 through equation 30 can be used.

$$N_{tj} = b \times \int_0^{\varepsilon_{tfj}} \frac{\sigma_t(\varepsilon_t)}{\phi_j} \times d\varepsilon \tag{24}$$

Where:

N_{tj} = tensile component of the normal force at increment j.

ε_{tfj} = strain at the extreme tensile fiber at increment j

ϕ_j = beam curvature at increment j.

$$M_{tj} = \alpha_{nj}\ h \times N_{tj} - b \times \int_0^{\varepsilon_{tfj}} \sigma_t(\varepsilon_t) \times \left(\frac{\varepsilon_t}{\phi_j^{\acute{e}}} \right) \times d\varepsilon \text{ at increment } j \tag{1}$$

Where:

M_{tj} = tensile component of the applied moment at increment j.

α_{nj} = distance from the tensile face to the neutral axis divided by the height of the specimen at increment j.

$\phi^{\acute{e}}_j$ = beam curvature at the elastic limit at increment j.

$$N_{tj+1} = b \times \int_0^{\varepsilon_{tfj+1}} \frac{\sigma_t(\varepsilon_t)}{\phi_{j+1}} \times d\varepsilon \tag{26}$$

Where:

N_{tj+1} = tensile component of the normal force at increment $j + 1$.

ε_{tfj+1} = strain at the extreme tensile fiber at increment j+1

ϕ_{j+1} = beam curvature at increment $j + 1$.

$$M_{tj+1} = \alpha_{nj+1} h \times N_{tj+1} - b \times \int_0^{\varepsilon_{tfj+1}} \sigma_t(\varepsilon_t) \times \left(\frac{\varepsilon_t}{\phi^{\acute{e}}_{j+1}} \right) \times d\varepsilon \text{ at increment } j + 1 \tag{27}$$

Where:

M_{tj+1} = tensile component of the applied moment at increment $j + 1$.

α_{nj+1} = distance from the tensile face to the neutral axis divided by the height of the specimen at increment $j + 1$.

$\phi^{\acute{e}}_{j+1}$ = beam curvature at the elastic limit at increment $j + 1$.

$$N_{tj+1} = b \times \int_0^{\varepsilon_{tfj+1}} \frac{\sigma_t(\varepsilon_t)}{\phi_{j+1}} \times d\varepsilon + b \times \int_{\varepsilon_{tfj}}^{\varepsilon_{tfj+1}} \frac{\sigma_t(\varepsilon_t)}{\phi_{j+1}} \times d\varepsilon = \frac{\phi_j}{\phi_{j+1}} \times N_{tj} + b \times \int_{\varepsilon_{tfj}}^{\varepsilon_{tfj+1}} \frac{\sigma_t(\varepsilon_t)}{\phi_{j+1}} \times d\varepsilon \tag{28}$$

$$M_{tj+1} = \alpha_{nj+1} h \times N_{tj+1} - b \times \int_0^{\varepsilon_{tj}} \sigma_t(\varepsilon_t) \times \left(\frac{\varepsilon_t}{\phi_{j+1}^{\acute{e}}} \right) \times d\varepsilon - b \times \int_{\varepsilon_{tj}}^{\varepsilon_{tj+1}} \sigma_t(\varepsilon_t) \times \left(\frac{\varepsilon_t}{\phi_{j+1}^2} \right) \times d\varepsilon \tag{29}$$

$$M_{tj+1} = \alpha_{nj+1} h \times N_{tj+1} + \frac{\phi_j^2}{\phi_{j+1}^2} \times \left(M_{tj} - \alpha_{nj} h \times N_{tj}\right) - b \times \int_{\varepsilon_{tj}}^{\varepsilon_{tj+1}} \sigma_t(\varepsilon_t) \times \left(\frac{\varepsilon_t}{\phi_{j+1}^2}\right) \times d\varepsilon \tag{30}$$

For equation 28 and equation 30, the last term can be expressed in discrete form with the method of integration by trapezoid, as shown in equation 31 and equation 32.

$$\int_{\varepsilon_{tfj}}^{\varepsilon_{tfj+1}} \frac{\sigma_t(\varepsilon_t)}{\phi_{j+1}} \times d\varepsilon = \frac{1}{\phi_{j+1}} \times \frac{\sigma_{tj+1} + \sigma_{tj}}{2} \times \left(\varepsilon_{tj+1} - \varepsilon_{tj}\right) \tag{31}$$

Where:

σ_{tj+1} = tensile stress at increment $j + 1$.
σ_{tj} = tensile stress at increment j.
ε_{tj+1} = tensile strain at increment $j + 1$.

$$\int_{\varepsilon_{tfj}}^{\varepsilon_{tfj+1}} \frac{\sigma_t(\varepsilon_t) \times \varepsilon_t}{\phi^2{}_{j+1}} \times d\varepsilon = \frac{1}{\phi^2{}_{j+1}} \times \frac{\sigma_{tj+1} \times \varepsilon_{tj+1} + \sigma_{tj} \times \varepsilon_{tj}}{2} \times \left(\varepsilon_{tj+1} - \varepsilon_{tj}\right) \tag{32}$$

Thus, equation 33 and equation 34 can be solved for as follows:

$$N_{tj+1} = \frac{\phi_j}{\phi_{j+1}} \times N_{tj} + b \times \frac{1}{\phi_{j+1}} \times \frac{\sigma_{tj+1} + \sigma_{tj}}{2} \times \left(\varepsilon_{tj+1} - \varepsilon_{tj}\right) \tag{33}$$

$$M_{tj+1} = \alpha_{nj+1} h \times N_{tj+1} + \frac{\phi_j^2}{\phi_{j+1}^2} \times \left(M_{tj} - \alpha_{nj} h \times N_{tj}\right) - b \times \frac{1}{\phi_{j+1}^2} \times \frac{\sigma_{tj+1} \times \varepsilon_{tj+1} + \sigma_{tj} \times \varepsilon_{tj}}{2} \times \left(\varepsilon_{tj+1} - \varepsilon_{tj}\right) \tag{34}$$

For each increment j and $j + 1$, equation 35 through equation 37 can be solved for as follows:

$$N_{cj} + N_{tj} = 0 \tag{35}$$

Where N_{cj} is the compression component of the normal force at increment j.

$$M_{cj} + M_{tj} = M_{j-\text{experimental}} \tag{36}$$

Where:

M_{cj} = compression component of the applied moment at increment j.
$M_{j\text{-experimental}}$ = experimental moment at increment j.

$$\phi_j = \phi_{j-\text{experimental}} = \frac{216}{23} \times \frac{\delta_{mj}}{L^2} \tag{37}$$

Where:

$\phi_{j\text{-experimental}}$ = experimental beam curvature at increment j.
δ_{mj} = midspan deflection at increment j.

As a consequence, solving this inverse problem consists of determining the parameter α_{nj+1} by increments in order to satisfy mechanical equilibrium in the section.

The methods proposed by Qian and Li and Rigaud et al. used a similar relationship to associate the deflection of the prism to the curvature at the load point or at midspan.[54,55] This relationship is based on elastic structural mechanics and is considered reasonably valid for nonlinear behavior. Nevertheless, the use of this relationship for nonlinear behavior induces an overestimation of the deflection for a given curvature along the middle-third span or an underestimation of the curvature for a given value of deflection. As a consequence, the methods based on this mechanical assumption perform the following:

- Underestimate the real strain during the hardening phase.
- Overestimate the postcracking stress.

To quantify the strength overestimation induced by the mechanical assumption used by Qian and Li and Rigaud et al. to convert the deflection into curvature, a bending-moment deflection curve is generated from an initial bending-moment-curvature curve. This is done by a direct calculation (double integration of the curvature over the length of the test specimen) and then converted in a bending-moment-curvature curve thanks to the considered mechanical assumption.[54,55] An inverse analysis is also realized, and the result is compared with the initial tensile stress–strain relationship. The following values have been used in order to fix the geometrical parameters:

- **Width of test specimen (*b*)**: 50.8 mm (2 inches).
- **Height of test specimen (*h*)**: 50.8 mm (2 inches).
- **Shear span length (*a*)**: 76 mm (3 inches).
- **Span length (*L*)**: 229 mm (9 inches).

A parametric study was conducted to quantify the strength overestimation induced by the mechanical assumption used by Qian and Li and Rigaud et al.[54,55] In the context of this research, the range of parametric values concerning the tensile properties (table 14) was reduced to be more precise.

Table 14. Range of material parameters used in the parametric study.

Variable	Lower Value	Upper Value
First Cracking Strength, MPa (psi)	6 (870)	12 (1,740)
Ultimate Tensile Strength, MPa (psi)	6 (870)	14 (2,030)
Tensile Strain Capacity	0.001	0.014
Modulus of Elasticity, GPa (ksi)	50 (7,252)	65 (9,427)

Twenty cases were investigated concerning this process, one of which is detailed in this report. The considered tensile stress–strain relationship is a hardening curve, as shown in figure 40 through figure 44, with modulus of elasticity (E) = 50,000 MPa (7,250 ksi), first cracking strength (f_{tc}) = 6 MPa (0.87 ksi), and ultimate tensile strength (f_{tu}) = 10 MPa (0.145 ksi) at a strain limit (ε_{end}) = 0.010.

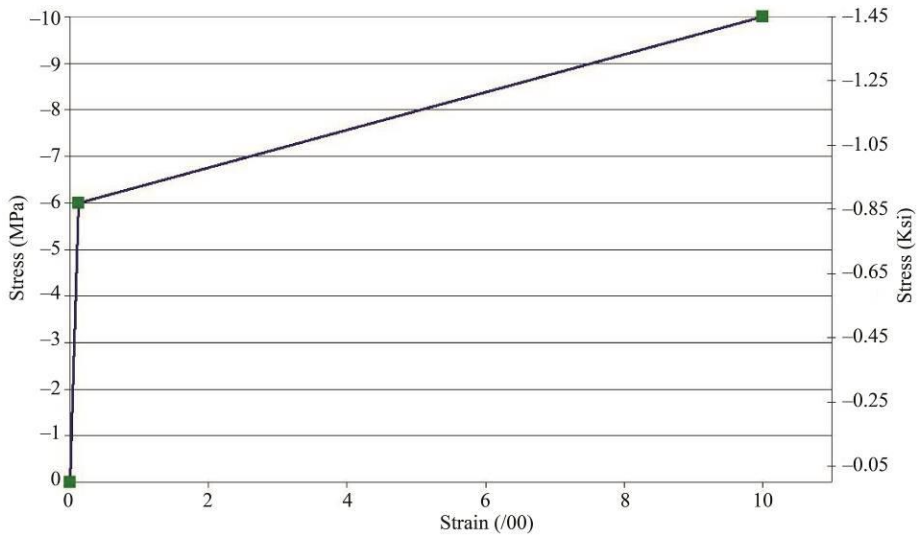

Figure 40. Graph. Tensile stress–strain relationship used for the Rigaud et al. method.[55]

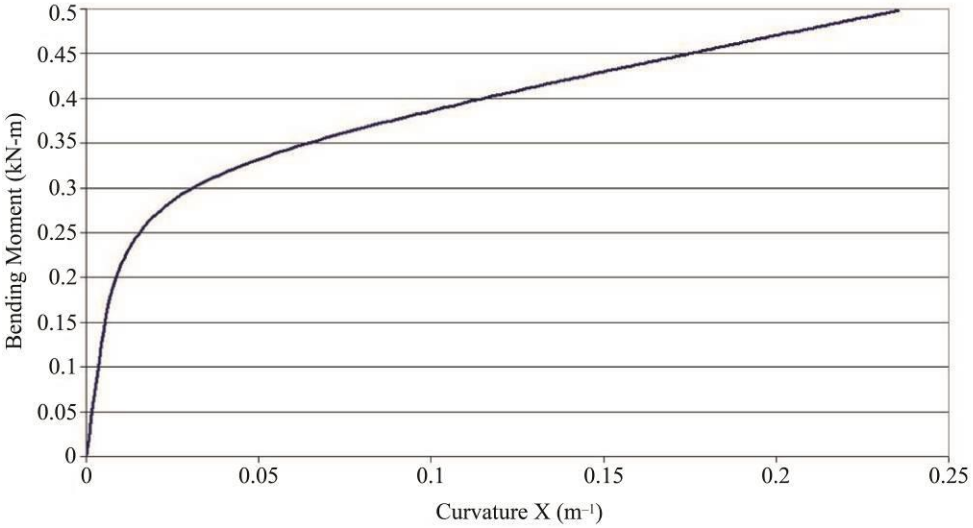

1 kN-m = 8.85 kip-inch.
1 m^{-1} = 0.0254 inch-1.

Figure 41. Graph. Bending-moment curvature.

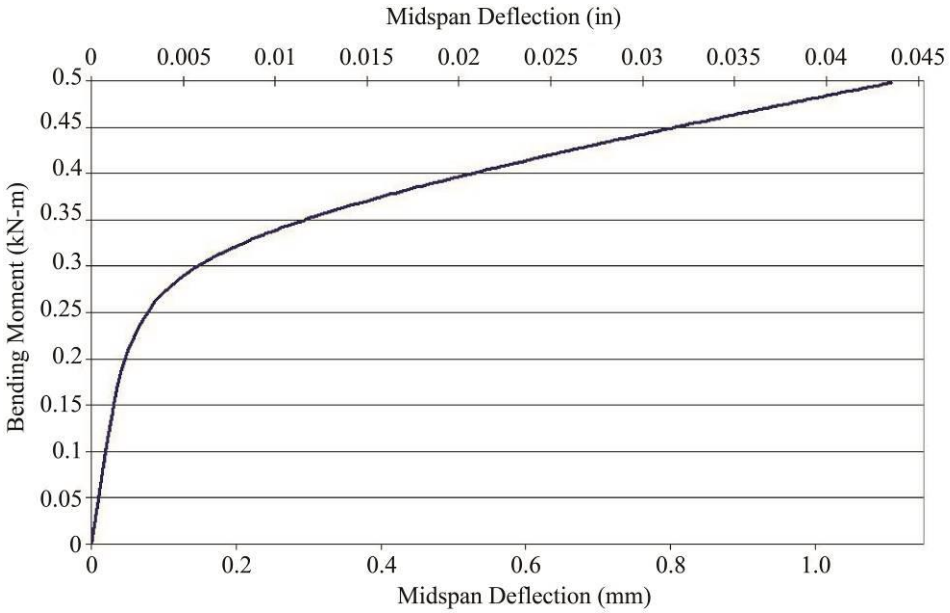

© IFSTTAR.
1 kN-m = 8.85 kip-inch.
1 mm = 0.039 inch.

Figure 42. Graph. Bending-moment deflection curve obtained after direct calculation (double integration of the curvature over the length of the prism).

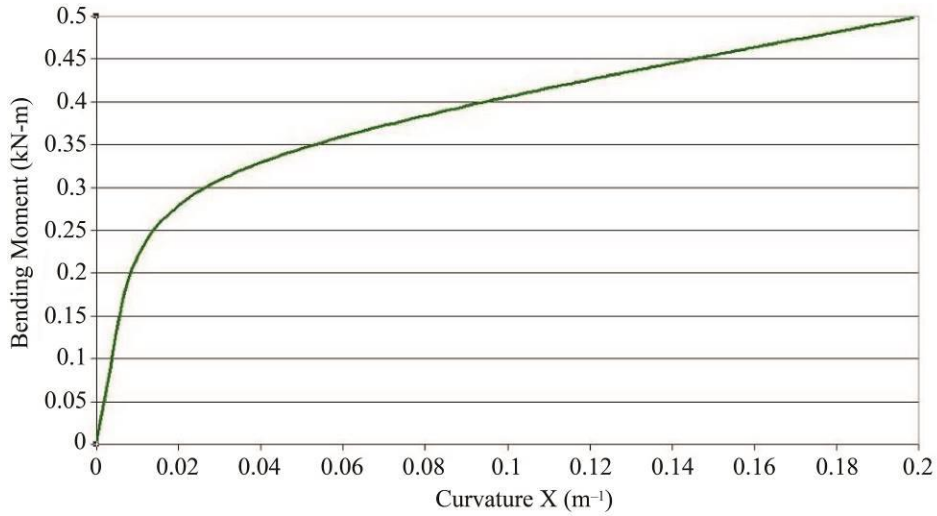

© IFSTTAR.
1 kN-m = 8.85 kip-inch.
1 m^{-1} = 0.0254 in-1.

Figure 43. Graph. Bending-moment-curvature curve obtained with the mechanical assumption used by Qian and Li and Rigaud et al.

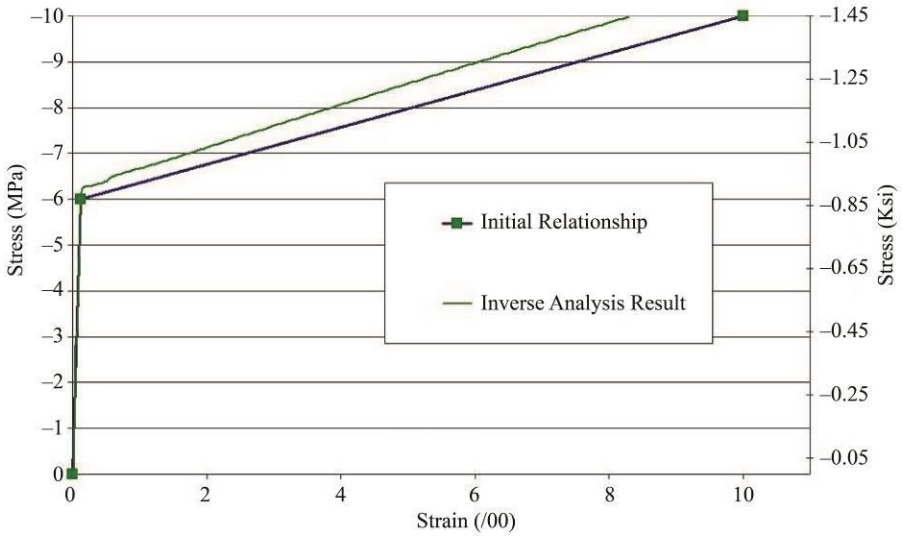

Source: © IFSTTAR.

Figure 44. Graph. Comparison between inverse analysis results and initial tensile stress–strain relationship.

In this particular case, the average overestimation of stress in the tensile stress–strain relationship was equal to 5.9 percent, and the underestimation of hardening strain was equal to 17 percent. Throughout the analysis, the average overestimation of strength (observed in the 20 studied cases) was equal to 4.8 percent, and the average underestimation of hardening strain was close to 20 percent (with a minimum equal to 12 percent and a maximum close to 30 percent). In conclusion, the main effect of the mechanical assumption used to convert the deflection into curvature was on the strain at crack localization. The effect on the stress stayed relatively minor.

Association Farnçaise de Génie Civil–Service d'étude des transports, des routes et de leure aménagement (AFGC-SETRA) Method[(4)]

The Association Française de Génie Civil–Service d'étude des transports, des routes et de leure aménagement (AFGC-SETRA) method, which is based on the measurement of the applied load and the midspan deflection during an FT, can be used to obtain a bilinear tensile stress–strain relationship of the tested material. From the average and characteristic curves, the maximum moment of the average curve ($M^{max}_{Average\text{-}curve}$) obtained from testing and the maximum moment of the characteristic curve ($M^{max}_{Chara\text{-}curve}$) obtained from testing can be deduced. These values are also used in the simplified inverse analysis in order to obtain the mean and characteristic tensile stress–strain relationship. This evaluation method is based on the equilibrium of moments and forces in a section analysis. It is assumed that the UHPC constitutive law can be represented by a simplified curve such as that shown in figure 45.

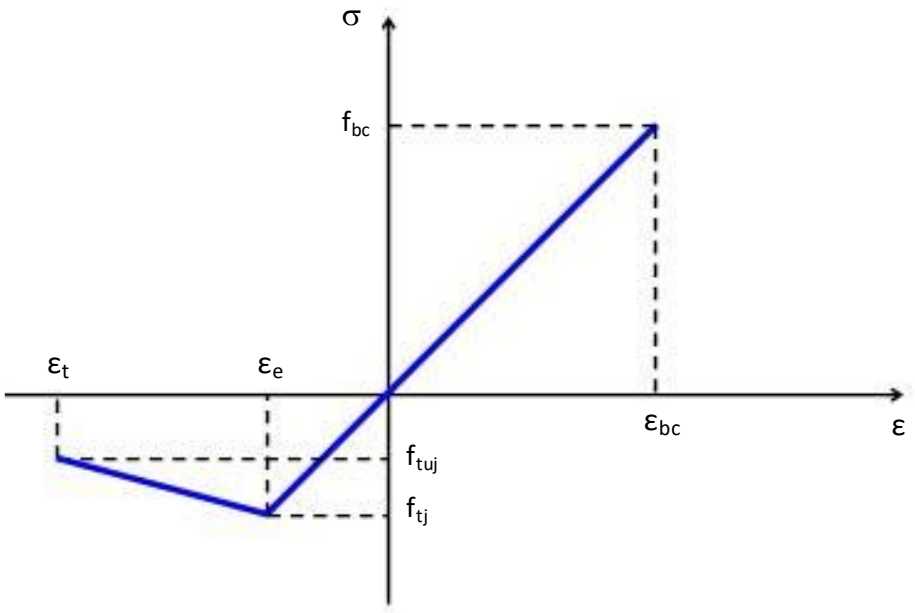

Figure 45. Graph. AFGC-SETRA method stress–strain constitutive relationship.[(4)]

Where:

ε_t = tensile strain.
ε_e = tensile strain capacity of the cementitious matrix.
σ = stress.
f_{bc} = compressive stress limit (i.e., $0.6 \times f'_c$, where f'_c is the compressive strength).
f_{tj} = tensile strength of the cementitious matrix.
f_{tuj} = ultimate tensile strength.
ε_{bc} = strain corresponding to f_{bc}.
ε = strain.

In a first approach, ε_{end} is assumed to be equal to 0.010. The strain and stress distributions in the compressed zone are considered as linear, as shown in figure 46.

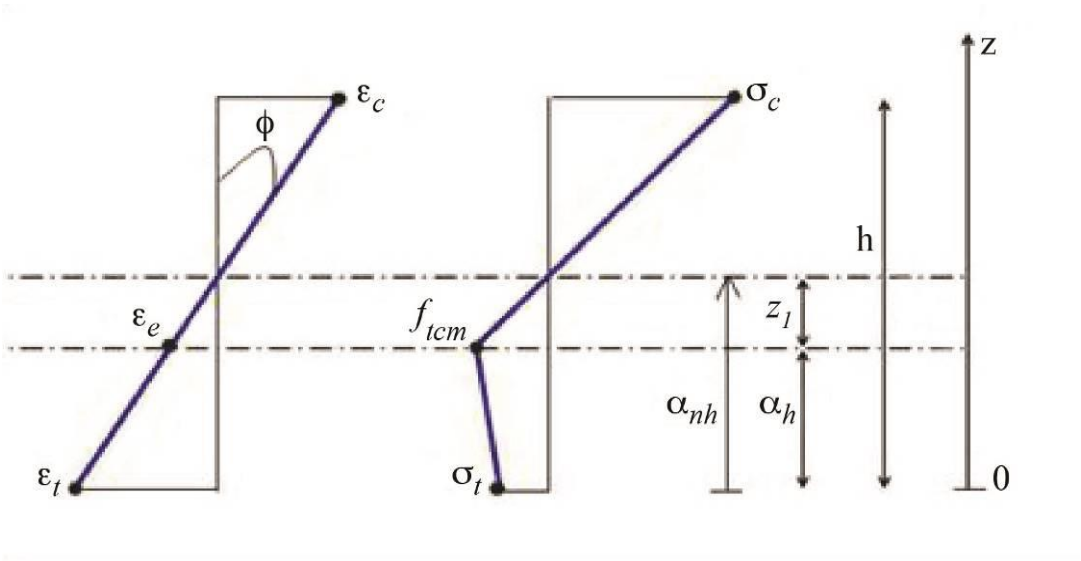

Figure 46. Graph. AFGC-SETRA method stress and strain distributions.[4]

Where:

ϕ = beam curvature.
ε_c = compressive strain.
ε_t = tensile strain.
σ_c = compressive stress.
σ_t = tensile stress.
α_n = distance from the tensile face to the neutral axis divided by the height of the specimen.
f_{tcm} = cementitious matrix strength (without fibers).
h = height of the specimen.
α = unitless parameter to determine height of a specimen with respect to the total height of the specimen.
z_1 = cementitious matrix strength depth parameter.
z = distance from the tensile face of the test specimen.

The stresses in the cracked depth (σ_f) and in the uncracked depth (σ_b) are solved for in equation 38 and equation 39, respectively.

$$\sigma_f(z) = f_{tcm} + E \cdot \phi \cdot (z - \alpha h) \cdot \frac{f_{tu} - f_{tcm}}{E \cdot \varepsilon_t - f_{tcm}} \quad (38)$$

Where:

f_{tcm} = cementitious matrix strength (without fibers).
f_{tu} = ultimate tensile strength.

$$\sigma_b(z) = f_{tcm} + E \cdot \phi \cdot (z - \alpha h) \quad (39)$$

The balance of normal forces in the cracked section is detailed using the previous stress expressions. Equation 40 and equation 41 can be solved for as follows:

$$\alpha(\phi) = \frac{1}{1-K} \cdot \left[1 - \sqrt{\frac{2 \cdot f_{tcm} \cdot (K-1)}{E \cdot \phi \cdot h} + K} \right] \tag{40}$$

Where K is the stress ratio.

$$K = \frac{f_{tu} - f_{tcm}}{E\varepsilon_{end} - f_{tcm}} \tag{41}$$

The balance of moments in the cracked section gives the following expression in equation 42.

$$M_r(\phi) = \frac{f_{tcm} \times b \times h^2}{2} + \frac{E \times \phi \times b}{6} \times \left[\alpha(\phi)^3 \times h^3 \times (1-K) - 3 \times \alpha(\phi) \times h^3 + 2 \times h^3 \right] \tag{42}$$

Where M_r is the resistant moment of the section. Thus, the resistant moment of the section can be calculated for any value of curvature, ϕ.

Process of the Simplified Inverse Method

The data necessary to perform the inverse analysis and obtain the tensile stress–stain relationship from the characteristic bending moment versus midspan deflection curve include the following:

- Instantaneous E used to get $\varepsilon_{bc} = f_{bc}/E$ (f_{bc} is determined by compressive tests) and $\varepsilon_e = f_{tcm\text{-}chara}/E$, where $f_{tcm\text{-}chara}$ is the characteristic tensile strength of the cementitious matrix.
- Specimen height (h).
- Specimen width (b).
- Characteristic tensile strength of UHPC matrix ($f_{tcm\text{-}chara}$) where $f_{tcm} < 0$.
- Maximum bending moment obtained from flexural testing ($M^{max}_{Chara\text{-}curve}$).

The objective was to determine the value of f_{tu} (where $f_{tu} < 0$). To do this, iterations were carried out on f_{tu}. For each f_{tu} value, the $M_{max}(\phi)/\phi$ curve was plotted by varying ϕ from the beam curvature at the tensile elastic limit (ϕ_0) to the value of ϕ corresponding to the maximum moment. ϕ_0 is solved for in equation 43.

$$\phi_0 = -\frac{2 \times f_{tcm}}{E \times h} \tag{43}$$

Iteration on f_{tu} was carried out until a maximum moment equal to M_{max} of the tests was obtained. A value of 0.010 for ε_{end} was only used to construct the bilinear curve. It does not represent the midspan strain at the bottom flange at M_{max}, which is expressed by equation 44 and equation 45.

$$\frac{\varepsilon_e}{z_1} = \frac{\varepsilon_{end}}{\alpha_n h} \tag{44}$$

$$z_1 = -\frac{f_{tcm}}{E \times \phi} \tag{45}$$

This latter value of ε_{end} limits the part of the constructed curve, which has a mechanical meaning and can be used for the design, as shown in figure 47.

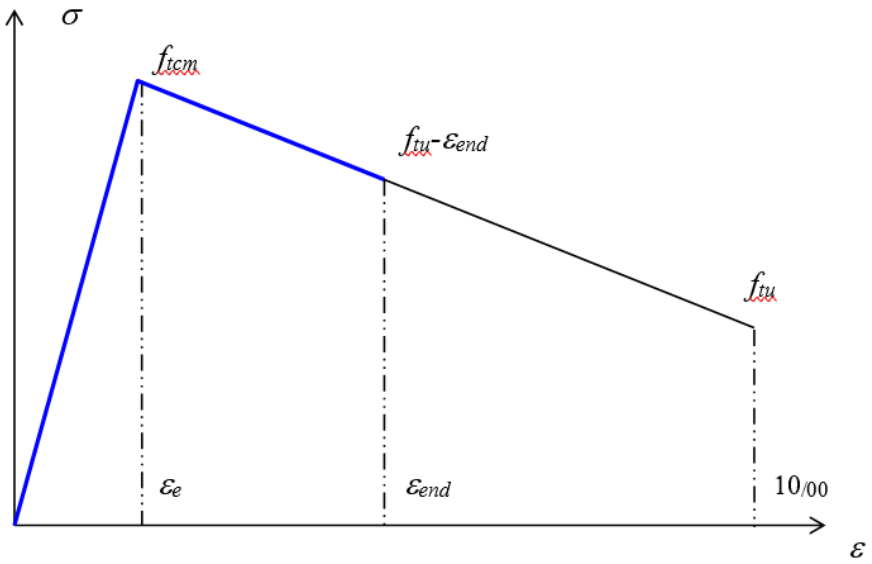

Figure 47. Graph. Bilinear curve obtained with the simplified inverse method.

This method is applicable for softening stress–strain relationships, but in the case of hardening curves, the result depends on the considered range of curvature. Indeed, the greater the importance of the range of curvature, the more important ε_{end} becomes while the ultimate stress decreases. The result stops evolving when the considered range of curvature induces a softening curve ($f_{tu} < f_{tcm}$). Nevertheless, the corresponding midspan strain at the bottom flange is unrealistic.

Synthesis of Inverse Analysis Methods

Table 15 summarizes the advantages and the disadvantages of the different inverse analysis methods described previously. All of the assumptions used to simplify the calculation induced an overestimation of strength and/or an underestimation of the real strain capacity. The safe and efficient use of UHPC for structural applications needs to know the real mechanical characteristics of this material and the influence of the testing method on these properties. As a consequence, it is necessary to develop methods to describe the real behavior of the material in reducing the initial assumptions.

Table 15. Synthesis of inverse analysis methods.

Inverse Analysis Method	Advantages	Disadvantages
JCI method[56,57]	Simplicity of post-treatment (i.e., no iteration).	• Simplified stress–strain relationship. • Strength overestimation. • Curvature measurement required.
Qian and Li method[54,59,60]	Simplicity of post-treatment (no iteration and no calculation).	• Simplified stress–strain relationship. • Strength overestimation. • Real strain capacity underestimation. • Master curves necessary for each specimen size and for each bending configuration.
Hinge model[52]	• Point-by-point stress–strain relationship. • Influence of the localization and also softening σ-w behavior taken into account.	• Difficulty of the post-treatment implementation of the hinge model. • Necessity to identify the actual localization from experimental observations.
Rigaud et al. method[55]	Point-by-point stress–strain relationship.	• Post-treatment iteration required for each moment-deflection response point. • Strength overestimation. • Real strain capacity underestimation.
AFGC-SETRA method[4]	Simplicity of post-treatment; iteration required just for deflection at point of maximum moment.	• Simplified stress–strain relationship. • Applicable only for softening stress–strain relationships. • Difficulty to determine the real UHPC matrix strength (f_{tcm}).

Proposed Flexural Test Methods

Two inverse analysis methods are discussed in this section: inverse analysis based on the strain measurement method and inverse analysis based on deflection measurement.[18]

Inverse Analysis Based on Strain Measurement Method[18]

The inverse analysis based on the strain measurement method, which was developed by Baby et al. and based on the measurement of the applied load and of the midspan strain at the bottom flange during an FT, can be used to obtain the stress–strain law of the tested material.[18]

Concerning the instrumentation, the test setup requires two LVDTs used as extensometers, which are put on each specimen to measure the midspan strain at the bottom flange. Use of staggered LVDTs allows for the identification of crack localization.

The experimental bending-moment midspan strain at the bottom flange curve is converted into the tensile stress–strain curve thanks to an inverse method based on the equilibrium of moments and forces in a section analysis for each value of midspan strain at the bottom flange and corresponding bending moment.

This approach, based on the method described in Rigaud et al., does not require prior assumption of the profile of the tensile stress–strain relationship.[55] The main difference with Rigaud et al. is the fact that the experimental data (i.e., the midspan strain at the extreme tension fiber) used in the inverse method is directly measured and not derived from a global measurement.[55]

The strain and stress distributions in the compressed zone are considered linear. The schematic illustration was shown previously in figure 39. This inverse analysis uses the same approach as Rigaud et al., with a discretization of the tensile stress–strain relationship.[55] As a consequence, the solving of this inverse problem consists of determining the parameter α_{nj+1} in increments to satisfy mechanical equilibrium in the section.

At each loading step, the procedure in equation 46 is used to solve the problem. For loading step $j + 1$ (all parameters at loading step j are considered as already determined), the measured tensile strain at increment $j + 1$ ($\varepsilon_{tj+1-measured}$) is taken as the average of the two measured midspan strains at loading step $j + 1$, and the value of α_{nj+1} is assumed.

$$\varepsilon_{tj+1} = \frac{\alpha_{nj} \times h}{\alpha_{nj} \times h + OPD} \times \varepsilon_{tj+1-measured} \tag{46}$$

Where:

ε_{tj+1} = tensile strain at increment $j + 1$.
OPD = off-plane distance.

In order to take into account the *OPD* of LVDTs (where eccentricity in this study is equal to 7 mm (0.28 inch)), the beam curvature at increment $j + 1$ (ϕ_{j+1}) can be defined using equation 47. The compressive component of the normal force can be calculated from equation 48. The compressive and tensile components add to zero as shown in equation 49.

$$\phi_{j+1} \approx tan\,\phi_{j+1} = \frac{\varepsilon_{tj+1}}{\alpha_{nj+1} \times h} \tag{47}$$

$$N_{cj+1} = b \times E \times \phi_{j+1} \times \left(\alpha_{nj+1} - 1\right)^2 \times \frac{h^2}{2} \tag{48}$$

$$N_{tj+1} + N_{cj+1} = 0 \tag{49}$$

Where N_{cj+1} is compressive component of the formal force at increment $j + 1$.

Equation 49 can be rewritten as in equation 50.

$$N_{tj+1} = -N_{cj+1} \tag{50}$$

The tensile component of the normal force can then be calculated from equation 51.

$$N_{tj+1} = \frac{\phi_j}{\phi_{j+1}} \times N_{tj} + b \times \frac{1}{\phi_{j+1}} \times \frac{\sigma_{tj+1} + \sigma_{tj}}{2} \times \left(\varepsilon_{tj+1} - \varepsilon_{tj}\right) \tag{51}$$

Solving equation (51) for σ_{tj+1} yields equation 52 as follows:

$$\sigma_{tj+1} = \left(N_{tj+1} - \frac{\phi_j}{\phi_{j+1}} \times N_{tj} \right) \times \frac{2 \times \phi_{j+1}}{b \times \left(\varepsilon_{tj+1} - \varepsilon_{tj}\right)} - \sigma_{tj} \tag{52}$$

The tensile and compressive components of the applied moment can then be calculated from equation 53 and equation 54.

$$M_{tj+1} = \alpha_{nj+1} h \times N_{tj+1} + \frac{\phi_j^2}{\phi_{j+1}^2} \times \left(M_{tj} - \alpha_{nj} h \times N_{tj}\right) - b \times \frac{1}{\phi_{j+1}^2} \times \frac{\sigma_{tj+1} \times \varepsilon_{tj+1} + \sigma_{tj} \times \varepsilon_{tj}}{2} \times \left(\varepsilon_{tj+1} - \varepsilon_{tj}\right) \tag{53}$$

$$M_{cj+1} = b \times E \times \phi_{j+1} \times \left(2 + \alpha_{nj+1}^3 - 3\alpha_{nj+1}\right) \times \frac{h^3}{6} \tag{54}$$

Where M_{cj+1} = compressive component of the applied moment at increment $j + 1$.

The value of α_{nj+1} from equation 54 is iterated as follows in equation 55:

$$M_{cj+1} + M_{tj+1} - M_{j+1-experimental} = 0 \tag{55}$$

Initialization of the Process

To start the incremental process, the following values and relationships were used:

- Tensile strain at increment 1, ε_{t1}, = 1 microstrain.
- Tensile stress at increment 1, σ_{t1}, = $E \times \varepsilon_{t1}$.
- Distance from the tensile face to the neutral axis divided by the height of the specimen at the initial increment, $\ell_{n1,}$ = 0.5.

Stabilization of Convergence

Since the description of the test results is discrete, with the inverse method using a derivative of the moment curve, oscillation of the tensile stress–strain relationship often occurred. It can be stabilized by correcting iteration j after calculating iteration $j + 1$. In practice, it is sufficient to reposition the stress of iteration j by determining a moving average of the following type using equation 56.

$$\sigma_{tj} = \left(2 \times \sigma_{tj} + \sigma_{tj+1}\right) \times \frac{1}{3} \quad (56)$$

If the stress does not vary suddenly (which is the case in practice), this correction does not affect the response of the method and leads to more realistic results. It should be observed that this stabilization operation must be carried out at the end of each iteration step.

Validation of the Process

The validation of the proposed model is established through a simple case wherein the bending-moment strain curve is generated by a direct calculation and is then verified through inverse analysis to be similar to the tensile stress–strain relationship used in the direct calculation.

The following values and concepts have been used in order to fix the different parameters:

- **Width of specimen (*b*)**: 100 mm (3.94 inches).
- **Height of specimen (*h*)**: 100 mm (3.94 inches).
- **Modulus of elasticity (*E*)**: 64.4 GPa (9,338 ksi).
- **Tensile stress–strain relationship**: Elastic-perfectly plastic relationship is shown in figure 48, where $\sigma_{plastic}$ = 10 MPa (1.45 ksi).

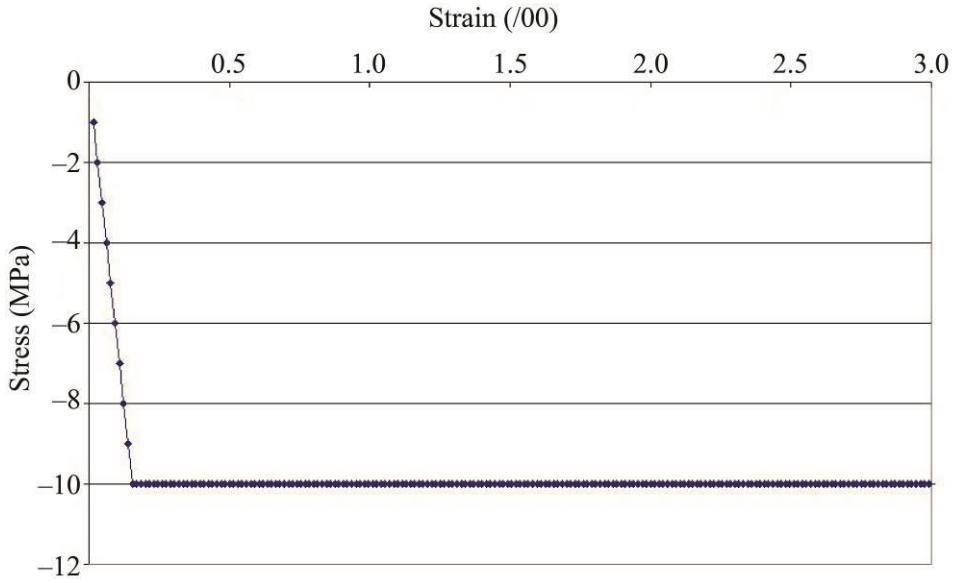

1 MPa = 0.145 ksi.

Figure 48. Graph. Tensile stress–strain relationship used for the validation of the proposed inverse analysis based on strain measurement method.

The direct calculation gives the following bending-moment strain curve, as shown in figure 49. The tensile stress–strain relationship obtained with the inverse analysis is presented in figure 50.

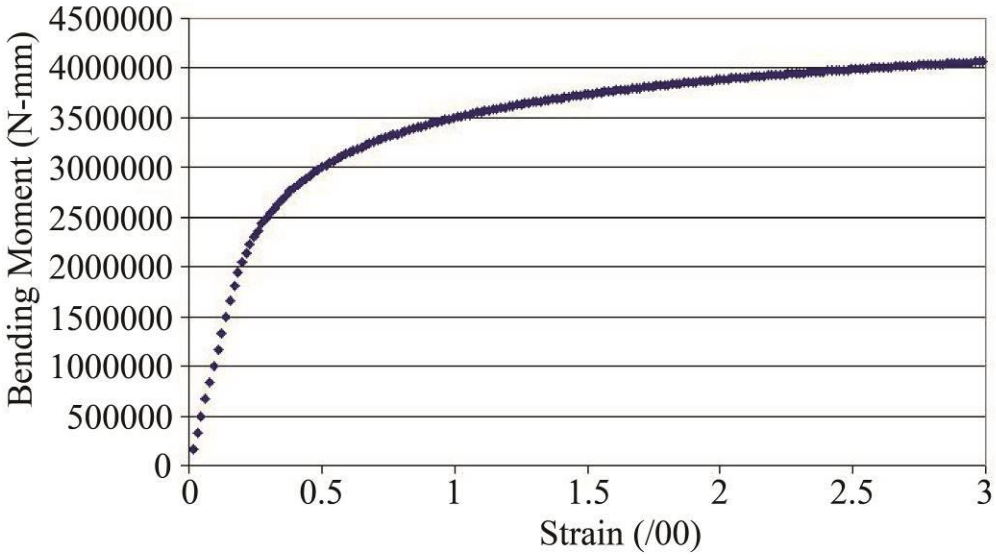

1 N-mm = 8.85 lb-inch.

Figure 49. Graph. Bending-moment strain curve obtained after direct calculation.

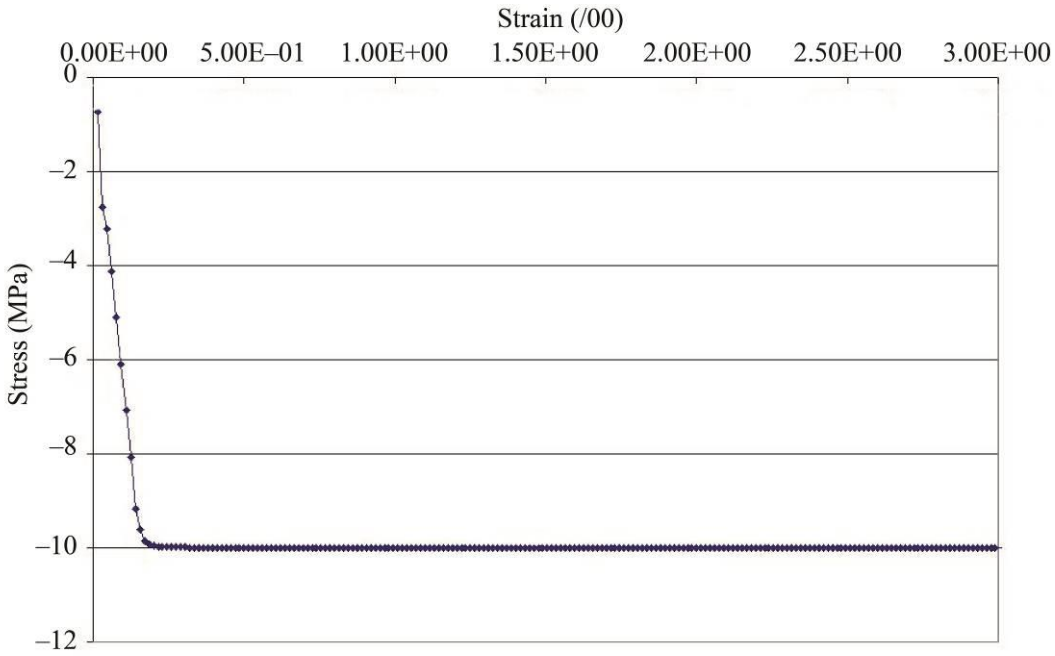

1 MPa = 0.145 ksi.

Figure 50. Graph. Tensile stress–strain relationship obtained with the proposed inverse analysis based on strain measurement method.

Detection of Crack Localization

Except for the Hinge model, in the inverse analysis methods described by Kanakubo, Qian and Li, and Rigaud et al., the crack localization is assumed to correspond with the maximum bending stress.[52–55] Nevertheless, in some cases, the crack localization can occur before reaching the maximum bending stress.[62]

Referring to the analysis of FTs on CEMTEC$_{multiscale}$®, which is another cementitious composite material, the behavior of UHPC tested in an FT configuration can be schematically described in four steps, as shown in figure 51.[65]

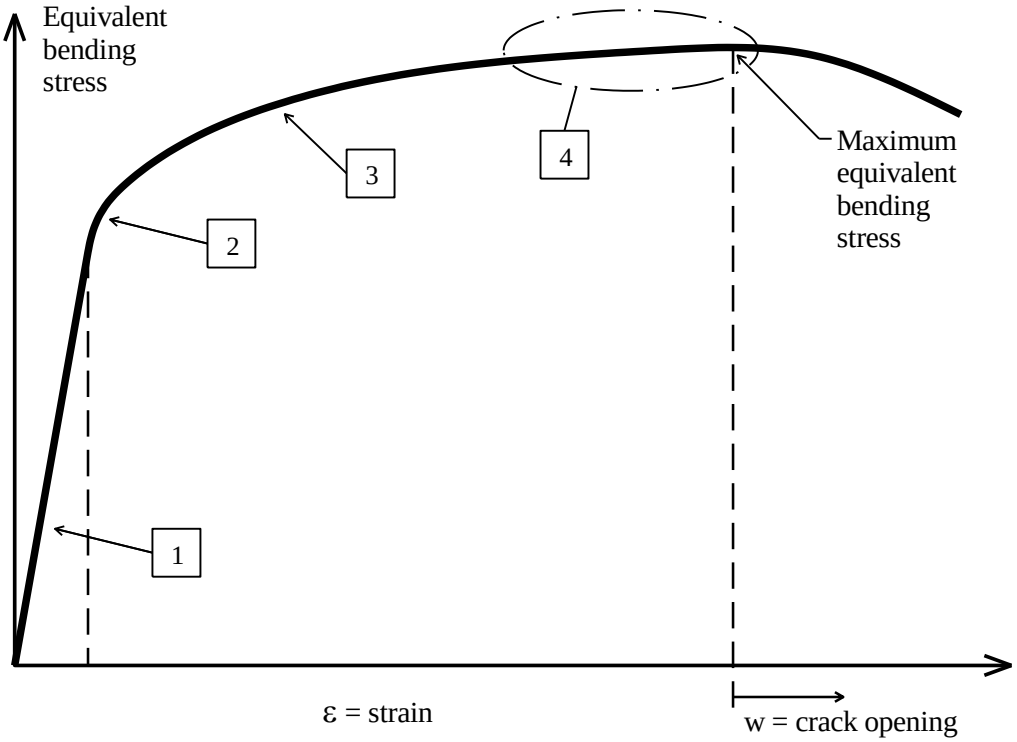

Source: Modified by FHWA from Parant and Rossi 2008.[65]

Figure 51. Graph. UHPC equivalent bending stress versus strain and crack-opening response.

The steps are described in further detail as follows:

1. The behavior of a prism is linear elastic until the tensile strength of the cementitious matrix is reached, which also corresponds to the beginning of damage and loss of linearity.

2. The load increases with a coalescence of some micro-cracks in meso-cracks following a random repartition. For classic UHPC, such as UHPC-F and UHPC-B in the present study, the load (or stress) increase during this step is relatively limited because of the dimensions of fibers, which are less efficient at this scale to control crack opening.

3. The opening of some meso-cracks cannot be controlled efficiently. Their coalescence induces some macrocracks (which are invisible without a magnifying glass). The cracking process continues for a bigger crack opening that is controlled more efficiently by the long fibers.

4. The force increases until the number of cracks stops increasing. This step is reached when the crack opening exceeds the level of efficiency of the fibers that control this behavior. The damage is also localized with the occurrence of a failure crack. In this method, turning to staggered LVDTs allows detection of crack localization with an identification of the elastic unloading (as shown in figure 52). In some cases, two localized cracks can occur before reaching the main failure crack (as shown in cases figure 52-A and figure 52-B), or the localized crack can be detected by both LVDTs (as shown in figure 52-C). For the latter case, the crack localization is assumed to correspond with the maximum bending stress.

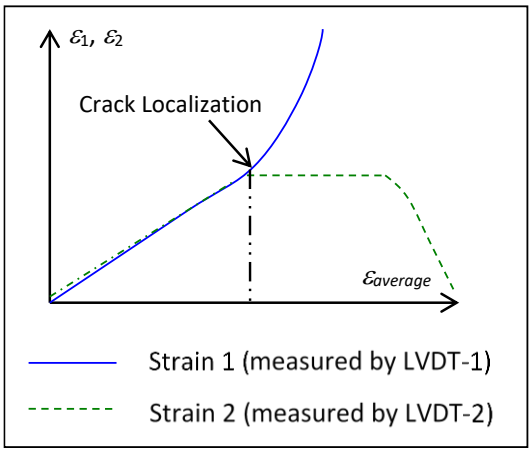

A. Case A.

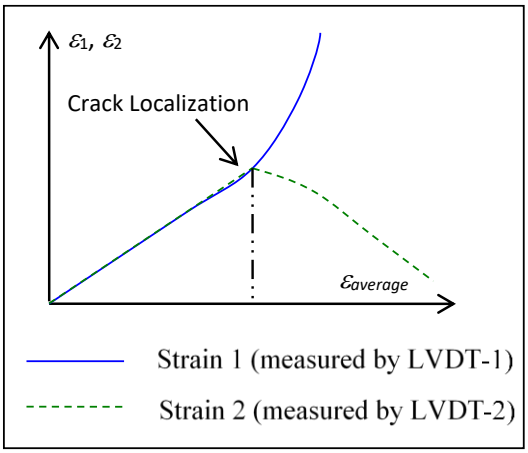

B. Case B.

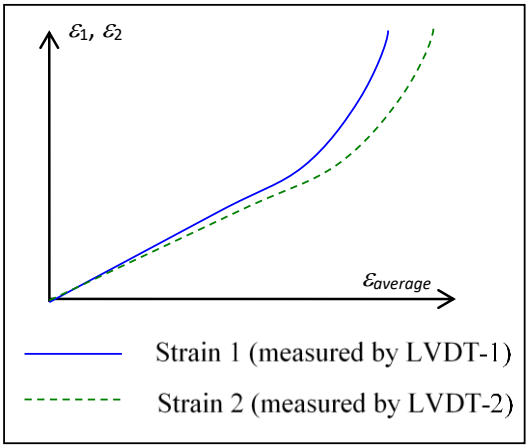

C. Case C.

Figure 52. Graphs. Proposed method to detect crack localization.

Inverse Analysis Based on Deflection Measurement

The methods proposed by Qian and Li and Rigaud et al. used a similar relationship to compare the deflection of the prism to the curvature at the load point or at the midspan.[54,55] This relationship was based on structural elastic mechanics and was considered reasonably valid for nonlinear behavior. Nevertheless, the use of this relationship for nonlinear behavior induces an overestimation of the deflection for a given curvature along the middle-third span or an underestimation of the curvature for a given value of deflection. As a consequence, the methods based on this mechanical assumption underestimate the real strain during the hardening phase and overestimate the postcracking stress.

To obtain more realistic results, it is necessary to consider the real calculation of the deflection. Two integrations of the curvature over the length of the prism have to be performed. It is not practical to express the curvature in closed form for a cracked specimen because a complicated equation would be required. Therefore, numerical integration is used. In the case of this study, the trapezoidal rule was used, although any numerical integration technique is acceptable.

Concerning the method proposed by Qian and Li, the following two plots of a master curve based on a parametric study can be realized for each test configuration:[54]

- A master curve obtained by using the mechanical assumption on the relationship between the curvature and deflection which is referred to as the "Qian and Li method."

- A master curve obtained from the real calculation of the deflection (i.e., double integration of the curvature over the length of the prism). The method associated with this master curve is referred to as the "modified Qian and Li method."

In both cases, the curvature is considered uniform in the constant bending-moment zone. The numerical integration has been realized with a constant interval of 1 mm (0.039 inch). Note that a comparable calculation with an interval of 0.1 mm (0.039 inch) was completed, with the results showing a maximal difference of less than 0.5 microstrain.

Compared to the Qian and Li method, the calculation of deflection corresponds to the midspan deflection (not to the load point), and the stress distribution in the compressed zone is considered linear (which is more realistic for UHPC). In the context of this research, the range of parametric values concerning the tensile properties (previously presented in table 14) was reduced to be more precise.

For each test configuration, 126 cases were investigated in the parametric study, with the range of material parameters shown in table 14. Eighteen linear curves were obtained and used to plot the master curves, as shown in figure 53 through figure 55 and table 16. Note that bending configuration S pertains to four-point bending on the shorter 229-mm (9-inch) span, and bending configuration L pertains to four-point bending on the longer 356-mm (14-inch) span. Bending configuration B pertains to four-point bending on the 100-mm by 100-mm (3.94-inch by 3.94-inch) cross section with a 305-mm (12-inch) span. Details on the testing arrangements are provided in the Specimens and Parameters section later in this chapter.

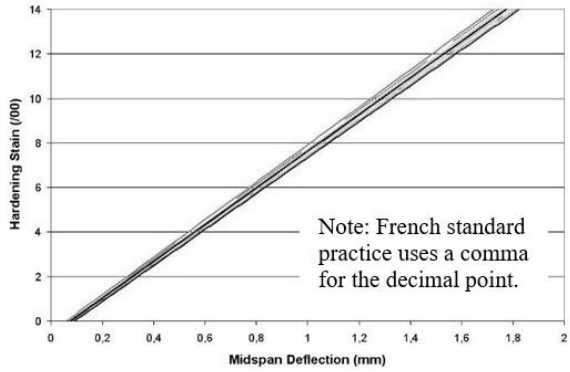

A. Qian and Li method.

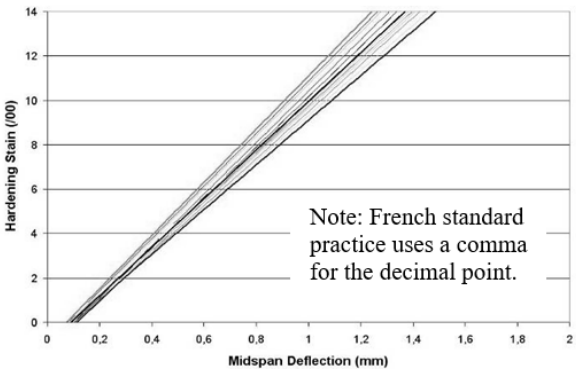

B. Modified Qian and Li method.

Figure 53. Graphs. Bending configuration S—tensile strain capacity and deflection capacity relationship.

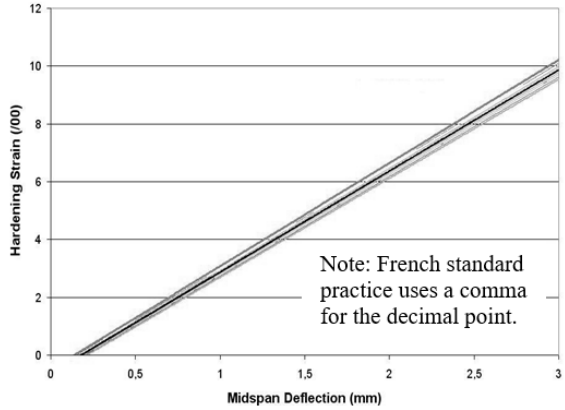

A. Qian and Li method.

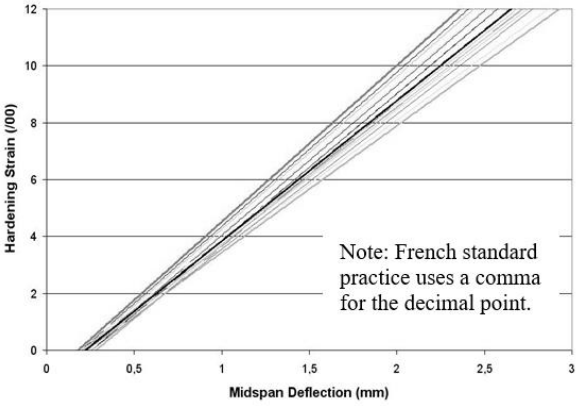

B. Modified Qian and Li method.

Figure 54. Graphs. Bending configuration L—tensile strain capacity and deflection capacity relationship.

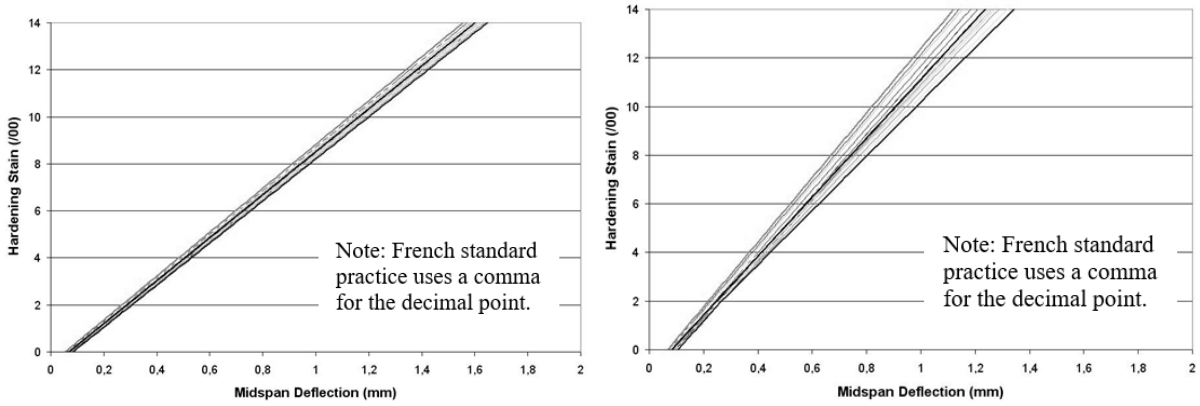

A. Qian and Li method.

B. Modified Qian and Li method.

Figure 55. Graphs. Bending configuration B—tensile strain capacity and deflection capacity relationship.

Table 16. Equations used to calculate the tensile strain capacity for each configuration using the Qian and Li and modified Qian and Li methods.

Bending Configuration	Test Method	Mean Hardening Strain	Maximum Hardening Strain	Minimum Hardening Strain
S	Qian and Li	$\varepsilon = 8.24 \times d - 0.62$	$\varepsilon = 8.42 \times d - 0.5$	$\varepsilon = 8.08 \times d - 0.74$
S	Modified Qian and Li	$\varepsilon = 10.94 \times d - 0.98$	$\varepsilon = 11.97 \times d - 0.86$	$\varepsilon = 10.1 \times d - 1.02$
L	Qian and Li	$\varepsilon = 3.5 \times d - 0.62$	$\varepsilon = 3.57 \times d - 0.5$	$\varepsilon = 3.43 \times d - 0.74$
L	Modified Qian and Li	$\varepsilon = 4.93 \times d - 1.08$	$\varepsilon = 5.49 \times d - 0.97$	$\varepsilon = 4.52 \times d - 1.17$
B	Qian and Li	$\varepsilon = 9.13 \times d - 0.62$	$\varepsilon = 9.33 \times d - 0.5$	$\varepsilon = 8.95 \times d - 0.74$
B	Modified Qian and Li	$\varepsilon = 12.13 \times d - 1$	$\varepsilon = 13.28 \times d - 0.88$	$\varepsilon = 11.19 \times d - 1.03$

d = deflection capacity.

The approach with a real calculation of the deflection (by integrating twice the curvature over the length of the prism) induces an increase of the mean tensile strain capacity and an increase of the deviation.

Concerning the Qian and Li and modified Qian and Li methods, the following details pertain to the determination of the tensile strength by using a master curve correlating the normalized MOR with the effective tensile strength (MOR/f_{tb}). In the context of this research, a master curve was constructed for each specimen size with a reduced range of parametric tensile property values (table 17) to be more precise. Compared with the initial method, the stress distribution in the compressed zone was considered linear (which is more realistic for UHPC). For each specimen size, 90 cases were investigated in the parametric study, with the range of material parameters shown in table 17. A total of 10 linear curves were obtained and used to plot the master curves (figure 56 and table 18).

Table 17. Range of material parameters used in parametric studies to construct the MOR/f_{tb} strain capacity relationship.

Effective Tensile Strength, MPa (ksi)	Tensile Strain Capacity	Modulus of Elasticity, GPa (ksi)
6–14 (0.87–2.0)	0.0005–0.0140	50–65 (7,250–9,430)

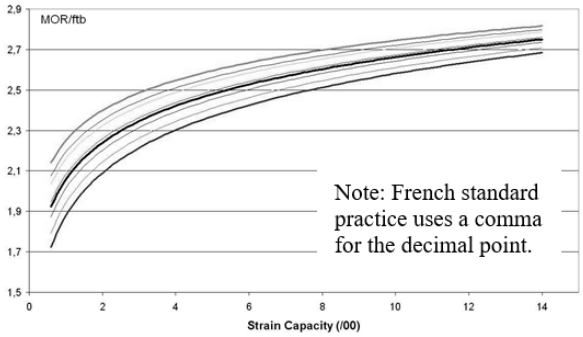

© IFSTTAR.

A. Specimen dimensions of 51 by 51 mm (2.0 by 2.0 inches).

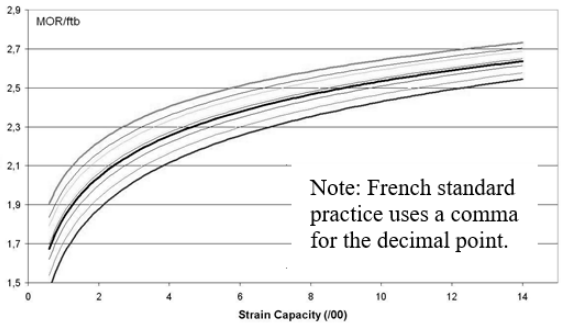

© IFSTTAR.

B. Specimen dimensions of 100 by 100 mm (3.94 by 3.94 inches).

Figure 56. Graphs. MOR/f_{tb} strain capacity relationship.

Table 18. Equations to calculate the tensile strength for each specimen size.

Specimen Dimensions	Mean MOR/ f_{tb}	Maximum MOR/f_{tb}	Minimum MOR/f_{tb}
51 by 51 mm (2.01 by 2.10 inches)	$0.2625 \times \ln(\varepsilon) - 2.0572$	$0.2147 \times \ln(\varepsilon) - 2.2499$	$0.3053 \times \ln(\varepsilon) - 1.8779$
100 by 100 mm (3.94 by 3.94 inches)	$0.3056 \times \ln(\varepsilon) - 1.8301$	$0.2617 \times \ln(\varepsilon) - 2.0406$	$0.3419 \times \ln(\varepsilon) - 1.6417$

Concerning the method proposed by Rigaud et al., a preliminary inverse analysis method can be used to determine the curvature from the deflection measurement.[55] This first inverse analysis method is based on the real calculation of the deflection with a double-numerical integration of the curvature over the length of the specimen. The method associated with this first analysis is called the Baby et al. method.[19] The process used in this study is described in figure 57.

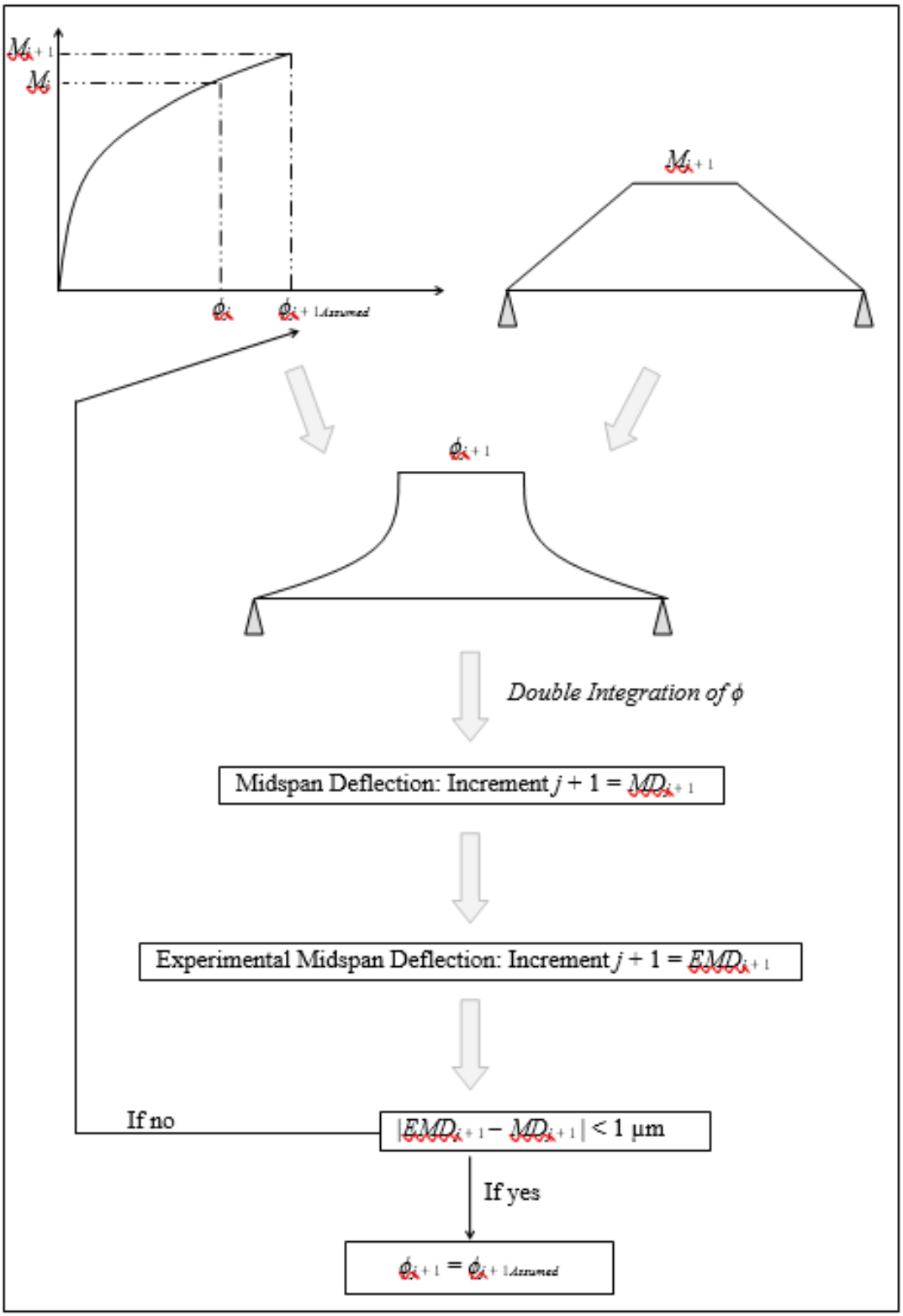

Figure 57. Flowchart. First inverse analysis algorithm using the Baby et al. method.[19]

Where:

M_{j+1} = moment at increment $j + 1$.
M_j = moment at increment j.
ϕ_j = beam curvature at increment j.
ϕ_{j+1} = beam curvature at increment $j + 1$.
$\phi_{j+1Assumed}$ = assumed beam curvature at increment $j + 1$.
MD_{j+1} = model-based midspan deflection at increment $j + 1$.
EMD_{j+1} = experimental midspan deflection at increment $j + 1$.

Validation of the Process

The validation of the proposed method in the present study was established through a simple case in which a bending-moment deflection curve was generated by a direct calculation (i.e., double integration of the curvature over the length of the prism). After, the result was verified with an inverse analysis that was similar to the bending-moment curvature relationship used in the direct calculation.

The following values and assumed responses were used to fix the different parameters:

- **Width of the prism (*b*)**: 50.8 mm (2 inches).
- **Height of the prism (*h*)**: 50.8 mm (2 inches).
- **Shear span (*a*)**: 76 mm (3 inches).
- **Total span length (*L*)**: 229 mm (9 inches).
- **Modulus of elasticity (*E*)**: 60 GPa (8,700 ksi).
- **Tensile stress–strain relationship**: Elastic-perfectly plastic relationship is shown in figure 58, where $\sigma_{plastic}$ = 6 MPa (0.87 ksi).

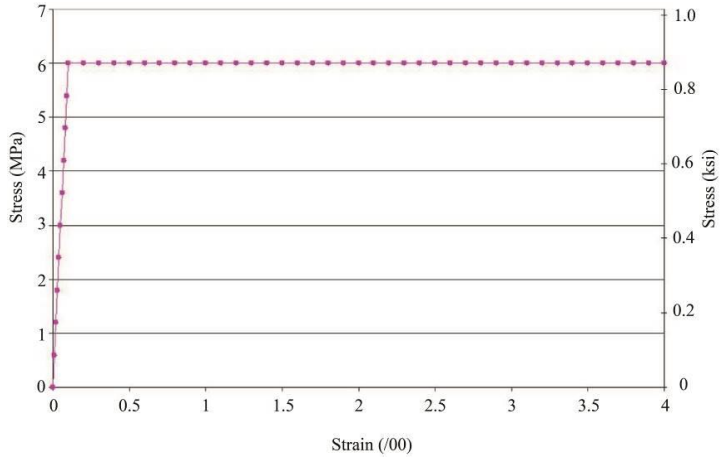

Figure 58. Graph. Tensile stress–strain relationship used for validation of the proposed inverse analysis based on deflection measurement method.

The bending moment versus curvature relationship (figure 59) and the bending moment versus midspan deflection relationship (figure 60) can be directly calculated, with the relationship obtained via inverse analysis in figure 61. The deviation between the two methods is plotted in figure 62 as a function of midspan deflection.

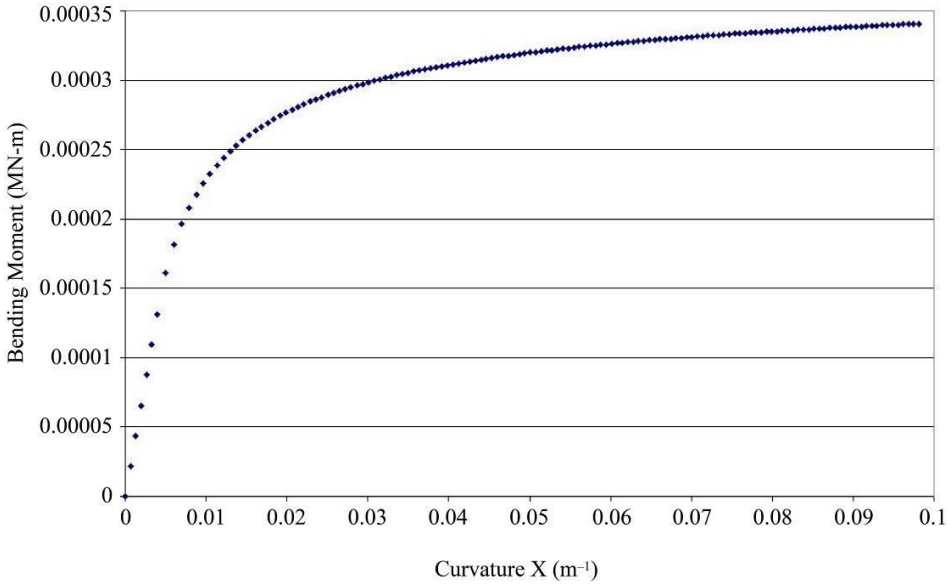

1 MN-m = 8,850 kip-inch.
1 m-1 = 0.0254 inch-1.

Figure 59. Graph. Bending-moment-curvature curve obtained after direct calculation from the proposed inverse analysis based on deflection measurement method.

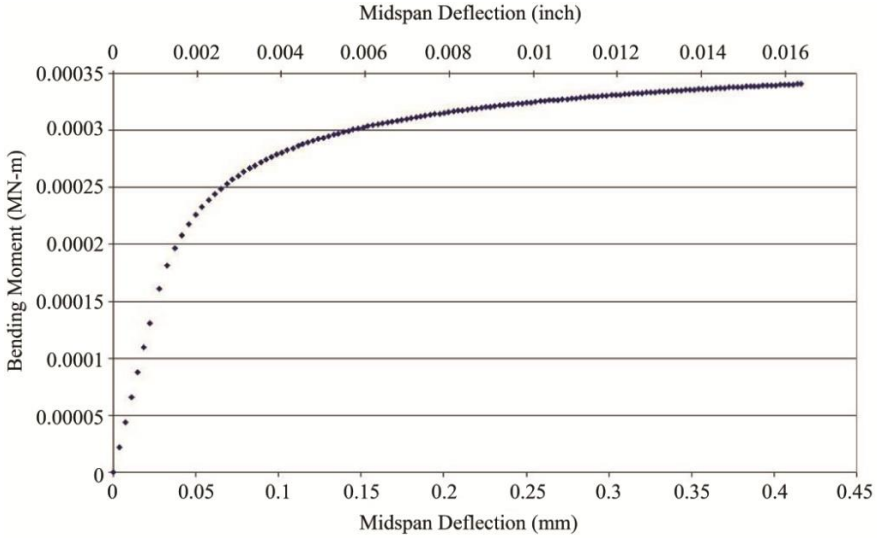

1 MnN-m = 8,850 kip-inch.
1 mm = 0.039 inch.

Figure 60. Graph. Bending-moment deflection curve obtained after direct calculation from double integration of the curvature over the length of the prism.

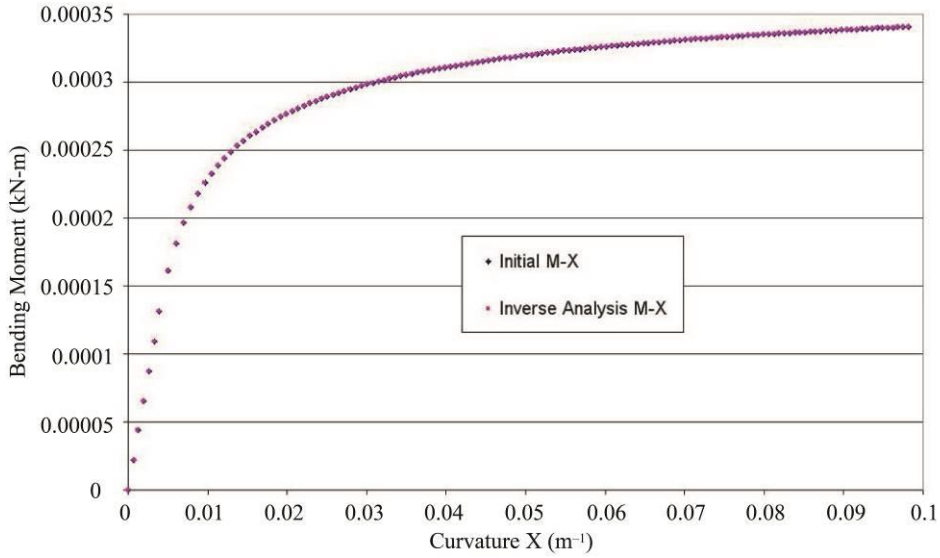

© IFSTTAR.
1 MN-m = 8,850 kip-inch.
1 m-1 = 0.0254 inch^{-1}.
M-X = moment-curvature

Figure 61. Graph. Bending-moment-curvature curves obtained after direct calculation and with inverse analysis.

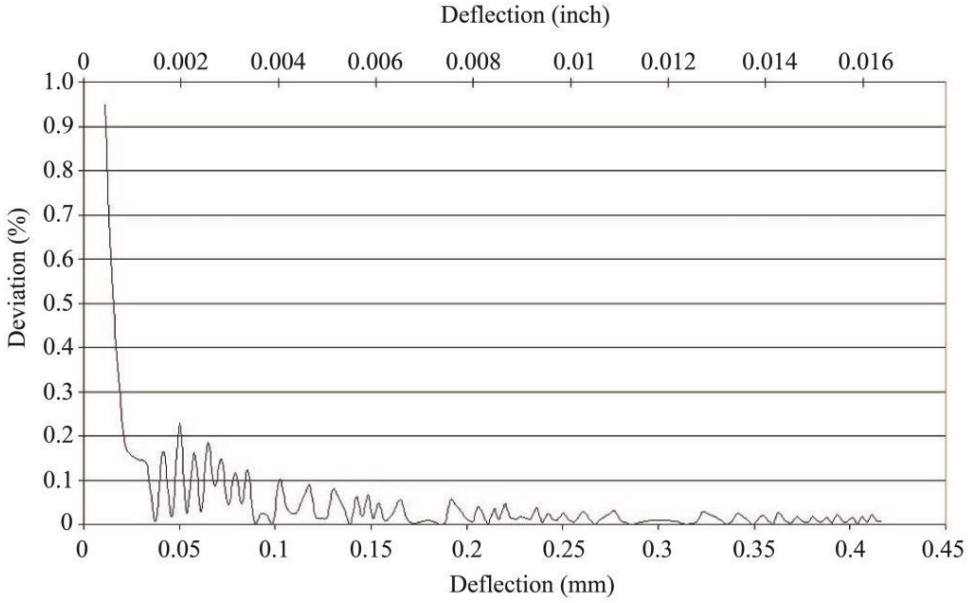

© IFSTTAR.
1 mm = 0.039 inch.

Figure 62. Graph. Deviation expressed in percentage between both curvatures (after direct calculation and with inverse analysis) versus deflection.

The deviation between both curvatures was less than 1 percent and quickly decreased to less than 0.2 percent. After this first inverse analysis, the method proposed by Rigaud et al. and described previously can be used to obtain the tensile stress–strain relationship.[(55)]

Specimens and Parameters

Concerning bending tests, the ASTM C1018 loading apparatus used to test the prisms is capable of testing multiple prism sizes.[64] The rollers and their support blocks are movable to allow for lower support spans from 152 to 381 mm (6 to 15 inches) and upper loading spans from 51 to 152 mm (2 to 6 inches).

The AFGC provisions on UHPC recommended a preferred standard molded specimen size of 280 by 70 by 70 mm (11 by 2.8 by 2.8 inches) for F1A, F1B, F1C, F2A, F2B, and F2C (a with fiber length of 12 mm (0.47 inch)) and 400 by 100 by 100 mm (15.7 by 3.9 by 3.9 inches) for B2 (with a fiber length of 20 mm (0.79 inch)), resulting in a four-point loading configuration with a 210-mm (8.3-inch) lower span for F1A, F1B, F1C, F2A, F2B, and F2C and 300-mm (11.8-inch) lower span for B2.[4]

For bending tests, the length of the constant bending-moment zone should be the same as the length under constant stress in the DTTs in order to decrease the statistical effects on results. Considering all these requirements, the bending test program included two sizes of prism cross sections and three loading configurations, as shown in figure 63. The intent of the second bending configuration, L, is to limit the amplitude of shear strains and to favor similitude of the stress state for the lower part of the bent prism (in tension) as compared to the specimen tested in the DTT. Bending configuration B was chosen to characterize B2 with a size of prism recommended by AFGC provisions.[4]

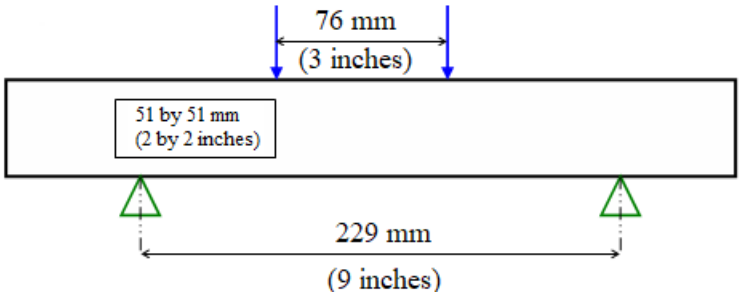

A. Bending configuration S.

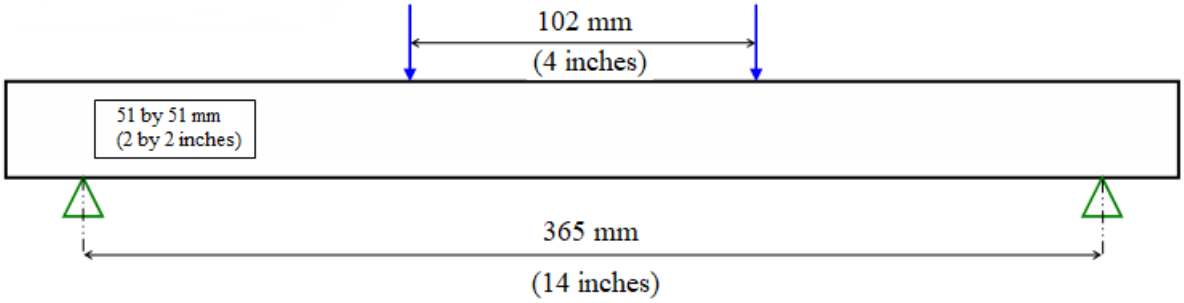

B. Bending configuration L.

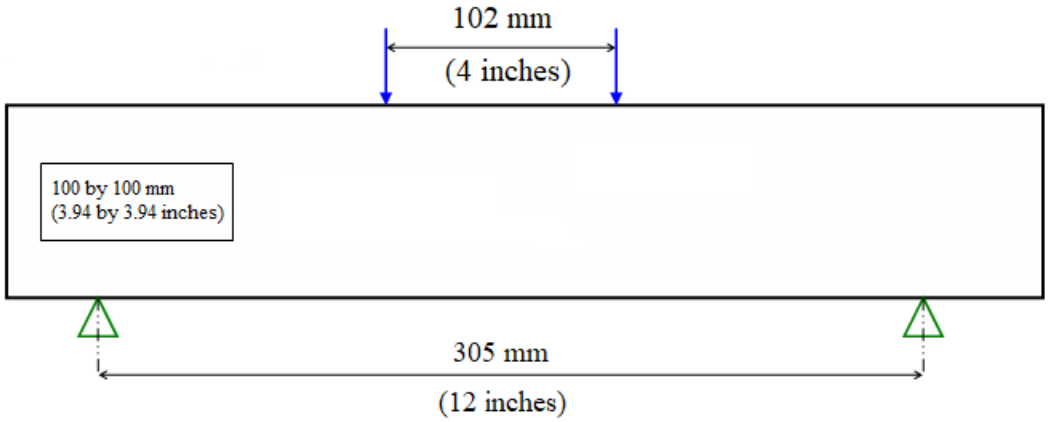

C. Bending configuration B.

Figure 63. Illustrations. Experimental programs for different bending configurations.

The cross sections that were investigated were 51 by 51 mm (2 by 2 inches) and 100 by 100 mm (3.94 by 3.94 inches). The 51- by 51-mm (2- by 2-inch) prisms were cast in lengths of 305 and 432 mm (12 and 17 inches). The 100- by 100-mm (3.94- by 3.94-inch) prisms were cast in a length of 400 mm (15.75 inches).

To gain an understanding of the influence of the bending test configuration (particularly configurations S and L), it was necessary to avoid the effect of fiber alignment, which was

increased for the longer prisms. As a consequence, for batch F1B, every second 432-mm (17-inch)-long prism was cut to be tested in configuration S (as denoted by "S-Cut" in the specimen group name). The remaining ones were tested in configuration L.

Table 19 provides information related to the nomenclature of specimens tested in bending. The specific dimensions of each specimen were measured via caliper. The widths and the depths were the average of three measurements realized at the center of prism and at ±38 mm (±1.5 inch) of the center for configuration S and at ±51 mm (±2 inches) for configurations L and B.

Table 19. Nomenclature of specimens with associated testing configuration.

Specimen Group Name	Batch Name	Bending Configuration	Number of Specimens	Specimen Cross-Sectional Width by Height, mm by mm (Inches by Inches)	Specimen Length, mm (Inches)
B2-S	B2	S	5	51 by 51 (2 by 2)	305 (12)
B2-L	B2	L	6	51 by 51 (2 by 2)	432 (17)
B2-B	B2	B	6	100 by 100 (4 by 4)	400 (16)
F1A-S	F1A	S	6	51 by 51 (2 by 2)	305 (12)
F1A-L	F1A	L	5	51 by 51 (2 by 2)	432 (17)
F2A-S	F2A	S	6	51 by 51 (2 by 2)	305 (12)
F2A-L	F2A	L	5	51 by 51 (2 by 2)	432 (17)
F1B-S	F1B	S	6	51 by 51 (2 by 2)	305 (12)
F1B-S-Cut	F1B	S	5	51 by 51 (2 by 2)	432 (17)
F1B-L	F1B	L	5	51 by 51 (2 by 2)	432 (17)
F1C-S	F1C	S	6	51 by 51 (2 by 2)	305 (12)
F1C-L	F1C	L	5	51 by 51 (2 by 2)	432 (17)

Loading Setup and Instrumentation

All of the bending tests involved four-point flexural loading of small-scale concrete prisms. During the test, the load, the deflection of the prism, and the midspan strain at the bottom flange were measured. These data were then used with the previously described inverse analysis to determine the postcracking behavior of the UHPC material.

The control of the test was accomplished by completing the test in a computer-controlled, servo-hydraulic load frame. The control signal was the actuator displacement; the imposed rate was equal to 0.250 mm (0.001 inch) per minute as recommended by the French provisions on UHPC.[(4)]

As shown in figure 64, the two upper load points and the two lower support points were steel rollers that imparted no axial restraint on the prism. The blocks under the upper rollers were supported by 51-mm (2-inch)-deep solid steel beams that were connected to a spherical bearing, which ensured that all rollers were bearing on the prism during the test. This assembly, shown in figure 65, had to be set on the specimen before the start of the test. As a consequence, the influence of upper block's weight (26 kg (57 lb)) was considered by an analytical post-treatment. Table 20 gives the midspan stress at the bottom flange induced by the weight of the assembly.

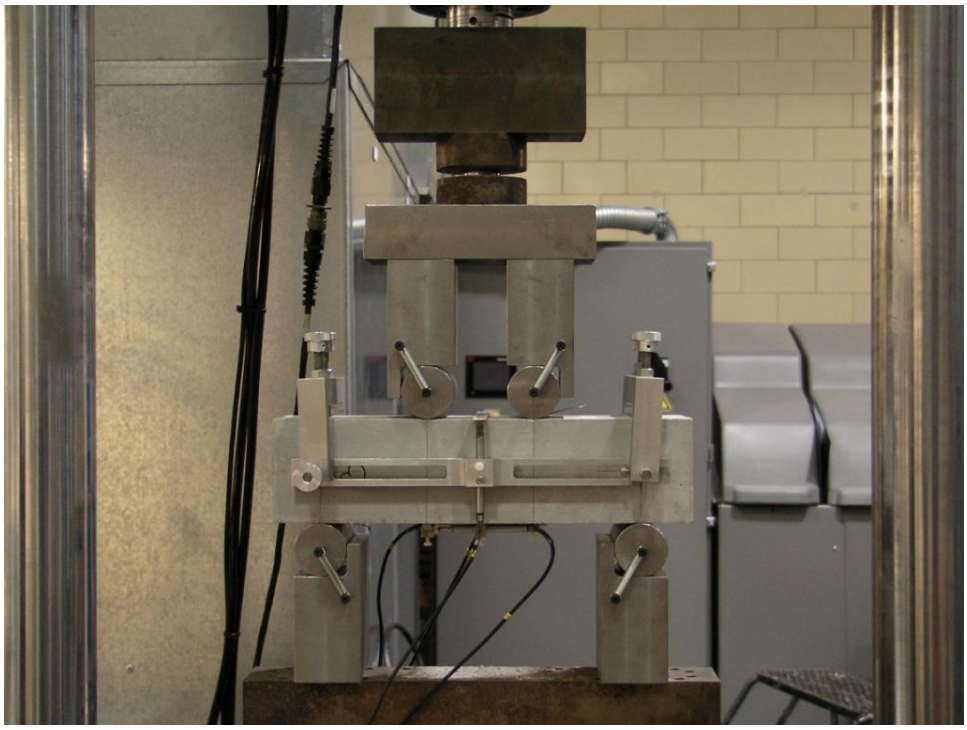

Source: FHWA.

Figure 64. Photo. Prism flexural test setup for all bending configurations.

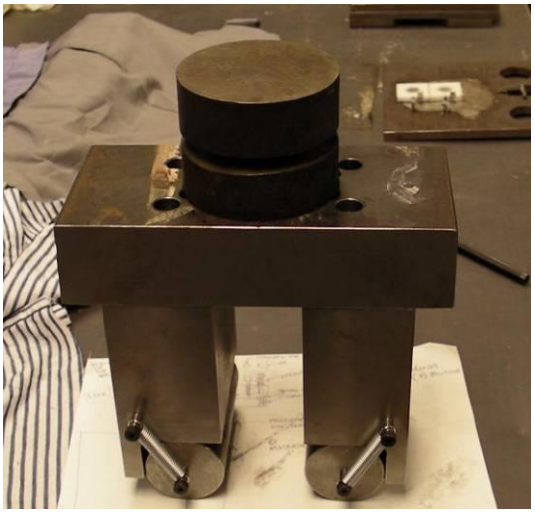

Source: FHWA.

Figure 65. Photo. Upper block showing rollers and spherical bearing.

Table 20. Midspan stress at the bottom flange induced by the upper block's weight.

Configuration	Initial Midspan Stress on Bottom Flange, MPa (ksi)
S	0.45 (0.065)
L	0.75 (0.109)
B	0.08 (0.012)

Torsional effects caused by misalignment between the planes of the prism faces and the rollers were overcome by placing individual shims between each roller and its bearing block. Concerning the instrumentation, the deflection-measuring system must measure net specimen deformation values exclusive of any extraneous effects. To meet these requirements, a yoke, shown in figure 64, that was similar to that described in ASTM C1018 was used to measure the midspan deflections.[(64)] LVDTs were attached to the yoke on each side of the specimen at the midspan, and the yoke was attached to the specimen at the middepth over the support points. The LVDTs beared on a plate that was epoxied to the compression face and extended to hang over the sides of the prism.

Two LVDTs were used for strain measurement. They were fixed on each specimen to measure the midspan strain at the bottom flange (figure 66 and figure 67). Using staggered LVDTs helped distinguish the onset of bifurcation of the cracking process with crack localization over one of the gauge lengths while cracking remained diffuse over the other gauge length.

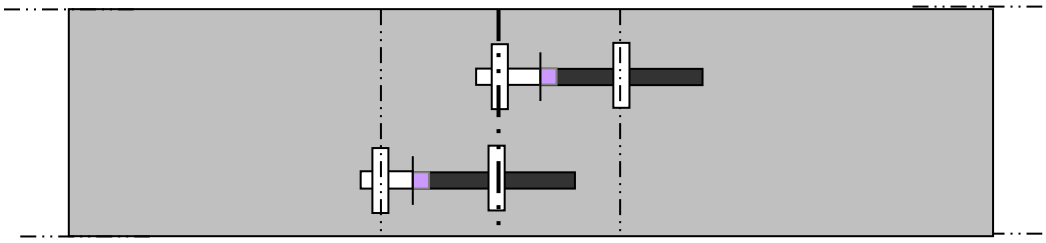

Figure 66. Illustration. View of the bottom flange of the midspan strain measurement.

Source: FHWA.

Figure 67. Photo. View of the bottom flange of the midspan strain measurement with staggered extensometers.

Table 21 provides information about the gauge length of the extensometers for each configuration.

Table 21. Gauge length of extensometers at the bottom flange for each configuration.

Bending Configuration	Gauge Length, mm (Inches)
S	38 (1.5)
L	51 (2)
B	51 (2)

The following procedure was used to complete each test:

1. Center the prism in the load frame with its screeded face oriented toward the front- and the vertical-molded faces placed as top and bottom faces.

2. Set the upper loading beam on the specimen.

3. Place individual shims between rollers and their bearing locations on the side of the roller away from the test specimen to avoid misalignment between the planes of the prism faces and the rollers.

4. Set the yoke and LVDTs in place.

5. Start recording the data through an analog data acquisition system, where the acquisition frequency equals 5 Hz.

6. Use the actuator displacement for the control signal for the servo-hydraulic actuation system with an initial rate (which is used for the approach) equal to 1 mm (0.04 inch) per minute. (Note that when the midspan stress at the bottom flange is approximately equal to 0.5 MPa (0.07 ksi), the applied rate becomes 0.25 mm (0.001 inch) per minute.)

7. Stop the test after a midspan deflection ensures that the maximum strength for each specimen has been recorded—2 mm (0.08 inch) for bending configurations S and B and 3 mm (0.12 inch) for bending configuration L.

TEST RESULTS

The test results are presented and analyzed in this section.

Equivalent Bending Stress Versus Midspan Deflection—Midspan Strain at the Bottom Flange

For each batch, the FTs were completed more than 3 months after casting. Thus, even for UHPC without steam treatment, the mechanical properties were considered sufficiently stabilized.

The load versus midspan deflection and load versus midspan strain at the bottom flange were normalized using the measured specimen geometry to create equivalent bending stress versus

midspan deflection and equivalent bending stress versus midspan strain at the bottom flange plots. These plots are found in the next two sections of the report.

The expression of equivalent bending stress, σ_{equi}, is solved for in equation 57 as follows:

$$\sigma_{equi} = \frac{6 \cdot M}{b \cdot h^2} \tag{57}$$

The results consider the initial load induced by the weight of the upper block, including the rollers and the spherical bearing. Concerning the bottom flange strain at the midspan, the effect of the additional lever arm due to sensors fixation devices has to be deduced (figure 68). The neutral axis is assumed to be located at the mid-height of the prism. As a consequence, the correction of midspan strain at the bottom flange can be solved for using equation 58.

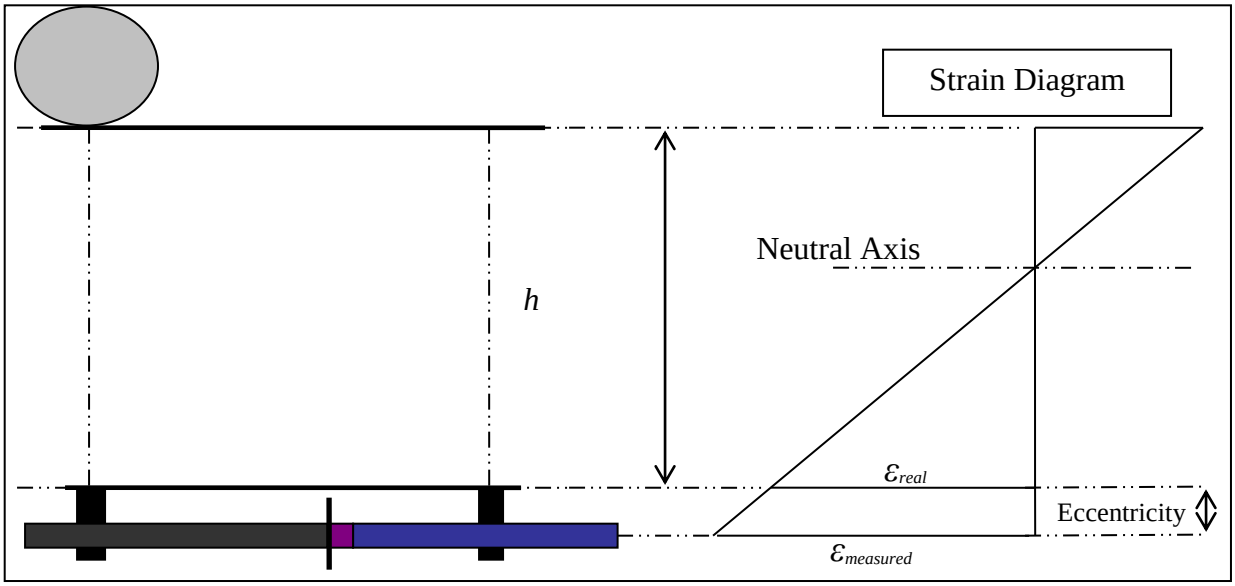

Figure 68. Illustration. Effect of the additional lever arm due to sensor fixation on the strain measurement.

Where:

ε_{real} = actual midspan strain at the bottom flange.
$\varepsilon_{measured}$ = measured midspan strain at the bottom flange.

$$\varepsilon_{corrected} = \frac{0.5 \cdot h}{0.5 \cdot h + OPD} \times \varepsilon_{measured} \tag{58}$$

Where:

$\varepsilon_{corrected}$ = corrected midspan strain at the bottom flange.
OPD = off-plane distance (equal to 7 mm (0.28 inch) in this study).

In the forthcoming report sections, Analysis of Hardening Strains and Tensile Stress–Strain Relationship, for each strain measurement, the position of the neutral axis was determined through the inverse analysis method based on strain measurements.

The analysis presented in this section of the report only presents the following sampled data allowing statistical treatment (mean and characteristic curves):

- Equivalent bending stress versus midspan deflection.
- Equivalent bending stress versus midspan strain at the bottom flange.

Concerning the sampled data for equivalent bending stress versus midspan deflection, the sampling was realized using a linear interpolation with a constant interval equal to 0.0100 mm (0.0004 inch) on the measurement of the midspan deflection.

Concerning the data for equivalent bending stress versus midspan strain at the bottom flange, the sampling used a linear interpolation with an interval on the average of the two measured midspan strains at the bottom flange equal to 10 microstrain from 0 to 350 microstrain and equal to 100 microstrain from 350 microstrain to the maximum strain (with a standard upper limit of 12,000 microstrain).

The statistical treatment for each interval of deflection or strain includes determination of the mean value of the equivalent bending stress (with six or five specimens by batch) and the standard deviation. The characteristic curve point-by-point was also obtained in subtracting from the mean value the corresponding standard deviation multiplied by the Student coefficient (Student's law with 5 percent quantile) equal to 2.015 for six specimens and 2.132 for five specimens.

Equivalent Bending Stress Versus Midspan Deflection

Figure 69 and figure 70 present the average and the characteristic curves for all the batches, respectively, for bending configuration S.

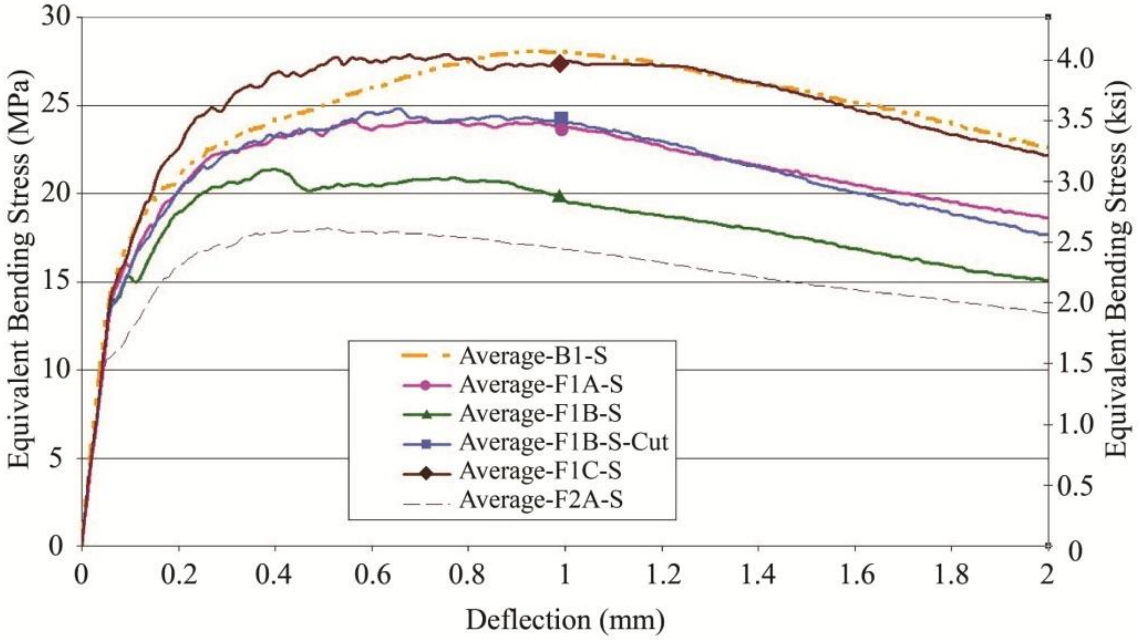

1 mm = 0.039 inch.

Figure 69. Graph. Equivalent bending stress versus midspan deflection showing average curve for each batch for bending configuration S.

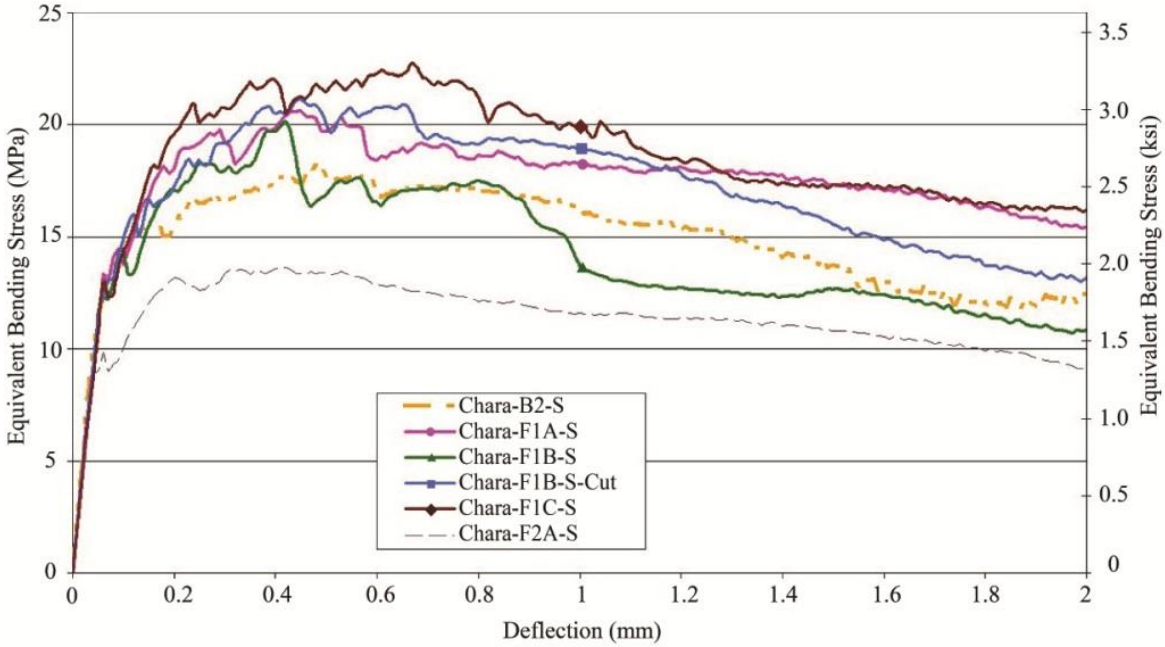

Figure 70. Graph. Equivalent bending stress versus midspan deflection showing characteristic curve for each batch for bending configuration S.

The average and characteristic equivalent bending stress versus midspan deflection curves are presented in figure 71 and figure 72, respectively, for bending configuration L.

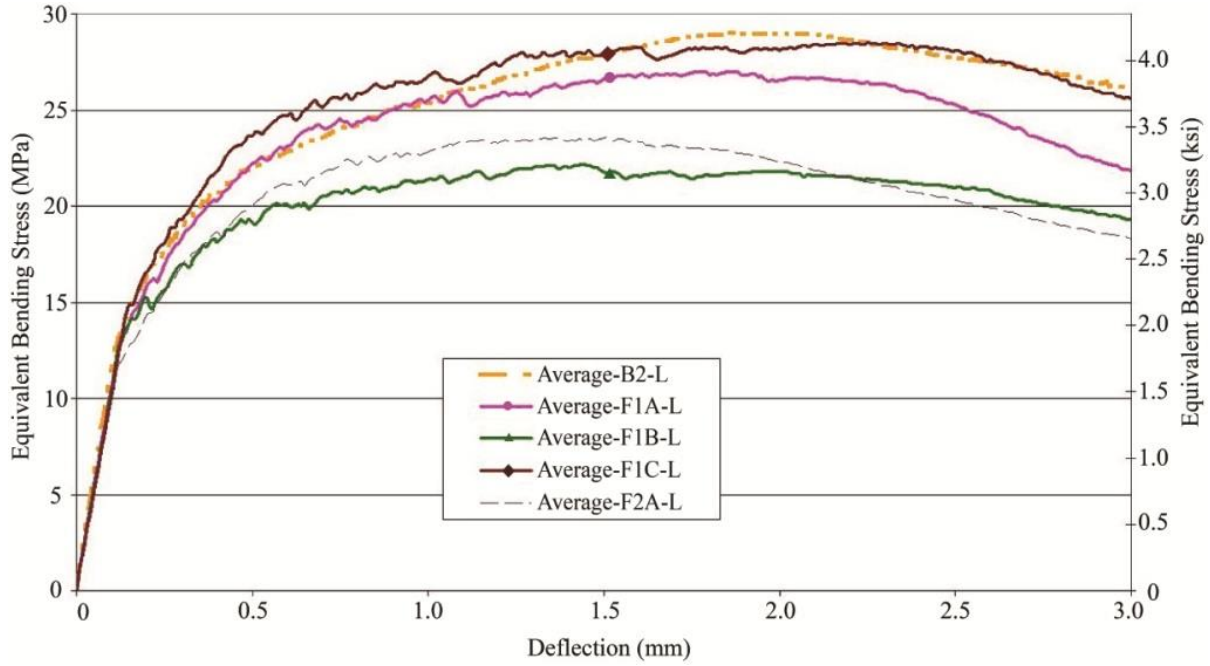

Figure 71. Graph. Equivalent bending stress versus midspan deflection showing average curve for each batch for bending configuration L.

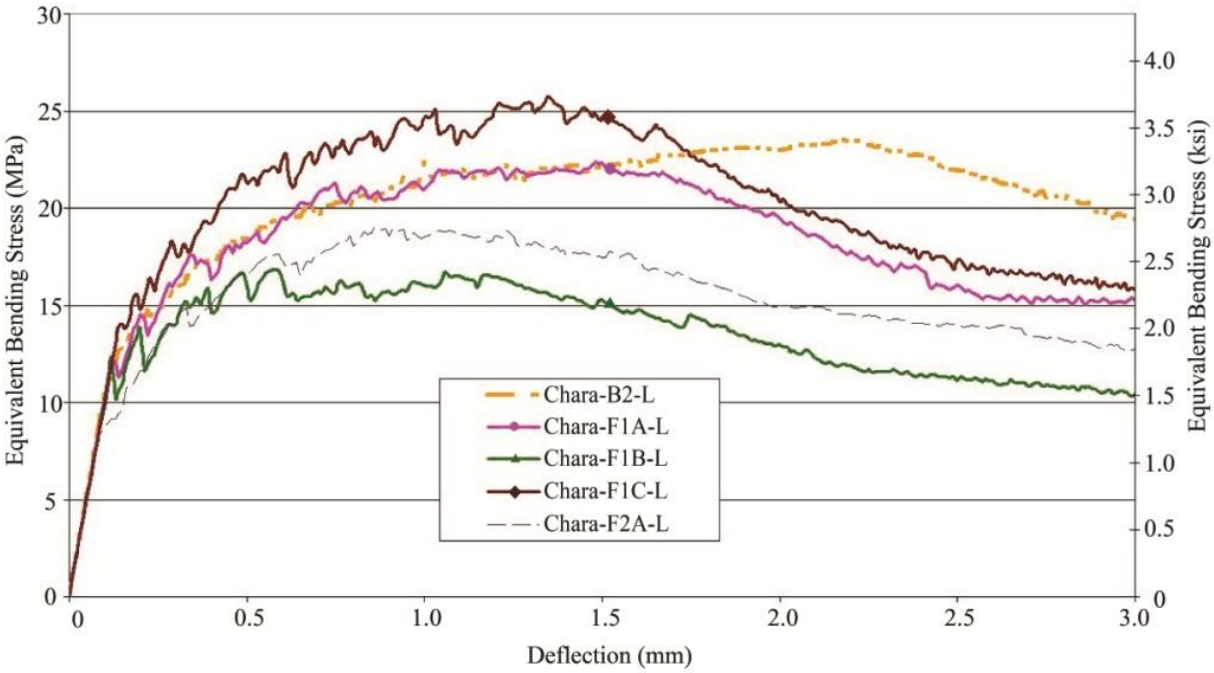

Figure 72. Graph. Equivalent bending stress versus midspan deflection showing characteristic curve for each batch for bending configuration L.

The average and characteristic equivalent bending stress versus midspan deflection curves are presented in figure 73 and figure 74, respectively, for bending configuration B.

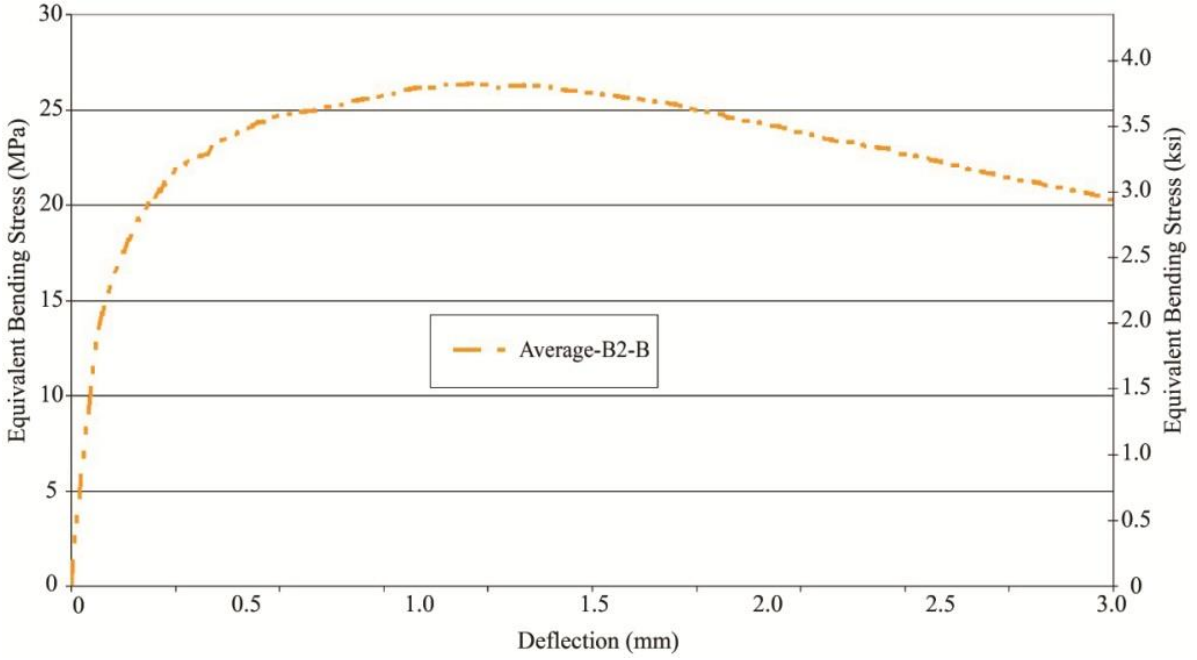

Figure 73. Graph. Equivalent bending stress versus midspan deflection showing average curve for bending configuration B.

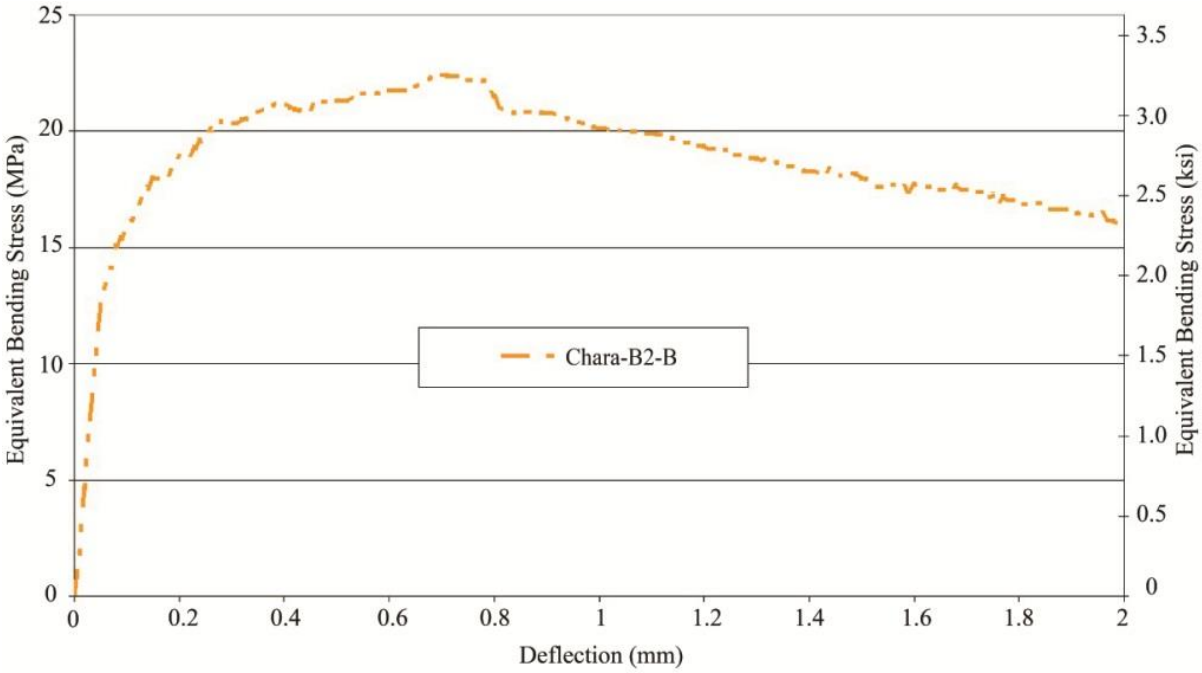

Figure 74. Graph. Equivalent bending stress versus midspan deflection showing characteristic curve for bending configuration B.

Table 22 presents the maximum values observed from the analyses of the average and characteristic equivalent bending stress versus midspan deflection curves for all the batches and configurations.

Table 22. Maximum values observed from the analyses of the average and characteristic equivalent bending stress versus midspan deflection curves.

Batch Name	Test Configuration	Specimen Group Name	Number of Specimens	Maximum Average Curve Equivalent Bending Stress, MPa (ksi)	Maximum Characteristic Curve Equivalent Bending Stress, MPa (ksi)
B2	S	B2-S	5	28.1 (4.07)	18.2 (2.63)
B2	L	B2-L	6	29.0 (4.20)	23.5 (3.41)
B2	B	B2-B	6	26.4 (3.82)	22.4 (3.25)
F1A	S	F1A-S	6	24.1 (3.50)	20.6 (2.99)
F1A	L	F1A-L	5	27.0 (3.92)	22.4 (3.24)
F2A	S	F2A-S	6	18.0 (2.62)	13.6 (1.97)
F2A	L	F2A-L	5	23.6 (3.42)	15.3 (2.22)
F1B	S	F1B-S	6	21.4 (3.10)	20.2 (2.92)
F1B	S	F1B-S-Cut	5	24.8 (3.60)	21.2 (3.07)
F1B	L	F1B-L	5	22.2 (3.21)	16.8 (2.44)
F1C	S	F1C-S	6	27.9 (4.04)	22.8 (3.30)
F1C	L	F1C-L	5	28.5 (4.13)	25.7 (3.73)

The following preliminary comments can be drawn from these experimental result:

- The comparison of results between F1A and F2A showed a well-known effect of the steam treatment on the mechanical properties.
- The higher percentage of fibers for F1C compared with F1A and F1B induced an improvement of the experimental results particularly for the characteristic curves.
- In comparing the results of F1A and F1B, some deviations were observed following batches for a given UHPC.

Equivalent Bending Stress Versus Midspan Strain at the Bottom Flange

The average and characteristic equivalent bending stress versus midspan strain at the bottom flange curves are discussed from initial elastic loading through a standard upper limit equal to 15,000 microstrain. The localization occurred at a strain level less than 15,000 microstrain. After reaching localization, the displacement measured by the LVDTs was considered a crack opening. Regardless, the concept of strain was used over the whole test duration to compare the different curves for all the batches. Figure 75 and figure 76 present the average and the characteristic curves for all the batches, respectively, for bending configuration S.

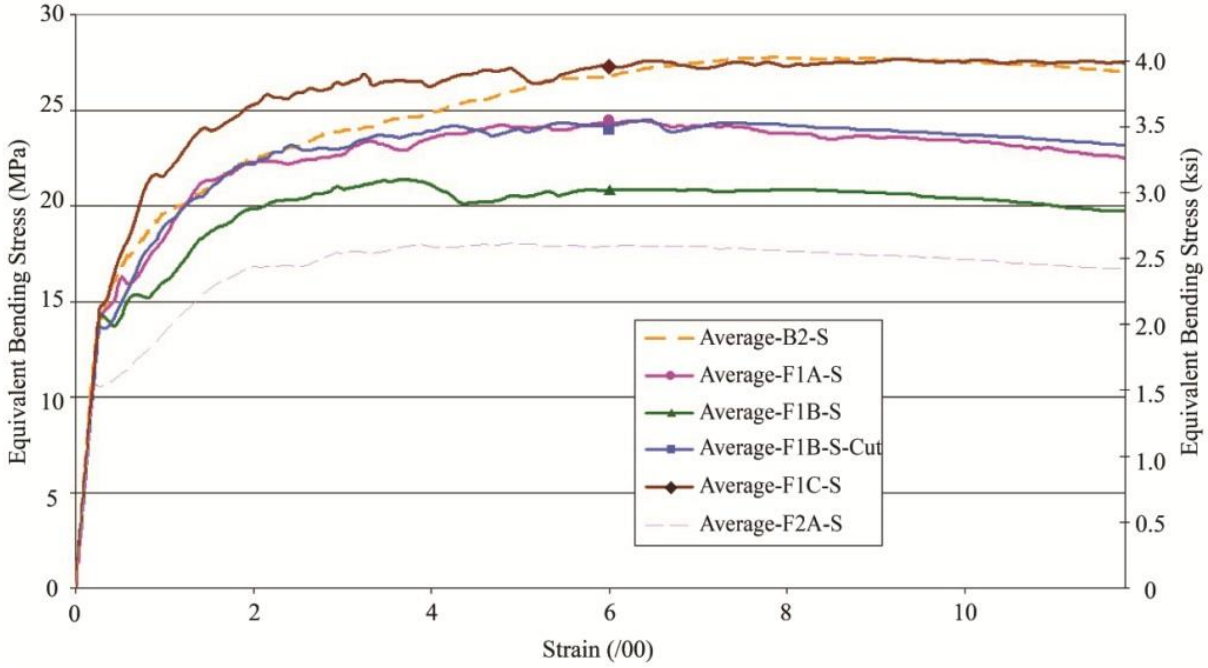

Figure 75. Graph. Equivalent bending stress versus midspan strain at the bottom flange showing average curve for each batch for bending configuration S.

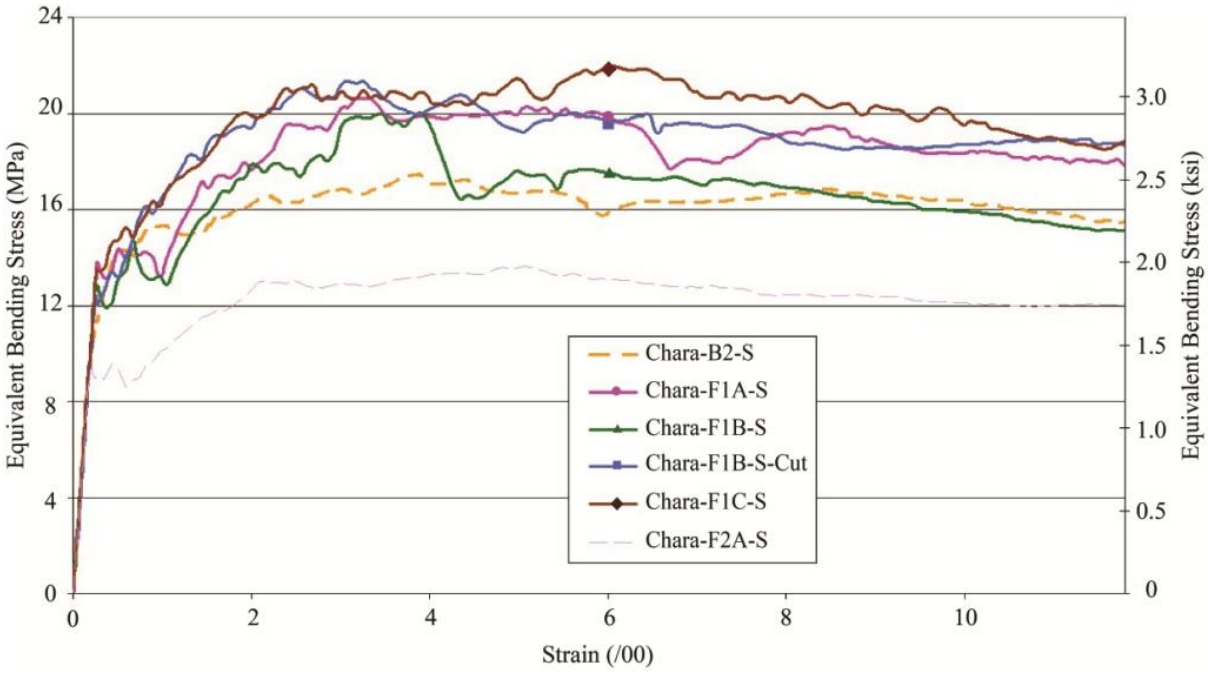

Figure 76. Graph. Equivalent bending stress versus midspan strain at the bottom flange showing characteristic curve for each batch for bending configuration S.

Figure 77 and figure 78 show the average and characteristic equivalent bending stress versus midspan strain at the bottom flange curves, respectively, for bending configuration L.

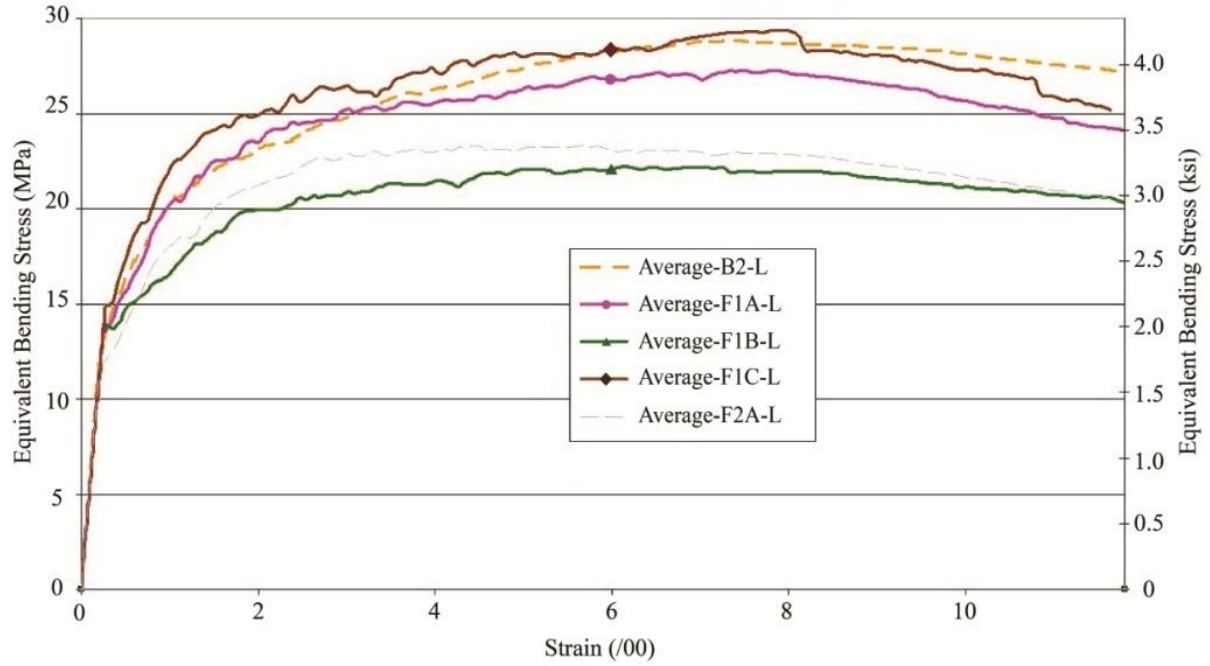

Figure 77. Graph. Equivalent bending stress versus midspan strain at the bottom flange showing average curve for each batch for bending configuration L.

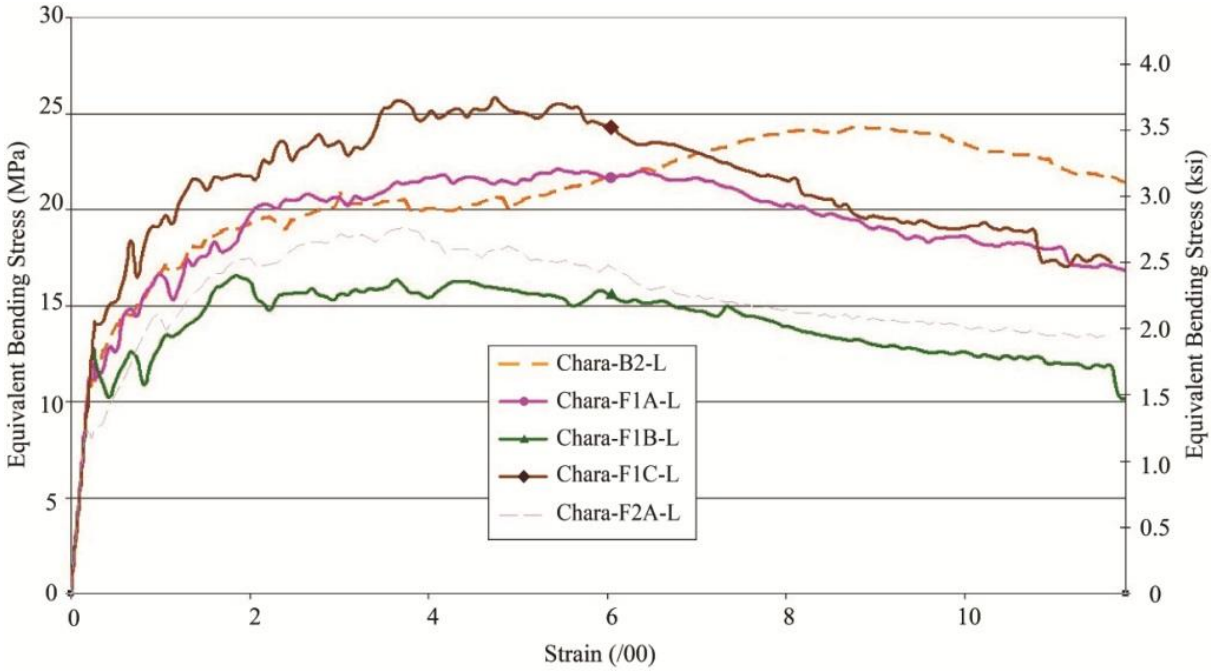

Figure 78. Graph. Equivalent bending stress versus midspan strain at the bottom flange showing characteristic curve for each batch for bending configuration L.

Figure 79 and figure 80 provide the average and characteristic equivalent bending stress versus midspan strain at the bottom flange curves, respectively, for bending configuration B.

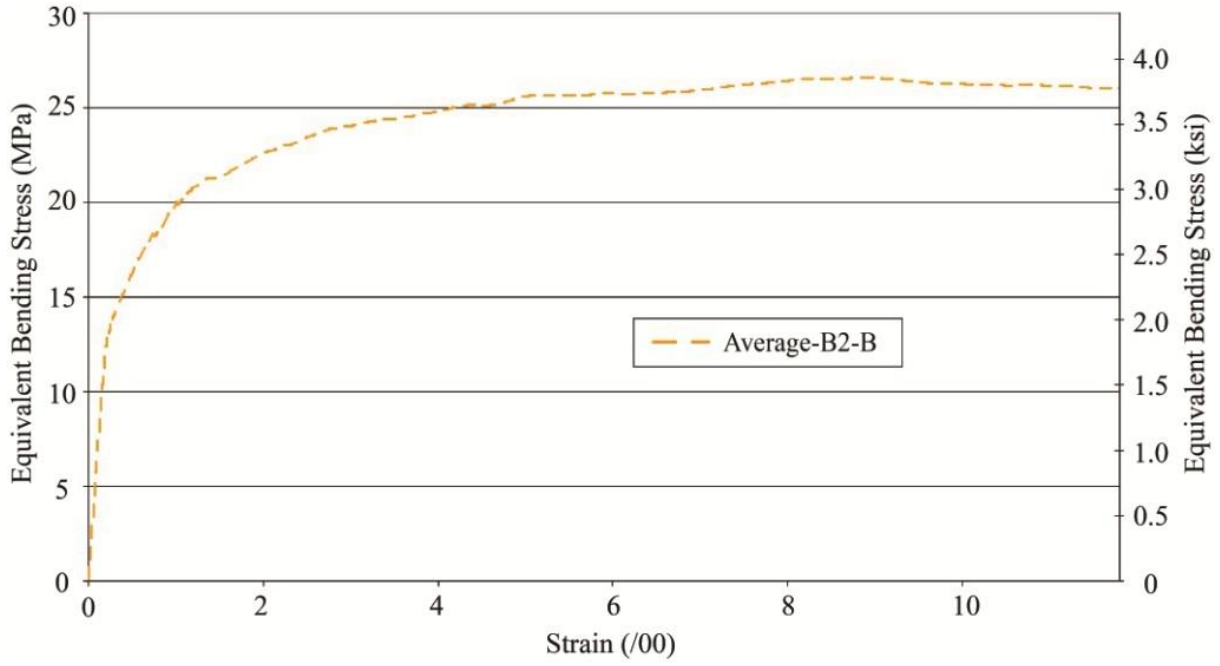

Figure 79. Graph. Equivalent bending stress versus midspan strain at the bottom flange showing average curve for each batch for bending configuration B.

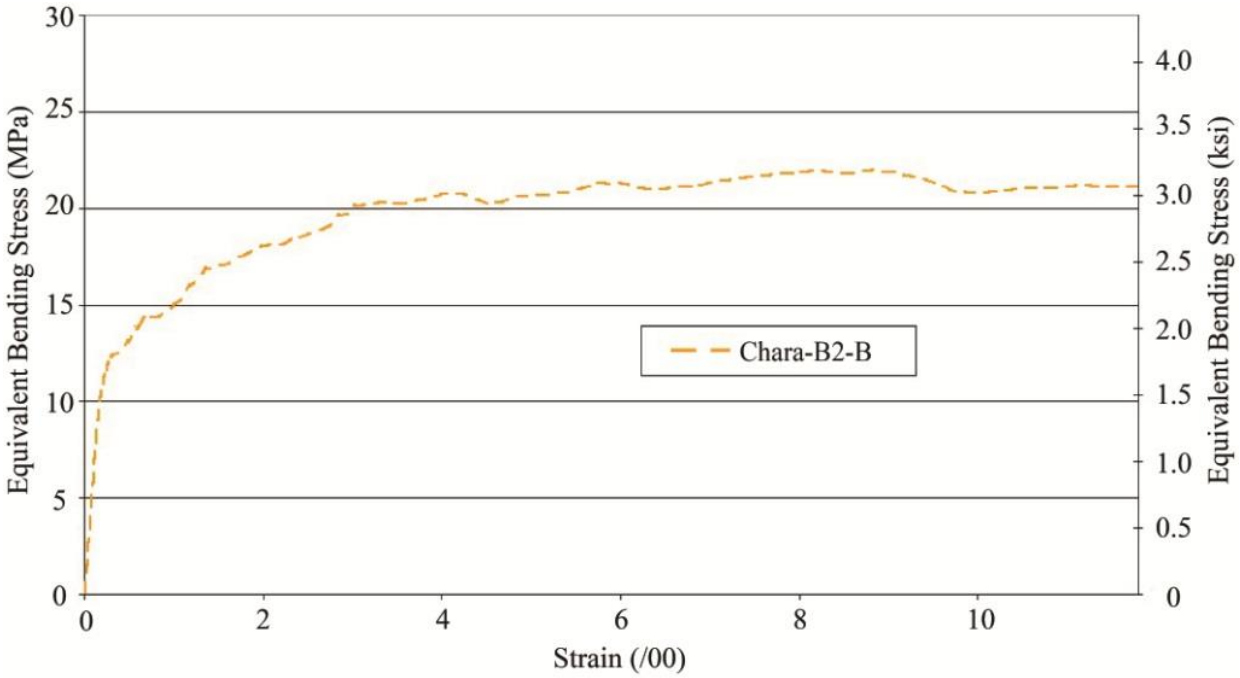

Figure 80. Graph. Equivalent bending stress versus midspan strain at the bottom flange showing characteristic curve for each batch for bending configuration B.

Contrary to the equivalent bending stress versus midspan deflection curves, the equivalent bending stress versus midspan strain at the bottom flange curves (figure 81 to figure 84) allowed a direct complete comparison of data between configurations with the following limits:

- The assumption (neutral axis at the midheight of the prism) to take into account the effect of the additional lever arm due to sensors fixation devices was not true after entering the inelastic (i.e., cracking) portion of the behavior.

- After crack localization, the crack opening was sensitive to a scale effect with the height of the prisms.

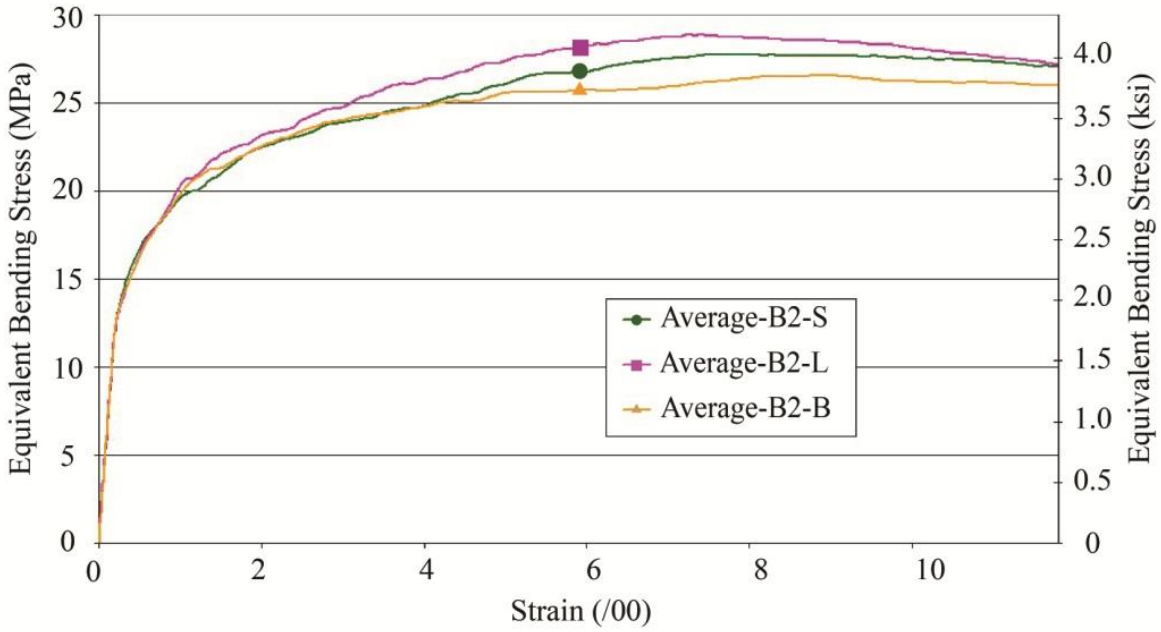

Figure 81. Graph. Equivalent bending stress versus midspan strain at the bottom flange showing average curve for each test configuration in batch B2.

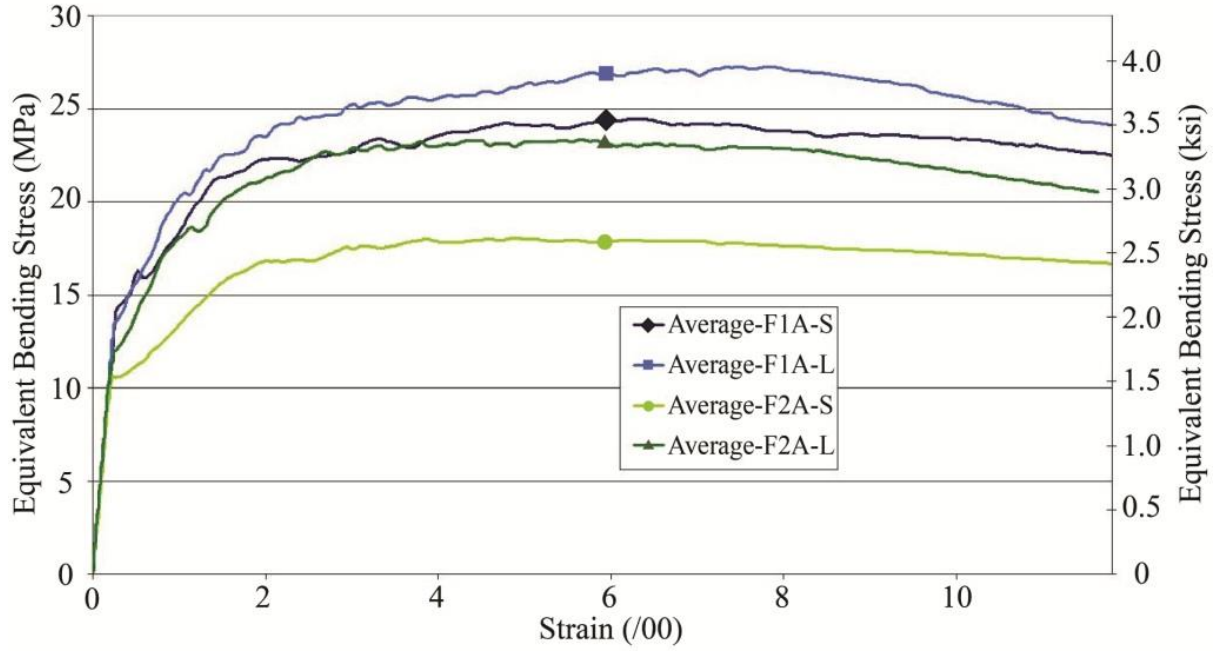

Figure 82. Graph. Equivalent bending stress versus midspan strain at the bottom flange showing average curve for bending configurations S and L in batch FA.

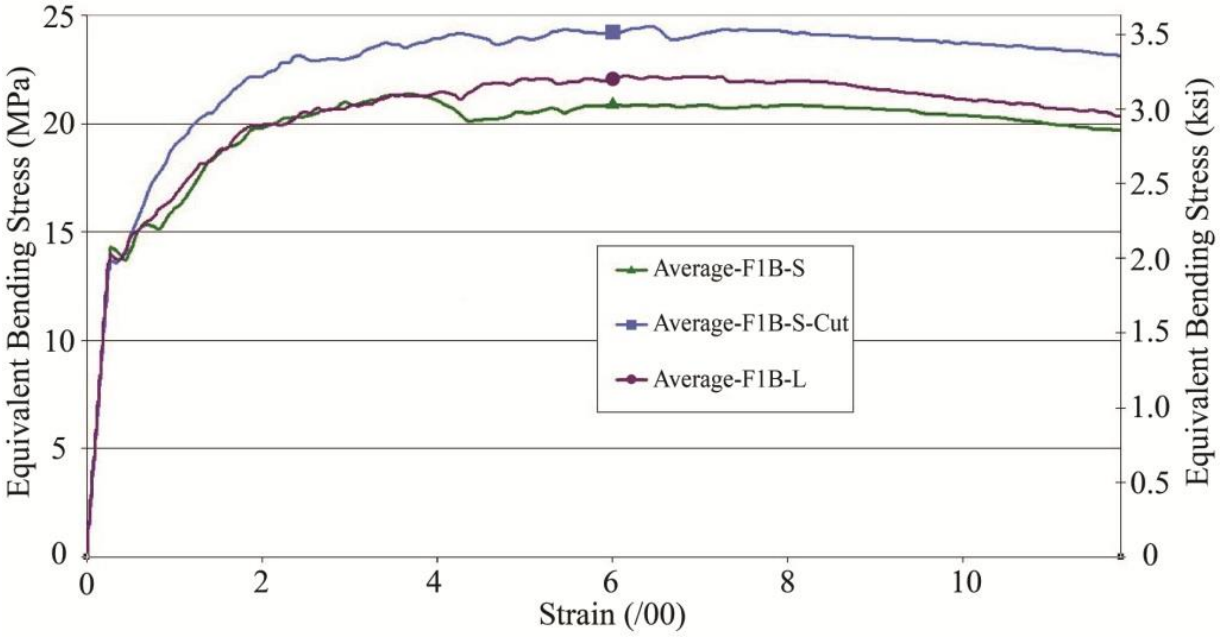

Figure 83. Graph. Equivalent bending stress versus midspan strain at the bottom flange showing average curve for bending configurations S and L in batch F1B.

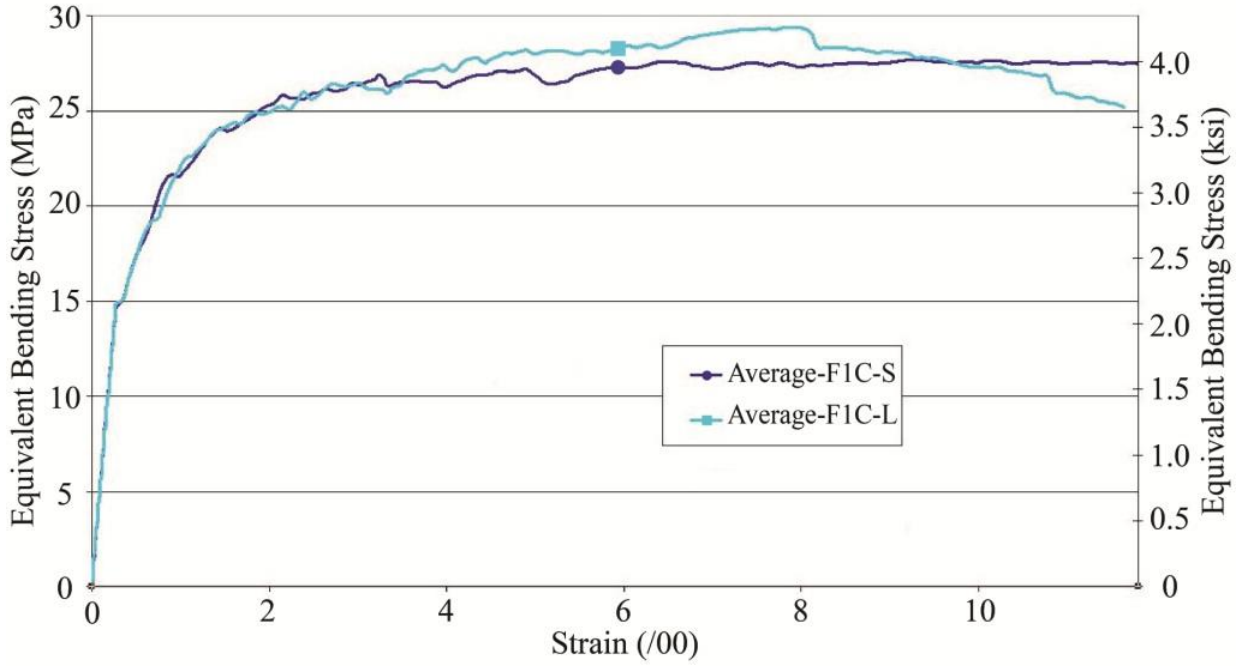

Figure 84. Graph. Equivalent bending stress versus midspan strain at the bottom flange showing average curve for bending configurations S and L in batch F1C.

Table 23 presents the deviation between test configurations S and L in terms of average maximum equivalent bending stress for all of the batches. For configuration L, the length of the constant bending-moment zone (102 mm (4 inches)) was more important than in configuration S (76 mm (3 inches)). As a consequence, a statistical size effect, which induced a lower mean value, would have been expected. Nevertheless, the experimental results showed the contrary phenomenon (i.e., the results for configuration L were higher than configuration S), which could be explained by the fact that the longer the prism, the more preferential is the orientation of the fibers. The statistical size effect between both configurations of test was observed only for batch F1B. Indeed, similar prisms made of F1B were tested in both configurations—F1B-S-Cut (maximum average curve was equal to 24.8 MPa (3.6 ksi) and F1B-L (maximum average curve) was equal to 22.2 MPa (3.21 ksi)).

Table 23. Average maximum equivalent bending stress for the test configurations S and L.

Batch Name	Test Configuration	Specimen Group Name	Number of Specimens	Maximum of the Average Curve Equivalent Bending Stress, MPa (ksi)	Deviation Between Configurations (Percent)
B2	S	B2-S	5	27.8 (4.03)	+3.8
B2	L	B2-L	6	28.9 (4.18)	+3.8
F1A	S	F1A-S	6	24.5 (3.55)	+10.2
F1A	L	F1A-L	5	27.2 (3.95)	+10.2
F2A	S	F2A-S	6	18.0 (2.61)	+22.8
F2A	L	F2A-L	5	23.4 (3.39)	+22.8
F1B	S	F1B-S	6	21.4 (3.10)	+3.7
F1B	L	F1B-L	5	22.2 (3.22)	+3.7
F1C	S	F1C-S	6	27.7 (4.01)	+5.7
F1C	L	F1C-L	5	29.4 (4.26)	+5.7

Analysis of the Elastic Behavior: Young's Modulus and Limit of Linearity

Young's modulus and the limit of linearity (generally considered as the limit of the regime with full fiber–matrix bond) could be determined from the equivalent bending stress versus midspan deflection and equivalent bending stress versus midspan strain at the bottom flange curves.

Results Based on the Equivalent Bending Stress Versus Midspan Deflection Curve

The elastic part of the equivalent bending stress versus midspan deflection responses were analyzed to determine the modulus and the limit of linearity. On the raw data for each batch, the inflection $\Delta\sigma_E$ (change in equivalent stress) was visually located, and the recordings corresponding to the interval ($\Delta\sigma_E/3$ and $2 \times \Delta\sigma_E/3$) were linearized. Each straight line, thus, served to calculate *E* from the elastic-range slope.

In order to find the first cracking stress, the following procedure was used for each curve:

1. The straight sections beyond $\Delta\sigma_E$ were extended; this curve is referred to as the "linear part."

2. The raw curve was compared with the linear part for each point of the curves. The linear raw curve and nonlinear raw curve were determined using equation 59 and equation 60.

$$\frac{|\sigma_{Linear\ -Part} - \sigma_{Raw-Curve}|}{|\sigma_{Linear\ -Part}|} \times 100 < 1\% \quad (59)$$

Where:

$\sigma_{Linear\text{-}Part}$ = straight sections of the equivalent stress (σ_E)–midspan deflection (δ_m) curve beyond $\Delta\sigma_E$.

$\sigma_{Raw\text{-}Curve}$ = any section of the σ_E-δ_m curve.

$$\frac{|\sigma_{Linear\ -Part} - \sigma_{Raw\ -Curve}|}{|\sigma_{Linear\ -Part}|} \times 100 > 1\% \quad (60)$$

Due to the noise of the recordings, some point could be considered as nonlinear, whereas the raw curve was still in the linear part. Consequently, the limit of linearity stress corresponded to the last point considered as linear.

Table 24 and table 25 present the first cracking stress and Young's modulus obtained from the analysis of the equivalent bending stress versus midspan deflection curve for all batches, respectively.

Table 24. Limit of linearity stress from the equivalent bending stress versus midspan deflection curve.

Batch Name	Test Configuration	Specimen Group Name	Average Limit of Linearity, MPa (ksi)	Characteristic Limit of Linearity, MPa (ksi)
B2	S	B2-S	10.8 (1.57)	9.0 (1.31)
B2	L	B2-L	11.2 (1.62)	9.8 (1.42)
B2	B	B2-B	11.5 (1.67)	9.0 (1.31)
F1A	S	F1A-S	14.9 (2.16)	13.6 (1.97)
F1A	L	F1A-L	13.5 (1.96)	10.1 (1.46)
F2A	S	F2A-S	10.3 (1.49)	8.2 (1.19)
F2A	L	F2A-L	10.4 (1.51)	7.1 (1.03)
F1B	S	F1B-S	14.5 (2.10)	12.2 (1.77)
F1B	S	F1B-S-Cut	13.1 (1.90)	11.6 (1.68)
F1B	L	F1B-L	14.2 (2.06)	12.1 (1.75)
F1C	S	F1C-S	15.2 (2.20)	13.9 (2.02)
F1C	L	F1C-L	14.8 (2.15)	13.5 (1.96)

Table 25. Young's modulus from the equivalent bending stress versus midspan deflection curve.

Batch Name	Test Configuration	Specimen Group Name	Mean Young's Modulus, GPa (ksi)
B2	S	B2-S	59.5 (8630)
B2	L	B2-L	60.1 (8715)
B2	B	B2-B	56.3 (8160)
F1A	S	F1A-S	50.2 (7283)
F1A	L	F1A-L	54.1 (7845)
F2A	S	F2A-S	50.5 (7322)
F2A	L	F2A-L	54.7 (7933)
F1B	S	F1B-S	51.0 (7393)
F1B	S	F1B-S-Cut	51.5 (7464)
F1B	L	F1B-L	53.1 (7704)
F1C	S	F1C-S	51.3 (7443)
F1C	L	F1C-L	52.7 (7639)

Concerning the first cracking stress, the following conclusions could be drawn from the experimental results:

- There was a lack of scale effect for batch B2. There was not a brittle transition after reaching the cementitious matrix strength. The behavior of this material was directly plastic, and there was no scale effect for materials with an elastic-perfectly plastic behavior.

- The characteristic limit of linearity results for batches F1A, F1B, and F1C with steam treatment were notably higher than those for batch B2. An explanation of this experimental observation is the existence of a scale effect on the results of specimens in F1A, F1B, and F1C. For this latter, after reaching the cementitious matrix strength, there was a nonperfectly brittle transition before an efficient activation of fibers. This transition was sensitive to the scale effect, which induced difficulties on the analysis of experimental results concerning the limit of linearity.[5] The following was noted:[5]

  > This effect does not exist with perfectly brittle materials, and is dependent among other things on the specimen's geometry and the material's damage mechanism. This means that during a bending test, the specimen is subjected to a compressive-tensile stress gradient, and the material is damaged by micro-cracking ahead of the crack front, in order to reduce the stress concentrations. This fracture area enables load transfer to be maintained and creates the scale effect. (p. 32)

  In order to confirm the commentary of Chanvillard and Rigaud, it should be necessary to test in flexure some prisms of higher depth made out of F1 (with steam treatment).[5]

- The improvement induced by the steam treatment on the mechanical characteristics was confirmed by the comparison of results between F1A and F2A batches.

A comparison of results for configurations S and L was difficult due to two existing phenomena that induced contradictory effects. Specifically, the longer the prism, the more preferential the orientation of fibers. The fibers provide a limited but non-negligible portion of the materials resistance up to the limit of linearity, as shown in equation 61.

$$Limit\ of\ Linearity = f_{tcm} \times \left(1 + \psi \times V_f \times \frac{E_c}{E_f}\right) \quad (61)$$

Where:

f_{tcm} = cementitious matrix strength (without fibers).
ψ = coefficient of orientation.
V_f = percentage of fibers.
E_c = modulus of cementitious matrix.
E_f = modulus of elasticity of fibers.

As a consequence, the higher the ψ, the higher the limit of linearity. In configuration L, the constant bending-moment length was more important than in configuration S. Consequently, there was a statistical scale effect that induced a lower mean value of the limit of linearity for configuration L.

Results Based on the Equivalent Bending Stress Versus Midspan Strain at the Bottom Flange Curve

Concerning the midspan strain at the bottom flange, the effect of sensors' *OPD*, which will overestimate the strain as shown in figure 68, has been taken into account. For the analysis of the elastic part of the curves, the influence of this eccentricity was corrected with equation 62.

$$\varepsilon_{real} = \frac{0.5 \cdot h}{0.5 \cdot h + OPD} \times \varepsilon_{measured} \tag{62}$$

The previously discussed procedure used for the equivalent bending stress versus midspan deflection curve was applied for the equivalent bending stress versus midspan strain at the bottom flange curve (with ε_{real}) to find the modulus and the first cracking stress for each batch. The only difference with the previous procedure was the comparison between the raw curve and the linear part, which is highlighted in equation 63 and equation 64.

$$\frac{|\sigma_{Linear\ -Part} - \sigma_{Raw\ -Curve}|}{|\sigma_{Linear\ -Part}|} \times 100 < 0.5\% \tag{63}$$

$$\frac{|\sigma_{Linear\ -Part} - \sigma_{Raw\ -Curve}|}{|\sigma_{Linear\ -Part}|} \times 100 > 0.5\% \tag{64}$$

Table 26 and table 27 present the limit of linearity and the Young's modulus obtained from the analysis of the equivalent bending stress versus midspan strain at the bottom flange curve for all the of batches, respectively.

Table 26. Limit of linearity determined from the equivalent bending stress versus midspan strain at the bottom flange response.

Batch Name	Test Configuration	Specimen Group Name	Mean Limit of Linearity, MPa (ksi)	Characteristic Limit of Linearity, MPa (ksi)
B2	S	B2-S	10.4 (1.51)	8.2 (1.19)
B2	L	B2-L	11.9 (1.73)	10.4 (1.51)
B2	B	B2-B	11.0 (1.60)	8.5 (1.23)
F1A	S	F1A-S	14.8 (2.15)	13.6 (1.97)
F1A	L	F1A-L	13.5 (1.96)	10.6 (1.54)
F2A	S	F2A-S	10.1 (1.46)	8.2 (1.19)
F2A	L	F2A-L	11.5 (1.67)	7.7 (1.12)
F1B	S	F1B-S	14.3 (2.07)	11.8 (1.71)
F1B	S	F1B-S-Cut	13.2 (1.91)	11.1 (1.61)
F1B	L	F1B-L	14.2 (2.06)	12.1 (1.75)
F1C	S	F1C-S	15.0 (2.18)	12.9 (1.87)
F1C	L	F1C-L	14.6 (2.12)	12.6 (1.83)

Table 27. Young's modulus determined from the equivalent bending stress versus midspan strain at the bottom flange response.

Batch Name	Test Configuration	Specimen Group Name	Mean Young's Modulus, GPa (ksi)
B2	S	B2-S	60.1 (8720)
B2	L	B2-L	60.2 (8735)
B2	B	B2-B	63.5 (9205)
F1A	S	F1A-S	52.4 (7605)
F1A	L	F1A-L	55.2 (8007)
F2A	S	F2A-S	51.2 (7429)
F2A	L	F2A-L	55.0 (7975)
F1B	S	F1B-S	53.3 (7733)
F1B	S	F1B-S-Cut	52.9 (7667)
F1B	L	F1B-L	54.2 (7853)
F1C	S	F1C-S	54.3 (7876)
F1C	L	F1C-L	54.0 (7826)

The results from the analysis of the equivalent bending stress versus midspan deflection responses and the equivalent bending stress versus midspan strain at the bottom flange responses are compared in table 28 and figure 85 as well as table 29 and figure 86. Both analyses had similar results (deviation less than 5 percent) except in two cases. These two cases corresponded to test configuration L in which the shear span was larger (with the ratio of the shear span to specimen depth, a/h, equal to 2.5). As a consequence, for this configuration, the first crack can sometimes occur on the outside of the constant bending-moment zone.

Table 28. Limit of linearity comparison of results.

Batch Name	Test Configuration	Specimen Group Name	Mean Limit of linearity Deflection Analysis at 1 Percent, MPa (ksi)	Mean Limit of Linearity Strain Analysis at 0.5 Percent, MPa (ksi)	Deviation Between Deflection Analysis and Strain Analysis, Percent
B2	S	B2-S	10.8 (1.57)	10.4 (1.51)	4.5
B2	L	B2-L	11.2 (1.62)	11.9 (1.73)	6.8
B2	B	B2-B	11.5 (1.67)	11.0 (1.60)	4.3
F1A	S	F1A-S	14.9 (2.16)	14.8 (2.15)	0.5
F1A	L	F1A-L	13.5 (1.96)	13.5 (1.96)	0.1
F2A	S	F2A-S	10.3 (1.49)	10.1 (1.46)	1.4
F2A	L	F2A-L	10.4 (1.51)	11.5 (1.67)	10.6
F1B	S	F1B-S	14.5 (2.10)	14.3 (2.07)	1.2
F1B	S	F1B-S-Cut	13.1 (1.90)	13.2 (1.91)	0.6
F1B	L	F1B-L	14.2 (2.06)	14.2 (2.06)	0.0
F1C	S	F1C-S	15.2 (2.20)	15.0 (2.18)	1.2
F1C	L	F1C-L	14.8 (2.15)	14.6 (2.12)	1.7

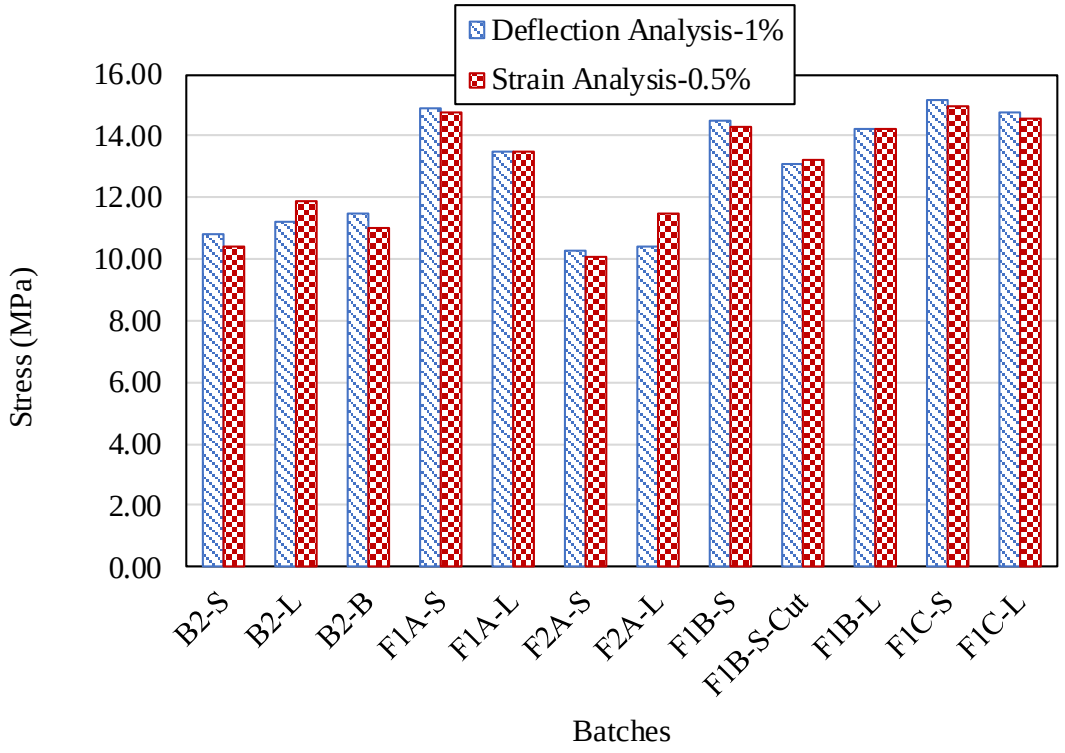

Source: FHWA.

Figure 85. Graph. Comparison of results for first cracking strength.

Table 29. Young's modulus comparison of results.

Batch Name	Test Configuration	Specimen Group Name	Mean Young's Modulus Deflection Analysis, GPa (ksi)	Mean Young's Modulus Strain Analysis, GPa (ksi)	Deviation Between Modulus Deflection Analysis and Modulus Strain Analysis, Percent
B2	S	B2-S	59.5 (8630)	60.1 (8720)	1.0
B2	L	B2-L	60.1 (8715)	60.2 (8735)	0.2
B2	B	B2-B	56.3 (8160)	63.5 (9205)	12.8
F1A	S	F1A-S	50.2 (7283)	52.4 (7605)	4.4
F1A	L	F1A-L	54.1 (7845)	55.2 (8007)	2.1
F2A	S	F2A-S	50.5 (7322)	51.2 (7429)	1.5
F2A	L	F2A-L	54.7 (7933)	55.0 (7975)	0.5
F1B	S	F1B-S	51.0 (7393)	53.3 (7733)	4.6
F1B	S	F1B-S-Cut	51.5 (7464)	52.9 (7667)	2.7
F1B	L	F1B-L	53.1 (7704)	54.2 (7853)	1.9
1C	S	F1C-S	51.3 (7443)	54.3 (7876)	5.8
1C	L	F1C-L	52.7 (7639)	54.0 (7826)	2.4

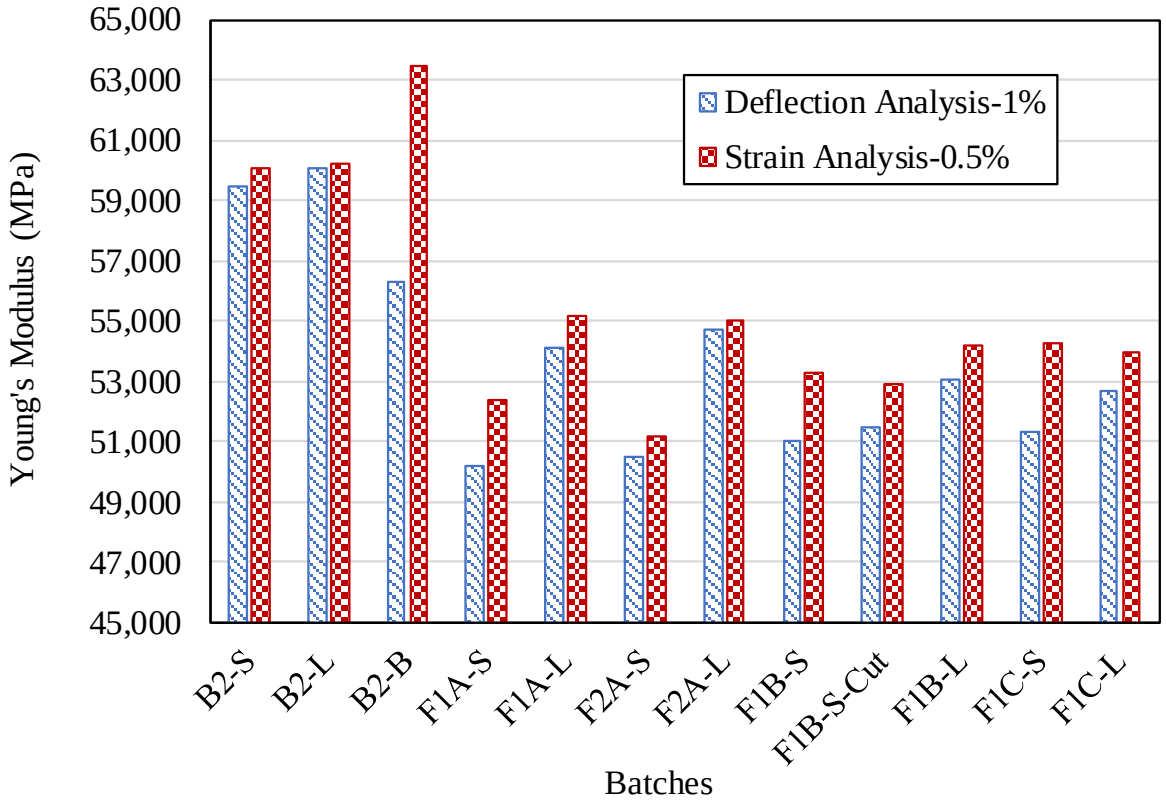

Source: FHWA.

Figure 86. Graph. Young's modulus comparison of results.

Both analyses (i.e., the equivalent bending stress versus midspan deflection curve and the equivalent bending stress versus midspan strain at the bottom flange curve) induced similar results for specimen groups that were tested in bending configuration L. It was not the case for the other configurations, particularly for the bending configuration B in which the ratio of shear span/specimen height was the lowest (equal to 1). For this situation, the deflection due to shear was not negligible.

Analysis of Hardening Strains

This section discusses the analysis of the experimentally obtained hardening strains, details on different analysis methods, and a comparison of experimental results.

Adopted Approach to Analyze the Experimental Results

In the case of UHPC with a hardening behavior under tension, during an FT on an unnotched specimen, a multiple fine-cracking (with a crack spacing between $L_f/2$ and L_f, where L_f is the fiber length) occurred. This cracking scheme induced a lack of macroscopic localization of damage and the development of pseudo-hardening strain.[66] Thus, it was relevant to use a stress–strain relationship to characterize the UHPC behavior under tension.

In the case of UHPC with a softening behavior under tension, during an FT on an unnotched specimen, a multiple macrocracking (with a crack spacing between $h/2$ and h, where h is the specimen height) occurred.[3] In that case, it was more relevant to use a stress-crack opening approach to characterize the UHPC behavior under tension.

In the context of this study, only UHPC with a hardening behavior under tension was considered. Thus, the approach described in figure 87 was adopted. A complete analysis of all cases can be found in *Contribution to Identification of UHPFRC Tensile Constitutive Behaviour and Accounting for Structural Design*.[67]

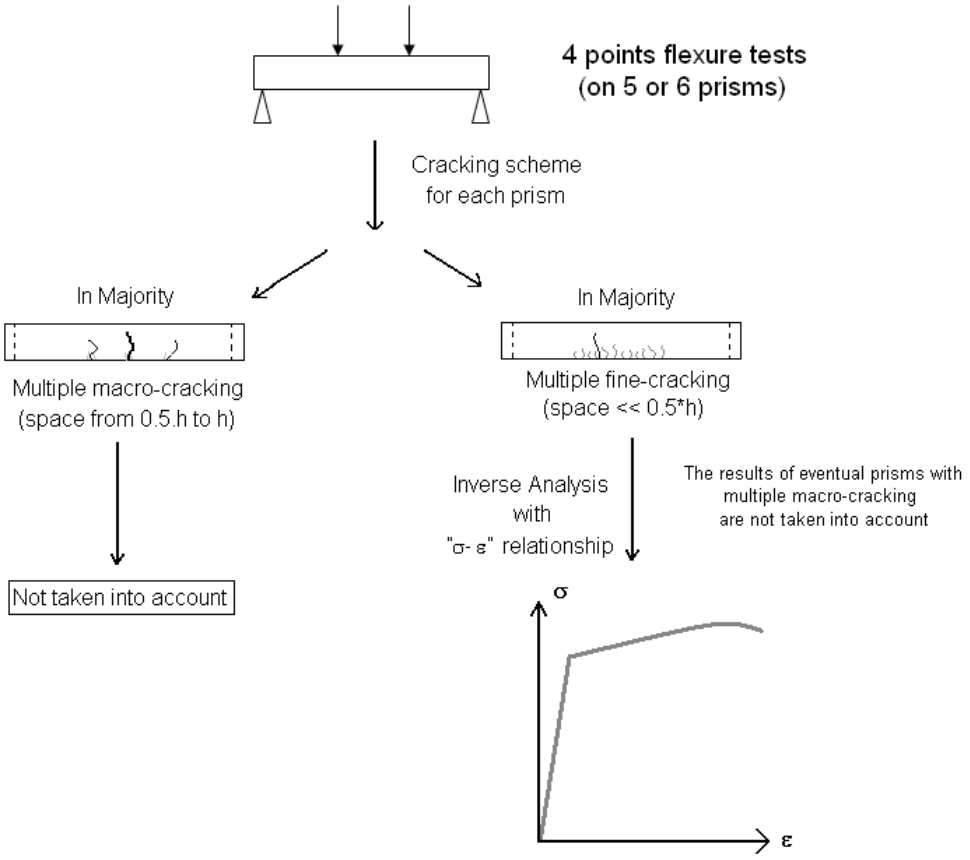

Figure 87. Flowchart. Adopted approach to analyze the results obtained from four-point FTs on unnotched prisms.

The experimental results, in particular the cracking scheme identified for each prism, allowed for the following to be distinguished:

- Specimen groups characterized by multiple fine cracking, which indicated a strain-hardening behavior under tension.

- Specimen groups characterized by multiple macrocracking (space between 0.5*h* and *h*), which indicated a softening behavior under tension.

It was noted that all tested prisms were characterized by a hardening behavior under flexure. Table 30 gives a first synthesis issued from cracking scheme observations realized for each specimen.

Table 30. Behavior under tension for each specimen group deduced from cracking scheme determined for each prism.

Specimen Group Name	Number of Tested Prisms	Number of Prisms with Multiple Fine Cracking	Number of Prisms with Multiple Macrocracking	Adopted Approach	
				Inverse Analysis to Obtain Stress–Strain Response	Number of Prisms Taken into Account
B2-S	5	5	—	Yes	5
B2-L	6	6	—	Yes	6
B2-B	6	6	—	Yes	6
F1A-S	6	3	3	Yes	3
F1A-L	5	5	—	Yes	5
F1B-S	6	1	5	No	Not taken into account
F1B-S-Cut	5	4	1	Yes	4
F1B-L	5	2	3	No	Not taken into account
F2A-S	6	—	6	No	Not taken into account
F2A-L	5	5	—	Yes	5
F1C-S	6	6	—	Yes	6
F1C-L	5	5	—	Yes	5

—No specimens.

For a given material, the behavior under tension can be different in similar batches. It underlines the significant influence of UHPC casting method on the mechanical characteristics.

A comparison of results obtained with short and long prisms for UHPC-F (with V_f equal to 2 percent) enabled the identification of the influence of preferential fiber orientation. Whereas the constant bending-moment zone was longer for long prisms as opposed to short specimens, the long prisms were characterized in all cases (excepted for specimen group F1B-L) by multiple fine cracking.

As indicated in figure 87, the experimental results of specimen groups characterized by multiple fine cracking were analyzed from a stress–strain approach. The prism groups characterized by multiple macrocracking were taken into account.

Details on the Different Methods to Identify the Hardening Strain

The hardening strain for each specimen tested in bending can be identified using one of the following four methods:

- **Strain measurement maximum stress**: The hardening strain is identified as the midspan strain (i.e., average measurement of both staggered LVDTs installed on the bottom flange) corresponding with the maximum equivalent bending stress.[(18)]

- **Strain measurement elastic unloading**: The hardening strain is expressed as the midspan strain (i.e., average measurement of both staggered LVDTs installed on the bottom flange) corresponding with an identification of the elastic unloading, as explained in figure 52.[18]

- **Qian and Li method**: The hardening strain is identified thanks to the master curve (with mechanical assumption) constructed for each test configuration.[54]

- **Modified Qian and Li method**: The hardening strain is identified thanks to the master curve (with direct calculation of deflection) constructed for each test configuration.[54]

Concerning the midspan strain at the bottom flange (measured by staggered LVDTs), the results presented in this section consider the effect of sensors' *OPD*, as discussed previously and shown in figure 68. The influence of this *OPD* was considered due to the result of the inverse analysis realized for each specimen using equation 65.

$$\varepsilon_{corrected} = \frac{\alpha_n \cdot h}{\alpha_n \cdot h + OPD} \times \varepsilon_{measured} \tag{65}$$

In the strain measurement elastic-unloading method, detection of crack localization was realized with an identification of the elastic unloading. The following three idealized cases have to be taken into account (as explained in figure 52):

- The following three observations can be made (figure 52-A):

    1. Displacements measured by both LVDTs increase.

    2. One of both displacements stops increasing or does not increase much anymore.

    3. An unloading branch occurs with a decreasing branch for one or both displacements.

- Crack localization detected with the staggered LVDTs corresponds approximately to the maximum of equivalent bending stress, as shown in figure 52-B.

- Crack localization is assumed to correspond with the maximum bending stress, as shown in figure 52-C.

In figure 52-A, the maximum of equivalent bending stress corresponds to the initiation of the unloading branch, as described in observation 3 and as shown in the figure 88. Thus, at the occurrence of the second cracking observation, the force continues increasing. It has to be recognized that, in some cases, the precise transition point between the different steps was not easily detected.

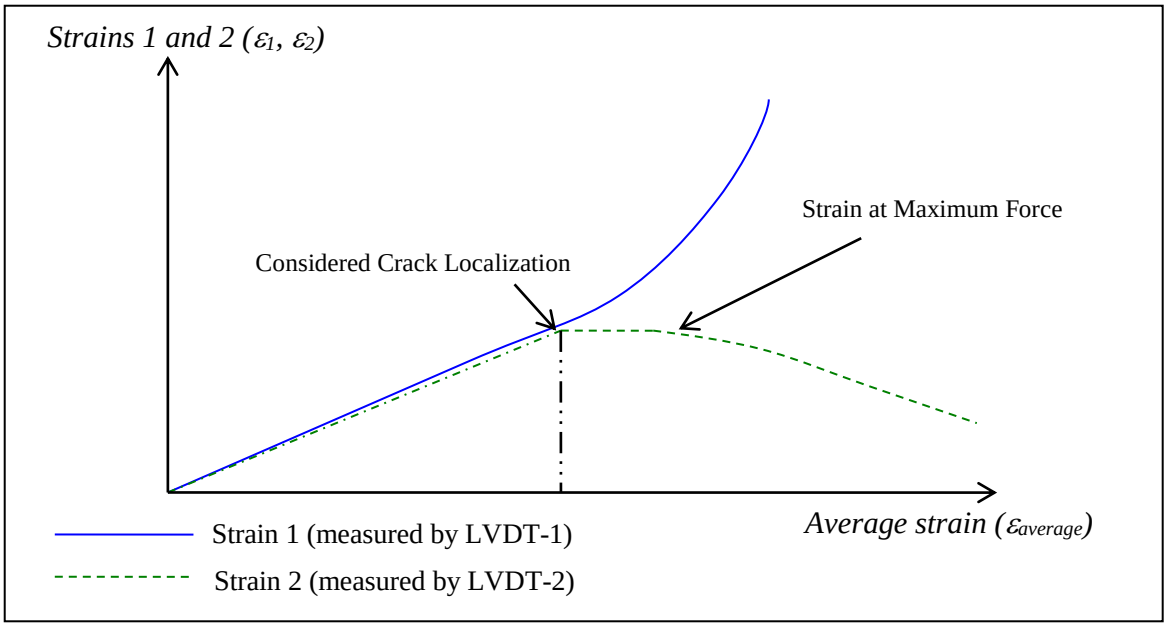

Figure 88. Graph. Strain measurement elastic unloading details.

Concerning the strain measurement maximum stress and strain measurement elastic unloading methods, before reaching crack localization, a difference between the slope of both curves (i.e., strain 1 versus average strain and strain 2 versus average strain) was observed for many specimens (figure 89). This difference indicates that the damage was not homogeneous in the constant bending length and was more concentrated in a particular zone. This phenomenon induced a dependence of the measured crack localization strain following the measurement basis length. For this reason, it may be interesting to compare at crack localization the average and the minimum of both staggered LVDT measurements.

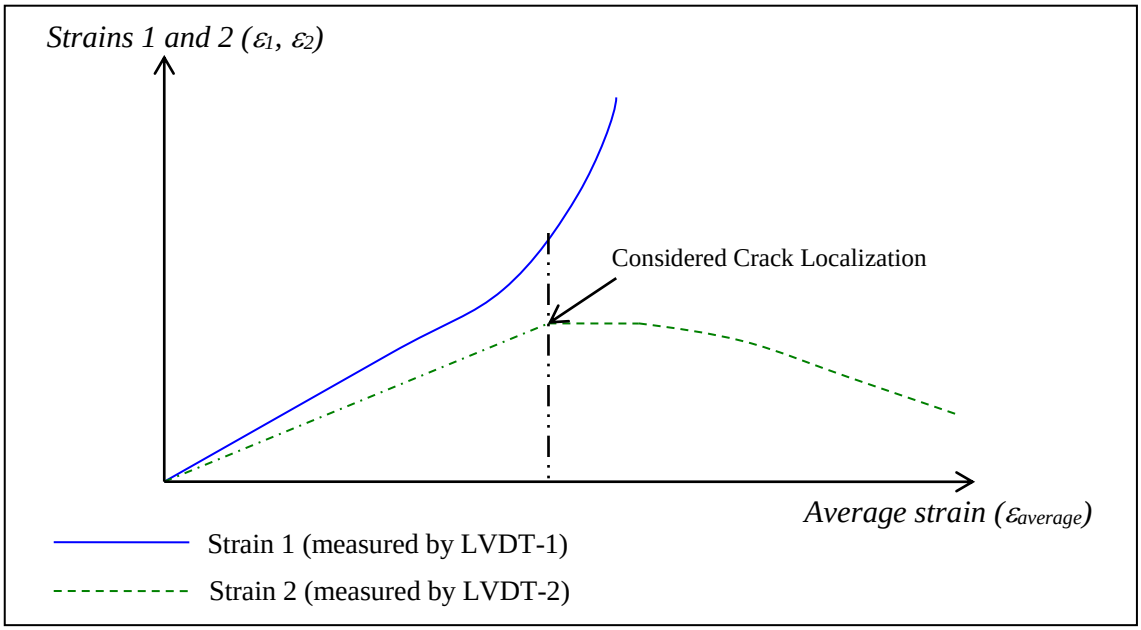

Figure 89. Graph. Deviation between the slopes of strain 1 versus average strain and strain 2 versus average strain curves before reaching crack localization.

Experimental Results—Comparison of Different Methods

This section presents only the average and standard deviation experimental results (figure 90 and table 31).

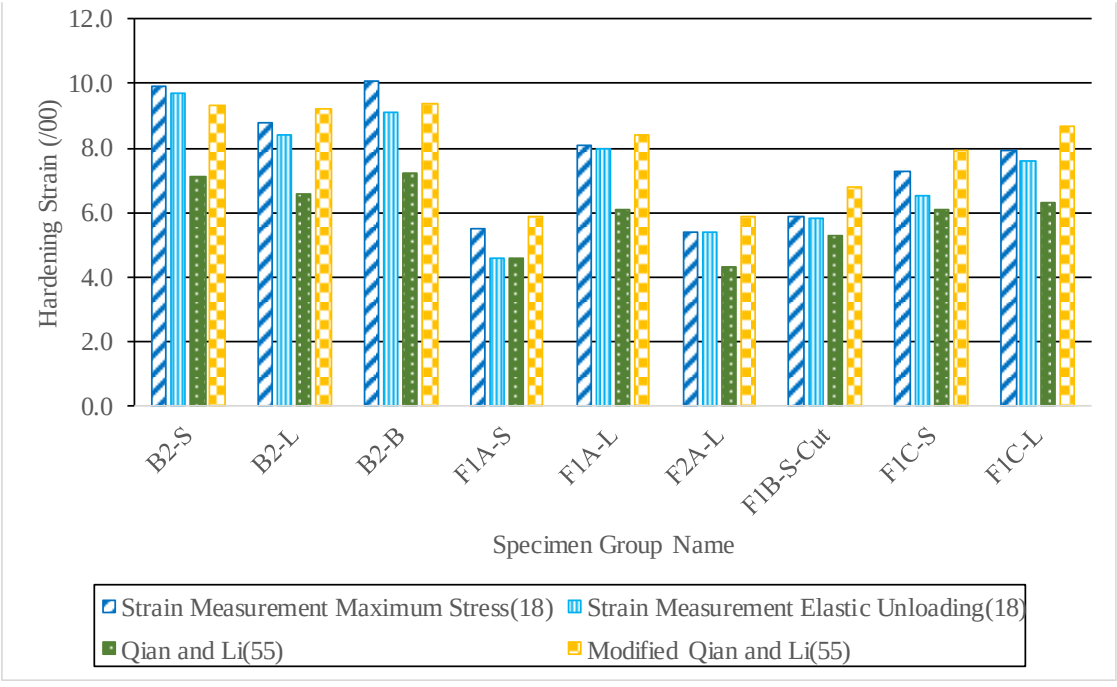

Source: FHWA.

Figure 90. Graph. Average hardening strain for each batch.

Table 31. Average hardening strain with standard deviation for each batch for the four different test methods.

Batch Name	Test Configuration	Specimen Group Name	Average Strain at Localization (Percent)				Standard Deviation for Average Strain at Localization (Percent)			
			Strain Measurement Maximum Stress[18]	Strain Measurement Elastic Unloading[18]	Qian and Li[54]	Modified Qian and Li[54]	Strain Measurement Maximum Stress[18]	Strain Measurement Elastic Unloading[18]	Qian and Li[54]	Modified Qian and Li[54]
B2	S	B2-S	9.9	9.7	7.1	9.3	1.8	2.1	1.7	2.3
B2	L	B2-L	8.8	8.4	6.6	9.2	2.1	2.3	1.1	1.6
B2	B	B2-B	10.1	9.1	7.2	9.4	1.4	2.0	1.4	1.9
F1A	S	F1A-S	5.5	4.6	4.6	5.9	2.1	1.5	1.4	1.9
F1A	L	F1A-L	8.1	8.0	6.1	8.4	1.5	1.6	1.4	2.0
F2A	L	F2A-L	5.4	5.4	4.3	5.9	2.5	2.5	1.3	1.8
F1B	S	F1B-S-Cut	5.9	5.8	5.3	6.8	2.3	2.2	1.6	2.1
F1C	S	F1C-S	7.3	6.5	6.1	7.9	3.6	2.9	1.8	2.4
F1C	L	F1C-L	7.9	7.6	6.3	8.7	2.1	2.0	2.2	3.1

For each specimen group, the average hardening strain was calculated using equation 66.

$$\varepsilon_{Average\text{-}Hardening\text{-}Strain} = \frac{1}{n_{spe}} \times \sum_{i=1}^{n_{spe}} \varepsilon_{Specimen\text{-}i} \quad (66)$$

Where:

$\varepsilon_{Average\text{-}Hardening\text{-}Strain}$ = average hardening strain.
n_{spe} = number of specimens considered.
$\varepsilon_{Specimen\text{–}i}$ = hardening strain.

For each specimens group, the minimum hardening strain can be calculated using equation 67.

$$\varepsilon_{Min\text{-}Hardening\text{-}Strain} = \frac{1}{n_{spe}} \times \sum_{i=1}^{n_{spe}} \varepsilon_{Min\text{-}Specimen\text{-}i} \quad (67)$$

Where:

$\varepsilon_{Min\text{-}Hardening\text{-}Strain}$ = average minimum hardening strain.
$\varepsilon_{Min\text{-}Specimen\text{-}i}$ = minimum measured strain value.

The maximum difference concerning the average hardening strain between the normal and modified Qian and Li methods based on the midspan strain measurement at the bottom flange was equal to 12 percent (specimen group F1A-S). Concerning the methods based on the deflection measurement, the mechanical assumption used to convert the deflection to curvature induced an underestimation of the strain corresponding to the maximum equivalent bending stress. This underestimation was, on average, 21 percent. This conclusion is similar to the results obtained with the parametric study described previously.

The comparison between the strain measurement maximum stress analysis and the modified Qian and Li method (the deviation between both methods was, on average, 9 percent) indicates that it may be possible to evaluate the midspan strain at the bottom flange corresponding to the maximum force in using an inverse analysis based on the direct calculation of deflection.

Concerning the strain measurement elastic unloading method, the comparison at crack localization between the average and the minimum of both staggered LVDT measurements is presented in table 32. The deviation between the average strain and the average minimum strain was approximately 20 percent for the majority of specimen groups except for specimen group F2A-L, which was 10 percent. This deviation was high, which could be explained by the relatively low number of cracks in the gauge length. Indeed, the maximum gauge length was equal to $5 \times L_{f\text{-}max}$, where $L_{f\text{-}max}$ is the maximum fiber length, and the average space between cracks is approximately $0.75 \times L_f$.[39] Thus, testing with a longer constant bending-moment zone may reduce this deviation.

Table 32. Average strain and average minimum strain at crack localization for strain measurement elastic unloading method.

Batch Name	Test Configuration	Specimen Group Name	Average Strain at Crack Localization (Percent)		Average Minimum Strain at Crack Localization (Percent)		Deviation Between Average and Minimum Strain (Percent)
			Average Strain	Standard Deviation	Average Minimum Strain	Standard Deviation	
B2	S	B2-S	9.7	2.1	7.6	3.2	22
B2	L	B2-L	8.4	2.3	6.9	3.0	18
B2	B	B2-B	9.1	2.0	6.9	2.6	24
F1A	S	F1A-S	4.6	1.5	3.5	2.1	24
F1A	L	F1A-L	8.0	1.6	6.5	3.2	19
F2A	L	F2A-L	5.4	2.5	4.9	2.1	10
F1B	S	F1B-S-Cut	5.8	2.2	4.8	2.3	17
F1C	S	F1C-S	6.5	2.9	4.8	2.3	26
F1C	L	F1C-L	7.6	2.0	6.2	3.7	18

Tensile Stress–Strain Relationship

The process for constructing the tensile stress–strain relationship curves and the results derived from the experimental tests are presented herein.

Details on the Construction of Curves

This section presents different tensile stress–strain relationships for each batch. The following three point-by-point inverse analysis methods were tested:

- Baby et al.'s inverse method based on strain measurement.[(18)]
- Rigaud et al.'s inverse method based on deflection measurement with a mechanical assumption to convert the deflection into curvature.[(55)]
- Baby et al.'s inverse method based on deflection measurement using a first analysis with a double integration of the curvature to obtain the bending-moment curvature relationship.[(19)]

These methods have to be compared with a simplified inverse analysis. The AFGC method is not applicable to hardening stress–strain curves.[(4)] Moreover, for this analysis, the value of the first cracking stress was necessary. Nevertheless, as explained previously, the value of the first cracking stress obtained with FTs could not be directly used for some specimen groups due to a scale effect. For these materials, after reaching the cementitious matrix strength, there was a nonperfectly brittle transition before activating the fibers with efficiency. This transition was sensitive to the scale effect, which induced difficulties for the analysis of experimental results concerning the first cracking stress.

For these reasons, the Qian and Li method was chosen as a simplified inverse analysis to compare with the results obtained from the point by point methods.[54] The following two types of Qian and Li methods were tested:

- Qian and Li method with the master curve strain capacity–deflection capacity constructed from a mechanical assumption to convert the deflection in curvature.[54]

- Modified Qian and Li method modified with the master curve strain capacity–deflection capacity constructed in using a double integration of the curvature.

For both methods, only mean master curves were used to quantify (on average for each specimen group and for average and characteristic curves) the deviation in terms of strength and strain capacity between these simplified inverse analyses and the point-by-point methods.

For average curves, the following two tensile stress–strain relationships were constructed from the raw result of each point-by-point inverse analysis:

- Sampled curve obtained in using a third-degree polynomial interpolation with an interval on the strain equal to 50 microstrain.

- Bilinear curve obtained using a linear interpolation of the postcracking part of the raw curve.

Figure 91 explains the process used to construct the different curves.

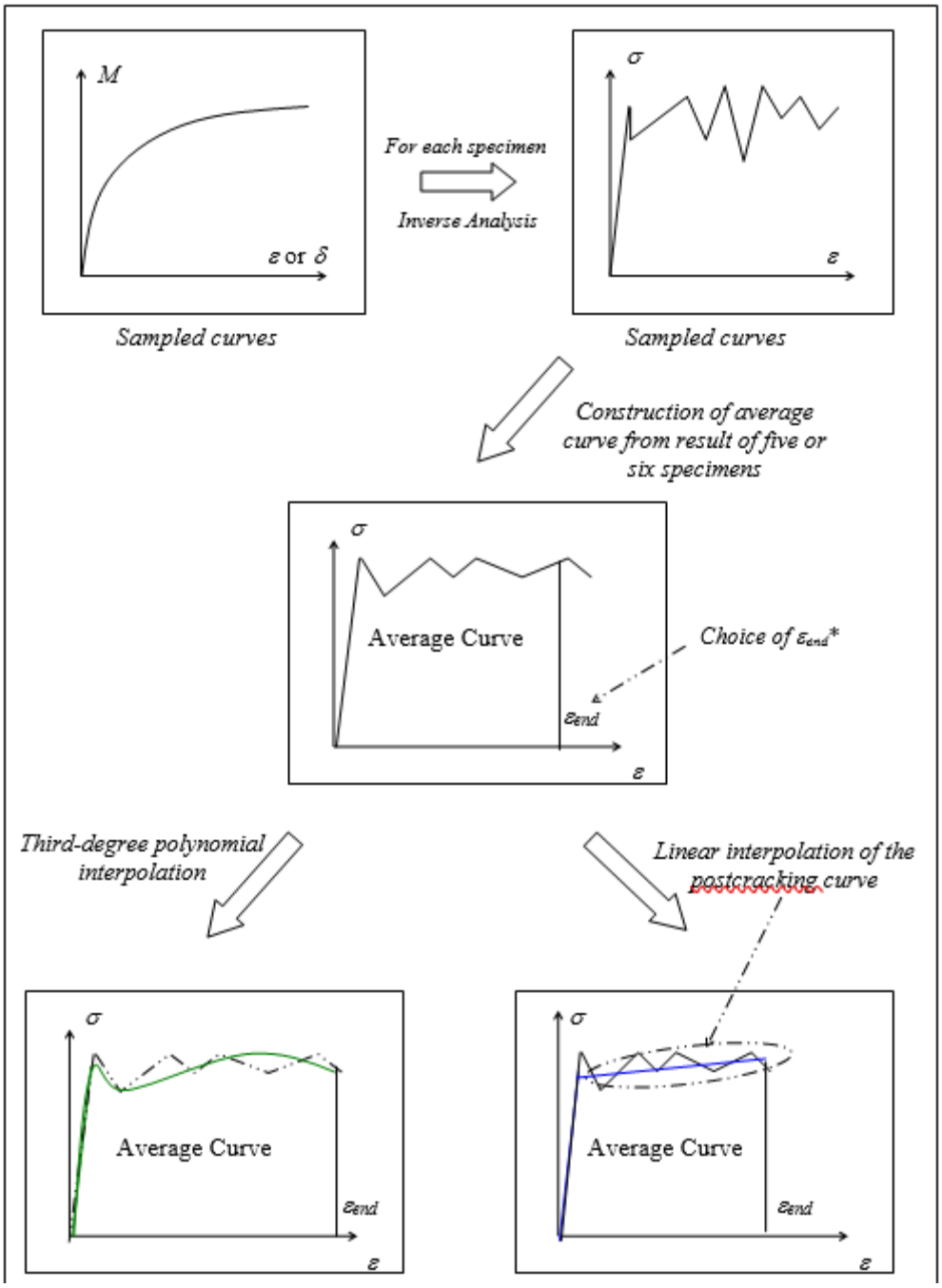

© IFSTTAR.

*Choice of ε_{end} is explained in the latter portion of this section of the report.

Figure 91. Flowchart. Constructing tensile stress–strain relationship average curves.

The strain limit (ε_{end}) for the tensile stress–strain relationship is the minimum of the strain limit associated with the average hardening strain (ε_{end1}) and the strain limit associated with an irreversible decrease of the stress–strain relationship (ε_{end2}), respectively.

For each batch, the strain limit associated with the average hardening strain can be calculated according to equation 68.

$$\varepsilon_{end1} = \frac{1}{n_{spe}} \cdot \sum_{i=1}^{n_{spe}} \varepsilon_{Specimen-i} \quad (68)$$

Before reaching the maximum equivalent bending stress, the load hardly increased, and the internal lever arm continued to be longer. As a consequence, the stress at the bottom flange had already begun to decrease. The crack localization occurred before reaching the maximum bending stress.

In some cases, the difference between ε_{end1} and ε_{end2} was not negligible. It has to be noted that the process of applying the inverse analysis methods to the average bending-moment strain or bending-moment midspan deflection curves had similar results to the process described in the point-by-point analyses (in taking into account the same ε_{end}). This observation is only available for average curves.

Concerning the bilinear relationship, the scheme detailed in figure 92 explains the method used to construct this curve.

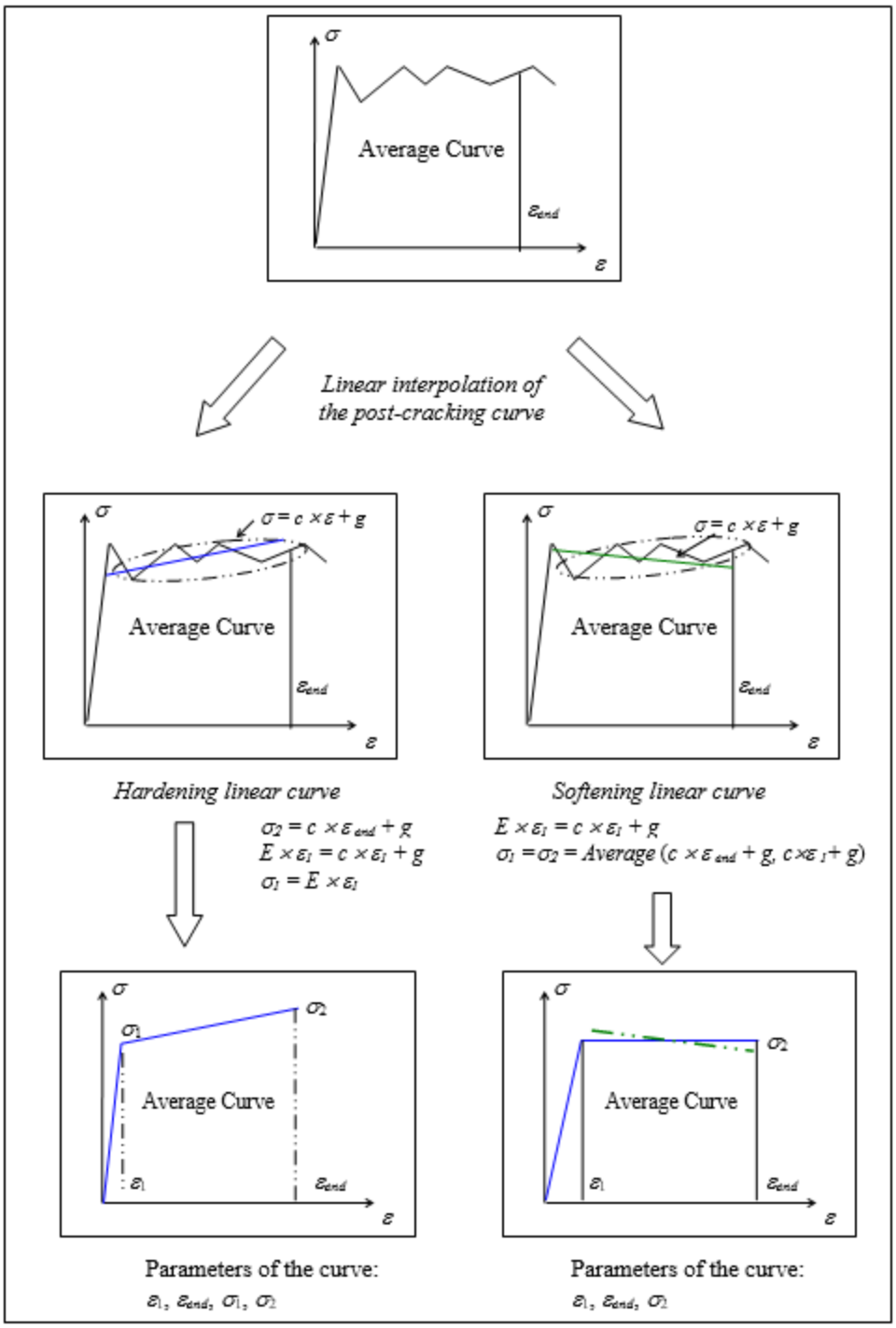

Figure 92. Flowchart. Constructing bilinear tensile stress–strain relationship curves.

For the average curves obtained with the simplified inverse analysis (Qian and Li and modified Qian and Li methods), the scheme shown in figure 93 explains the process used to construct these curves.[(54)]

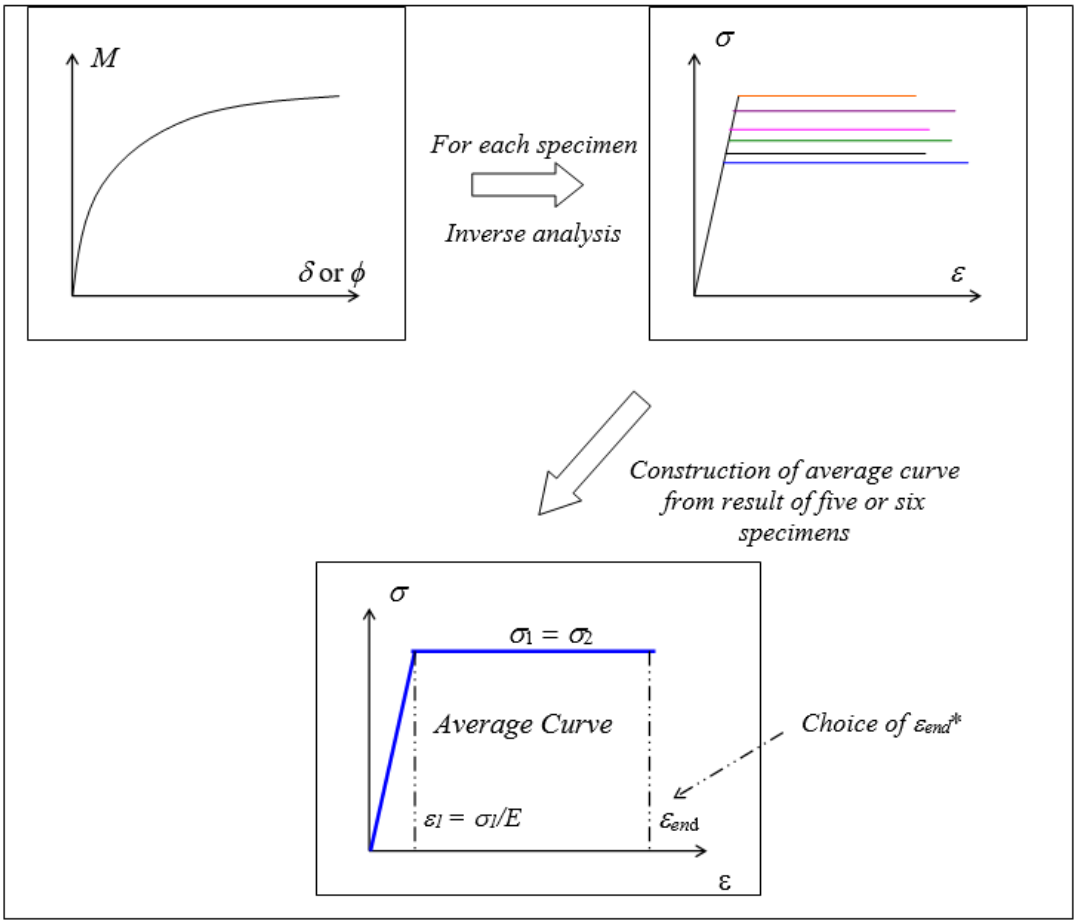

© IFSTTAR.
*Choice of ε_{end} is explained in the latter portion of this section of the report.

Figure 93. Flowchart. Constructing tensile stress–strain relationship average curves based on simplified inverse analysis of Qian and Li method.

For each batch, equation 68 can be used to calculate ε_{end}.

Concerning characteristic curves, only bilinear stress–strain relationships were constructed. The following different processes can be used to construct the characteristic curves:

- Process based on the fracture energy related to strain hardening materials.
- Process where the statistical treatment consists of determining a characteristic curve point-by-point from the average value and standard deviation of stress for each value of strain.

Fracture energy (G_f) is defined as the amount of dissipated work (W) needed to generate a unit crack with two completely separated crack surfaces. The evaluation of G_f of strain-hardening FRC unnotched specimens under direct tension is described by Wille and Naaman.[(68)] The distinction between the fracture energy dissipated during strain hardening per unit area to generate a number of cracks ($G_{f,A,n}$) and the fracture energy dissipated during softening per unit area ($G_{f,B}$) is necessary (figure 94).

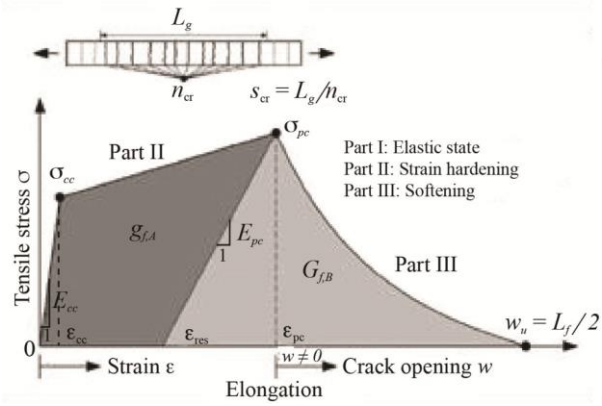

Modified from © 2010 Korea Concrete Institute.

A. Elongation.

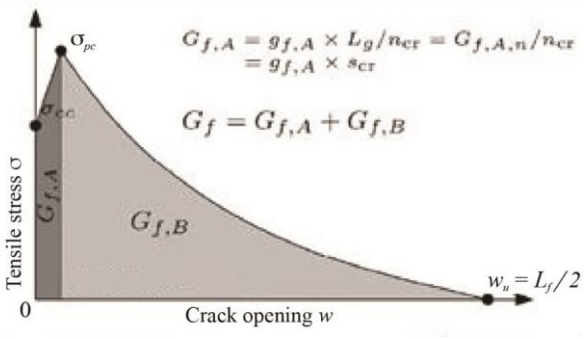

Modified from © 2010 Korea Concrete Institute.

B. Crack opening.

Figure 94. Graphs. Definition of fracture energy related to strain hardening material.[68]

Where:

L_g = gauge length.
n_{cr} = number of cracks.
s_{cr} = crack spacing.
σ_{cc} = first cracking stress.
I = moment of inertia.
E_{cc} = precracking stiffness.
ε_{cc} = first cracking strain.
$g_{f,A}$ = fracture energy dissipated during strain hardening per unit volume.
ε_{pc} = strain associated with maximum postcracking stress.
σ_{pc} = maximum postcracking stress.
E_{pc} = stiffness at peak load.
w = crack opening.
w_u = maximum crack opening.
L_f = fiber length.
w_{pc} = permanent crack opening.
$G_{f,A}$ = fracture energy dissipated during strain hardening per unit area for area A.
$G_{f,B}$ = fracture energy dissipated during strain hardening per unit area for area B.

$G_{f,A,n}$ depends on L_g used in measuring strain and represents the energy needed to generate n_{cr} cracks with a w_{pc}. The crack localization is assumed to occur at peak stress. Thus, $G_{f,B}$ represents the energy per ligament area to separate the localized crack starting from a residual crack opening of $w_{pc.}$ This latter is determined from the residual strain, which particularly depends on σ_{pc}, ε_{pc}, and stiffness at the maximum E_{pc}. Both $G_{f,A}$ and $G_{f,,\mathrm{B}}$ can be expressed using equation 69 and equation 70. Equation 71 defines w_{pc} as needed for equation 70.

$$G_{f,A} = \left[\int_0^{\varepsilon_{pc}} \sigma(\varepsilon) \cdot d\varepsilon - \frac{1}{2} \cdot \frac{\sigma_{pc}^2}{E_{pc}} \right] \times \frac{L_g}{n_{cr}} = \frac{G_{f,A,n}}{n_{cr}} \quad (69)$$

$$G_{f,B} = \int_{w_{pc}}^{w_u} \sigma(w) \cdot w \tag{70}$$

$$w_{pc} = \varepsilon_{res} \cdot s_{cr} = \left(\varepsilon_{pc} - \frac{\sigma_{pc}}{E_{pc}} \right) \times \frac{L_g}{n_{cr}} \tag{71}$$

G_f needed to generate a unit crack with two completely separated crack surfaces is solved for using equation 72.

$$G_f = G_{f,A} + G_{f,B} \tag{72}$$

$G_{f,A,n}$ can be considered to construct the characteristic curve in assuming that this energy per unit area follows the Student statistical law and in also using the characteristic fracture energy dissipated during strain hardening per unit area to generate cracks ($G^*_{f,A,n}$), which is solved for in equation 73.

$$G^*_{f,A,n} = G_{Average\text{-}f,A,n} - k(n) \times S \tag{73}$$

Where:

$G_{Average\text{-}f,A,n}$ = average fracture energy dissipated during strain hardening per unit area to generate n_{cr}.
$k(n)$ = Student coefficient depending on the number of tested specimens.
S = standard deviation.

The characteristic curve is obtained in applying an affinity (parallel to the vertical axis) to the average stress–strain relationship with a ratio equal to $G^*_{f,A,n}/G_{Average\text{-}f,A,n}$. Through this method, the hardening strain or the strain at crack localization taken into account is similar for the average and characteristic curves. As a consequence, the real ductility of the tested material could be overestimated. The other process (which has been chosen in this study) to construct the characteristic relationship consists of determining for each interval of deflection or strain the mean value of bending moment or tensile stress (with six or five specimens by batch) and the standard deviation. The characteristic curve point by point is also obtained by subtracting from the mean value the corresponding standard deviation multiplied by the Student coefficient (Student's law with 5 percent quantile) equal to 2.015 for six specimens and 2.132 for five prisms. Figure 95 details the different methods that can be used to obtain the bilinear characteristic curve.

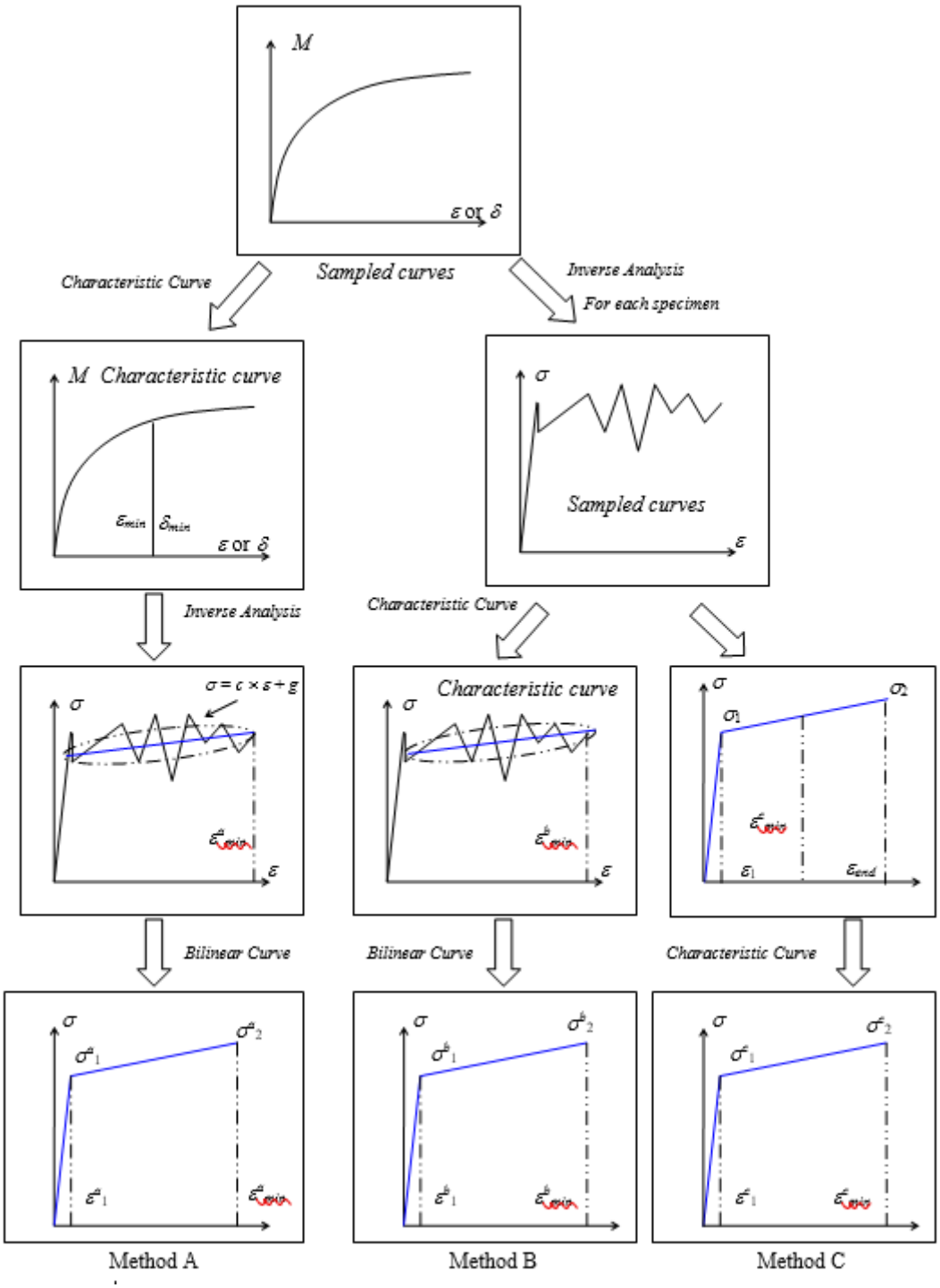

Figure 95. Flowchart. Constructing tensile stress–strain bilinear characteristic curves.

Where:

δ_{min} = minimum midspan deflection limit from the tests.
ε_{min} = minimum strain limit from the series of tests.
c = slope of the stress–strain curve.
g = stress intercept of the stress–strain curve.
ε^a_{min} = minimum strain limit associated with method A.
ε^b_{min} = minimum strain limit associated with method B.
ε^c_{min} = minimum strain limit associated with method C.
σ^a_1 = cracking stress associated with method A.
σ^a_2 = maximum stress associated with method A.
σ^b_1 = cracking stress associated with method B.
σ^b_2 = maximum stress associated with method B.
σ^c_1 = cracking stress associated with method C.
σ^c_2 = maximum stress associated with method C.
ε^a_1 = elastic strain limit associated with method A.
ε^b_1 = elastic strain limit associated with method B.
ε^c_1 = elastic strain limit associated with method C.

For each specimen, ε_{end} (method C) for the tensile stress–strain relationship is the minimum of the following strains:

- Strain at the maximum equivalent bending stress.
- Strain corresponding to an identification of the elastic unloading for specimen *i.*
- Strain corresponding to an irreversible decreasing of stress in the stress–strain curve.

The minimum strain relationship is defined in equation 74.

$$\varepsilon^b{}_{\min} = \varepsilon^c{}_{\min} = Min_{i=1}^{5or6}\left(\varepsilon_{Specimen-i}\right) \tag{74}$$

$\varepsilon_{Specimen\text{-}i}$ is the minimum of the following strains:

- Strain at the maximum equivalent bending stress.
- Strain corresponding to an identification of the elastic unloading for specimen *i.*
- Strain corresponding to an irreversible decreasing of stress in the stress–strain curve.

For each batch, ε^a_{min} (method C) is the minimum of the following strains:

- $Min_{i=1}^{5or6}\left(\varepsilon_{Specimen-i}\right)$, where $\varepsilon_{Specimen\text{-}i}$ is the minimum of the following strains:
    - Strain at the maximum equivalent bending stress.
    - Strain corresponding to an identification of the elastic unloading for specimen *i.*
- Strain corresponding to an irreversible decreasing of the stress in the stress–strain curve obtained from the inverse analysis of the characteristic bending-moment strain or deflection relationship.

It has to be noted that in all cases tested in this study, the deviation between ε^{a}_{min} and ε^{b}_{min} or ε^{c}_{min} was negligible (i.e., strain less than 0.000150).

Methods A, B, and C from figure 95 were tested for all specimen groups with the inverse analysis based on strain measurement. The comparison was realized in considering the following relative deviations shown in equation 75 and equation 76.

$$A - B = \frac{(\sigma_2^a - \sigma_2^b) + (\sigma_1^a - \sigma_1^b)}{\sigma_2^a + \sigma_1^a} \times 100 \tag{75}$$

Where $A - B$ is the relative deviation between methods A and B.

$$C - B = \frac{(\sigma_2^c - \sigma_2^b) + (\sigma_1^c - \sigma_1^b)}{\sigma_2^c + \sigma_1^c} \times 100 \tag{76}$$

Where $C - B$ is the relative deviation between methods C and B.

The deviations $A - B$ and $C - B$ were, on average, equal 21 percent with a maximum deviation of close to 40 percent. Since the assessment of the test results was discrete, with the point-by-point inverse methods using a derivative of the moment curve, their results were sensitive to a sudden variation of this curve. As a consequence, these kinds of inverse analyses induced an overestimation of the standard deviation (in term of stress for a given value of strain) for each specimen group, particularly for those with disturbed raw moment curves.

To avoid this phenomenon, method A was used, which gave similar results to method C—the average deviation between both methods was equal to 2 percent with a maximum deviation close to 7 percent. Moreover, method A, which is further described in the following paragraphs, was faster than the others.

Concerning the characteristic curves obtained with the simplified inverse analysis methods (i.e., Qian and Li and modified Qian and Li), figure 96 explains the processes that can be used to construct these curves.[54]

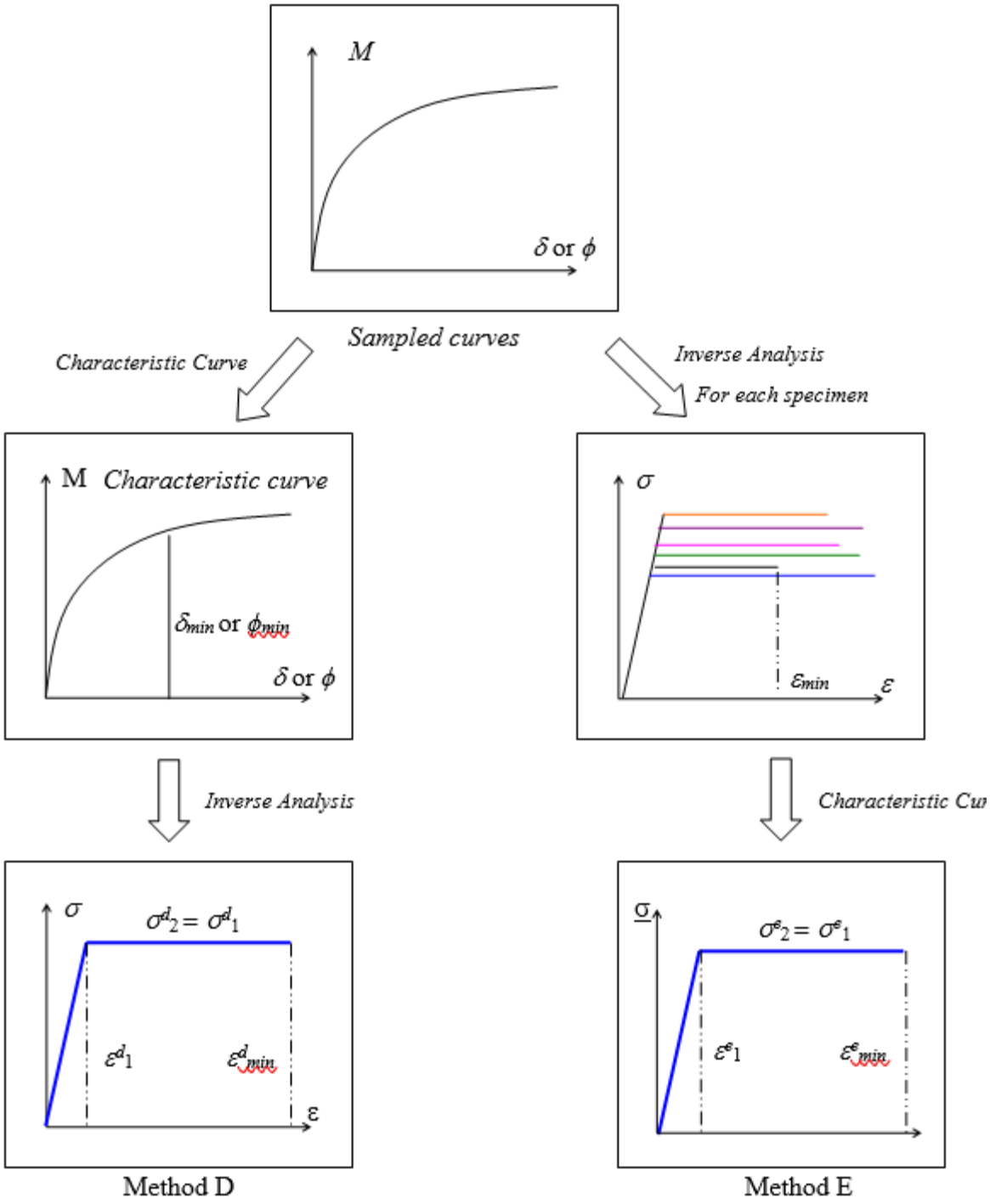

Figure 96. Flowchart. Constructing tensile stress–strain relationship characteristic curves based on Qian and Li's simplified inverse analysis.

Where:

ϕ_{min} = minimum beam curvature limit from the series of tests.
σ^d_1 = cracking stress associated with method D.
σ^d_2 = maximum stress associated with method D.
σ^e_1 = cracking stress associated with method E.
σ^e_2 = maximum stress associated with method E.
ε^d_1 = elastic strain limit associated with method D.
ε^d_{min} = minimum strain limit associated with method D.
ε^e_1 = elastic strain limit associated with method E.
ε^e_{min} = minimum strain limit associated with method E.

The minimum strain relationship is defined in equation 77.

$$\varepsilon^d{}_{\min} = \varepsilon^e{}_{\min} = Min_{i=1}^{n_{spe}} \left(\varepsilon_{Specimen-i} \right) \quad (77)$$

Methods D and E in figure 96 are respectively similar to methods A and C in figure 95. A comparison of the four methods indicated that the average deviation was equal to 2.5 percent with a maximum deviation close to 6.5 percent. A particular trend with an overestimation or underestimation of strength for one of both processes has not been identified. The following subsections describe method D to use a similar process for all inverse analysis.

Experimental Results—Comparison of Different Methods

Concerning average curves, as explained previously, two kinds of tensile stress–strain relationships were constructed (i.e., third-degree polynomial interpolation and bilinear curve) from the raw results of the following point-by-point inverse analysis test methods:

- Baby et al.'s inverse method based on midspan strain measurement at the bottom flange.[18]
- Rigaud et al.'s inverse analysis based on deflection measurement with a mechanical assumption to convert the deflection into curvature.[55]
- Baby et al.'s inverse method based on deflection measurement using a first analysis with a double integration of the curvature to obtain the bending-moment curvature relationship.[19]

For bilinear curves, results of the following simplified inverse methods are also mentioned:

- Qian and Li with the master curve strain capacity-deflection capacity constructed from a mechanical assumption to convert the deflection in curvature.[54]
- Modified Qian and Li with the master curve strain capacity-deflection capacity constructed using a double integration of the curvature.

For the bilinear curves obtained from the inverse analysis developed by Baby et al., the average strain (based on all specimens for each batch) corresponding to the minimum of both staggered LVDTs measured at crack localization ($\varepsilon_{min\text{-}crack}$) is also mentioned in addition to ε_{end}.[18]

Concerning characteristic tensile stress–strain relationships, the results of all tested methods (i.e., only bilinear curves) are plotted in figure 97 through figure 114 as well as table 33 and table 34.

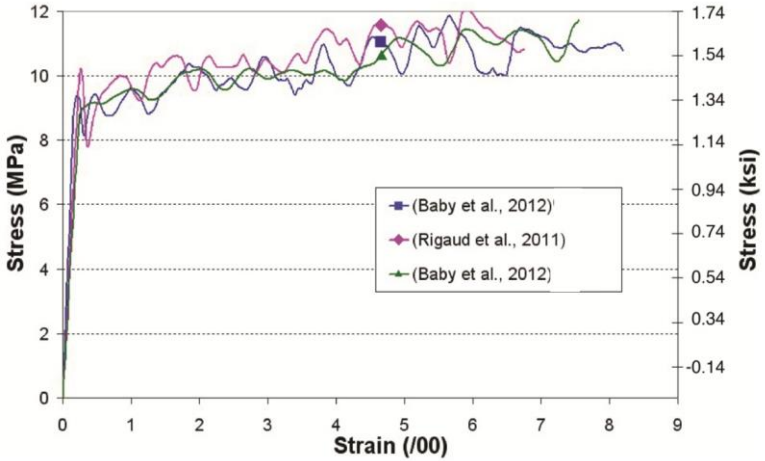

© IFSTTAR. Data from references 18, 55, and 19.

A. Third-degree polynomial interpolation.

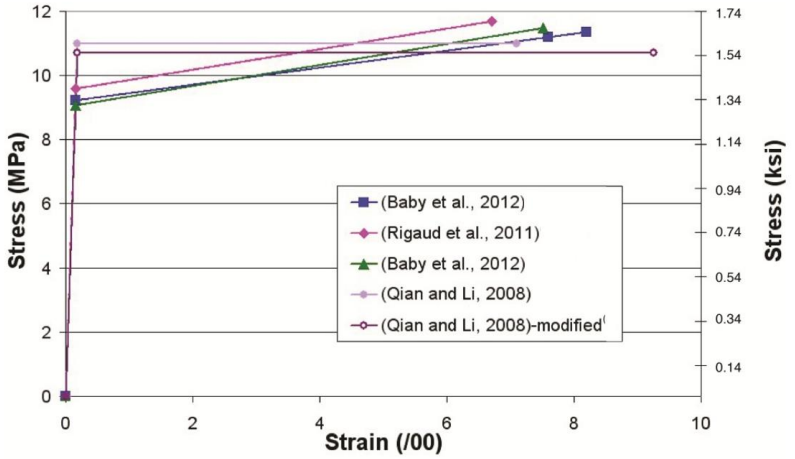

© IFSTTAR. Data from references 18, 55, 19, and 54.

B. Bilinear curve.

Figure 97. Graphs. Average tensile stress–strain relationships for batch B2A-S.

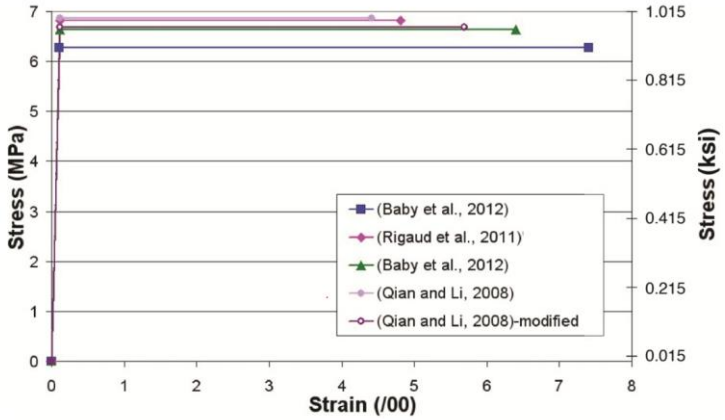

© IFSTTAR. Data from references 18, 55, 19, and 54.

Figure 98. Graph. Characteristic tensile stress–strain curves for batch B2A-S obtained from different inverse analysis methods.

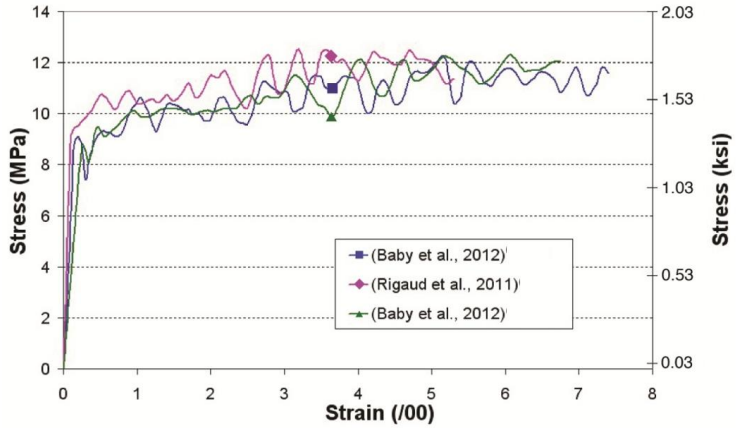

© IFSTTAR. Data from references 18, 55, and 19.

A. Third-degree polynomial interpolation.

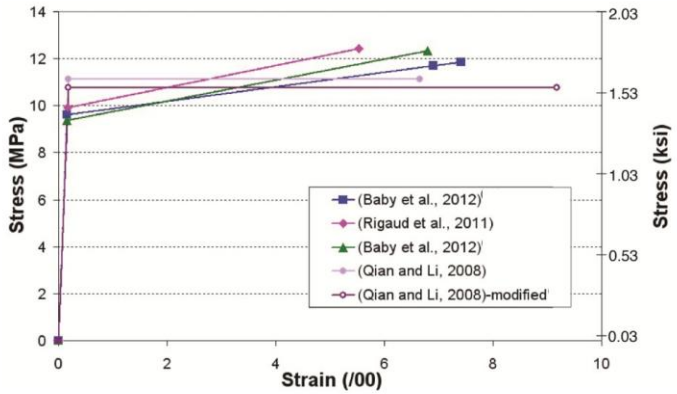

© IFSTTAR. Data from references 18, 55, 19, and 54.

B. Bilinear curve.

Figure 99. Graphs. Average tensile stress–strain relationships for batch B2A-L.

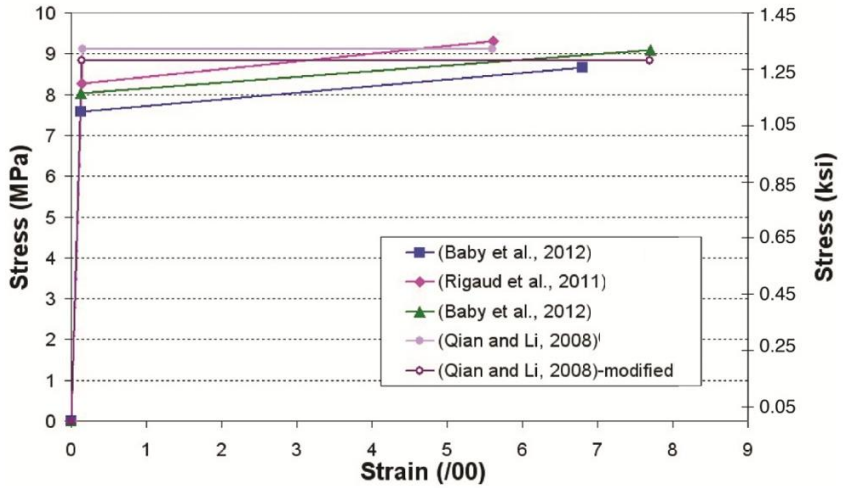

© IFSTTAR. Data from references 55, 19, and 54.

Figure 100. Graph. Characteristic tensile stress–strain curves for batch B2A-L obtained from different inverse analysis methods.

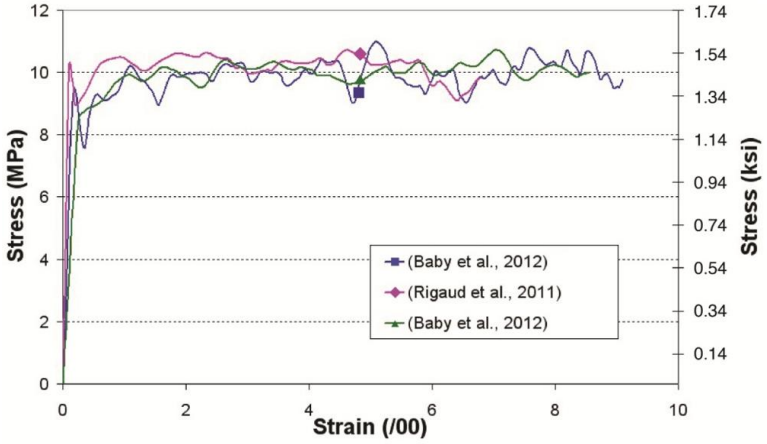

© IFSTTAR. Data from references 18, 55, and 19.

A. Third-degree polynomial interpolation.

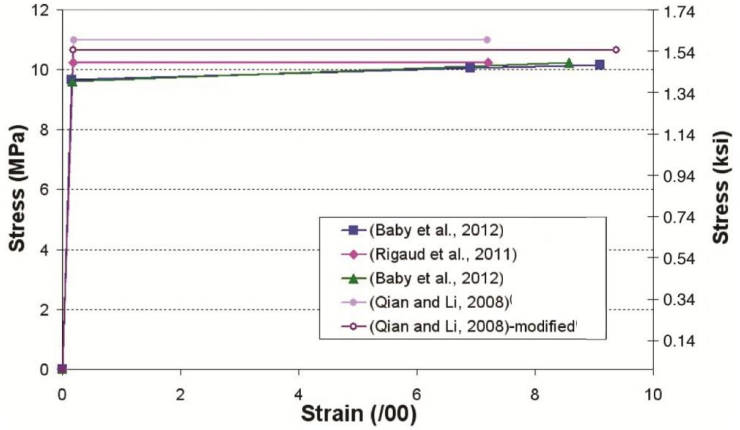

© IFSTTAR. Data from references 18, 55, 19, and 54.

B. Bilinear curve.

Figure 101. Graph. Average tensile stress–strain relationships for batch B2A-B.

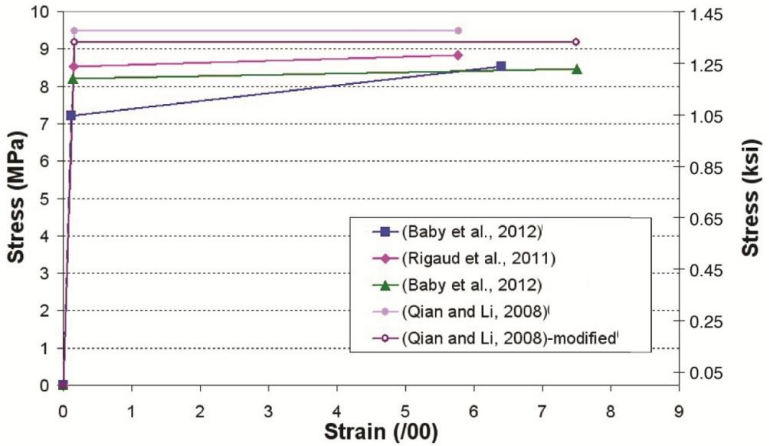

© IFSTTAR. Data from references 18, 55, 19, and 54.

Figure 102. Graph. Characteristic tensile stress–strain curves for batch B2A-B obtained from different inverse analysis methods.

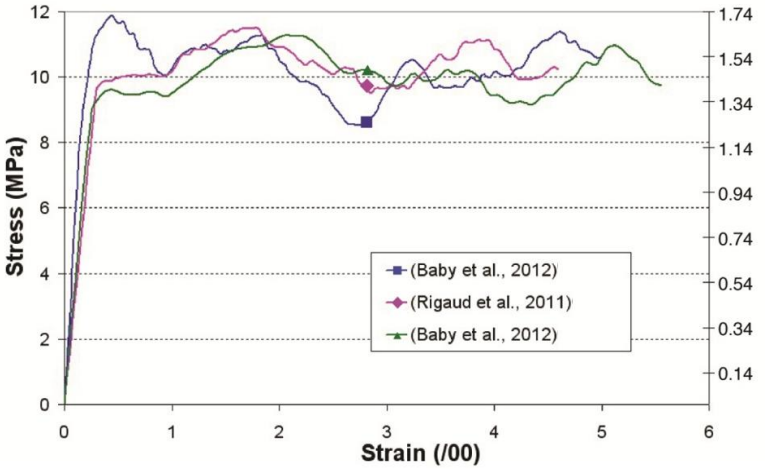

© IFSTTAR. Data from references 18, 55, and 19.

A. Third-degree polynomial interpolation.

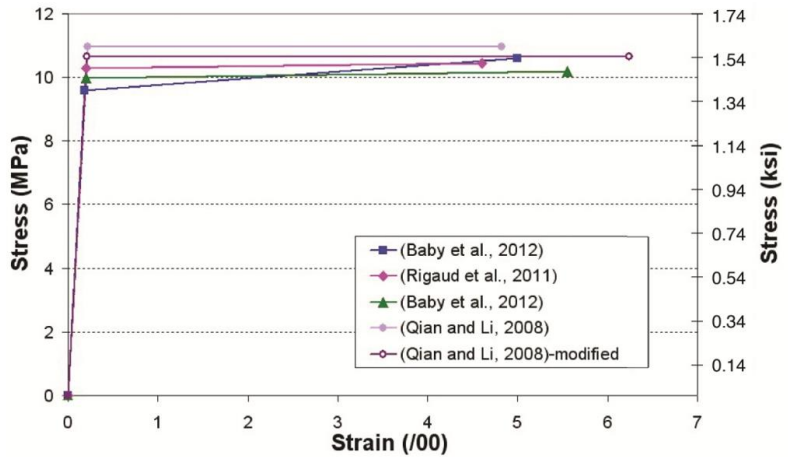

© IFSTTAR. Data from references 18, 55, 19, and 54.

B. Bilinear curve.

Figure 103. Graphs. Average tensile stress–strain relationships for batch F1A-S.

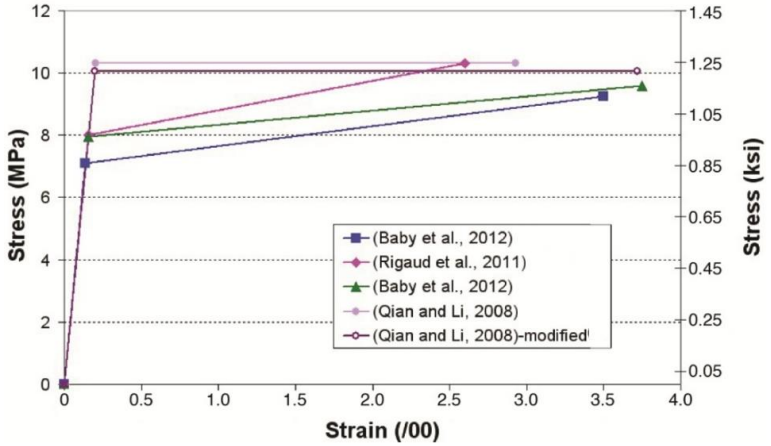

© IFSTTAR. Data from references 18, 55, 19, and 54.

Figure 104. Graph. Characteristic tensile stress–strain curves for batch F1A-S obtained from different inverse analysis methods.

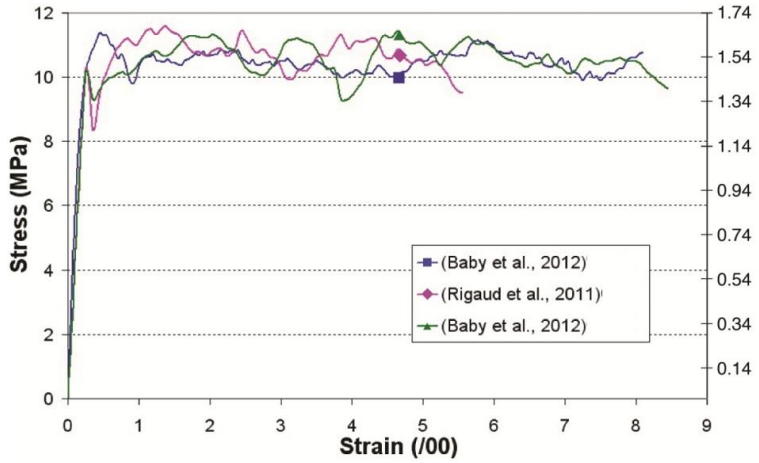

© IFSTTAR. Data from references 18, 55, and 19.

A. Third-degree polynomial interpolation.

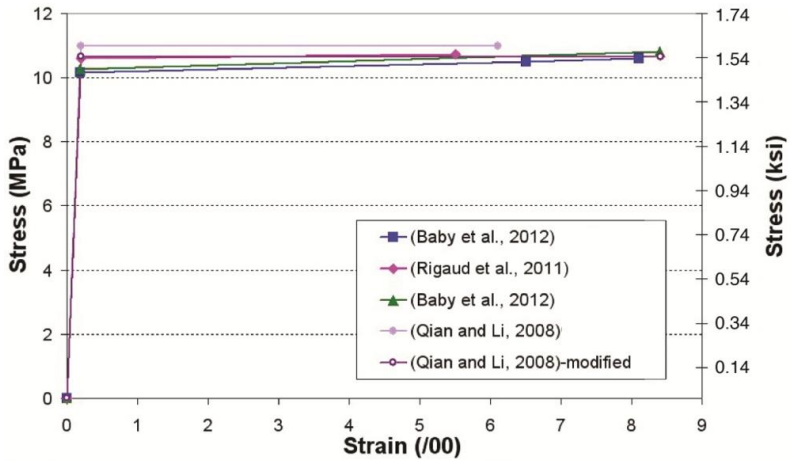

© IFSTTAR. Data from references 18, 55, 19, and 54.

B. Bilinear curve.

Figure 105. Graphs. Average tensile stress–strain relationships for batch F1A-L.

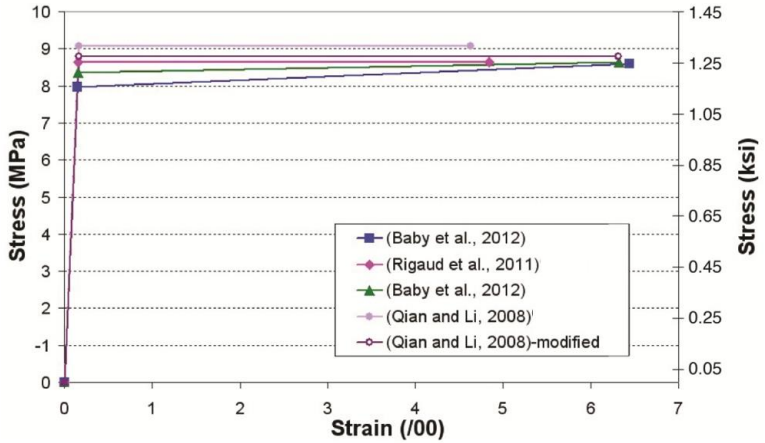

© IFSTTAR. Data from references 18, 55, 19, and 54.

Figure 106. Graph. Characteristic tensile stress–strain curves for batch F1A-L obtained from different inverse analysis methods.

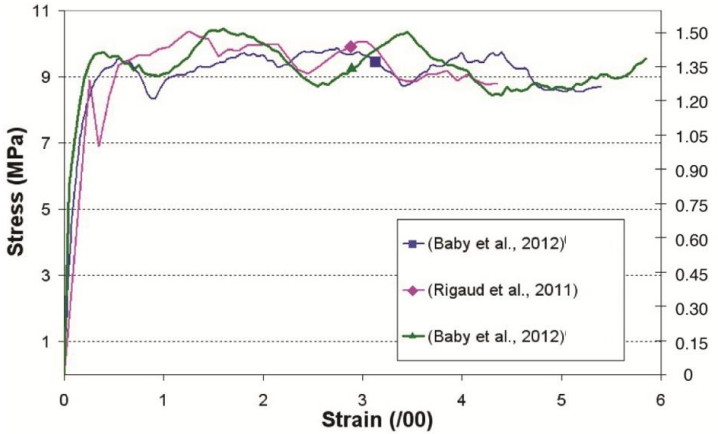

© IFSTTAR. Data from references 18, 55, and 19.

A. Third-degree polynomial interpolation.

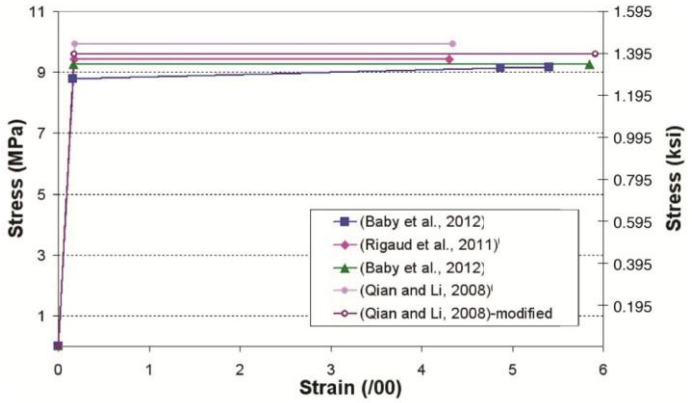

© IFSTTAR. Data from references 18, 55, 19, and 54.

B. Bilinear curve.

Figure 107. Graphs. Average tensile stress–strain relationships for batch F2A-L.

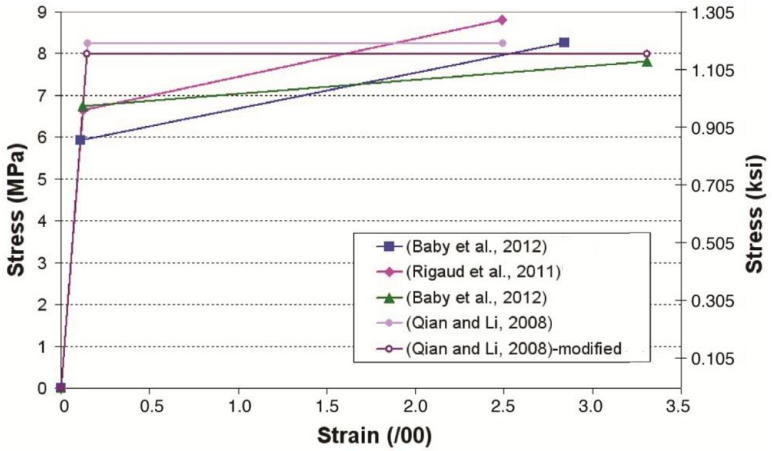

© IFSTTAR. Data from references 18, 55, 19, and 54.

Figure 108. Graph. Characteristic tensile stress–strain curves for batch F2A-L obtained from different inverse analysis methods.

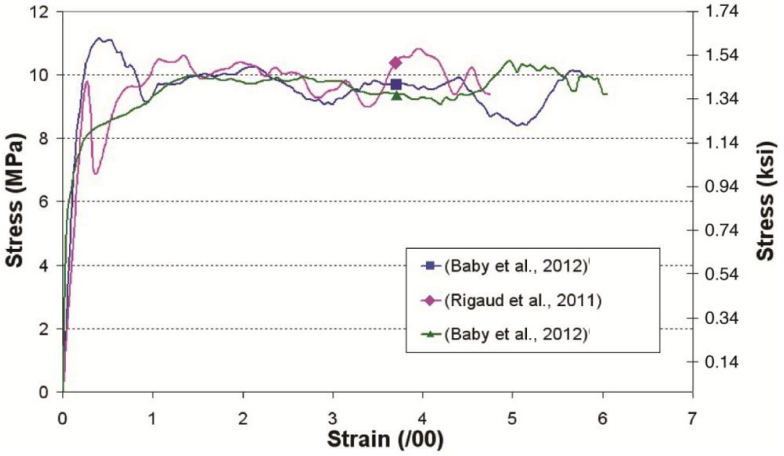

© IFSTTAR. Data from references 18, 55, and 19.

A. Third-degree polynomial interpolation.

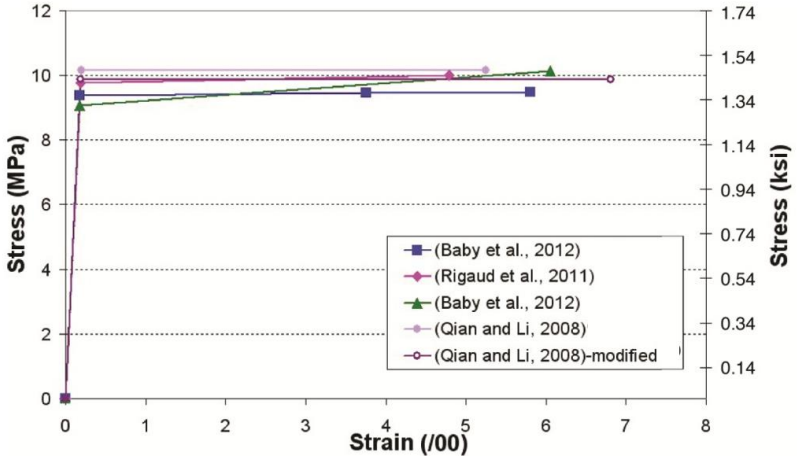

© IFSTTAR. Data from references 18, 55, 19, and 54.

B. Bilinear curve.

Figure 109. Graphs. Average tensile stress–strain relationships for batch F1B-S-Cut.

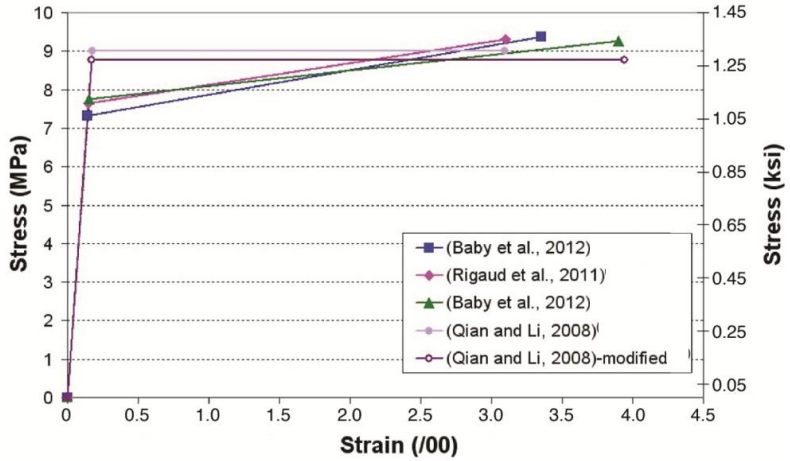

© IFSTTAR. Data from references 18, 55, 19, and 54.

Figure 110. Graph. Characteristic tensile stress–strain curves for batch F1B-S-Cut obtained from different inverse analysis methods.

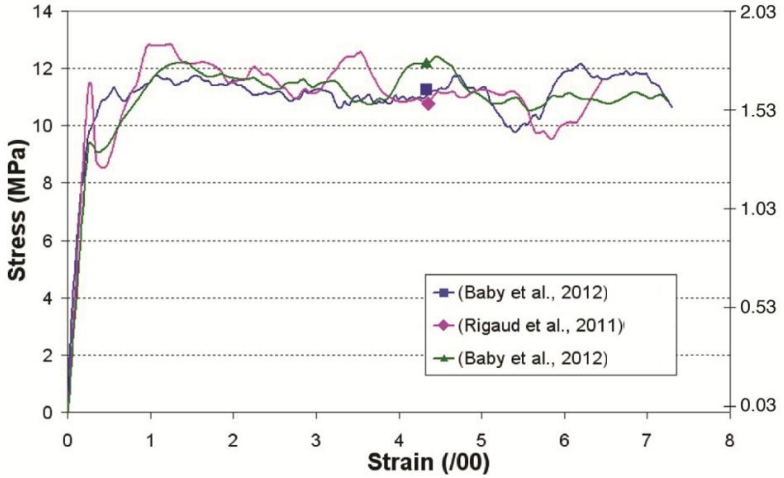

© IFSTTAR. Data from references 18, 55, and 19.

A. Third-degree polynomial interpolation.

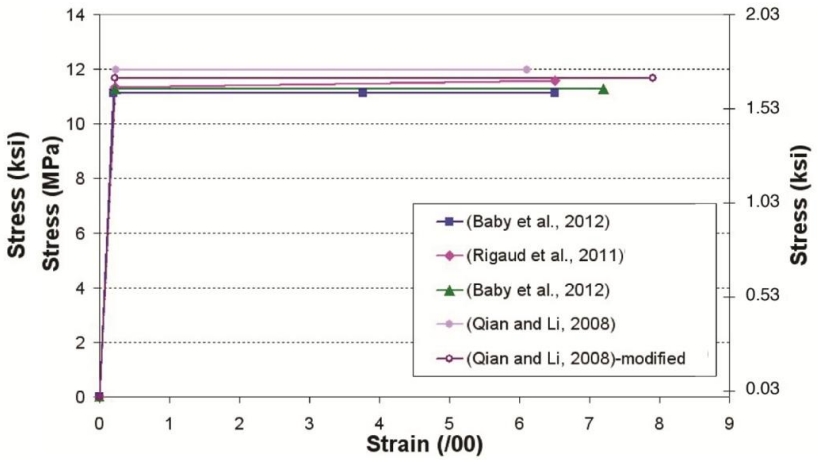

© IFSTTAR. Data from references 18, 55, 19, and 54.

B. Bilinear curve.

Figure 111. Graphs. Average tensile stress–strain relationships for batch F1C-S.

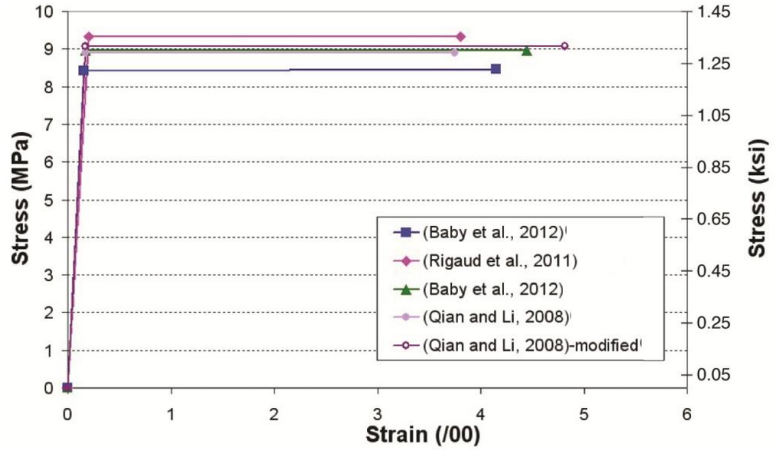

© IFSTTAR. Data from references 18, 55, 19, and 54.

Figure 112. Graph. Characteristic tensile stress–strain curves for batch F1C-S obtained from different inverse analysis methods.

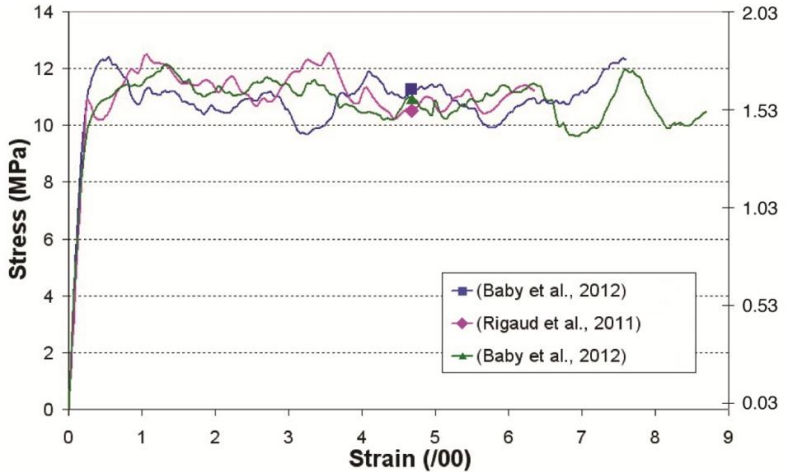

A. Third-degree polynomial interpolation.

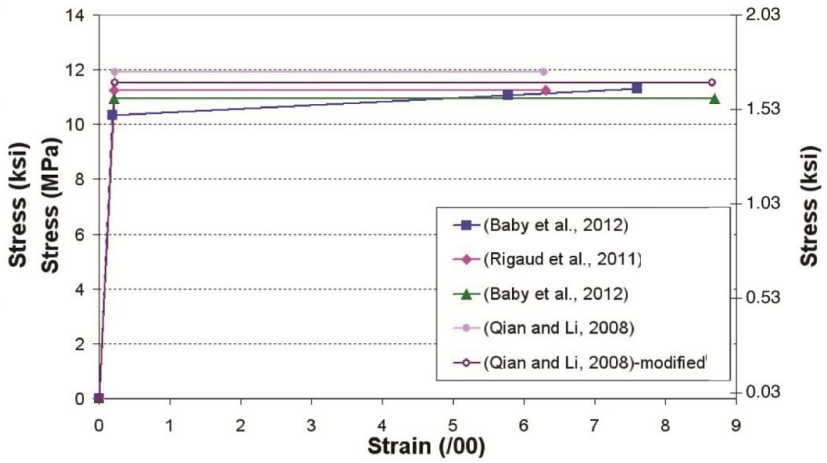

B. Bilinear curve.

Figure 113. Graphs. Average tensile stress–strain relationships for batch F1C-L.

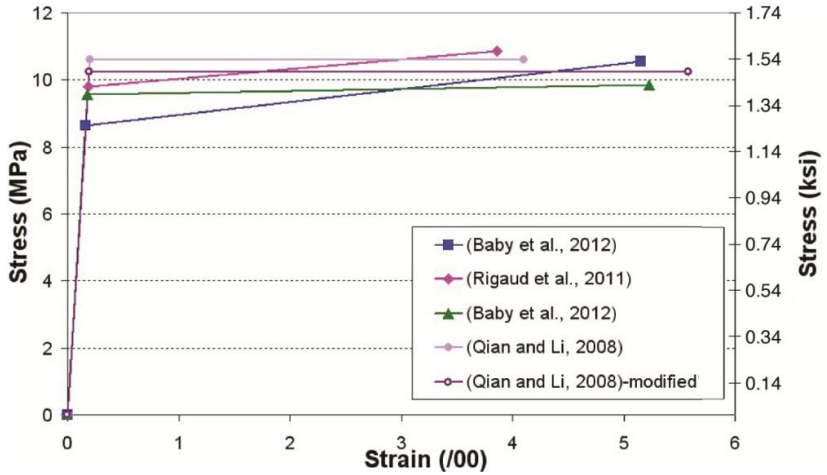

Figure 114. Graph. Characteristic tensile stress–strain curves for batch F1C-L obtained from different inverse analysis methods.

Table 33. Parameters of average bilinear curves for all batches and for each inverse analysis method.

Inverse Analysis Test Method	Variable	Specimen Batch								
		B2A-S	B2A-L	B2A-B	F1A-S	F1A-L	F1B-S-Cut	F2A-L	F1C-S	F1C-L
Baby et al.[18]	σ_1 (MPa)	9.2	9.6	9.7	9.6	10.2	9.4	8.8	11.1	10.4
Baby et al.[18]	σ_2 (MPa)	11.4	11.9	10.2	10.6	10.6	9.5	9.2	11.1	11.3
Baby et al.[18]	ε_1 (mm/m)	0.153	0.159	0.152	0.185	0.184	0.178	0.160	0.203	0.192
Baby et al.[18]	$\varepsilon_{end\text{-}ppt}$ (mm/m)	8.2	7.4	9.10	5.0	8.0	5.8	5.4	6.5	7.6
Rigaud et al.[55]	σ_1 (MPa)	9.6	9.9	10.2	10.3	10.6	9.8	9.4	11.3	11.2
Rigaud et al.[55]	σ_2 (MPa)	11.7	12.4	10.2	10.4	10.7	10.0	9.4	11.6	11.2
Rigaud et al.[55]	ε_1 (mm/m)	0.161	0.165	0.184	0.205	0.196	0.190	0.172	0.220	0.213
Rigaud et al.[55]	$\varepsilon_{end\text{-}ppt}$ (mm/m)	6.7	5.5	7.2	4.6	5.5	4.8	4.3	6.5	6.3
Baby et al.[19]	σ_1 (MPa)	9.1	9.4	9.6	10.0	10.3	9.1	9.3	11.3	10.9
Baby et al.[19]	σ_2 (MPa)	11.5	12.3	10.2	10.2	10.8	10.1	9.3	11.3	10.9
Baby et al.[19]	ε_1 (mm/m)	0.151	0.156	0.173	0.199	0.190	0.176	0.169	0.219	0.208
Baby et al.[19]	$\varepsilon_{end\text{-}ppt}$ (mm/m)	7.5	6.8	8.6	5.6	8.4	6.1	5.9	7.2	8.7
Qian and Li[54]	σ_1 (MPa)	11.0	11.1	11.0	11.0	11.0	10.1	9.9	12	11.9
Qian and Li[54]	σ_2 (MPa)	11.0	11.1	11.0	11.0	11.0	10.1	9.9	12	11.9
Qian and Li[54]	ε_1 (mm/m)	0.185	0.185	0.199	0.218	0.203	0.197	0.181	0.233	0.226
Qian and Li[54]	$\varepsilon_{end\text{-}simp}$ (mm/m)	7.1	6.6	7.2	4.8	6.1	5.3	4.3	6.1	6.3
Modified Qian and Li[54]	σ_1 (MPa)	10.7	10.8	10.6	10.7	10.6	9.9	9.6	11.7	11.5
Modified Qian and Li[54]	σ_2 (MPa)	10.7	10.8	10.6	10.7	10.6	9.9	9.6	11.7	11.5
Modified Qian and Li[54]	ε_1 (mm/m)	0.180	0.179	0.192	0.212	0.197	0.192	0.176	0.227	0.219
Modified Qian and Li[54]	$\varepsilon_{end\text{-}simp}$ (mm/m)	9.3	9.2	9.4	6.2	8.4	6.8	5.9	7.9	8.7

1 MPa = 0.145 ksi.
1 mm/m = 10^{-3}.
$\varepsilon_{end\text{-}ppt}$ = strain limit as determined by a point-by-point analysis method.
$\varepsilon_{end\text{-}simp}$ = strain limit as determined by a simplified analysis method.

Table 34. Parameters of characteristic bilinear curves for all batches and for each inverse analysis method.

Inverse Analysis Test Method	Variable	Specimen Batch								
		B2A-S	B2A-L	B2A-B	F1A-S	F1A-L	F1B-S-Cut	F2A-L	F1C-S	F1C-L
Baby et al.[18]	$\sigma^a{}_1$ (MPa)	6.3	7.6	7.2	7.1	8.0	7.3	5.9	8.4	8.7
Baby et al.[18]	$\sigma^a{}_1$ (MPa)	6.3	8.7	8.5	9.3	8.6	9.4	8.3	8.5	10.5
Baby et al.[18]	$\varepsilon^a{}_1$ (mm/m)	0.104	0.126	0.114	0.115	0.144	0.139	0.108	0.154	0.160
Baby et al.[18]	$\varepsilon^a{}_{min\text{-}ppt}$ (mm/m)	7.40	6.80	6.40	3.50	6.44	3.35	2.84	4.15	5.15
Rigaud et al.[55]	$\sigma^a{}_1$ (MPa)	6.8	8.3	8.5	8.0	8.6	7.6	6.7	9.3	9.8
Rigaud et al.[55]	$\sigma^a{}_1$ (MPa)	6.8	9.3	8.8	10.3	8.6	9.3	8.8	9.3	10.9
Rigaud et al.[55]	$\varepsilon^a{}_1$ (mm/m)	0.114	0.138	0.154	0.159	0.160	0.149	0.122	0.201	0.186
Rigaud et al.[55]	$\varepsilon^a{}_{min\text{-}ppt}$ (mm/m)	4.8	5.6	5.8	2.6	4.8	3.1	2.5	3.8	3.9
Baby et al.[19]	$\sigma^a{}_1$ (MPa)	6.6	8.0	8.2	7.9	8.4	7.8	6.7	9.0	9.6
Baby et al.[19]	$\sigma^a{}_1$ (MPa)	6.6	9.1	8.5	9.6	8.6	9.3	7.8	9.0	9.9
Baby et al.[19]	$\varepsilon^a{}_1$ (mm/m)	0.110	0.133	0.148	0.158	0.154	0.151	0.123	0.174	0.182
Baby et al.[19]	$\varepsilon^a{}_{min\text{-}ppt}$ (mm/m)	6.4	7.7	7.5	3.8	6.3	3.9	3.3	4.5	5.2
Qian and Li[54]	$\sigma^d{}_1$ (MPa)	6.9	9.1	9.5	10.3	9.1	9.0	8.2	9.3	10.5
Qian and Li[54]	$\sigma^d{}_1$ (MPa)	6.9	9.1	9.5	10.3	9.1	9.0	8.2	9.3	10.5
Qian and Li[54]	$\varepsilon^d{}_1$ (mm/m)	0.115	0.152	0.172	0.205	0.168	0.175	0.151	0.181	0.200
Qian and Li[54]	$\varepsilon^d{}_{min\text{-}simp}$ (mm/m)	4.4	5.6	5.8	2.9	4.6	3.1	2.5	3.8	3.9
Modified Qian and Li[54]	$\sigma^d{}_1$ (MPa)	6.7	8.8	9.2	10.0	8.8	8.8	8.0	9.1	10.2
Modified Qian and Li[54]	$\sigma^d{}_1$ (MPa)	6.7	8.8	9.2	10.0	8.8	8.8	8.0	9.1	10.2
Modified Qian and Li[54]	$\varepsilon^d{}_1$ (mm/m)	0.112	0.147	0.167	0.200	0.162	0.170	0.146	0.176	0.193
Modified Qian and Li[54]	$\varepsilon^d{}_{min\text{-}simp}$ (mm/m)	5.7	7.7	7.5	3.7	6.3	3.9	3.3	4.8	5.2

1 MPa = 0.145 ksi.
1 mm/m = 10^{-3}.
$\varepsilon^a{}_{min\text{-}ppt}$ = minimum strain limit associated with method A determined by a point-by-point analysis method
$\varepsilon^d{}_{min\text{-}simp}$ = minimum strain limit associated with method D determined by a simplified analysis method

The inverse analysis method proposed by Baby et al. was chosen as a reference.[18] In the inverse analysis developed by Baby et al., the spatial variation of the curvature (following the prism abscissa) was established with realistic assumptions.[19] However, in the Baby et al. method using strain measurement at the bottom flange, it is not necessary to consider the evolution of the curvature in the variable moment zone.[18] Moreover, the use of a pair of staggered LVDTs allows for the identification of the crack localization (not assumed to occur at the maximum load) and an eventual important nonhomogeneity of the multiple fine cracking in the constant moment zone. For these reasons, all the comparisons are realized in reference to the results of the Baby et al. method using strain measurement.[18]

Concerning the point-by-point inverse methods, in considering the average stress of the postcracking part of the bilinear tensile stress–strain curve ($(\sigma_1 + \sigma_2)/2$), the average overestimation of stress (for the whole of batches) induced by the mechanical assumption to convert the deflection into curvature is equal to the following in comparison with the results of Baby et al.:[18]

- A total of 4 percent with a maximum close to 6 percent for average curves.
- A total of 7.5 percent with a maximum close to 11 percent for characteristic curves.

In terms of strain, the average underestimation of strain at crack localization obtained with the inverse method based on deflection measurement with mechanical assumption is equal to the following:

- A total of 17 percent with a maximum close to 32 percent for average curves.
- A total of 18 percent with a maximum close to 35 percent for characteristic curves.

These results confirmed the conclusions described throughout the presentations of inverse analysis methods in this chapter. The underestimation of strain at crack localization induced by the mechanical assumption used by Rigaud et al. and Qian and Li is not negligible.[55,54] The overestimation of strength is relatively minor.

In applying a similar approach and in comparing the method based on strain measurement with the inverse analysis using a deflection measurement associated to a real calculation, the average deviation of stress (for all the batches) is equal to the following in comparison with the results of Baby et al.:[18]

- A total of 1.2 percent with a maximum at 2.9 percent for average relationships.
- A total of 4 percent with a maximum at 6.7 percent for characteristic relationships.

Concerning the considered strain at crack localization, the average deviation is equal to the following:

- A total of 7.7 percent with a maximum close to 12.6 percent for average curves.
- A total of 9.8 percent with a maximum close to 15.6 percent for characteristic curves.

Conversely to the inverse method with mechanical assumption, a particular trend with an overestimation or underestimation of strain at crack localization (or hardening strain) has not

been identified. Thus, it seems possible to evaluate the tensile stress–strain relationship of UHPC tested in four-point bending configuration using an inverse analysis based on the direct calculation of deflection.

Concerning the simplified inverse analysis using the Qian and Li method and the modified Qian and Li method, the average overestimation of stress (for all the batches) is equal to the following in comparison with the results of Baby et al.:[54,18]

- **Average curves**: The average overestimation of stress was 7.7 percent with a maximum close to 12 percent for Qian and Li method and 5 percent with a maximum close to 8 percent for the modified Qian and Li method.[54]

- **Characteristic curves**: The average overestimation of stress was 11.4 percent with a maximum close to 21 percent for the Qian and Li method and 8.9 percent with a maximum close to 19 percent for the modified Qian and Li method.[54]

The overestimation of strength, which is more important for both simplified inverse analyses, was due to the assumption of uniform stress distribution along the tensile height. In terms of strain, the average deviation of strain at crack localization is equal to the following:

- **Average curves**: The average deviation of strain at crack localization was 16 percent, with a maximum close to 30 percent for the Qian and Li method and 15 percent with a maximum close to 40 percent for the modified Qian and Li method.[54]

- **Characteristic curves**: The average deviation of strain at crack localization was 17 percent, with a maximum close to 41 percent for the Qian and Li method and 12 percent with a maximum close to 30 percent for the modified Qian and Li method.[54]

Concerning the Qian and Li method, a particular trend with underestimation of strain at crack localization (or pseudo-hardening strain) was identified.[54]

The point-by-point Rigaud et al. inverse method and the simplified Qian and Li method use the same mechanical assumption to convert the deflection into curvature.[55,54] Nevertheless, in the point-by-point inverse methods, the final strain ε_{end} or ε_{min} were determined in taking into account the strain corresponding to an irreversible decrease of the stress in the stress–strain curve. As a consequence, the final strain obtained with the Rigaud et al. method is often less than the final strain resulting from Qian and Li, 2008 method, particularly for the average curves.[55,54] The same argument can be applied for the Baby et al. method and modified Qian and Li method.[19] Table 35 and table 36 compile the advantages and the disadvantages of the different inverse analysis methods investigated in this study.

Table 35. Synthesis of tested inverse analysis using the point-by-point methods.

Inverse Analysis Method	Advantages	Disadvantages
Baby et al.[18]	• Uses point-by-point stress–strain relationship. • Is able to detect an eventual decrease of tensile stress before reaching maximum load.	• Post-treatment iteration required for each moment-deflection (M-δ) point.
Rigaud et al.[55]	• Uses point-by-point stress–strain relationship. • Is able to detect an eventual decrease of tensile stress before reaching maximum load.	• Post-treatment iteration required for each M-δ point. • Strength overestimation. • Real strain capacity underestimation.
Baby et al.[19]	• Uses point-by-point stress–strain relationship. • Is able to detect an eventual decrease of tensile stress before reaching maximum load.	• Two inverse analysis methods. • Post-treatment iteration required for each M-δ point.

Table 36. Synthesis of tested inverse analysis using point-by-point simplified methods.

Inverse Analysis Method	Advantages	Disadvantages
Qian and Li[54]	• Simplicity of post-treatment (no iteration and no calculation). • Eventual simplicity of experimental procedure (midspan deflection measurement not necessary; load displacement can be enough).	• Master curves necessary for each specimen size and for each bending configuration. • Strength overestimation. • Real strain capacity underestimation when crack localization occurs at maximum load. • Unable to detect an eventual decrease of tensile stress before reaching maximum load.
Modified Qian and Li[54]	• Simplicity of post-treatment (no iteration and no calculation). • Eventual simplicity of experimental procedure (midspan deflection measurement not necessary; load displacement can be enough). • Real strain capacity estimation when crack localization occurs at maximum load.	• Master curves necessary for each specimen size and for each bending configuration. • Strength overestimation. • Unable to detect an eventual decrease of tensile stress before reaching maximum load.

CHAPTER 6. SPLITTING CYLINDER TEST (SCT)

INTRODUCTION

SCT was engaged as a third method for assessing the tensile mechanical properties of UHPC. This chapter describes the test method and presents the test results.

TEST METHOD

SCT is a commonly applied test method for indirectly assessing the tensile cracking strength of concrete. It relies on the unique mechanical property set of concrete, with compressive strength generally in the vicinity of an order of magnitude higher than the tensile strength. In the test, two compressive line loads are applied along opposing sides of a concrete core or cylinder. The compressive force generates a lateral expansion of the cylinder. The elastic lateral expansive stresses are nearly uniform along the loaded plane, allowing for an estimation of the tensile cracking strength of the concrete.

ASTM C496 was modified for use in this test program.[21] This standardized test method is generally applicable for conventional concretes but is not necessarily applicable for FRCs. In the standard test method, the tensile cracking strength is calculated based on the peak applied load and the geometry of the test specimen. However, the postcracking tensile strength of FRC combined with the biaxial state-of-stress generated in this test method present the possibility that the peak stress carried by the specimen may not coincide with the cessation of elastic behaviors. As such, the test method must be supplemented to facilitate the capture of the load at first cracking of the specimen.

Two specific modifications to the standard test method were implemented. First, the lateral expansion of the cylinder perpendicular to the loaded plane was electronically measured and captured throughout the entire test. The measurement allowed for an assessment of the cessation of elastic behavior and thus an indication of first cracking. The second modification was an increase in the load rate from 1.0 to 3.5 MPa/minute (150 to 500 psi/minute) splitting tensile stress. This modification allows for reasonable test duration. This modified test procedure is discussed more fully in “Practical Means for Determination of the Tensile Behavior of Ultra-High Performance Concrete.”[23]

Figure 115 shows the types of results captured during the completion of this test method. Although first cracking of the specimen may or may not be apparent through visual or audible indications, the electronically captured data clearly indicate a discontinuity in the lateral expansion consistent with the cessation of elastic behaviors.

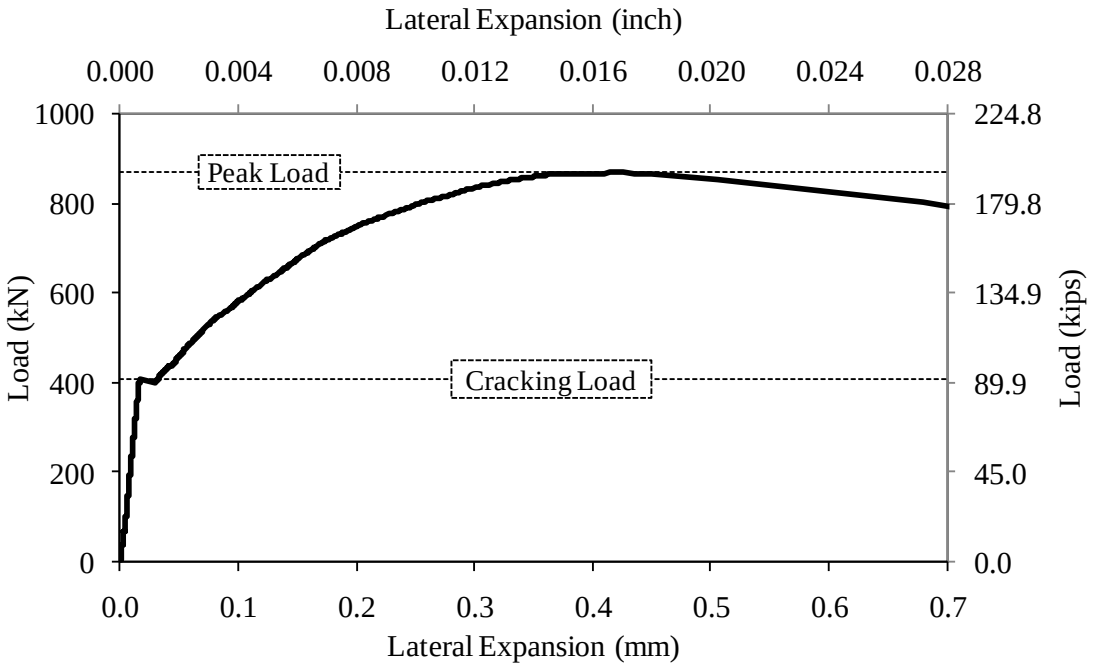

Source: FHWA.

Figure 115. Graph. Sample load versus lateral expansion result from a SCT completed on a UHPC cylinder.

TEST RESULTS

Three cylinders were cast for each of the five UHPC batches included in this study. The cylinders cast for the UHPC-F batches were 102 mm (4 inches) in diameter, while the cylinders cast for the UHPC-B batch were 110 mm (4.33 inches) in diameter. In all cases, the ends of the cylinders were ground plane prior to testing. The length-to-diameter ratio of each cylinder was approximately 1.9.

The test results for the cylinders are presented in table 37. The full results for each specimen are were compiled but were not able to be included in the report due to administrative restrictions. The tests were completed approximately 4 months after casting, which was similar to the test completion timeframe for the other tests discussed in this report.

Table 37. SCT results.

Batch Name	Test Number	Density, kg/m^3 (lb/ft^3)	Cracking Strength, MPa (ksi)	Peak Strength, MPa (ksi)
B2A	1	2681 (167.4)	8.40 (1.22)	29.4 (4.26)
B2A	2	2706 (168.9)	7.19 (1.04)	26.8 (3.88)
B2A	3	2688 (167.8)	6.81 (0.99)	25.2 (3.66)
F1A	1	2558 (159.7)	9.00 (1.31)	25.5 (3.70)
F1A	2	2573 (160.6)	10.07 (1.46)	22.2 (3.22)
F1A	3	2565 (160.1)	—	—
F1B	1	2569 (160.4)	9.47 (1.37)	25.4 (3.69)
F1B	2	2558 (159.7)	9.35 (1.36)	21.2 (3.08)
F1B	3	2552 (159.3)	10.61 (1.54)	20.1 (2.91)
F1C	1	2576 (160.8)	10.94 (1.59)	22.8 (3.30)
F1C	2	2581 (161.1)	9.96 (1.45)	24.4 (3.54)
F1C	3	2558 (159.7)	12.62 (1.83)	24.9 (3.61)
F2A	1	2529 (157.9)	4.99 (0.72)	20.8 (3.01)
F2A	2	2523 (157.5)	5.88 (0.85)	21.0 (3.04)
F2A	3	2531 (158.0)	4.10 (0.60)	20.8 (3.02)

—The test was not completed properly and thus data were not available.

The density results were consistent within each batch of specimens. The average density of the B2A batch specimens was 2,692 kg/m^3 (168.0 lb/ft^3). The average densities of steam treated UHPC-F batches F1A, F1B, and F1C were 2,565, 2,560, and 2,571 kg/m^3 (160.1, 159.8, and 160.5 lb/ft^3), respectively. The average density of the untreated UHPC-F batch specimens was 2,528 kg/m^3 (157.8 lb/ft^3).

The average cracking strength for the B2A batch was 7.5 MPa (1.08 ksi) with a standard deviation of 0.83 MPa (0.12 ksi). The average cracking strength for batch F1A was 9.5 MPa (1.38 ksi) with a standard deviation of 0.76 MPa (0.11 ksi). The average cracking strength for batch F1B was 9.8 MPa (1.42 ksi) with a standard deviation of 0.70 MPa (0.10 ksi). The average cracking strength for batch F1C was 11.2 MPa (1.62 ksi) with a standard deviation of 1.35 MPa (0.20 ksi). The average cracking strength for batch F2A was 5.0 MPa (0.72 ksi) with a standard deviation of 0.89 MPa (0.13 ksi).

The average peak strength for the B2A batch was 27.1 MPa (3.93 ksi) with a standard deviation of 2.1 MPa (0.30 ksi). The average peak strength for batch F1A was 23.9 MPa (3.46 ksi) with a standard deviation of 2.3 MPa (0.34 ksi). The average peak strength for batch F1B was 22.2 MPa (3.23 ksi) with a standard deviation of 2.8 MPa (0.41 ksi). The average peak strength for batch F1C was 24.0 MPa (3.48 ksi) with a standard deviation of 1.1 MPa (0.16 ksi). The average peak strength for batch F2A was 20.8 MPa (3.02 ksi) with a standard deviation of 0.1 MPa (0.02 ksi).

CHAPTER 7. DISCUSSION OF RESULTS

INTRODUCTION

This chapter compiles, compares, and discusses the results presented in earlier chapters of this report. The typical response observed during the UHPC DTTs is discussed first. This is followed by a detailed analysis of the direct tension results including the development of characteristic stress–strain responses. Comparisons between direct tension, flexural tension, and split cylinder tension results are then presented.

TYPICAL UNIAXIAL STRESS–STRAIN RESPONSE OF UHPC

The overall results observed throughout the DTT program implemented herein indicate that the conceptual UHPC tensile mechanical response can be described as shown in figure 116. This idealized representation includes four distinct phases: (1) elastic, (2) multicracking, (3) crack straining, and (4) localized. As their names suggest, these phases refer to specific performance states that occur through the uniaxial straining of the UHPFRC. Note that this conceptual response is highly dependent on the efficiency of the fiber reinforcement and may not be observed in practice if appropriate fiber reinforcement dosage, dispersion, or orientation are not achieved.

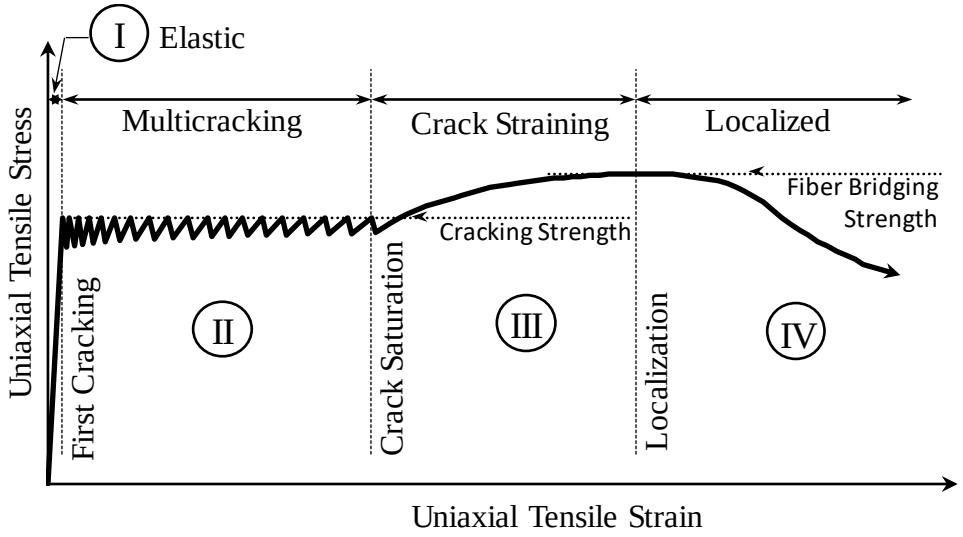

Source: FHWA.

Figure 116. Graph. Idealized tensile mechanical response of UHPC.

Phase 1, the elastic phase, refers to the global elastic straining of the composite section. This behavior continues through first cracking of the section, which occurs at the tensile strength of the cementitious composite. Phase 2, the multicracking phase, refers to the portion of the behavior wherein the cementitious matrix repeatedly cracks within the gauge length. Given that the postcracking strength of each cracked section as afforded by the steel fiber reinforcement is greater than the cementitious matrix cracking strength, the specimen accumulates elastic strain both within cracks and in the uncracked sections of the cementitious matrix between cracks but

does not experience widening of individual cracks. This phase is characterized by a nearly constant hardening stress level, which is attributed to the homogeneity of the cementitious matrix. Phase 3, the crack-straining phase, is the portion of the behavior characterized by the accumulation of strain within the existing set of cracks. At the start of this phase, the crack density, which is a function of the fiber reinforcement dispersion, orientation, geometry, and bond properties, is such that the generation of additional cracks is unlikely. The increasing strain is thus predominantly due to an increasing crack opening as opposed to further crack initiation. In this phase, a degrading increase in stress capacity is observed as the fiber reinforcement undergoes a combination of elastic straining and interface debonding. The phase ends when the fiber bridging stress is reached leading to crack localization. The fourth and final phase, localization, is characterized by a widening of an individual crack as the fibers bridging that crack fully debond and pull out of the matrix. The remainder of the specimen elastically unloads in this phase, meaning that the behaviors in this phase are based on crack-opening, not strain. The specimen stress continually decreases through this phase.

The idealized response described can be observed in the specific responses of the test specimens. As an example, figure 117 shows the response of a specimen from batch B2A. This figure affords both an expanded view of the elastic response through first cracking (figure 117-A) as well as a global view of the tensile response through 1 percent strain (figure 117-B). Note that first cracking occurred at a decreased stress level as compared to the plateau stress in the multicracking phase. This reduced stress level is attributed to minor bending strains imparted into the specimen during initial gripping in the test machine. First cracking seems to relieve the flexural component of these stresses, thus allowing for a generally consistent cementitious matrix cracking threshold through the remainder of the multicracking phase. The reduction in bending strains after first cracking was verified through comparison of individual LVDT readings to the average of the four readings from an individual test specimen. Also note that the point denoted as "crack saturation" is not necessarily the last crack since higher stresses in the subsequent phase could generate a small number of additional cracks, but instead indicates that the behavior is changing from deformation dominated by matrix cracking to deformation dominated by straining within existing cracks.

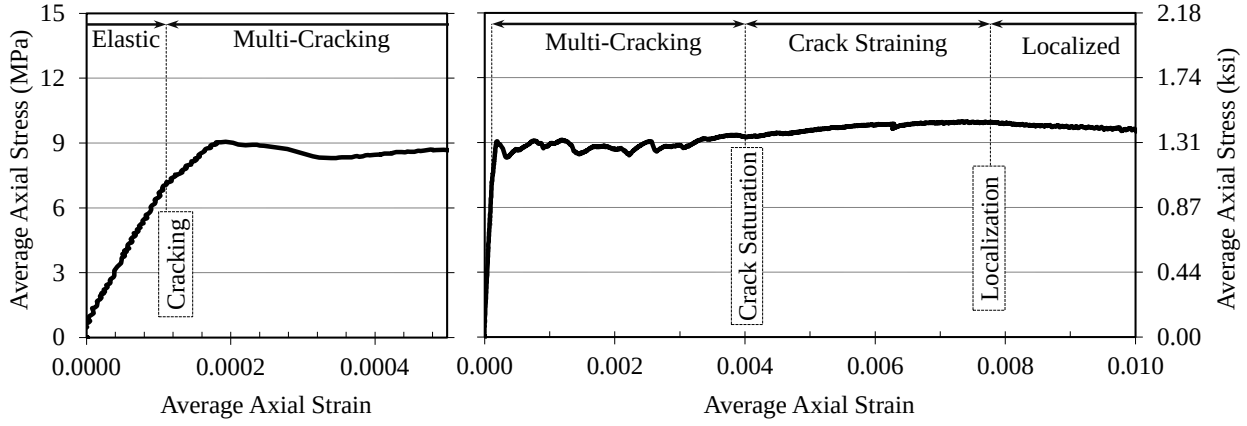

Source: FHWA.

Figure 117. Graph. Uniaxial tensile stress–strain response from a specimen in batch B2A.

ANALYSIS OF DTT RESULTS

Combining the discrete stress–strain responses from individual specimens provides a robust means of quantitatively assessing the tensile mechanical performance of a UHPC. Given the distinctly different behaviors that occur before and after cracking, this analysis was completed in two parts. First, the elastic behaviors up to first cracking were combined. Second, the postcracking behaviors were combined.

The tensile elastic behavior of UHPC was assumed to be linear elastic through first cracking. As such, combination of elastic behaviors focused on the captured modulus of elasticity results, which were previously presented in table 5. After discarding results invalidated by early cracking or high gripping strains, the average results were calculated for each set of specimens. The postcracking behavior of the seven sets of UHPC specimens was analyzed separately. First, valid tests were identified. Recall that each set of specimens included either five or six nominally identical replicates. Within this analysis, a number of test specimens within some sets were discarded. Exclusion of a test specimen may have resulted from misapplication of test procedure, proportionally large bending stresses applied during gripping, strain localization outside of gauge length, or non-strain-hardening response of specimen. Figure 118 through figure 124 provide results from these analyses with the number of valid tests for each set circled in the upper right corner. For the valid tests in each set, the average and standard deviation of stress at strain intervals of 0.000005 were calculated. This average curve is also presented in these figures. The average response was then used to calculate the postcracking portion of the design response of the particular set of UHPC specimens. The design response is based on the conceptual tensile mechanical stress–strain response of UHPC presented in figure 116. It includes a linear elastic portion emanating from the elastic phase, followed by a plastic portion emanating from the multicracking phase.

The elastic portion of the design response is based on the average modulus of elasticity obtained from valid tests. This portion of the behavior extends from the initiation of tensile straining through its intersection with the plastic portion of the behavior. The plastic portion of the behavior is defined to extend from the elastic portion through the strain at the conclusion of the crack-straining phase. The stress level is calculated as the average stress between 300 microstrain and the average strain at the conclusion of the multicracking phase. Note that 300 microstrain was arbitrarily chosen as it both exceeds the cracking strain and is early in the postcracking response. The intersection of the elastic and plastic portions of the behavior is defined as the design stress and design strain at first cracking.

Finally, the characteristic response was calculated for each set of specimens. The elastic portion of the behavior remains the same through its intersection with the plastic portion. This characteristic strain value was calculated by subtracting the standard. The plastic portion of the response is defined to extend from the elastic portion through the characteristic value of the strain at the conclusion of the crack-straining phase deviation times the t-Student coefficient from the average value at localization. The stress level for the plastic portion of the characteristic response was calculated as the characteristic value of the average stress between 300 microstrain and the minimum strain from an individual specimen in a set at the conclusion of the multicracking phase.

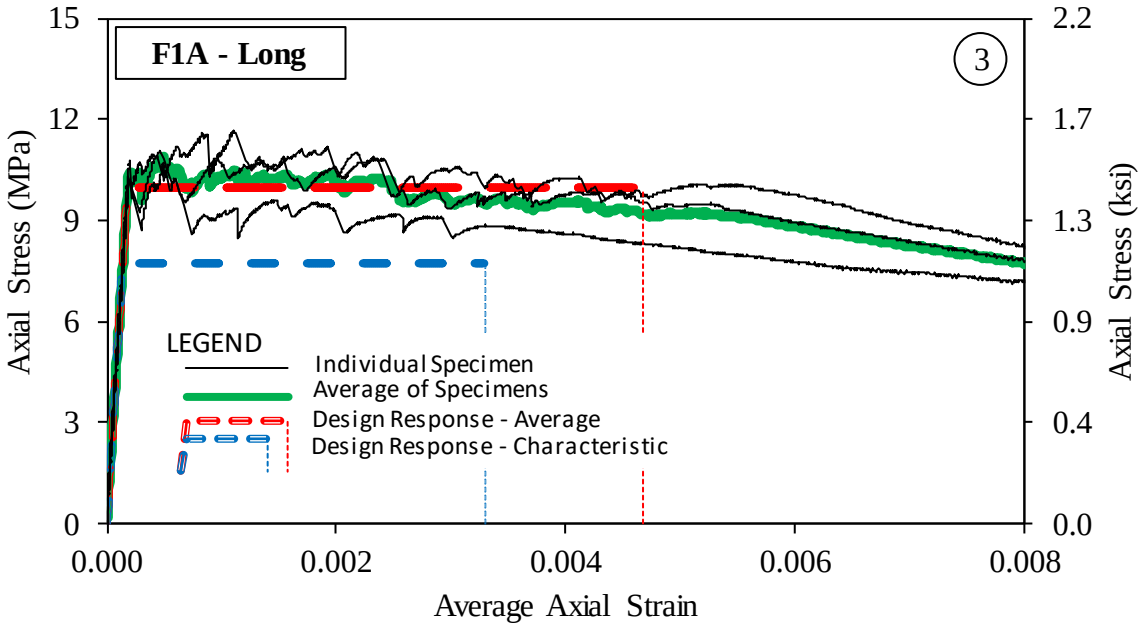

Source: FHWA.

Figure 118. Graph. DTT stress–strain results, average response, and characteristic response as obtained from specimen F1A long.

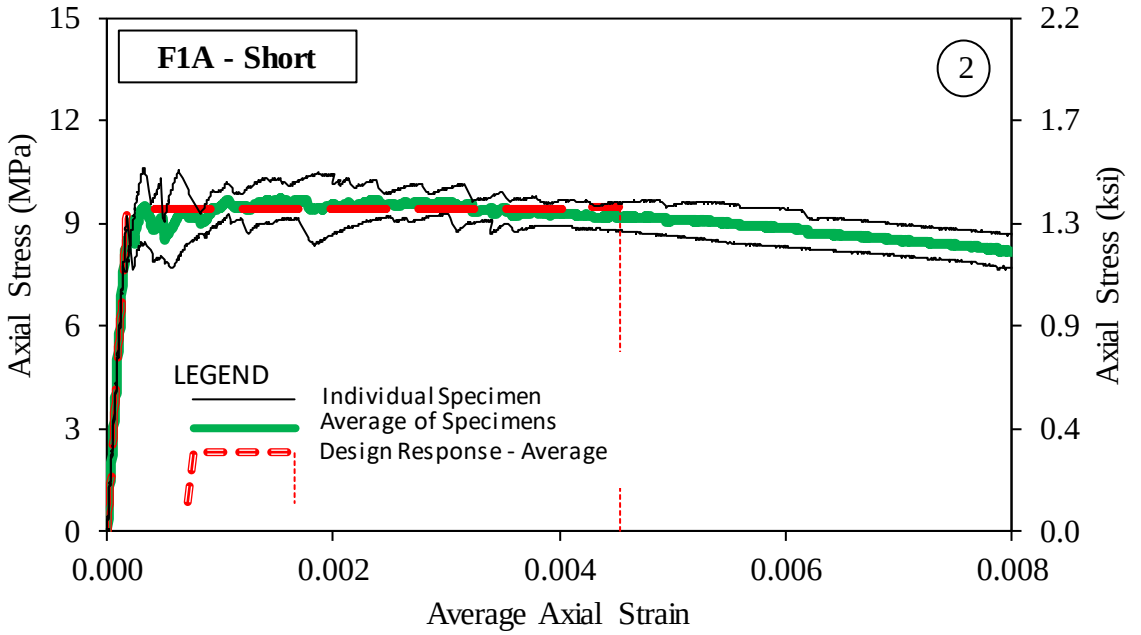

Source: FHWA.

Figure 119. Graph. DTT stress–strain results, average response, and characteristic response as obtained from specimen F1A short.

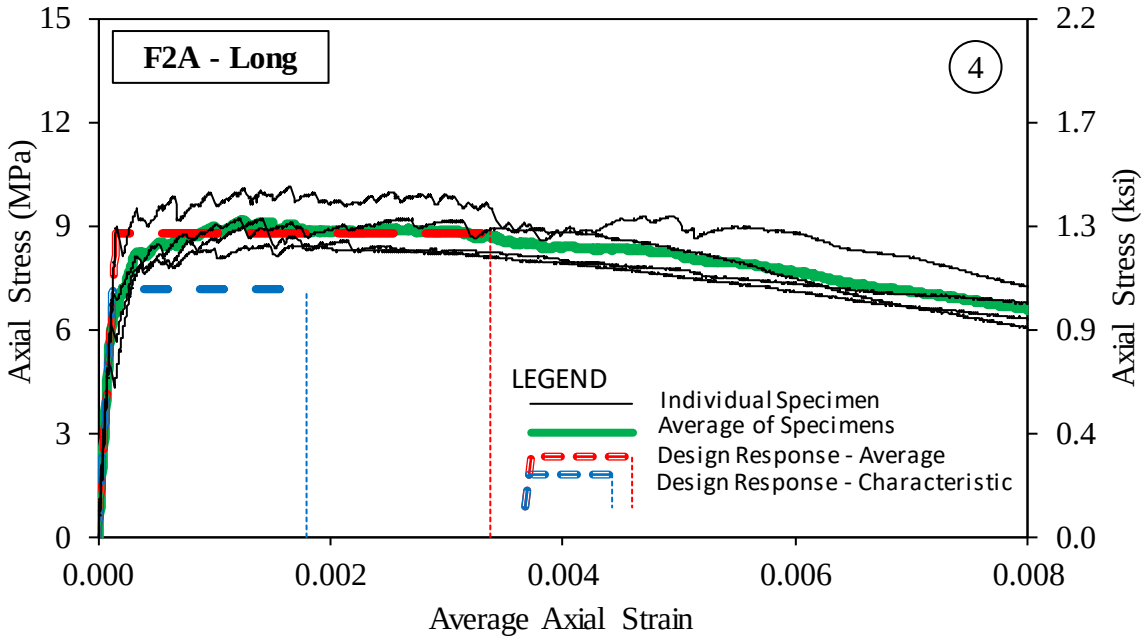

Source: FHWA.

Figure 120. Graph. DTT stress–strain results, average response, and characteristic response as obtained from specimen F2A long.

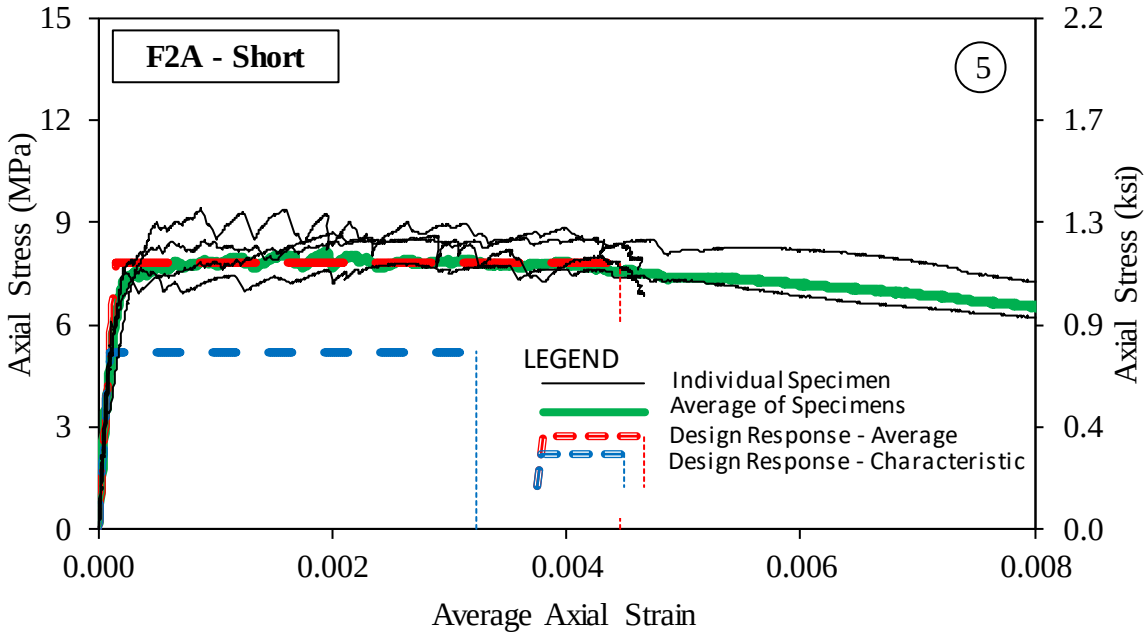

Source: FHWA.

Figure 121. Graph. DTT stress–strain results, average response, and characteristic response as obtained from specimen F2A short.

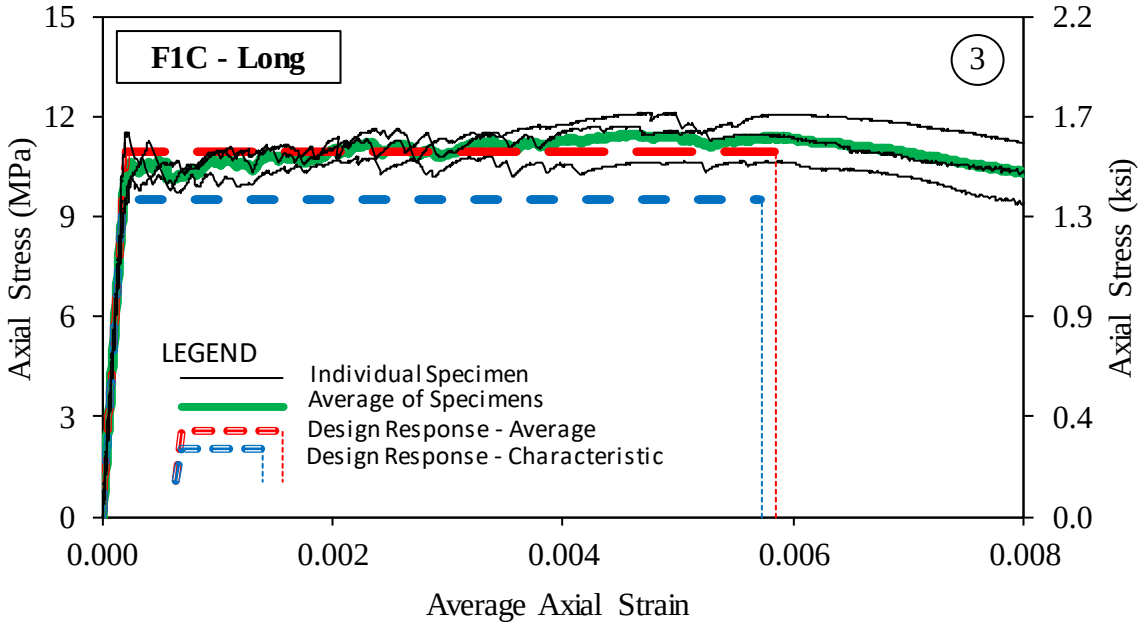

Source: FHWA.

Figure 122. Graph. DTT stress–strain results, average response, and characteristic response as obtained from specimen F1C long.

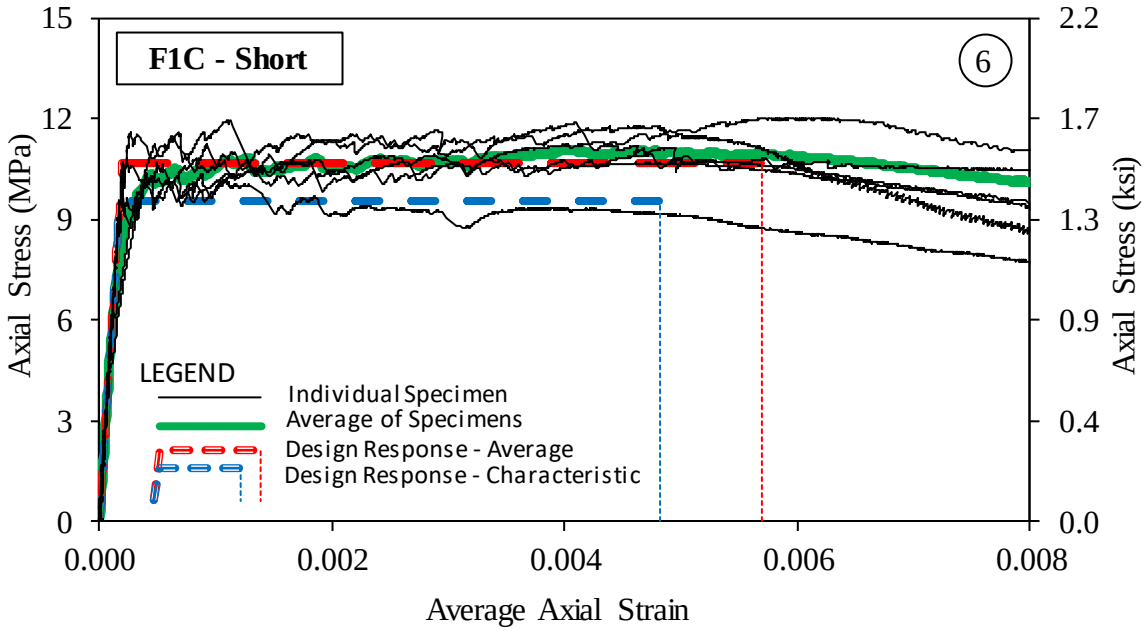

Source: FHWA.

Figure 123. Graph. DTT stress–strain results, average response, and characteristic response as obtained from specimen F1C short.

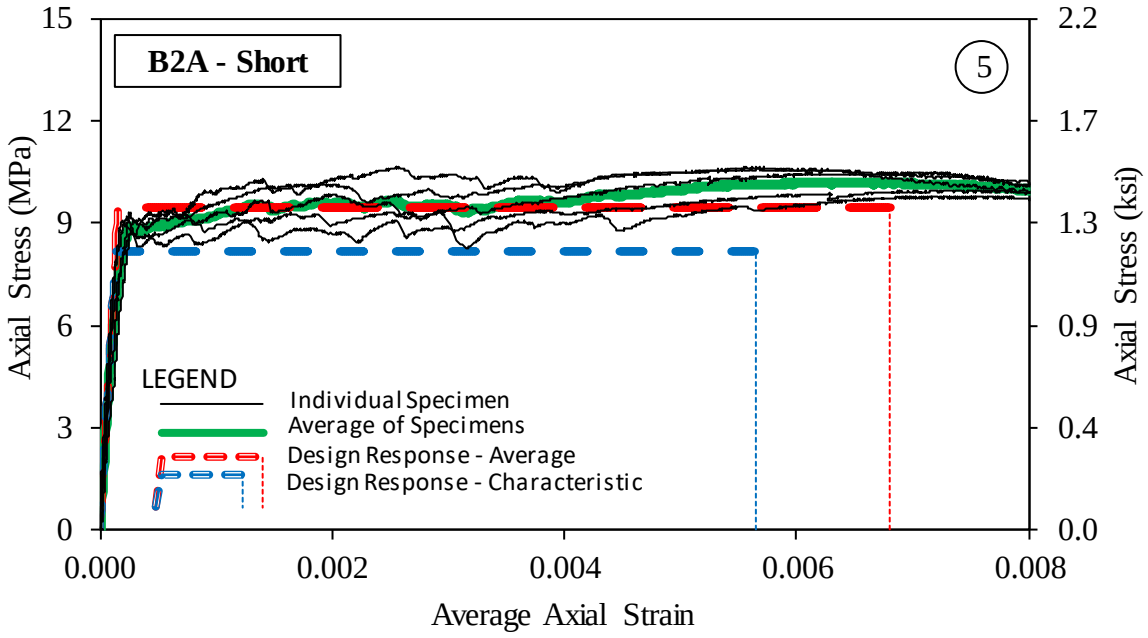

Source: FHWA.

Figure 124. Graph. DTT stress–strain results, average response, and characteristic response as obtained from specimen B2A short.

Figure 125 illustrates the average response, the average design response, and the characteristic design response of a UHPC. Note that only two acceptable test results were obtained for F1A-short (figure 119), and thus, a statistical treatment of the results is not appropriate.

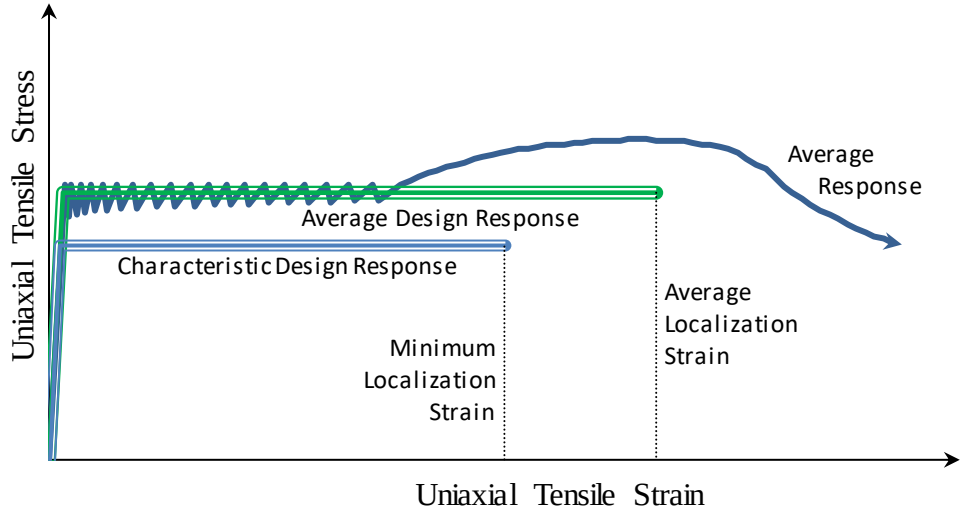

Source: FHWA.

Figure 125. Graph. Idealized tensile mechanical average response, average design response, and characteristic design response of a UHPC.

COMPARISON OF DTT AND FT RESULTS

In figure 126, the average tensile stress–strain relationships obtained from the proposed point-by-point inverse methods and the average experimental curves obtained from the DTTs are presented for each specimen group.

To compare the results derived from the proposed inverse analysis methods (i.e., Baby et al., the Rigaud et al., and the Qian and Li methods) with the DTT results, bilinear curves were constructed from the sampled tensile stress–strain responses obtained through the DTTs (refer to graphs presented from figure 118 to figure 125). (See references 18, 19, 55, and 54.) This comparison is detailed in table 38 to table 41.

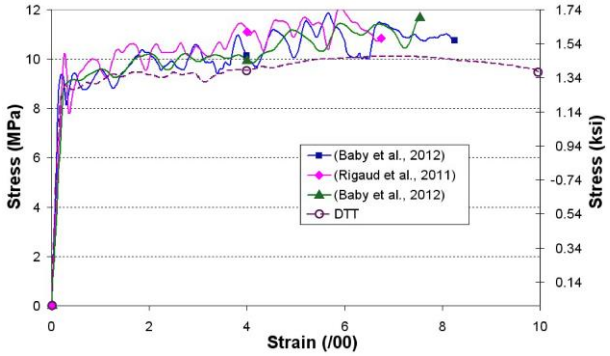

Source: FHWA. Data from references 18, 55, and 19.

A. B2A short.

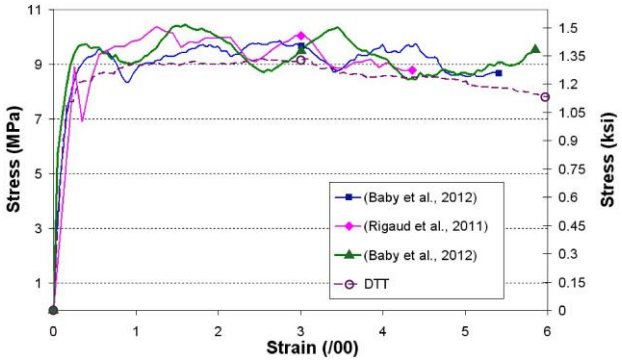

Source: FHWA. Data from references 18, 55, and 19.

B. F2A long.

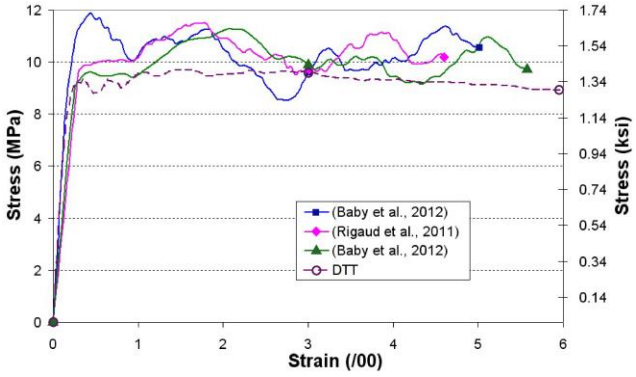

Source: FHWA. Data from references 18, 55, and 19.

C. F1A short.

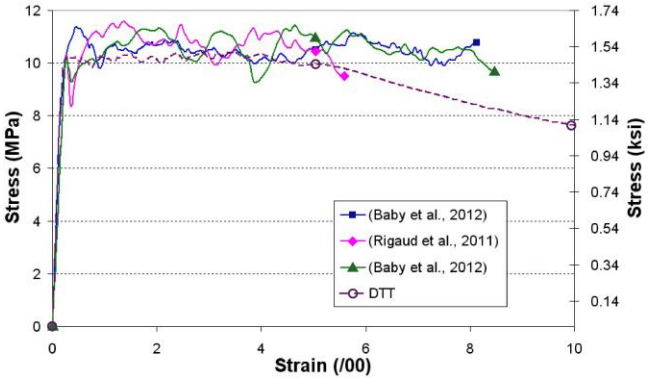

Source: FHWA. Data from references 18, 55, and 19.

D. F1A long.

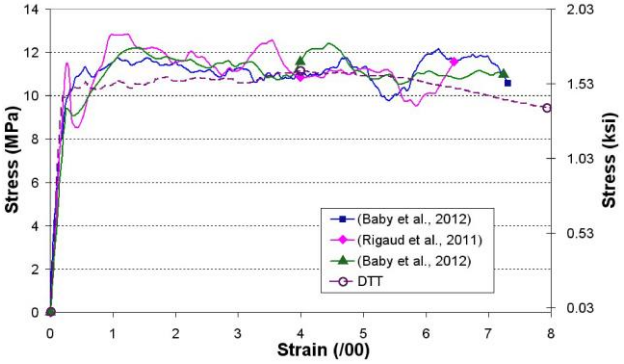

Source: FHWA. Data from references 18, 55, and 19.

E. F1C short.

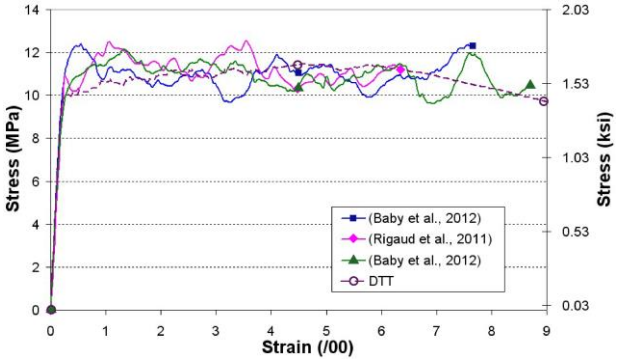

Source: FHWA. Data from references 18, 55, and 19.

F. F1C long.

Figure 126. Graphs. Average tensile stress–strain curves showing FTs associated with point-by-point inverse analysis test methods and DTTs.

Table 38. Characteristic average bilinear tensile stress–strain relationships for each specimen group derived from inverse analysis methods versus results obtained from DTTs.

Test Method	Variable	Specimen Batch					
		B2A-S	F1A-S	F1A-L	F2A-L	F1C-S	F1C-L
Baby et al.[19]	$\sigma^a{}_1$ (MPa)	9.1	10.0	10.3	9.3	11.3	10.9
Baby et al.[19]	$\sigma^a{}_2$ (MPa)	11.5	10.2	10.8	9.3	11.3	10.9
Baby et al.[19]	ε_1	0.000151	0.000199	0.000190	0.000169	0.000219	0.000208
Baby et al.[19]	$\varepsilon_{end\text{-}ppt}$	0.007500	0.005600	0.008400	0.005900	0.007200	0.008700
Baby et al.[18]	$\sigma^a{}_1$ (MPa)	9.2	9.6	10.2	8.8	11.1	10.3
Baby et al.[18]	$\sigma^a{}_2$ (MPa)	11.4	10.6	10.6	9.2	11.1	11.3
Baby et al.[18]	ε_1	0.000153	0.000185	0.000184	0.000160	0.000203	0.000192
Baby et al.[18]	$\varepsilon_{end\text{-}ppt}$	0.008200	0.005000	0.008000	0.005400	0.006500	0.007600
Rigaud et al.[55]	$\sigma^a{}_1$ (MPa)	9.6	10.3	10.6	9.4	11.3	11.2
Rigaud et al.[55]	$\sigma^a{}_2$ (MPa)	11.7	10.4	10.7	9.4	11.6	11.2
Rigaud et al.[55]	ε_1	0.000161	0.000205	0.000196	0.000172	0.000220	0.000213
Rigaud et al.[55]	$\varepsilon_{end\text{-}ppt}$	0.006700	0.004600	0.005500	0.004300	0.006500	0.006300
Qian and Li[54]	$\sigma^a{}_1$ (MPa)	11.0	11.0	11.0	9.9	12.0	11.9
Qian and Li[54]	ε_1	0.000185	0.000218	0.000203	0.000181	0.000233	0.000226
Qian and Li[54]	$\varepsilon_{end\text{-}simp}$	0.007100	0.004800	0.006100	0.004300	0.006100	0.006300
DTT	$\sigma^a{}_1$ (MPa)	9.5	9.4	10.0	8.8	10.7	11.0
DTT	ε_1	0.000144	0.000167	0.000180	0.000155	0.000185	0.000194
DTT	$\varepsilon_{end\text{-}dtt}$	0.007400	0.002500	0.004200	0.003000	0.004800	0.006000

1 MPa = 0.145 ksi.

$\varepsilon_{end\text{-}simp}$ = strain limit as determined by a simplified analysis method.

$\varepsilon_{end\text{-}dtt}$ = strain limit as determined by the DTT.

Table 39. Characteristic bilinear tensile stress–strain relationships for each specimen group derived from inverse analysis methods versus results obtained from DTTs.

Test Method	Variable	Specimen Batch					
		B2A-S	F1A-S	F1A-L	F2A-L	F1C-S	F1C-L
Baby et al.[19]	σ^c_1 (MPa)	6.6	7.9	8.4	6.7	9.0	9.6
Baby et al.[19]	σ^c_2 (MPa)	6.6	9.6	8.6	7.8	9.0	9.9
Baby et al.[19]	ε_1	0.000110	0.000158	0.000154	0.000123	0.000174	0.000182
Baby et al.[19]	$\varepsilon_{min\text{-}ppt}$	0.006400	0.003800	0.006300	0.003300	0.004500	0.005200
Baby et al.[18]	σ^c_1 (MPa)	6.3	7.1	8.0	5.9	8.4	8.6
Baby et al.[18]	σ^c_2 (MPa)	6.3	9.3	8.6	8.3	8.5	10.5
Baby et al.[18]	ε_1	0.000104	0.000115	0.000144	0.000108	0.000154	0.000160
Baby et al.[18]	$\varepsilon_{min\text{-}ppt}$	0.007400	0.003500	0.006440	0.002840	0.004150	0.005150
Rigaud et al.[55]	σ^c_1 (MPa)	6.8	8.0	8.6	6.7	9.3	9.8
Rigaud et al.[55]	σ^c_2 (MPa)	6.8	10.3	8.6	8.8	9.3	10.9
Rigaud et al.[55]	ε_1	0.000114	0.000159	0.000160	0.000122	0.000201	0.000186
Rigaud et al.[55]	$\varepsilon_{min\text{-}ppt}$	0.004800	0.002600	0.004800	0.002500	0.003800	0.003900
Qian and Li[54]	σ^c_1 (MPa)	6.9	10.3	9.1	8.3	9.3	10.5
Qian and Li[54]	ε_1	0.000115	0.000205	0.000168	0.000151	0.000181	0.000200
Qian and Li[54]	$\varepsilon_{min\text{-}simp}$	0.004400	0.002900	0.004600	0.002500	0.003800	0.003900
DTT	σ^c_1 (MPa)	7.6	—	7.7	7.1	9.5	9.5
DTT	ε_1	0.000130	—	0.000140	0.000110	0.000160	0.000165
DTT	$\varepsilon_{min\text{-}dtt}$	0.005600	—	0.003000	0.001500	0.003900	0.005200

1 MPa = 0.145 ksi.

—The data from this particular set of test specimens did not produce data that could be summarized in this table.

Table 40. General comparison of the results derived from inverse analysis methods with the DTTs results (average curves) used as reference.

Average Curve	Comparison	Tensile Strength (Percent)	Strain Capacity (Percent)
Baby et al.[18]	Global trend	Overestimation	Overestimation
Baby et al.[18]	Average deviation	+3.5	+38
Baby et al.[18]	Maximum deviation	+7.8	+51
Baby et al.[18]	Minimum deviation	–0.5	+18
Rigaud et al.[55]	Global trend	Overestimation	Overestimation
Rigaud et al.[55]	Average deviation	+6.4	+26
Rigaud et al.[55]	Maximum deviation	+10.8	+46
Rigaud et al.[55]	Minimum deviation	+2.7	+0
Baby et al.[19]	Global trend	Overestimation	Overestimation
Baby et al.[19]	Average deviation	+4.5	+41
Baby et al.[19]	Maximum deviation	+7.8	+55
Baby et al.[19]	Minimum deviation	+0.0	+11
Qian and Li[54]	Global trend	Overestimation	Overestimation
Qian and Li[54]	Average deviation	+10.7	+28
Qian and Li[54]	Maximum deviation	+14.5	+48
Qian and Li[54]	Minimum deviation	+7.3	+6

Table 41. General comparison of the results derived from inverse analysis methods with the DTTs results (characteristic curves) used as reference.

Characteristic Curve	Comparison	Tensile Strength (Percent)	Strain Capacity (Percent)
Baby et al.[18]	Global trend	No trend	Overestimation
Baby et al.[18]	Average deviation	–2.1	+31
Baby et al.[18]	Maximum deviation	+8.5	+44
Baby et al.[18]	Minimum deviation	–23	+12
Rigaud et al.[55]	Global trend	Overestimation	Overestimation
Rigaud et al.[55]	Average deviation	+5.2	+11
Rigaud et al.[55]	Maximum deviation	+16.1	+28
Rigaud et al.[55]	Minimum deviation	–14	–17
Baby et al.[19]	Global trend	No trend	Overestimation
Baby et al.[19]	Average deviation	+1.4	+31
Baby et al.[19]	Maximum deviation	+10.3	+45
Baby et al.[19]	Minimum deviation	–17.4	+13
Qian and Li[54]	Global trend	Overestimation	Overestimation
Qian and Li[54]	Average deviation	+7.7	+9
Qian and Li[54]	Maximum deviation	+20.7	+28
Qian and Li[54]	Minimum deviation	–12.3	–27

In terms of strength, the proposed point-by-point inverse analysis methods slightly overestimated the strength when considering average curves and underestimated the postcracking stress when considering characteristic curves. For example, the Rigaud et al. method and the Qian and Li simplified inverse method slightly overestimated the stress for average and characteristic curves.[55,54]

In terms of strain, the Rigaud et al. method and the Qian and Li method results were closer to the DTT results than the proposed inverse procedure. Nevertheless, this smaller deviation was due to the co-existence of the following two opposed effects when considering the Rigaud et al. method and the Qian and Li method:

- The flexural tests involve an overestimation of the strain capacity due to the fact that the side under higher tension corresponds to the zone where the preferential orientation of fibers is optimal. This phenomenon has already been observed by Tailhan et al. on a multiscale, cement-based composite.[38] Completing the tests on larger prisms would minimize the strain gradient effect and thus would allow the results to be closer to the DTT results. Investigating this size effect was outside of the scope of this experimental program.

- As explained previously, the Rigaud et al. and the Qian and Li methods underestimate the real strain capacity in flexural configuration due to the mechanical assumption used to convert the deflection into curvature.[55,54]

In terms of strength, the comparison between DTT results and both inverse methods based on flexural tests presents different results when considering the average or characteristic curves. This change is due to a statistical size effect. For the flexural tests, the tensile area is smaller than in the DTTs. As a consequence, on average, the results are better for flexural tests, but the impact of an eventual composite (matrix and fibers) flaw is greater and the standard deviation is more important. Thus, the characteristic strength can be inferior for flexural tests.

COMPARISON OF DTT, FT, AND SCT RESULTS

All three general tension tests implemented in this study afford an indication of the tensile cracking strength of the UHPC. Table 42 provides a compilation of cracking strength results previously presented elsewhere in this report. The DTT cracking strength values relate to the average stress during the multicracking phase, as presented in table 10. The FT cracking strength values relate to the average limit of linearity, as presented in table 38. Values from test specimens that exhibited multiple macrocracking in bending are not provided since these test results cannot be appropriately analyzed through a stress–strain based inverse analysis approach. The split cylinder cracking strength results pertain to the average cracking strength values, as presented in table 37.

Table 42. Comparison of cracking strength test results.

Specimen Group Name	DTT Cracking Strength, MPa (ksi)	FT Cracking Strength, MPa (ksi)	SCT Cracking Strength, MPa (ksi)
B2A-S	9.36 (1.36)	10.30 (1.49)	7.47 (1.08)
B2A-L	—	10.75 (1.56)	7.47 (1.08)
B2A-B	—	9.95 (1.44)	7.47 (1.08)
F1A-S	9.18 (1.33)	10.10 (1.46)	9.54 (1.38)
F1A-L	9.97 (1.45)	10.40 (1.51)	9.54 (1.38)
F1B-S	7.75 (1.12)	*	9.81 (1.42)
F1B-S-Cut	—	9.45 (1.37)	9.81 (1.42)
F1B-L	—	*	9.81 (1.42)
F1C-S	10.49 (1.52)	11.10 (1.61)	11.17 (1.62)
F1C-L	10.59 (1.54)	11.30 (1.57)	11.17 (1.62)
F2A-S	7.76 (1.13)	*	4.99 (0.72)
F2A-L	8.47 (1.23)	9.00 (1.31)	4.99 (0.72)

—Appropriate comparison test not completed.
*Performance of test specimens did not allow for inverse analysis determination of cracking strength.

The results presented for this comparison include all of the FT groups, with corresponding results from the appropriate direct tension and splitting tension groups. The long and short specimen denominations are not relevant to the splitting tension tests, and thus, those results were applied across the relevant batch of UHPC.

Based on the available datasets, a limited number of observations can be presented. In a general sense, the cracking strength results for the B2A, F1A, F1B, and F1C datasets all appear to be within 25 percent of one another. The lone outlier is the splitting tensile results from F2A, which are significantly lower than the corresponding DTT and FT results.

CHAPTER 8. CONCLUSIONS

INTRODUCTION

The research program discussed herein focused on the development of tension test methods for UHPC-class materials. In particular, this investigation developed a DTT method for UHPC, furthered the development of existing FT methods, and developed characteristic tensile stress–strain responses for multiple UHPC formulations. Results from portions of this research program are also published in peer-reviewed journal articles.[17–19] Conclusions resulting from this study are presented in the following subsection. A brief discussion of ongoing and future research related to this topic is presented immediately thereafter.

CONCLUSIONS

The following conclusions are presented based on the research presented in this report.

DTT conclusions include the following:

- The DTT method developed and demonstrated herein presents a reliable, practical method through which the tensile stress–strain response of UHPC can be captured.
- The test method meets key testing requirements, including the ability to be completed on cast or extracted specimens, the ability to be completed quickly, and the ability to be completed in commercially available testing machines.
- The test method, through the avoidance of empirical relationships or sophisticated analyses, affords the opportunity to validate other UHPC tension test methods.
- The use of longer test specimens is recommended. Longer test specimens allow for a reduction in the magnitude of bending stresses imparted during the initial gripping of the test specimen.
- The uniaxial tensile response of UHPC was observed to include four distinct phases. The elastic phase encompasses the straining of the intact cementitious composite and ceases at the first cracking of the matrix. The multicracking phase begins at first cracking of the matrix and continues at a relatively stable stress level while many additional tensile cracks appear. The crack-straining phase begins after multicracking and includes a minimal increase in stress while existing individual cracks widen. The localization phase begins at the conclusion of crack straining when an individual crack begins to significantly widen as the fibers bridging that crack debond and pullout of the matrix.

- The developed test method allows for the determination of the tensile stress–strain response of UHPC and thus facilitates the development of strain-based structural design criteria for this class of concrete.

- The UHPC formulations tested herein tended to express mechanical properties beyond those normally associated with structural concrete. These formulations exhibited elastic modulus in excess of 54 GPa (7,832.04 ksi), tensile cracking strength in excess of 7.6 MPa (1.1 ksi), maximum tensile strength in excess of 8.3 MPa (1.2 ksi), and tensile strain at crack localization in excess of 0.0034.

Prism FT conclusions include the following:

- The FT method developed and demonstrated herein presents a capable means of assessing the tensile stress–strain response of UHPC while minimizing the assumptions that can introduce uncertainty in the results. Specifically, a priori assumption of the shape of the tensile stress–strain response is not required.

- Capturing tensile strain measurements on the tensile face of the prism during an FT is a practical means to facilitate simplification of the inverse analysis through which the tensile stress–strain response is developed.

- This test method tends to report slightly higher tensile strength results than those observed with the DTT. These results also display greater scatter, thus leading to lesser characteristic strength values.

- Larger prism cross sections are recommended, as they can provide a reduced strain gradient in the cross section and, thus, greater accuracy in the tensile response of interest.

SCT conclusions include the following:

- SCT can provide an indication of the tensile cracking strength of the UHPC; however, first cracking must be carefully monitored to ensure that the cracking strength is not overestimated.

- The split cylinder cracking strength tends to be generally similar to the DTT and FT cracking strengths. However, for one set of specimens the split cylinder value was significantly below the corresponding direct and flexure values.

ONGOING AND FUTURE RESEARCH

The results of this study demonstrate both the enhanced tensile mechanical properties of UHPC-class materials while also delivering a practical direct method through which to capture those properties. Further research is underway at FHWA to both refine the details of the test method and to characterize a broader selection of UHPC formulations.[69,70] Future efforts will likely also focus on the replication of the developed direct test method in external laboratories and the eventual standardization of the test method.

REFERENCES

1. Richard, P. and Cheyrezy, M. (1995). "Composition of Reactive Powder Concretes," *Cement and Concrete Research*, *25*(7), pp. 1,501–1,511, Elsevier, Amsterdam, Netherlands.

2. Naaman, A.E. and H.W. Reinhardt (1996). "Characterization of High Performance Fiber Reinforced Cement Composites—HPFRCC," *High Performance Fiber Reinforced Cement Composites 2*, pp. 1–24, E&FN Spon, London, England.

3. Behloul, M. (1996). *Analyse et modélisation du comportement d'un matériau à matrice cimentaire fibrée à ultra hautes performances*, Ph.D. Thesis, E.N.S., Cachan, France.

4. Association Française de Génie Civil– Service d'étude des transports, des routes et de leurs aménagement (AFGC-SETRA). (2002). *Ultra High Performance Fibre-Reinforced Concretes*, Interim Recommendations, SETRA, Bagneux, France.

5. Chanvillard, G. and Rigaud, S. (2003). "Complete Characterization of Tensile Properties of Ductal® UHPFRC According to the French Recommendations," *Proceedings of the Fourth International RILEM Workshop on High-Performance Fiber-Reinforced Cement Composites (HPFRCC4)*, Ann Arbor, MI.

6. Graybeal, B. (2006). *Material Property Characterization of Ultra-High Performance Concrete*, Report No. FHWA-HRT-06-103, Federal Highway Administration, Washington, DC.

7. Walraven, J. (2009). "High Performance Fiber Reinforced Concrete: Progress in Knowledge and Design Codes," *Materials and Structures*, *42*(9), pp. 1,247–1,260, Springer, Paris, France.

8. Toutlemonde, F. and Resplendino, J. (2010). *Designing and Building with UHPFRC: State of the Art and Development*, ISTE-Wiley, London, England.

9. Graybeal, B. (2011). U*ltra-High Performance Concrete*, Report No. FHWA-HRT-11-038, Federal Highway Administration, Washington, DC.

10. Graybeal, B. (2006). *Structural Behavior of Ultra-High Performance Concrete Prestressed I-Girders*, Report No. FHWA-HRT-06-115, Federal Highway Administration, Washington, DC.

11. Fischer, G. and Li, V.C. (2007). "Effect of Fiber Reinforcement on the Response of Structural Members," *Engineering Fracture Mechanics*, *74*(1–2), pp. 258–272, Elsevier, Amsterdam, The Netherlands.

12. Sato, Y., Pansuk, W., Den Uijl, J.A., and Walraven, J.C. (2008). "Shear Capacity of High-Performance Fiber-Reinforced Concrete I-Beams," *Eighth International Symposium on Utilization of High-Strength and High-Performance Concrete*, pp. 369–376, Tokyo, Japan.

13. Graybeal, B. (2009). *Structural Behavior of a Prototype Ultra-High Performance Concrete Pi-Girder*, NTIS Report No. PB2009-115495, Federal Highway Administration, Washington, DC.

14. Baby, F., Billo, J., Renaud, J.C., Massotte, C., Marchand, P., and Toutlemonde, F. (2010). "Shear Resistance of Ultra High Performance Fibre-Reinforced Concrete I-Beams," *Fracture Mechanics of Concrete and Concrete Structures—High Performance, Fiber Reinforced Concrete, Special Loadings and Structural Applications*, pp. 1,411–1,417, Korea Concrete Institute, Seoul, Korea.

15. Toutlemonde, F., Foure, B., Sorelli, L., Baby, F., Marchand, P., and Ulm, F.J. (2010). "An Overview of Research Advances from 2002 Concerning UHPFRC, in View of Updating AFGC Recommendations," *Designing and Building with UHPFRC: State of the Art and Development*, ISTE-Wiley, London, England.

16. Bertram, G. and Hegger, J. (2010). "Pretensioned UHPC Beams With and Without Openings," *Proceedings of Third International Federation of Structural Concrete (fib) International Congress*, Washington, DC.

17. Graybeal, B. and Baby, F. (2013). "Development of a Direct Tension Test Method for Ultra-High-Performance Fiber-Reinforced Concrete," *ACI Materials Journal, 110*(2), pp. 177–186, American Concrete Institute, Farmington Hills, MI.

18. Baby, F., Graybeal, B., Marchand, P., and Toutlemonde, F. (2012). "A Proposed Flexural Test Method and Associated Inverse Analysis for UHPFRC," *ACI Materials Journal, 109*(5), pp. 545–555, American Concrete Institute, Farmington Hills, MI.

19. Baby, F., Graybeal, B., Marchand, P., and Toutlemonde, F. (2012). "UHPFRC Tensile Behavior Characterization: Inverse Analysis of Four-Point Bending Test Results," *Materials and Structures, 46*(8), pp. 1,337–1,354, Springer, Paris, France.

20. ASTM C78. (2008). "Standard Test Method for Flexural Strength of Concrete (Using Simple Beam with Third-Point Loading)," *Book of Standards Volume 04.02*, ASTM International, West Conshohocken, PA.

21. ASTM C496. (2002). "Standard Test Method for Splitting Tensile Strength of Cylindrical Concrete Specimens," *Book of Standards Volume 04.02*, ASTM International, West Conshohocken, PA.

22. ASTM C1609. (2010). "Standard Test Method for Flexural Performance of Fiber-Reinforced Concrete (Using Beam with Third-Point Bending)," *Book of Standards Volume 04.02*, ASTM International, West Conshohocken, PA.

23. Graybeal, B. (2006). "Practical Means for Determination of the Tensile Behavior of Ultra-High Performance Concrete," *Journal of ASTM International, 3*(8), 9, ASTM International, West Conshohocken, PA.

24. Gonnerman, H. and Shuman, E. (1928). “Compression, Flexural and Tension Tests of Plain Concrete,” ASTM *Proceedings*, *28*, pp. 527–564, ASTM International, West Conshohocken, PA.

25. Bureau of Reclamation. (1992). *Procedure for Direct Tensile Strength, Static Modulus of Elasticity, and Poisson’s Ratio of Cylindrical Concrete Specimens in Tension* (USBR 4914-92), *Concrete Manual, Part 2*, 9th Edition, U.S. Department of Interior, Washington, DC.

26. RILEM TC 162-TDF. (2001). “Test and Design Methods for Steel Fibre Reinforced Concrete—Recommendations: Uni-axial Tension Test for Steel Fibre Reinforced Concrete,” *Materials and Structures*, *34*(1), pp. 3–6, Springer, Paris, France.

27. Chanvillard, G. and Rigaud, S. (2003). “Complete Characterization of Tensile Properties of Ductal® UHPFRC According to the French Recommendations,” *Proceedings of the 4th International RILEM Workshop on High Performance Fiber Reinforced Cement Composites (HPFRCC4)*, p. 14, Ann Arbor, MI.

28. Wang, Y., Li, V.C., and Backer, S. (1990). “Experimental Determination of Tensile Behavior of Fiber Reinforced Concrete,” *ACI Materials Journal*, *87*(5), pp. 461–468, American Concrete Institute, Farmington Hills, MI.

29. Casanova, P. and Rossi, P. (1997). “Analysis and Design of Steel Fiber Reinforced Concrete Beams,” *ACI Structural Journal*, *94*(5), pp. 595–602, American Concrete Institute, Farmington Hills, MI.

30. Rossi, P. (1997). “High Performance Multimodal Fiber Reinforced Cement Composites (HPMFRCC): The LCPC Experience,” *ACI Materials Journal*, *94*(6), pp. 478–483, American Concrete Institute, Farmington Hills, MI.

31. Zhang, J., Stang, H., and Li, V. (2000). “Experimental Study on Crack Bridging in FRC Under Uniaxial Fatigue Tension,” *Journal of Materials in Civil Engineering*, *12*(1), pp. 66–73, American Society of Civil Engineers, Reston, VA.

32. Zheng, W., Kwan, A.K.H., and Lee, P.K.K. (2001). “Direct Tension Test of Concrete,” *ACI Materials Journal*, *98*(1), pp. 63–71, American Concrete Institute, Farmington Hills, MI.

33. Morris, A.D. and Garrett, G.G. (1981). “A Comparative Study of the Static and Fatigue Behavior of Plain and Steel Fibre Reinforced Mortar in Compression and Direct Tension,” *International Journal of Cement Composites and Lightweight Concrete*, *3*(2), pp. 73–91, Elsevier, Amsterdam, The Netherlands.

34. Saito, M. and Imai, S. (1983). “Direct Tensile Fatigue of Concrete by the Use of Friction Grips,” *ACI Journal*, *80*(5), pp. 431–438, American Concrete Institute, Farmington Hills, MI.

35. Dwarakanath, H.V. and Nagaraj, T.S. (1991). “Comparative Study of Predictions of Flexural Strength of Steel Fiber Concrete,” *ACI Structural Journal*, *88*(6), pp. 714–720, American Concrete Institute, Farmington Hills, MI.

36. Phillips, D.C. and Zhang, B.S. (1993). “Direct Tension Test on Notched and Unnotched Plain Concrete Specimens,” *Magazine of Concrete Research*, *45*(162), pp. 25–35, Institution of Civil Engineers, London, United Kingdom.

37. Boulay, C., Rossi, P., and Tailhan, J.-L. (2004). “Uniaxial Tensile Test on a New Cement Composite Having a Hardening Behaviour,” *Proceedings of the Sixth RILEM Symposium on Fibre-Reinforced Concretes (FRC)*, pp. 61–68, Varenna, Italy.

38. Tailhan, J.-L., Rossi, P., and Parant, E. (2004). “Inverse Numerical Approach to Determine the Uniaxial Tensile Behaviour of a Stress Hardening Cement Composite From Its Bending Behaviour,” *Proceedings of the Sixth RILEM Symposium on Fibre-Reinforced Concretes (FRC)*, pp. 913–922, Varenna, Italy.

39. Jungwirth J. (2006). *Zum Tragverhalten von zugbeanspruchten Bauteilen aus Ultra-Hochleistungs-Faserbeton*, Thesis No. 3429, École Polytechnique Fédérale de Lausanne, Lausanne, Switzerland.

40. Japan Society of Civil Engineers. (2008). “Recommendations for Design and Construction of High Performance Fiber Reinforced Cement Composites with Multiple Fine Cracks”, *Concrete Engineering Series 82*, Japan Society of Civil Engineers, Tokyo, Japan.

41. Wille, K., Kim, D.J., and Naaman, A.E. (2010). “Strain-Hardening UHP-FRC with Low Fiber Contents,” *Materials and Structures*, *44*(3), pp. 583–598, Springer, Paris, France.

42. Gopalaratnam, V. and Shah, S. (1985). “Softening Response of Plain Concrete in Direct Tension,” *ACI Journal*, *82*(3), pp. 310–323, American Concrete Institute, Farmington Hills, MI.

43. Kosa, K. and Naaman, A.E. (1990). “Corrosion of Steel Fiber Reinforced Concrete,” *ACI Materials Journal*, *87*(1), pp. 27–37, American Concrete Institute, Farmington Hills, MI.

44. Li, Z., Kulkarni, S.M., and Shah, S.P. (1993). “New Test Method for Obtaining Softening Response of Unnotched Concrete Specimen Under Uniaxial Tension,” *Experimental Mechanics*, *33*(3), pp. 181–188, Springer, Heidelberg, Germany.

45. Graybeal, B. (2010). *Simultaneous Structural and Environmental Loading of an Ultra-High Performance Concrete Component*, NTIS Report No. PB2010-110331, Federal Highway Administration, Washington, DC.

46. ASTM C39. (2001). “Standard Test Method for Compressive Strength of Cylindrical Concrete Specimens,” *Book of Standards Volume 04.02*, ASTM International, West Conshohocken, PA.

47. ASTM C469. (2002). “Standard Test Method for Static Modulus of Elasticity and Poisson’s Ratio of Concrete in Compression,” *Book of Standards Volume 04.02*, ASTM International, West Conshohocken, PA.

48. Graybeal, B. (2010). *Simultaneous Structural and Environmental Loading of an Ultra-High Performance Concrete Component*, NTIS Report No. PB2010-110331, Federal Highway Administration, Washington, DC.

49. ASTM E8. (2009). "Standard Test Methods for Tension Testing of Metallic Materials," *Book of Standards Volume 03.01*, ASTM International, West Conshohocken, PA.

50. Graybeal, B. (2009). *Structural Behavior of a 2nd Generation Ultra-High Performance Concrete Pi-Girder*, NTIS Report No. PB2009-115496, Federal Highway Administration, Washington, DC.

51. RILEM TC162-TDF. (2002). "Test and Design Methods for Steel Fibre Reinforced Concrete: Recommendations: Bending Test," *Materials and Structures*, *35*(9), pp. 579–582, Springer, Paris, France.

52. Ostergaard, L., Walter, R., and Olesen, J. (2005). "Method for Determination of Tensile Properties of Engineered Cementitious Composites (ECC)," *Proceedings of the Third International Conference on Construction Materials: Performance, Innovations and Structural Innovations (ConMat'05)*, Vancouver, British Columbia, Canada.

53. Kanakubo, T. (2006). "Tensile Characteristics Evaluation Method for DFRCC," *Journal of Advanced Concrete Technology*, *4*(1), pp. 3–17, Japan Concrete Institute, Tokyo, Japan.

54. Qian, S. and Li, V.C. (2008). "Simplified Inverse Method for Determining the Tensile Properties of SHCCs," *Journal of Advanced Concrete Technology*, *6*(2), pp. 353–363, Japan Concrete Institute, Tokyo, Japan.

55. Rigaud, S., Chanvillard, G., and Chen, J. (2011). "Characterization of Bending and Tensile Behaviors of Ultra-High Performance Concrete Containing Glass Fibers," *Proceedings of High Performance Fiber Reinforced Cement Composites 6*, pp. 359–366, Ann Arbor, MI.

56. JCI-S-003-2005. (2006). "Method of Test for Bending Moment-Curvature Curve of Fiber Reinforced Cementitious Composites," *Journal of Advanced Concrete Technology*, *4*(1), pp. 73–78, Japan Concrete Institute, Tokyo, Japan.

57. Kanakubo, T. (2006). "Tensile Characteristics Evaluation Method for DFRCC," *Journal of Advanced Concrete Technology*, *4*(1), pp. 3–17, Japan Concrete Institute, Tokyo, Japan.

58. Japan Concrete Institute. (2007). *Method of test for bending moment–curvature curve of fiber-reinforced cementitious composites*, Japan Concrete Institute Standard JCI-S-003-2007, Japan Concrete Institute, Tokyo, Japan. Available online: http://www.jci-net.or.jp/j/jci/study/jci_standard/JCI-S-003-2007-e.pdf, last accessed May 31, 2018.

59. Qian, S. and Li, V.C. (2007). "Simplified Inverse Method for Determining the Tensile Strain Capacity of SHCCs," *Journal of Advanced Concrete Technology*, *5*(2), pp. 235–246, Japan Concrete Institute, Tokyo, Japan.

60. Qian, S., Li, V.C., and Zhou, J. (2010). "Relating Tensile Properties with Flexural Properties in SHCC," *Proceedings of Fracture Mechanics for Concrete and Concrete Structures (FRAMCOS)-7*, Jeju, South-Korea.

61. Maalej, M. and Li, V.C. (1994). "Flexural/Tensile Strength Ratio in Engineered Cementitious Composites," *Journal of Materials in Civil Engineering*, *6*(4), pp. 513–528, American Society of Civil Engineers, Reston, VA.

62. Kabele, P. and Horii, H. (1997). "Analytical Model for Fracture Behavior of Pseudo Strain-Hardening Cement Composites," *Concrete Library International*, *29*, pp. 105–120, Japan Society of Civil Engineers, Tokyo, Japan.

63. Olesen, J.F. (2001). "Fictitious Crack Propagation in Fiber-Reinforced Concrete Beams," *Journal of Engineering Mechanics*, *127*(3), pp. 272–280, American Society of Civil Engineers, Reston, VA.

64. ASTM C1018. (1997). "Standard Test Method for Flexural Toughness and First-Crack Strength of Fiber-Reinforced Concrete (Using Beam With Third-Point Loading)," *Book of Standards Volume 04.02*, ASTM International, West Conshohocken, PA.

65. Parant, E. and Rossi, P. (2008). "Damage Mechanisms Analysis of a Multi-Scale Fibre Reinforced Cement-Based Composite Subjected to Impact and Fatigue Loading Conditions," *Cement and Concrete Research*, *38*(3), pp. 413–421.

66. Rossi, P., Arca, A., Parant, E., and Fakhri, P. (2005). "Bending and Compressive Behaviors of a New Cement Composite," *Cement and Concrete Research*, *35*(1), pp. 27–33, Elsevier, Amsterdam, The Netherlands.

67. Baby, F. (2012). *Contribution to Identification of UHPFRC Tensile Constitutive Behaviour and Accounting for Structural Design*, Ph.D. Dissertation, Paris-Est University, Paris, France.

68. Wille, K. and Naaman A.E. (2010). "Fracture Energy of UHP-FRC Under Direct Tensile Loading," *Proceedings of Fracture Mechanics for Concrete and Concrete Structures (FRAMCOS)-7*, Jeju, South-Korea.

69. Graybeal, B. (2015). "Tensile Mechanical Response of Ultra-High-Performance Concrete," *ASTM Advances in Civil Engineering Materials*, *4*(2), pp. 62–74, ASTM International, West Conshohocken, PA.

70. Maya Duque, L.F. and Graybeal, B. (2017). "Fiber Orientation Distribution and Tensile Mechanical Response of UHPFRC," *Materials and Structures*, *50*(1), p. 17, Springer, Paris, France.

HRDI-40/02-19(WEB)E